Measurement of the WW Production Cross Section in Proton-Proton Collisions at $\sqrt{s} = 8$ TeV with the ATLAS Detector and Limits on Anomalous Triple Gauge Boson Couplings

A Dissertation presented

by

Karen Chen

to

The Graduate School

in Partial Fulfillment of the

Requirements

for the Degree of

Doctor of Philosophy

in

Physics

Stony Brook University

August 2015

Stony Brook University

The Graduate School

Karen Chen

We, the dissertation committee for the above candidate for the

Doctor of Philosophy degree, hereby recommend

acceptance of this dissertation

John Hobbs - Dissertation Advisor
Professor, Physics and Astronomy

Abhay Deshpande - Chairperson of Defense
Professor, Physics and Astronomy

Patrick Meade - Internal Member
Assistant Professor, Physics and Astronomy

James Cochran - External Member
Professor, Physics and Astronomy, Iowa State University

This dissertation is accepted by the Graduate School

Charles Taber
Dean of the Graduate School

Abstract of the Dissertation

Measurement of the WW Production Cross Section in Proton-Proton Collisions at $\sqrt{s} = 8$ TeV with the ATLAS Detector and Limits on Anomalous Triple Gauge Boson Couplings

by

Karen Chen

Doctor of Philosophy

in

Physics

Stony Brook University

2015

WW production serves as an important test of the electroweak sector in the Standard Model. It can be sensitive to gauge boson self interactions as well as Higgs boson interactions. Deviations from the Standard Model prediction could arise from anomalous triple gauge couplings or the production of new particles that decay into electroweak bosons. Searches for new physics phenomena are conducted at high energy scales, but in order to constrain them at the electroweak scale, we need precision measurements of Standard Model processes.

In this Dissertation, the WW production cross section is measured with p-p collisions at $\sqrt{s} = 8$ TeV with 20.3 fb^{-1} of data collected by the ATLAS detector. We only consider WW production in the fully leptonic decay channels. The experimental signature consists of two oppositely charged leptons (e or μ) with additional $E_{\mathrm{T}}^{\mathrm{miss}}$. The main background contributions are Z+jets, top, W+jets, and other diboson production (WZ/ZZ/W$\gamma^{(*)}$). Data driven methods are used to estimate each background contribution except for the other diboson backgrounds, which are estimated from Monte Carlo simulations. Experimental and theoretical sources of systematic uncertainties are assessed and propagated to the final results. The measured total cross section is $71.0^{+1.1}_{-1.1}(\text{stat})^{+3.2}_{-3.1}(\text{theory})^{+4.8}_{-3.9}(\text{exp})^{+2.1}_{-2.0}(\text{lumi})$ pb.

An unfolding method is applied on differential cross section measurements to give kinematic distributions that can be compared directly to theoretical predictions. The differential leading lepton p_{T}distribution is used to search for anomalous WWZ and WWγ triple gauge couplings. The data is fitted and all coupling parameters are found to be consistent with the Standard Model values. 95% confidence level interval limits on anomalous coupling are derived and the limits are improved with respect to the previous 7 TeVWW analysis.

I dedicate this Dissertation to my family

Table of Contents

Contents

List of Figures

List of Tables

Acknowledgements

First and foremost, I want to thank my advisor and mentor, Professor John Hobbs. It's quite rare to find an advisor who is so knowledgeable and experienced in the field, but also understanding, supportive, and patient with his students. He was always there to talk, even when we were an ocean apart. He's an amazing mentor and I consider myself very lucky to be his student.

Of course, I must thank the members of the WW analysis team for their years of hard work. I want to especially thank the main analyzers: Marc-Andre, Dimitra, Yusheng, Kristin, Philip, Haolu, Jun, Jiri and Martin. This dissertation doesn't fully reflect the amount of work that really went into this analysis, since many of the cross checks and additional studies aren't included here.

I also want to acknowledge the members of the High Energy Physics group at Stony Brook. I want to thank Rafael Lopes de Sá, who I consider my big physics family brother, for showing me what real passion for physics looks like. I also want to thank Dean Schamberger, whose efforts at maintaining our computer cluster is often under-appreciated.

I also want to mention my fellow Stony Brook graduate students. I'm glad to be a part of such a collaborative environment and able to know such a diverse group of people. I want to especially thank my fellow board game players, in particular David Puldon and Ciprian Gal, for showing me that the best way to make lasting friends is to lie, betray, and mislead them every week in board games.

I could not have even made it to graduate school without the encouragement from Professor Michael Graf and Ryan Johnson from Boston College. You showed me what physics research is really like and gave me the confidence to grow into the person I am today.

Finally, this Dissertation could not have been possible without the continued support of my family and friends back home. I want to thank my parents for their years of hard work and love. I also want to thank my friends back home, Ming and Jenny, for keeping a place for me there even though I've been away for so long.

1 Theory and Introduction

1.1 Standard Model

The Standard Model (SM) [1] is a gauge theory that describes the electromagnetic, strong, and weak forces and interactions of the force carriers with quarks and leptons. Quantum electrodynamics (QED) is explained in Section 1.1.1. The strong force, color charge, and quarks are explained in Section 1.1.2 on quantum chromodynamics (QCD). The electroweak theory that unifies QED with the weak force is described in Section 1.1.3 and a description of electroweak symmetry breaking due to the Higgs mechanism can be found in Section 1.1.4.

1.1.1 Quantum Electrodynamics

The Lagrangian for theory of quantum electrodynamics (QED) is

$$\mathcal{L}_{QED} = -\frac{1}{4}F_{\mu\nu}F^{\mu\nu} + \bar{\psi}(i\not{D})\psi \tag{1}$$

where $F_{\mu\nu}$ is the electromagnetic field tensor, ψ is the spinor field of spin $\frac{1}{2}$ particles (e.g. electrons), and D_μ is the gauge covariant derivative. The Feynman slash notation, used in $\not{D}$ above, is defined for a four vector V as $\not{V} \equiv \gamma^\mu V_\mu$ with γ the usual relativistic gamma matrices.

$$\begin{aligned} F_{\mu\nu} &= \partial_\mu A_\nu - \partial_\nu A_\mu \\ D_\mu &= \partial_\mu + ieA_\mu \end{aligned} \tag{2}$$

where A^μ is the electromagnetic vector potential. The QED Lagrangian is invariant ($\delta\mathcal{L} = 0$) under the gauge transformation

$$\begin{aligned} \psi(x) &\rightarrow e^{i\alpha(x)}\psi(x) \\ A_\mu &\rightarrow A_\mu + \frac{1}{e}\partial_\mu\alpha(x) \end{aligned} \tag{3}$$

It is important to note that the A_μ field cannot have a mass term of the form $\frac{1}{2}m_\gamma^2 A_\mu A^\mu$ since this will break gauge invariance.

$$\frac{1}{2}m_\gamma^2 A_\mu A^\mu \rightarrow \frac{1}{2}m_\gamma^2\left(A_\mu + \frac{1}{e}\partial_\mu\alpha(x)\right)\left(A^\mu + \frac{1}{e}\partial^\mu\alpha(x)\right) \neq \frac{1}{2}m_\gamma^2 A_\mu A^\mu \tag{4}$$

This is not a problem for the photon field, A_μ, since the photon is known to be massless, but the same principle will hold for the electroweak model with the W and Z gauge bosons, which are known to be massive. At this point, this symmetry does not allow for the generation of massive gauge bosons, but it will be shown that the W and Z bosons acquire mass through spontaneous symmetry breaking with the Higgs mechanism.

Gauge invariance is not surprising given that in quantum mechanics, observables cannot depend on the phase of the wavefunction, only on the overall magnitude. This U(1) symmetry leads to conservation of electric charge. This follows from Noether's theorem, which states that for every symmetry in theory, there is a corresponding conserved current. In other words, when the Lagrangian is invariant under a set of changes, this leads to a conserved quantity or charge. In this case, the conserved quantity is the electric charge. It is no coincidence that e, the symbol used to represent the electric charge of an electron, is used as the coupling constant in Equation 2.

1.1.2 Quantum Chromodynamics

There are six flavors of quarks with fractional charge Qe. Quarks can fall into two classes:

- up type quarks: *up*, *charm*, and *top* (or u, c, t) with $Q = +2/3$
- down type quarks: *down*, *strange*, and *bottom* (or d, s, b) with $Q = -1/3$.

The (u, d) pairs make up a quark generation, and each generation is represented by a left handed doublet and right handed singlets in the following way:

$$\psi_u^{(L)} = \begin{pmatrix} u^{(L)} \\ d'^{(L)} \end{pmatrix}, \psi_c^{(L)} = \begin{pmatrix} c^{(L)} \\ s'^{(L)} \end{pmatrix}, \psi_t^{(L)} = \begin{pmatrix} t^{(L)} \\ b'^{(L)} \end{pmatrix}; u^{(R)}, s^{(R)}, t^{(R)}, c^{(R)}, s^{(R)}, b^{(R)} \tag{5}$$

Here, the negative isospin entries d', s', and b' from the left handed doublets are not the same as the fields d, s, and b. They are related by a unitary transformation, V_{ij}, defined by

$$\begin{pmatrix} d' \\ s' \\ b' \end{pmatrix} = \begin{pmatrix} V_{ud} & V_{us} & V_{ub} \\ V_{cd} & V_{cs} & V_{cb} \\ V_{td} & V_{ts} & V_{tb} \end{pmatrix} \begin{pmatrix} d \\ s \\ b \end{pmatrix} \tag{6}$$

This matrix is called the Cabibbo-Kobayashi-Maskawa (CKM) matrix. It was extended from a 2 × 2 matrix after the discovery of Charge-Parity (CP) violation which requires not two, but three quark generations.

In addition to having electric charge and isospin quantum numbers, quarks also have a color charge. Gluons mediate color change between quarks and act as the strong force carrier, analogously to photons as the electromagnetic force carrier in QED. The $SU(3)$ gauge theory describing the strong interaction between quarks and gluons is called quantum chromodynamics (QCD). The Lagrangian for QCD is given by

$$\mathcal{L}_{QCD} = -\frac{1}{4} F^i_{\mu\nu} F^{i\mu\nu} + \bar{\psi}(i \not{D})\psi \tag{7}$$

where ψ, are color fields, $F^i_{\mu\nu}$ is the field strength tensor for the eight gluon fields, G^i_μ, where $i = 1, \ldots, 8$, and D_μ is the covariant derivative.

$$F^i_{\mu\nu} = \partial_\mu G^i_\nu - \partial_\nu G^i_\mu - g_s f^{ijk} G^j_\mu G^k_\nu \tag{8}$$

$$D_\mu = \partial_\mu + i g_s G^i_\mu \left(\frac{1}{2} \lambda^i \right) \tag{9}$$

where g_s is the QCD gauge coupling constant, and f_{ijk} are the structure constants of $SU(3)$ defined by the generators of SU(3), T^i.

$$[T^i, T^j] = i f_{ijk} T^k \tag{10}$$

The QCD Lagrangian is invariant under the unitary transformation defined below:

$$U = e^{i\theta_a t^a} \tag{11}$$

$$\psi_i \to U\psi_i = \psi_i + i\theta_a T^a_{ij}\psi_j + ... \tag{12}$$

$$G^a_\mu \to UG^a_\mu U^\dagger - \frac{1}{g_s}(\partial_\mu U)U^\dagger = G^a_\mu - \frac{1}{g_s}\partial_\mu\theta_a - f_{abc}\theta_b G^c_\mu ... \tag{13}$$

This SU(3) symmetry leads to color conservation. In Feynman diagrams, it is often useful to represent gluons as two color and anti-color lines and quarks as a single color line. An example is given in Figure 1. The eight gluon color states can be represented in many ways, but this particular representation is equivalent to the Gell-Mann matrices. The Gell-Mann matrices, λ^i, are related to the generators by $T^i = \lambda_i/2$ and are listed below:

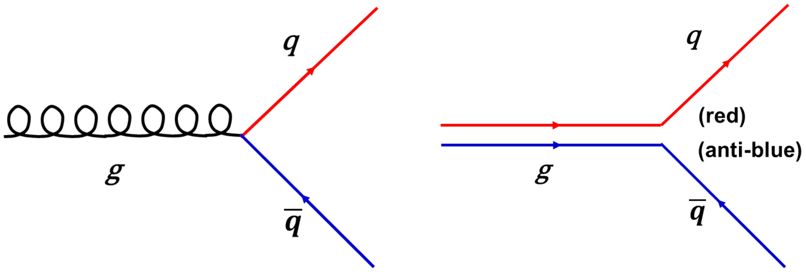

Figure 1: Gluons in Feynman diagrams. Two equivalent ways of representing color exchange between quarks where the gluon is represented by curls (left) or two colored lines (right).

$$\lambda^1 = \begin{pmatrix} 0 & 1 & 0 \\ 1 & 0 & 0 \\ 0 & 0 & 0 \end{pmatrix}, \quad \lambda^2 = \begin{pmatrix} 0 & i & 0 \\ -i & 0 & 0 \\ 0 & 0 & 0 \end{pmatrix}, \quad \lambda^3 = \begin{pmatrix} 1 & 0 & 0 \\ 0 & -1 & 0 \\ 0 & 0 & 0 \end{pmatrix},$$
$$\lambda^4 = \begin{pmatrix} 0 & 0 & 1 \\ 0 & 0 & 0 \\ 1 & 0 & 0 \end{pmatrix}, \quad \lambda^5 = \begin{pmatrix} 0 & 0 & -i \\ 0 & 0 & 0 \\ i & 0 & 0 \end{pmatrix},$$
$$\lambda^6 = \begin{pmatrix} 0 & 0 & 0 \\ 0 & 0 & 1 \\ 0 & 1 & 0 \end{pmatrix}, \quad \lambda^7 = \begin{pmatrix} 0 & 0 & 0 \\ 0 & 0 & -i \\ 0 & i & 0 \end{pmatrix}, \quad \lambda^8 = \begin{pmatrix} 1 & 0 & 0 \\ 0 & 1 & 0 \\ 0 & 0 & -2 \end{pmatrix}, \tag{14}$$

The gluon octet is given by

$$\begin{aligned} G^i = \Big\{ & \frac{1}{\sqrt{2}}\left(r\bar{b} + b\bar{r}\right), && \frac{-i}{\sqrt{2}}\left(r\bar{b} - b\bar{r}\right), && \frac{-i}{\sqrt{2}}\left(r\bar{r} + b\bar{b}\right), \\ & \frac{1}{\sqrt{2}}\left(r\bar{g} + g\bar{r}\right), && \frac{-i}{\sqrt{2}}\left(r\bar{g} - g\bar{r}\right), \\ & \frac{1}{\sqrt{2}}\left(b\bar{g} + g\bar{b}\right), && \frac{-i}{\sqrt{2}}\left(b\bar{g} - g\bar{b}\right), && \frac{-i}{\sqrt{6}}\left(r\bar{r} + b\bar{b} - 2g\bar{g}\right) \Big\} \end{aligned} \tag{15}$$

Given that gluons are given by a color and anti-color state and that there are three colors, one would expect nine gluons in total, but there are only eight listed above. Indeed, there is a ninth singlet state but it is not included in the theory.

$$\text{Singlet } G^9 = \frac{1}{\sqrt{3}}\left(r\bar{r} + b\bar{b} + g\bar{g}\right) \tag{16}$$

This singlet state is not included because its existence would allow for an unconfined gluon that can reach long distances. The strong force, as we understand it, is limited to short distances so the singlet state is forbidden.

1.1.3 Electroweak Theory

Leptons are spin $\frac{1}{2}$ particles that can interact with the electromagnetic and weak forces. There are total of six lepton flavors, three of which have charge $\pm 1e$ and three which are neutral (neutrinos).

- charged leptons: electron (e), muon (μ), and tau lepton (τ)
- neutrinos: electron neutrino (ν_e), muon neutrino (ν_μ) and tau neutrino (ν_τ)

Each ℓ, ν_ℓ pair makes up a leptonic generation. The electroweak theory uses three left-handed leptonic $SU(2)$ weak isospin doublets, $\psi_\ell^{(L)}$, and three right-handed singlets, $\ell^{(R)}$ with $\ell = e, \mu, \tau$. Since there are no right handed neutrinos, correspondingly, $\nu_e^{(R)}, \nu_\mu^{(R)}, \nu_\tau^{(R)}$ do not appear in the theory.

$$\psi_e^{(L)} = \begin{pmatrix} \nu_e^{(L)} \\ e^{(L)} \end{pmatrix}, \psi_\mu^{(L)} = \begin{pmatrix} \nu_\mu^{(L)} \\ \mu^{(L)} \end{pmatrix}, \psi_\tau^{(L)} = \begin{pmatrix} \nu_\tau^{(L)} \\ \tau^{(L)} \end{pmatrix}; e^{(R)}, \mu^{(R)}, \tau^{(R)}, \tag{17}$$

The electroweak Lagrangian includes gauge couplings and fermionic couplings.

$$\mathcal{L}_{EW} = \mathcal{L}_{gauge} + \mathcal{L}_{fermion} \tag{18}$$

$$\begin{aligned} \mathcal{L}_{gauge} &= -\frac{1}{4} W^a_{\mu\nu} W^{a\mu\nu} - \frac{1}{4} F_{\mu\nu} F^{\mu\nu} \\ W^a_{\mu\nu} &= \partial_\mu W^a_\nu - \partial_\nu W^a_\mu - g\epsilon_{abc} W^b_\mu W^c_\nu \\ F_{\mu\nu} &= \partial_\mu B_\nu - \partial_\nu B_\mu \end{aligned} \tag{19}$$

where W_μ and B_μ are the pure weak SU(2) and electromagnetic U(1) fields. ϵ_{abc} is the structure constant of SU(2). The covariant derivative is defined as

$$D_\mu \equiv \partial_\mu + igW^a_\mu T^a + i\frac{g'}{2} Y B_\mu \tag{20}$$

where $T^a = \sigma^a/2$ are the generators of SU(2) and are related to the Pauli matrices, σ. Y is the U(1) charge, or hypercharge. T^3 is the third component of the weak isospin. Y and T^3

are chosen such that they are related to the electric charge Q in units of e: $Y = 2(Q - T^3)$

$$\begin{aligned}
\mathcal{L}_{fermion} &= \sum_{fermions} \bar{\psi}_F i \not{D} \psi_F \\
&= \sum_{\ell=e,\mu,\tau} \bar{\psi}_\ell^{(L)} \left[i\not{\partial} - g \not{W}_a \left(\frac{1}{2}\sigma_a\right) + \frac{1}{2} g' \not{B} \right] \psi_\ell^{(L)} \\
&+ \sum_{\ell=e,\mu,\tau} \bar{\ell}^{(R)} \left[i\not{\partial} + g' \not{B} \right] \ell^{(R)} \\
&+ \sum_{q=u,c,t} \bar{\psi}_q^{(L)} \left[i\not{\partial} - g \not{W}_a \left(\frac{1}{2}\sigma_a\right) - \frac{1}{6} g' \not{B} \right] \psi_\ell^{(L)} \\
&+ \sum_{q=u,c,t,d,s,b} \bar{q}^{(R)} \left[i\not{\partial} - g' Q \not{B} \right] q^{(R)}
\end{aligned} \tag{21}$$

The covariant derivative is missing the $igW_\mu T^a$ term for the right handed fields. This is because the weak force can rotate a left-handed lepton into a left-handed neutrino, but since right handed neutrinos do not exist in the Standard Model, it cannot do the same for right handed particles.

Here, the W_μ and B_μ fields and fermions are all massless. In the next section, these fields will form the mass eigenstates that give rise to the massive W and Z bosons.

1.1.4 Spontaneous Symmetry Breaking and Higgs Mechanism

The Higgs mechanism augments the Standard Model Lagrangian with a scalar Higgs field with its own Lagrangian term. The Higgs scalar field is a SU(2) doublet of complex scalar fields, ϕ^+ and ϕ^0.

$$\phi = \begin{pmatrix} \phi^+ \\ \phi^0 \end{pmatrix} \tag{22}$$

The Higgs Lagrangian describing the scalar involves a kinetic term and a potential term.

$$\mathcal{L}_{Higgs} = (D_\mu \phi)^\dagger (D_\mu \phi) - V(\phi) \tag{23}$$

$$V(\phi) = -\mu^2 \phi^\dagger \phi + \lambda (\phi^\dagger \phi)^2 \tag{24}$$

For the unconvential sign choice of $\mu^2 > 0$ (so the “mass squared” term is overall negative), the potential has a minimum at a non-zero value of ϕ.

$$\left(\phi^\dagger \phi\right)_{min} = \frac{\mu^2}{2\lambda} \equiv v^2/2 \tag{25}$$

It is then convenient to reparameterize the real and imaginary parts of ϕ with the real fields $\eta(x)$ and $\xi_i(x)$ $(i = 1, 2, 3)$.

$$\phi = \exp\{i\xi_i \sigma^i / 2v\} \begin{pmatrix} 0 \\ \frac{1}{\sqrt{2}}[v + \eta(x)] \end{pmatrix} \tag{26}$$

Now ϕ is expressed in terms of distance $\eta(x)$ away from the mininum at $v/\sqrt{2}$, and the ξ_i give the position around the three-dimensional minimum. A gauge transformation can be used to cancel out the phase term with the three ξ_i fields such that the field simplifies to

$$\phi = \begin{pmatrix} 0 \\ \frac{1}{\sqrt{2}}[v + \eta(x)] \end{pmatrix} \tag{27}$$

This choice is called the unitary gauge. Using the covariant derivative as defined in Equation 20 with hypercharge Y = 1:

$$D_\mu = \partial_\mu - igW_{\mu,a}\left(\frac{1}{2}\sigma_a\right) + \frac{1}{2}ig'B_\mu \tag{28}$$

The Lagrangian density can be written as

$$(D_\mu\phi)^\dagger(D_\mu\phi) = \frac{1}{2}\frac{v^2}{4}\left[g^2(W_\mu^1)^2 + g^2(W_\mu^2)^2 + (-gW_\mu^3 + g'B_\mu)^2\right] + ... \tag{29}$$

grouped in terms of the mass eigenstates that correspond to the massive $W^\pm$ and Z bosons and massless photon.

$$\begin{aligned} W_\mu^\pm &= \frac{1}{\sqrt{2}}(W_\mu^1 \mp iW_\mu^2) && \text{with mass} && m_W = \frac{1}{2}vg \\ Z_\mu^0 &= \frac{1}{\sqrt{g^2 + g'^2}}(gW_\mu^3 - g'B_\mu) && \text{with mass} && m_Z = \frac{v}{2}\sqrt{g^2 + g'^2} \\ A_\mu &= \frac{1}{\sqrt{g^2 + g'^2}}(g'W_\mu^3 + gB_\mu) && \text{with mass} && m_A = 0 \end{aligned} \tag{30}$$

The fields W_μ^3 and B_μ have been rotated to define Z_μ and A_μ. The angle of rotation, θ_W is called the weak mixing angle or the Weinberg angle.

$$\begin{pmatrix} Z_\mu \\ A_\mu \end{pmatrix} = \begin{pmatrix} \cos\theta_W & -\sin\theta_W \\ \sin\theta_W & \cos\theta_W \end{pmatrix} \begin{pmatrix} W_\mu^3 \\ B_\mu \end{pmatrix} \tag{31}$$

The masses and coupling parameters can be expressed in terms of θ_W.

$$\begin{gathered} \sin\theta_W = \frac{g'}{\sqrt{g^2 + g'^2}}, \qquad \cos\theta_W = \frac{g}{\sqrt{g^2 + g'^2}} = \frac{m_W}{m_Z} \\ e = \frac{gg'}{\sqrt{g^2 + g'^2}}, \qquad g = \frac{e}{\sin\theta_W}, \qquad g' = \frac{e}{\cos\theta_W} \end{gathered} \tag{32}$$

It is important to observe that the coupling constants, g and g', are not independent. They are related by the electric charge, e, and are of the same magnitude.

The fermions acquire mass through Yukawa interactions with the Higgs scalar.

$$\mathcal{L}_{Yukawa} = \sum_{fermions} \Gamma\bar{\psi}_F^{(L)}\phi\psi_F^{(R)} \tag{33}$$

where Γ are the Yukawa couplings for each of the quarks and leptons. If ϕ is in the unitary gauge (Equation 27), then the Yukawa interaction becomes

$$\begin{aligned}\mathcal{L}_{Yukawa} = &\sum_{m,n} \Gamma^{u}_{m,n} \bar{\psi}^{(L)}_{u_m} \left(\frac{v+\eta}{\sqrt{2}}\right) \psi^{(R)}_{u_m} + \Gamma^{d}_{m,n} \bar{\psi}^{(L)}_{u_m} \left(\frac{v+\eta}{\sqrt{2}}\right) \psi^{(R)}_{d_n} \\ &+ \sum_{m} \Gamma^{\ell}_{m} \bar{\psi}^{(L)}_{\ell_m} \left(\frac{v+\eta}{\sqrt{2}}\right) \psi^{(R)}_{\ell_m} \end{aligned} \tag{34}$$

where m, n are the sums over the generations of quarks (u and d) and leptons (ℓ). The Yukawa interaction gives mass terms for the fermions as well as couplings between the Higgs and quarks/leptons. The terms that are proportional to v will lead to masses that depend on the unknown Yukawa couplings.

$$M_{m,n} = \Gamma_{m,n} \frac{v}{\sqrt{2}} \tag{35}$$

In the unitary gauge when $\phi^+ \to 0$, the mass terms for the neutrinos go to zero. The next section will summarize the particles in the Standard Model and their masses.

1.1.5 Summary of Standard Model Particles

The elementary particles of the Standard Model include quarks, leptons, four gauge bosons (gluon, photon, W, and Z boson), and the Higgs boson. Leptons and quarks are both fermions with spin $\frac{1}{2}$. Six leptons (electron, electron neutrino, muon, muon neutrino, tau, and tau neutrino) and six quarks (up, down, top, bottom, charm, and strange) can be paired to form three generations consisting of a pair of leptons or a pair of quarks. Table 1 summarizes the properties of the leptons and quarks. In the Standard model, gauge bosons mediate the electroweak and strong forces. The photon mediates the electromagnetic force, while the W and Z bosons mediate the weak force. Gluons mediate the strong force between color charged particles. The Higgs boson explains the masses of the W and Z bosons through electroweak symmetry breaking and the masses of the fermions from Yukawa interactions. Table 1 summarizes the properties of gauge bosons and the Higgs boson.

Testing the Standard Model WW Production Although the Standard Model has been tested with great precision, the electroweak symmetry breaking sector with the Higgs boson is interesting to study, especially before the discovery of the Higgs boson. One of the ways to probe this sector is to study WW production and and the W and Higgs boson coupling. In addition to explaining the origin of the W and Z masses, the Higgs boson is also responsible for restoring unitarity in longitudinal WW scattering ($W_L W_L \to W_L W_L$). Some of the Feynman diagrams involved with WW scattering can include triple gauge boson self couplings (WWZ or WWγ) or quadratic gauge boson couplings with four W bosons. The sum of these diagrams (excluding those that involve the Higgs boson) will lead to scattering amplitudes that grow with s^2. This means that at sufficiently high energies, the scattering amplitudes will eventually violate unitarity. However, if the diagrams with Higgs and vector boson couplings are included, then the WW scattering amplitude no longer grows with s.

In other words, the the Higgs boson is responsible for restoring unitarity in longitudinal WW scattering ($W_LW_L \rightarrow W_LW_L$). WW production can be used to probe gauge boson self couplings as well as interactions with the Higgs boson in the Standard Model.

Leptons (spin = 1/2)		
Name	Mass (MeV)	Electric Charge
electron neutrino	0	0
electron	0.511	-1
muon neutrino	0	0
muon	105.7	-1
tau neutrino	0	0
tau	1777	-1

Quarks (spin = 1/2)		
Name	Mass (GeV)	Electric Charge
up	2.3×10^{-3}	2/3
down	4.8×10^{-3}	-1/3
charm	1.275	2/3
strange	95×10^{-3}	-1/3
top	173	2/3
bottom	4.18	-1/3

Table 1: Summary of leptons and quarks in the Standard Model. Neutrinos have no mass in the Standard Model, but evidence has shown that they have very small masses up to $\mathcal{O}$(eV) or $\mathcal{O}$(MeV) depending on the neutrino generation.

Electroweak (spin = 1)		
Name	Mass (GeV)	Electric Charge
photon	0	0
W^+ boson	80.4	+1
W^- boson	80.4	-1
Z boson	91.2	0

Strong (spin = 1)		
Name	Mass (GeV)	Electric Charge
gluon	0	0

Higgs (spin = 0)		
Name	Mass (GeV)	Electric Charge
Higgs boson	125	0

Table 2: Summary of gauge bosons and Higgs boson in the Standard Model.

1.2 Beyond the Standard Model

WW production may be sensitive to physics beyond the Standard Model. New physics introduces new production diagrams which can the alter total or differential production cross sections. Examples of beyond the Standard Model physics include theories that involve new particles that decay into vector bosons [2] or decay into leptons with $E_{\mathrm{T}}^{\mathrm{miss}}$, sharing the same final state [3, 4].

1.2.1 Anomalous triple gauge boson couplings

The Lagrangian for beyond the Standard Model physics can be parameterized in terms of anomalous triple gauge boson couplings, which are general constructs independent of any particular model.

$$\begin{aligned} L = ig_{WWV}(g_1^V(W^+_{\mu\nu}W^{-\mu} - W^{+\mu}W^-_{\mu\nu})V^\nu + \kappa_V W^+_\mu W^-_\nu V^{\mu\nu} + \frac{\lambda_V}{M_W^2}W^{\nu+}_\mu W^{-\rho}_\nu V^\mu_\rho \\ + ig_4^V W^+_\mu W^{-\nu}(\partial^\mu V^\nu + \partial^\nu V^\mu) - ig_5^V \epsilon^{\mu\nu\rho\sigma}(W^+_\mu \partial_\rho W^-_\nu - \partial_\rho W^+_\mu W^-_\nu)V_\sigma \\ + \widetilde{\kappa}_V W^+_\mu W^-_\nu \widetilde{V}^{\mu\nu} + \frac{\widetilde{\lambda}_V}{M_W^2} W^{\nu+}_\mu W^-_\nu \widetilde{V}^\mu_\rho) \end{aligned} \tag{36}$$

If only terms that conserve Charge and Parity (C and P) separately are considered,

$$L = ig_{WWV}(g_1^V(W^+_{\mu\nu}W^{-\mu} - W^{+\mu}W^-_{\mu\nu})V^\nu + \kappa^V W^+_\mu W^-_\nu V^{\mu\nu} + \frac{\lambda^V}{M_W^2}W^{\nu+}_\mu W^{-\rho}_\nu V^\mu_\rho)) \tag{37}$$

where V = Z or γ; $W^\pm_{\mu\nu} = \partial_\mu W^\pm_\nu - \partial_\nu W^\pm_\mu$; $V_{\mu\nu} = \partial_\mu V_\nu - \partial_\nu V_\mu$. The overall coupling constants g_{WWV} are given by $g_{WW\gamma} = -e$ and $g_{WWZ} = -e\cot(\theta_W)$.

In the Standard Model, three of these coupling parameters are non-zero: $g_1^Z = 1$, $\kappa^Z = 1$, and $\kappa^\gamma = 1$ and the remainder are zero. Electromagnetic gauge invariance requires that $g_1^\gamma = 1$. When considering the beyond the Standard Model (BSM) Lagrangian, BSM couplings are often expressed as deviations from the Standard Model:

$$\Delta g_1^Z = 1 - g_1^Z; \qquad \Delta\kappa^Z = 1 - \kappa^Z; \qquad \Delta\kappa^\gamma = 1 - \kappa^\gamma \tag{38}$$

Without any further considerations, these gauge boson self-interaction terms with anomalous couplings will violate unitarity at sufficiently high energies. To restore unitarity, dipole form factors are introduced.

$$\Delta g_1^V \to \frac{\Delta g_1^Z}{\left(1+\dfrac{\hat{s}}{\Lambda^2}\right)^2}, \qquad \Delta\kappa^V \to \frac{\Delta\kappa^V}{\left(1+\dfrac{\hat{s}}{\Lambda^2}\right)^2}, \qquad \lambda^V \to \frac{\lambda^V}{\left(1+\dfrac{\hat{s}}{\Lambda^2}\right)^2} \tag{39}$$

where $\hat{s}$ is the invariant mass of the vector boson pair and the form factor, Λ, is the mass scale at which new physics appears, typically taken to be in the TeV range.

Unitarity limits for different form factors are derived in Ref. [5]. The limits for dipole form factors are

$$\begin{aligned} |\Delta g_1^Z| \leq \frac{3.36\ \ \text{TeV}^2}{\Lambda^2} \qquad & |\Delta\kappa^Z| \leq \frac{3.32\ \ \text{TeV}^2}{\Lambda^2} \qquad && |\lambda^Z| \leq \frac{2.08\ \ \text{TeV}^2}{\Lambda^2} \\ & |\Delta\kappa^\gamma| \leq \frac{7.24\ \ \text{TeV}^2}{\Lambda^2} \qquad && |\lambda^\gamma| \leq \frac{3.84\ \ \text{TeV}^2}{\Lambda^2} \end{aligned} \tag{40}$$

One of the critiques against the framework of anomalous couplings is that these couplings are promoted from simple constants to arbitrary form factors [6]. Also, this form of the Lagrangian does not respect $SU(2) \times U(1)$ gauge invariance. An effective field theory approach removes these two complications.

1.2.2 Lagrangian in Effective Field Theory Approach

In the effective field theory approach [6], the effective Lagrangian is an expansion in operators which are $SU(2) \times U(1)$ gauge invariant and conserve charge and parity. The dimensionless coefficients, c_i, parameterize the strength of the coupling between new physics and Standard Model particles.

$$\mathcal{L} = \mathcal{L}_{SM} + \sum_i \frac{c_i}{\Lambda^2}\mathcal{O}_i \tag{41}$$

There are three dimension six operators, $\mathcal{O}_i$, that lead to anomalous triple vector boson couplings.

$$\begin{aligned} \mathcal{O}_{WWW} &= \text{Tr}[W_{\mu\nu}W^{\nu\rho}W_\rho^\mu] \\ \mathcal{O}_W &= (D_\mu\Phi)^\dagger\, W^{\mu\nu}\,(D_\nu\Phi) \\ \mathcal{O}_B &= (D_\mu\Phi)\, B^{\mu\nu}\,(D_\nu\Phi) \end{aligned} \tag{42}$$

where Φ is the Higgs doublet field and

$$\begin{aligned} D_\mu &= \partial_\mu + \frac{i}{2}g\tau^I W_\mu^I + \frac{i}{2}g' B_\mu^I \\ W_{\mu\nu} &= \frac{i}{2}g\tau^I\left(\partial_\mu W_\nu^I - \partial_\nu W_\mu^I + g\epsilon_{IJK}W_\mu^J W_\nu^K\right) \\ B_{\mu\nu} &= \frac{i}{2}g'\left(\partial_\mu B_\nu - \partial_\nu B_\mu\right) \end{aligned} \tag{43}$$

The anomalous coupling constants can be calculated in terms of the constants in the effective field theory or vice versa.

$$
\begin{aligned}
\Delta g_1^Z &= c_W \frac{m_Z^2}{2\Lambda^2} \\
\Delta\kappa^Z &= [c_W - \tan^2\theta_W c_B]\frac{m_W^2}{2\Lambda^2} \\
\Delta\kappa^\gamma &= (c_B + c_W)\,\frac{m_W^2}{2\Lambda^2} \\
\lambda^\gamma = \lambda^Z &= \frac{3m_W^2 g^2}{2\Lambda^2} c_{WWW} \qquad (44) \\
\frac{c_W}{\Lambda^2} &= \frac{2}{m_Z^2}\Delta g_1^Z \\
\frac{c_B}{\Lambda^2} &= \frac{2}{m_Z^2}(\Delta\kappa^\gamma - \Delta\kappa^Z) \\
\frac{c_{WWW}}{\Lambda^2} &= \frac{2}{3g^2 m_W^2}\lambda \qquad (45)
\end{aligned}
$$

In contrast to the anomalous couplings framework, the free parameters of an effective field theory are $c_{WWW}/\Lambda^2, c_W/\Lambda^2, c_B/\Lambda^2$, which do not require arbitrary form factors to restore unitarity.

1.2.3 Additional Constraints: LEP, HISZ, Equal Couplings

LEP Constraint From Equation 44, the LEP constraint [7] is defined by requiring:

$$
\begin{aligned}
\Delta g_1^Z &= \Delta\kappa^Z + \tan^2\theta_W \Delta\kappa^\gamma \\
\lambda^\gamma &= \lambda^Z \qquad (46)
\end{aligned}
$$

These restrictions, from $SU(2)\times U(1)$ gauge invariance, reduce the number of free anomalous coupling parameters to three. Equation 46 is referred to as the LEP constraints.

HISZ Constraint In addition to requiring $SU(2) \times U(1)$ gauge invariance, the choice of setting $c_W = c_B$ leads to what is called the Hagiwara-Ishihara-Szalapski-Zeppenfeld [8] (HISZ) constraint scenario.

$$
\begin{aligned}
\Delta g_1^Z &= \frac{\Delta\kappa^Z}{\cos^2\theta_W - \sin^2\theta_W} \\
\Delta\kappa^\gamma &= 2\Delta\kappa^Z \frac{\cos^2\theta_W}{\cos^2\theta_W - \sin^2\theta_W} \\
\lambda^\gamma &= \lambda^Z \qquad (47)
\end{aligned}
$$

Equal Couplings Constraint Under the Equal Couplings scenario, it is assumed that the couplings for the WWZ and $WW\gamma$ vertex are equal. This leaves two independent parameters.

$$\begin{aligned} g_1^Z &= g_1^\gamma = 1 \\ \Delta\kappa^\gamma &= \Delta\kappa^Z \\ \lambda^\gamma &= \lambda^Z \end{aligned} \tag{48}$$

1.3 WW Production and Cross Section

WW production is an important test of the electroweak sector in the Standard Model. It sensitive to both anomalous WWZ and $WW\gamma$ triple gauge couplings. In addition, it is an important background to many beyond the Standard Model searches and an irreducible background to Higgs boson searches. This section will describe W^+W^- production at leading order with a discussion of various higher order effects.

The dominant diagrams for W^+W^- production involve a quark and anti-quark initial state or a gluon gluon initial state. The leading order (LO) diagrams (Figure 2) involve u-channel or t-channel production through quark exchange or s-channel production with a Z or photon acting as a mediating particle. The s-channel diagram involves a triple vector gauge boson coupling, which is sensitive to potentially non-standard triple gauge couplings.

The gluon-gluon diagrams are next-to-next-to-leading order (NNLO) loop diagrams shown in Figure 3. At the Large Hadron Collider (LHC), which produces proton-proton collisions, the quark-quark diagrams dominate over the gluon-gluon diagrams. With the discovery of the Higgs boson [9, 10], the $gg \to H \to WW$ process is considered as signal and its contribution is also included in this analysis.

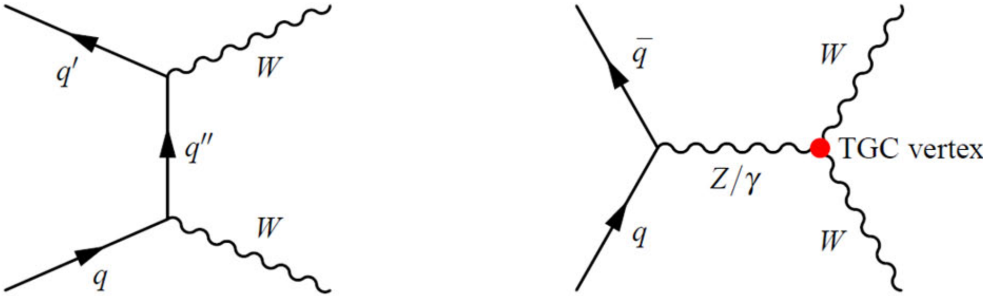

Figure 2: Leading order Feynman diagrams for WW production via quark and anti-quark initial states. The diagram on the right includes a triple gauge coupling (TGC) vertex indicated in red.

The full NNLO WW production cross section (including Higgs production) with center of mass energy at 8 TeVis determined to be $63.2^{+2.1}_{-2.2}$ pb (Section 3.2.1).

There are several other production mechanisms that are negligible and not included in this analysis. $\gamma\gamma$ initiated WW production is formally at the same order as the qq diagrams, but its contribution is negligible, since photon parton distribution functions (PDF) are much smaller than quark PDFs. Double parton interactions are also not included in this analysis,

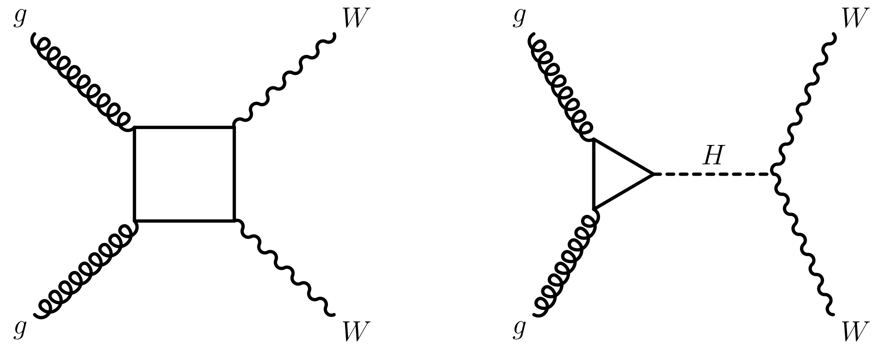

Figure 3: NNLO Feynman diagrams for WW production via gluon-gluon initial states. The right figure shows Higgs production and subsequent decays to WW.

as they were found to be negligible as well. WW production can also arise from a vector boson scattering (VBS) [11] production topologies (Figure 4). The VBS production is expected to have two forward, high p_{T}jets originating from the scattered quarks. VBS production is formally a higher order process and the contribution is suppressed by an analysis requirement that there can be no high p_{T}jets. For these reasons, VBS production is not included in this analysis.

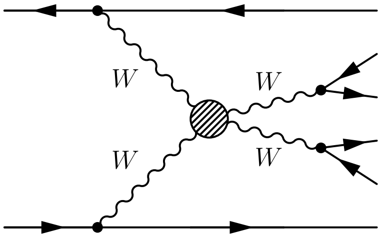

Figure 4: Vector boson scattering topology from [12].

In the next sections, several theoretical improvements that have been studied and/or applied in this analysis are described. High order electroweak corrections are described in Section 1.3.1. WW $p_{\mathrm{T}}$and jet veto resummation are described in Section 1.3.2.

1.3.1 Higher Order Electroweak Corrections

The leading order and NLO QCD calculations for WW production have been known for quite some time. Only recently, higher order electroweak (EW) calculations of $\mathcal{O}(\alpha_{EW}^3)$ have been presented in Refs. [13, 14, 15] for diboson production when both bosons are on-shell. These calculations involve loop diagrams such as those in Figure 5. The size of the EW corrections on WW production can be up to -30% for sensitive variables such as leading lepton p_{T}or WW p_{T}(Section 4.3.3), but the total integrated effect is only -1%. Hence, the effect of EW corrections will be small on the total cross section yet potentially large on measurements of differential distributions.

EW corrections and anomalous couplings can alter observables similarly in both size and shape. If EW corrections are neglected, this can fake a new physics signal with non-

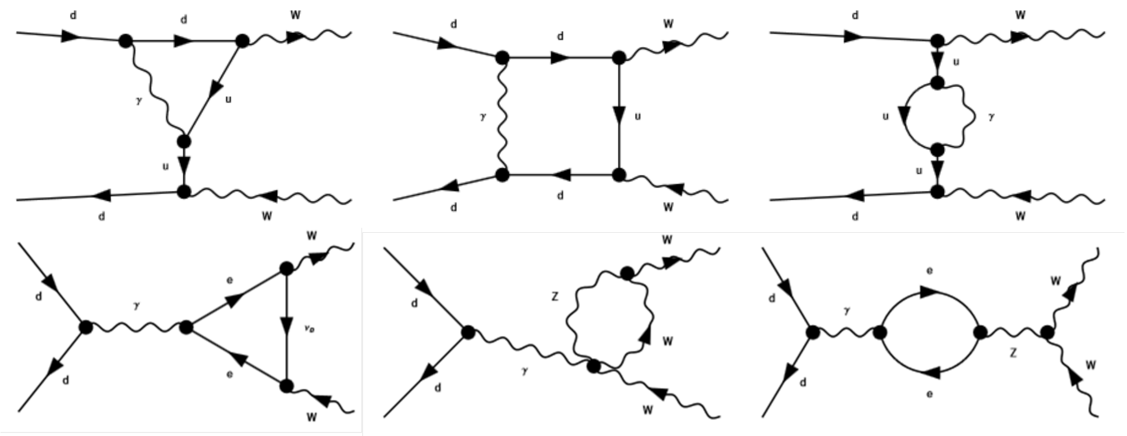

Figure 5: Example NLO EW diagrams for WW production.

Standard Model triple gauge boson couplings. These corrections are included in the limits on anomalous couplings and discussed in Section 4.3.3. For consistency, the much smaller EW corrections on the cross section measurement are also included in Section 3.9.

1.3.2 WW $p_{\mathrm{T}}$and Jet-Veto Resummation

Previous measurements of the WW cross section have resulted in moderate excesses [16, 17]. These excesses may be interpreted in the context of new physics at the electroweak scale. It may also suggest that we need a better theoretical understanding of WW production or specifically, the jet veto. An experimental jet veto requirement is used to reduce the large top background in WW measurements[1]. Events are rejected if there is at least one jet with $p_{\mathrm{T}} > p_{\mathrm{T}}^{\mathrm{veto}}$. Currently, the largest systematic uncertainties are those associated with the jet veto. Improvements in the theoretical understanding of the jet veto can be used to resolve these excesses.

Jet-veto threshold resummation Theoretically, the jet veto introduces a new mass scale in the calculation, $p_{\mathrm{T}}^{\mathrm{veto}}$ which is typically 25-30 GeV. This introduces large logarithms of the ratio $M_{\mathrm{WW}}/p_{\mathrm{T}}^{\mathrm{veto}}$, which Monte Carlo generators may not treat properly. Threshold resummation [18] uses a soft collinear effective field theory to resum these large logarithms. Reference [18] gives the theoretical WW 0-jet cross sections at 7 and 8 TeVusing $p_{\mathrm{T}}^{\mathrm{veto}} = 25, 30$ GeV and $\mathrm{R} = 0.4, 0.5$ corresponding to the experimental values used by ATLAS and CMS (Table 2 of [18]). To obtain the experimental WW 0-jet cross sections, the authors have reinterpreted the experimental results by applying a jet veto efficiency determined by the same parton shower and generator. However, the reinterpretation is not perfect, as the authors did not reproduce the same tunes used in the experimental analyses. They found that the threshold resummation resolves the discrepancies while also reducing scale uncertainties.

---

[1] In other diboson processes, the top background is smaller. This is because $t\bar{t}$ decays into two W bosons. For this reason, a jet veto is useful for WW measurements but not necessary in other diboson measurements.

WW p_{T}resummation The $p_{\mathrm{T}}$of the WW system and the probability for an event to pass the jet veto are strongly correlated. In p_{T}resummation [19], the shape of the p_{T}spectrum is corrected without changing the overall cross section. A good understanding of the shape of the WW $p_{\mathrm{T}}$is needed in the extrapolation from the fiducial cross section (with the jet veto) to the inclusive total cross section. p_{T}resummation can only change the total cross section indirectly through this extrapolation. The authors of Ref. [19] found that taking the NLO generated events after including parton showering and reweighting them to next-to-next-to leading log (NNLL) resummed p_{T}leads to an increase of 3-7% in the total measured cross section, depending on the choice of generator, parton shower and tunes. The impact on this analysis was studied using the same MC samples as those used in the analysis (See Section A). It was found that p_{T}resummation will lead to an increase of the total cross section by 4%. This is not a large enough effect to account for the 20% excess seen in the 8 TeV ATLAS and CMS measurements.

1.4 Event Generation and Monte Carlo Methods

Perturbative quantum field theory can be used to calculate tree level collisions and decays, but it cannot adequately describe a collision event at the LHC by itself. Many complex processes have to be included using Monte Carlo (MC) methods. This section will describe how MC programs are used to simulate different aspects of a collision event. The processes surrounding the hard scatter are listed below and shown in Figure 6.

Incoming hadron and parton distribution functions Incoming hadrons (represented by gray ellipses) contain quarks (or gluons) that participate in the hard scatter event. The probability for a parton (quark or gluon) to have a particular proton momentum fraction is given by parton distribution functions (PDF's). The determination of PDFs is carried out by several groups. Each group basically uses all the available data from deep inelastic scattering (DIS) experiments from HERA. Some include jet data from the Tevatron experiments. The CTEQ collaboration [20] uses a global fit under the framework of general-mass perturbative QCD. Their CT10 PDF set includes the HERA I data and Tevatron data. MSTW [21] uses a global fit under the framework of "leading twist fixed order collinear factorization in the MS scheme." The NNPDF analysis [22, 23] uses a neural network to train MC replicas of data.

Hard Scatter The hard scatter (represented by the yellow ellipse) involves the matrix element calculation and cross section. Fixed order MC generators implement the exact leading order (LO) or next-to-leading (NLO) matrix element calculations for a given process. Higher order matrix element calculations may also be available for some processes. Some programs (such as Sherpa [24]) have an option to include additional partons in the matrix element calculation. When this is done, the program includes higher order tree diagrams but does not include loop corrections from the full NLO calculation.

Radiation Initial state and final state radiation (represented by red lines) is modeled using parton showers (PS). Parton splitting functions are used to give a good description in the low energy limit.

Hadronization Color confinement leads to hadronization (represented green ellipses) of quarks. Two types of models are commonly used: the Lund string model (used by Pythia [25]) and the cluster model (used by Herwig [26] and Sherpa [24]). In the Lund string model, the quark/anti-quark pairs are modeled with a string between them. As the quarks drift apart, the string produces a confinement potential that grows until it snaps and creates a new quark and anti-quark pair at the torn ends. The cluster model is based on preconfinement. For each parton, there will be a color singlet partner and these color singlet pairs will have a mass spectrum that is independent of the process or energy. The cluster model considers mesonic quark anti-quark pairs as a cluster with a mass spectrum. If the cluster mass is above some cutoff value (typically a few GeV), the cluster will fission into two lighter clusters, until only stable hadrons are left.

Underlying event In multiple parton interactions, partons not involved in the hard scatter may interact with each other (blue lines). This can produce soft hadrons in the event.

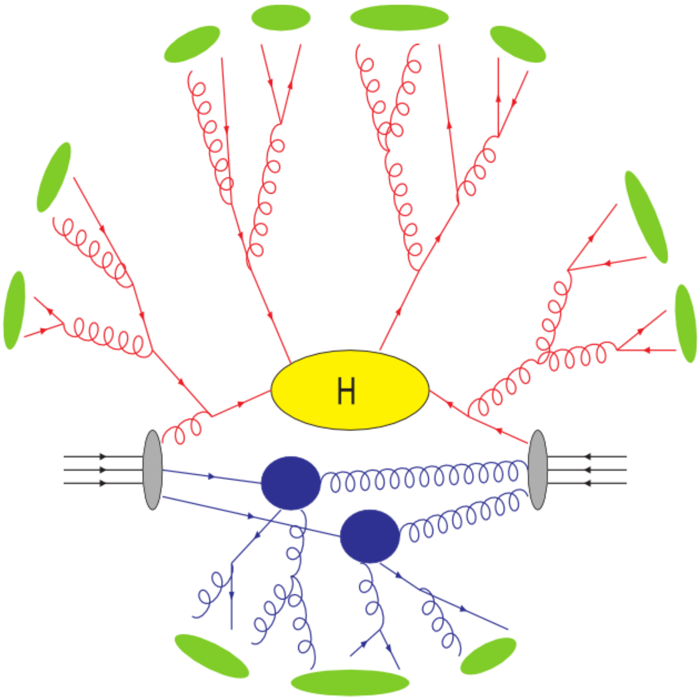

Figure 6: Diagram of an event after proton-proton collision [27]. The hard scatter is represented by a yellow ellipse in the middle. The red lines represent radiation and green ellipses represent hadronization. The blue lines represent underlying event. The blue lines represent multi-parton interactions (underlying event).

The various types of MC programs can be grouped into matrix element generators and calculators, parton shower programs, special purpose programs, and multipurpose programs. Examples of each type of MC program are given in Table 3. Matrix element generators include the LO or NLO matrix element calculation for the hard scatter and generates four vectors for the final state particles. Higher order matrix element calculators can be used to give a more precise cross-section calculation but cannot generate events. To make up for this, a leading order generator can be used to generate events where the leading order cross section is scaled to the higher order prediction. Parton shower programs simulate soft gluon radiation and hadronization of quarks. Special purpose programs are used to simulate specific processes (such as Tauola [28] for tau lepton decays and Photos [29] for QED radiative corrections in decays). Multipurpose programs can perform more than one function. MC programs are interfaced with one another to give a complete description of a collision.

Type of MC program	Examples
LO matrix element generators	Alpgen [30], AcerMC [31], MadGraph [32]
NLO matrix element generators	MC@NLO [33]
NLO matrix element calculators	MCFM [34, 35]
Multipurpose generators	Pythia [25], Herwig [26], Sherpa [24]
Special purpose generators	Tauola [28], Photos [29]

Table 3: Types of Monte Carlo (MC) programs and examples of each.

2 LHC and ATLAS

2.1 Large Hadron Collider

The Large Hadron Collider [36] (LHC) is a proton-proton[2] collider at the European Organization for Nuclear Research (CERN) located near the Franco-Swiss border in Geneva. The LHC consists of a 27 km long ring of superconducting magnets with supporting structures to accelerate the particles. The four main experiments at the LHC to study collision data are ATLAS, ALICE, CMS, and LHCB (Figure 7). The LHC operated at $\sqrt{s} = 7$ TeV in 2010 and 2011 and at $\sqrt{s} = 8$ TeV in 2012. On July 4, 2012, a particle consistent with the Higgs boson was discovered. In 2013 and 2014, the LHC was shutdown in preparation for the second run, where it will operate near its design energy at $\sqrt{s} = 14$ TeV. Currently, the LHC is back in operation and 13 TeVcollisions have begun in 2015 for the second run.

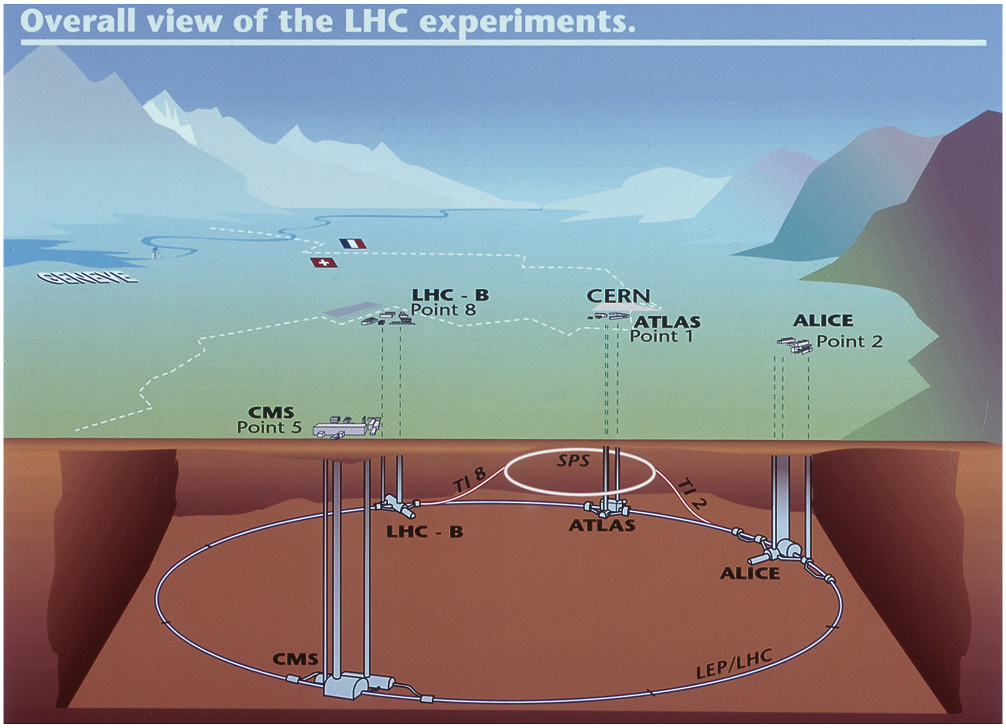

Figure 7: The four main detectors at the LHC.

2.1.1 Proton-Proton Collider

This section describes how protons are prepared for collisions at the interaction points located at each of the detectors. First, the electrons are stripped from hydrogen atoms to produce protons. The protons enter LINAC2 where protons are accelerated to 50 MeV and then fired into the Proton Synchrotron Booster (PSB). The PSB uses radio frequency (RF) cavities to accelerate protons to 1.4 GeV. The protons are then injected into the Proton Synchroton (PS) followed by the Super Proton Synchrotron (SPS) to be accelerated to 450 GeV. The

---

[2] The LHC can also produce heavy ion collisions (p-Pb or Pb-Pb) but these are not relevant for this thesis.

protons are injected into the two LHC beams pipes so that one beam can circulate in a clockwise direction and the other beam can circulate in an anti-clockwise direction. It takes about 20 minutes for the LHC to accelerate the beams to 4 TeV. Finally, the beams are made to intersect at the center of the four main detectors, where the products of their collisions can be studied.

2.1.2 Luminosity and Pileup

Luminosity can be expressed as the rate of inelastic collisions divided by the total inelastic cross section (σ_{inel}). If the collider operates at a revolution frequency of f_r and has n_b bunches crossing, then it can be expressed as

$$\mathcal{L} = \frac{\mu f_r n_b}{\sigma_{inel}} \tag{49}$$

where μ is the average number of interactions per bunch crossing. Event counting techniques can be used to calibrate for absolute luminosity, where the fraction of bunch crossings that result in detected events that satisfy some selection requirements is determined. The luminosity determination can be rewritten as

$$\mathcal{L} = \frac{\mu^{vis} f_r n_b}{\epsilon \sigma_{inel}} = \frac{\mu^{vis} f_r n_b}{\sigma_{inel}^{vis}} \tag{50}$$

where ϵ is the efficiency for an collision to satisfy the event requirements, and $\mu^{vis} = \epsilon\mu$ is the average number of interactions that pass the event selection per bunch crossing. Another way of calibrating is to use measured accelerator properties.

$$\mathcal{L} = \frac{n_b f_r n_1 n_2}{2\pi \Sigma_x \Sigma_y} \tag{51}$$

where n_1 and n_2 are the number of particles in the two beams, and Σ_x and Σ_y are the widths of the beam profile in the horizontal and vertical directions. The parameters Σ_x and Σ_y can be determined from van der Meer (vdM) scans. The total integrated luminosity delivered by the LHC for p-p collisions in 2012 at $\sqrt{s} = 8$ TeV is 22.8 fb^{-1}. This corresponds to 20.3 fb^{-1} of data recorded by the ATLAS detector for physics analysis. The total integrated luminosity for 2011 and 2012 can be seen in Figure 8.

Bunch Structure and Pileup The proton beams consist of a proton bunches with known gaps between the bunches. The LHC operating at design will use a 25 ns bunch structure with 72 bunches of protons (Figure 9). In 2012, the LHC operated at 50 ns bunch spacing under very high pileup conditions. In-time pileup occurs when there are additional proton-proton collisions on top of the hard scatter collision of interest. Out-of-time pileup occurs when there is a collision from the bunch previous or after the bunch with an interesting collision. This can happen if the detector electronics needs a longer time to process the data than the time between bunch crossings. Compared to 2011, where the average number of interactions per bunch crossing was 9.1, this was 20.7 in 2012 (See Figure 10).

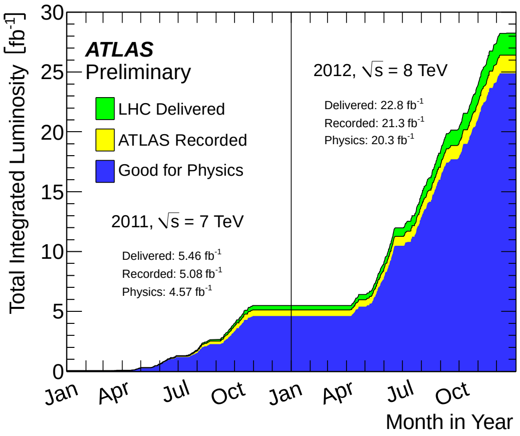

Figure 8: Total integrated luminosity during the 2011 and 2012 data taking period.

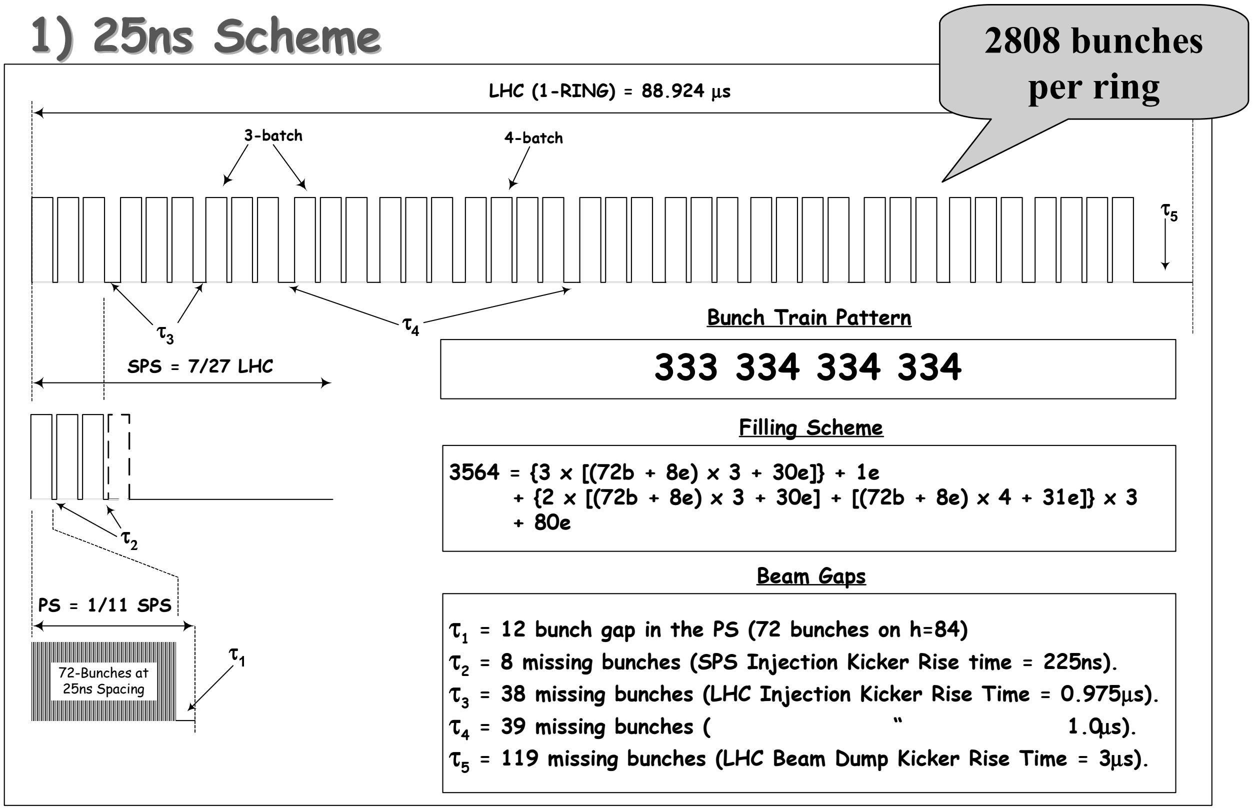

Bunch Train Pattern

333 334 334 334

Filling Scheme

3564 = {3 x [(72b + 8e) x 3 + 30e]} + 1e
+ {2 x [(72b + 8e) x 3 + 30e] + [(72b + 8e) x 4 + 31e]} x 3
+ 80e

Beam Gaps

τ_1 = 12 bunch gap in the PS (72 bunches on h=84)
τ_2 = 8 missing bunches (SPS Injection Kicker Rise time = 225ns).
τ_3 = 38 missing bunches (LHC Injection Kicker Rise Time = 0.975μs).
τ_4 = 39 missing bunches (" 1.0μs).
τ_5 = 119 missing bunches (LHC Beam Dump Kicker Rise Time = 3μs).

Figure 9: Bunch structure with 25 ns spacing.

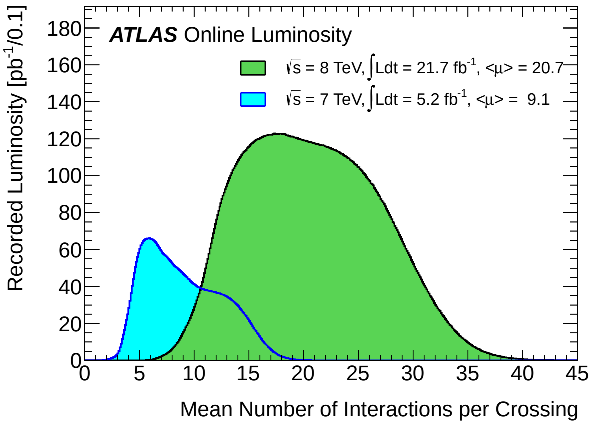

Figure 10: Mean number of interactions per bunch crossing in 2011 and 2012.

2.2 ATLAS Detector

The ATLAS detector [37] is a multi-purpose general particle physics detector. This section gives a brief description of the various sub-detectors. ATLAS uses a right handed coordinate system, with the z-axis pointing along the beamline, x-axis pointing towards the center of the LHC ring, and y-axis pointing upwards. The origin is at the interaction point, located in the nominal center of the detector. Cylindrical coordinates are also used where r is the radial distance from the z-axis, and ϕ is the azimuthal angle around the beam pipe. Pseudorapidity[3] is defined by $\eta = -\ln\left[\tan\left(\theta/2\right)\right]$, where θ is the polar angle.

Closest to the beamline are the inner detectors (Section 2.2.1) located within the central, superconducting solenoid which provides a magnetic field of 2 T. The inner detectors are used to track the trajectories of charged particles within $|\eta| < 2.5$ for charge identification and momentum measurements. The electromagnetic and hadronic calorimeters (Section 2.2.2) measure the energy of particles, providing a coverage of $|\eta| < 3.2$. The forward calorimeters extend the coverage up to $|\eta| < 4.9$. The muon system (Section 2.2.3) is located outside of the calorimeters in a magnetic field. The chambers provide precise muon measurements with a coverage of $|\eta| < 2.7$ and muon triggering in $|\eta| < 2.5$. ATLAS uses a three-level trigger system (Section 2.2.5) to filter out potentially interesting events for further physics analysis.

2.2.1 Inner Detectors and Tracking

The ATLAS inner detectors consist of a high granularity pixel detector, semiconductor tracker, and transition radiation tracker, all within a magnetic field of 2 T provided by a central solenoid magnet.

Pixel Detector The semiconductor pixel detector (Figure 11 and Figure 12) provides high granularity measurements as close to the interaction point as possible. This allows for precise vertex measurements which are necessary for impact parameter resolution and the ability to

---

[3] Pseudorapidity is identical to rapidity for massless particles. Rapidity is preferred over θ because it is Lorentz invariant under boosts in the z-direction. The calorimeter is segmented in pseudorapidity rather than linear directions so that the amount of energy is uniformly distributed.

distinguish relatively long lived particles such as B-hadrons. This detector consists of three concentric barrels with average radii of 5 cm, 9 cm and 12 cm with three disks perpendicular to the beam axis with radius 9-15 cm at each end. The pixel detectors are segmented in $R\phi$ and z, providing three precise measurements for each track.

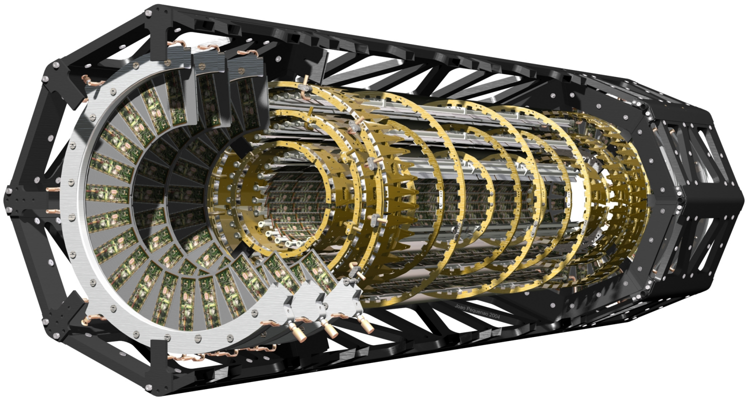

Figure 11: 3D model of ATLAS pixel detector [38].

Semiconductor Tracker The semiconductor tracker system consists of four double-layers of silicon microstrip detectors at radii of 30 mm, 37mm, 44cm, and 52cm in the barrel (Figure 12). The detectors used in the strips are very similar to those used in the pixel detector but have longer dimensions. Two detectors are mounted back-to-back on each layer, where one is oriented at a small 40 mrad stereo angle which allows for z-coordinate measurement.

Transition Radiation Tracker The transition radiation tracker (TRT) uses straw detectors. Each straw has a radius of 4 mm with a gold plated W-Re wire with a 30 μm radius. The barrel contains 50,000 straws, divided in two at the center while the endcap contains 320,000 straws, resulting in a total of 420,000 channels. The straws are filled with a nonflammable gas mixture of 70% Xe, 27% CO_2 and 3% O_2. The gas becomes ionized when a charged particle passes through and ionized electrons are collected in the anode wire. Transition radiation is strongest for low mass charged particles such as electrons, which results in very strong signals that can used in electron identification.

2.2.2 Calorimeters

The energy of charged and neutral particles is measured using the liquid argon (LAr) electromagnetic and tile hadronic calorimeters. The materials are chosen such that electrons and photons lose their energy mostly in the electromagnetic calorimeter but hadronic particles such as protons, neutrons, and pions will pass through and deposit energy mostly in the hadronic calorimeter. The calorimeter must be hermetic in order to infer the presence of neutrinos through transverse momentum imbalance ($E_{\mathrm{T}}^{\mathrm{miss}}$). The electromagnetic calorimeter covers $|\eta| < 3.2$, the hadronic barrel calorimeter covers $|\eta| < 1.7$, and hadronic endcap

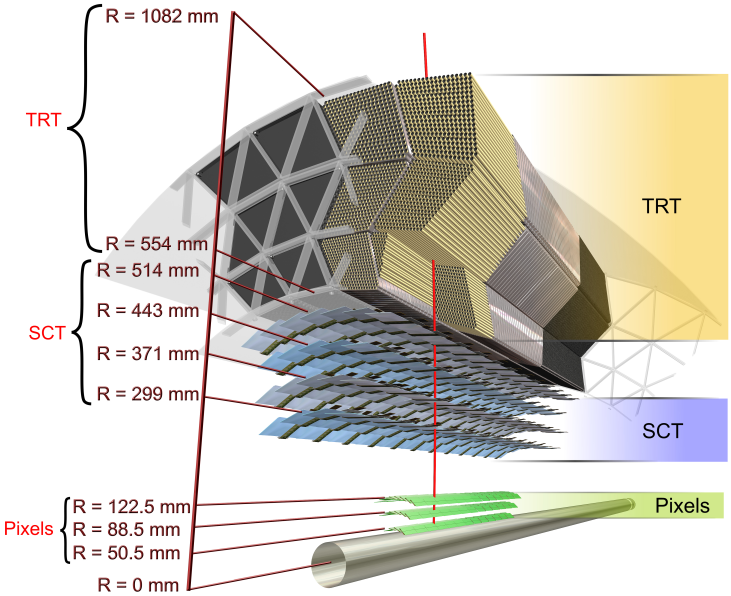

Figure 12: A slice of the ATLAS inner detector barrel which consists of layers from the pixel detector, semiconductor tracker (SCT), and transition radiation tracker (TRT) [39].

calorimeters cover $1.5 < |\eta| < 3.2$. The forward calorimeters cover the region $3.1 < |\eta| < 4.9$, fulfilling hermiticity requirements.

Electromagnetic Calorimeter The electromagnetic calorimeter consists of accordian shaped layers of lead absorbers and liquid argon (LAr) active material (Figure 13). The accordian shape ensures full azimuthal coverage (ϕ) without cracks. At high energies, electrons primarily lose energy in material through Bremsstrahlung radiation, while photons lose energy through pair production. In effect, interaction with the lead absorber will result in a shower of particles. The shape of the shower (its width and depth) is used in particle identification. The calorimeter consists of two barrel detectors covering $|\eta| < 1.475$ and two electromagnetic endcaps (EMEC) covering $1.375 < |\eta| < 3.2$. The calorimeter cells are segmented in ϕ and η, resulting in very fine granularity in the forward region. There are three layers in the barrel. The first layer is very finely segmented in η to provide excellent resolution. The second layer collects the largest fraction of the shower energy and the third layer contains only the tails of the shower energy and is more coarsely segmented than the second layer. In addition, a thin presampler layer is instrumented in the region $|\eta| < 1.8$ to measure the energy loss in front of the calorimeters.

Hadronic Calorimeter The hadronic calorimeter uses layers of plastic scintillator tiles as the active material and steel as the absorber medium. Hadrons interacting with the absorber will create showers (similar to electromagnetic showers of photons or electrons). When

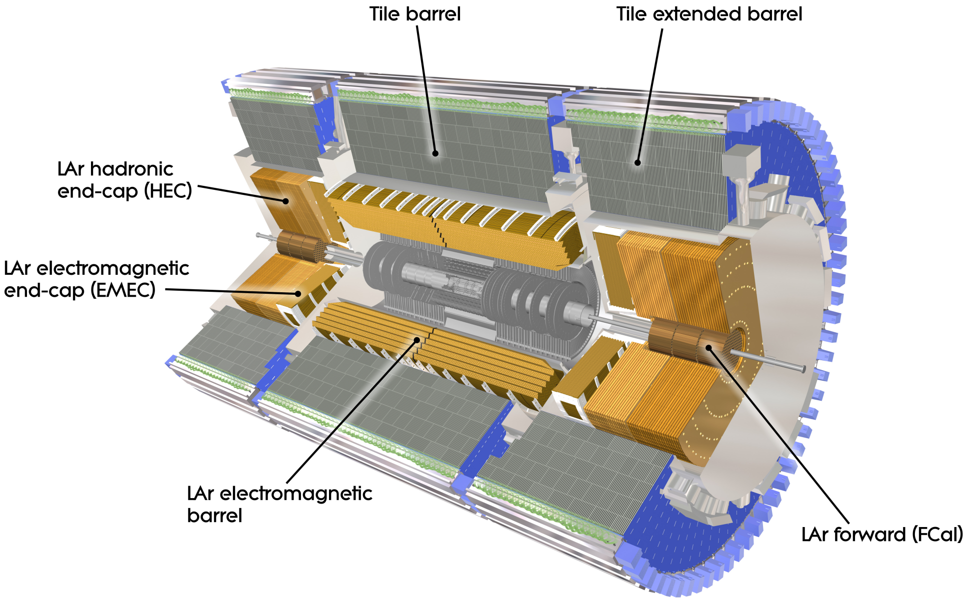

Figure 13: ATLAS electromagnetic and hadronic calorimeters [40].

a particle passes through the scintillator, light is emitted and measured by the detector. The tile calorimeter, including the barrel and extended barrels, cover the range $|\eta| < 1.7$. The hadronic end caps (HEC) covers the region $1.5 < |\eta| < 3.2$ using liquid argon and copper. The forward calorimeters (FCal) cover the region $3.1 < |\eta| < 4.9$. Each FCal has three modules, one electromagnetic module with a copper absorber (optimized for heat removal and resolution), and two hadronic modules with a tungsten absorber (optimized for containment and minimizing the lateral spread of hadronic showers).

2.2.3 Muon Spectrometer

Muons are the only detectable particles that can pass through the calorimeter absorbers without being stopped. The muon spectrometer is located in the outermost part of the detector (Figure 14).

The muon systems comprise of separate trigger chambers and precision tracking chambers (Figure 15). The tracking chambers in the barrel are located on or between the toroid magnets. There are three concentric cylindrical layers of eight large and eight small chambers, overlapping slightly in ϕ for full azimuthal coverage in the barrel. The end-cap chambers are wheels perpendicular to the z-axis located at $|z| \approx 7.4$ m, 10.8 m, 14 m, and 21.5 m from the interaction point. The monitored drift tube chambers (MDT) and cathode strip chambers (CSC) are used for precision tracking. The resistive plate chambers (RPC) and thin-gap chambers (TGC) are used for muon triggering in the regions $|\eta| < 1.05$ and $1.05 < |\eta| < 2.4$, respectively.

Muons are bent by the large toroid magnets in the range $|\eta| < 1.0$ and smaller magnets located in the endcap in the range $1.4 < |\eta| < 2.7$. The range $1.0 < |\eta| < 1.4$ is considered a transition region where the magnetic field is a combination from both toroid and endcap

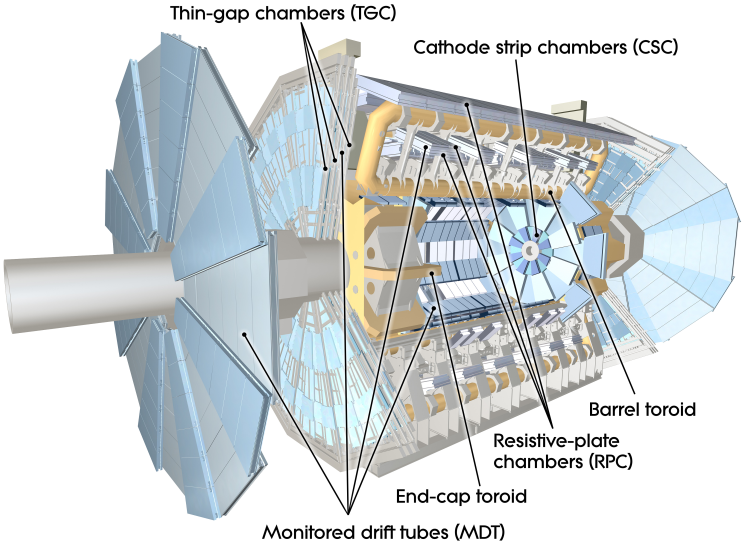

Figure 14: Components of the ATLAS muon spectrometer [41].

magnets. The toroid barrel magnet system consists of eight coils along the radial direction (See Figure 16).

Monitored Drift Tube Chambers The MDT chambers use drift tubes with a diameter of 30 mm similar to those used in the inner detector. The tubes are filled with 97% Ar and 3% CO_2 and ionized electrons are collected in the W-Re wire at the center. There are three layers of MDT chambers in the barrel and three endcap disks and each chamber is instrumented with 3-8 layers of drift tubes. The MDTs and RPCs in the barrel are shown in Figure 15.

Cathode Strip Chambers The MDT is replaced by CSC in $2.0 < |\eta| < 2.7$ due to higher counting rates in the innermost endcap layer. The CSC uses multiwire proportional chambers with cathode strips aligned orthogonal to the wires. This allows for the measurement of two coordinates from the detector. The CSC system consists of two disks with eight small and eight large chambers, with similar segmentation as for MDT chambers.

Resistive Plate Chambers RPCs consists of two parallel electrode plates with a small gap of 2 mm maintained by insulting spacers. In the middle barrel layer, two layers of RPCs sandwich a MDT layer. In the outer barrel layer, the RPC layer alternates between being below or above the MDT layer in the small and large octants, respectively. The position of the RPC layers in the barrel are shown in Figure 15. The outer layer allows for triggering on muons with 9-35 GeVp_T, while the inner layers allows for triggering in the range 6-9 GeV.

Thin-Gap Chambers The TGC uses the same operating principles as multiwire proportional chambers with high rate capability. The TGC serves triggering functionality while also providing a second azimuthal coordinate to complement the measurement from the MDTs.

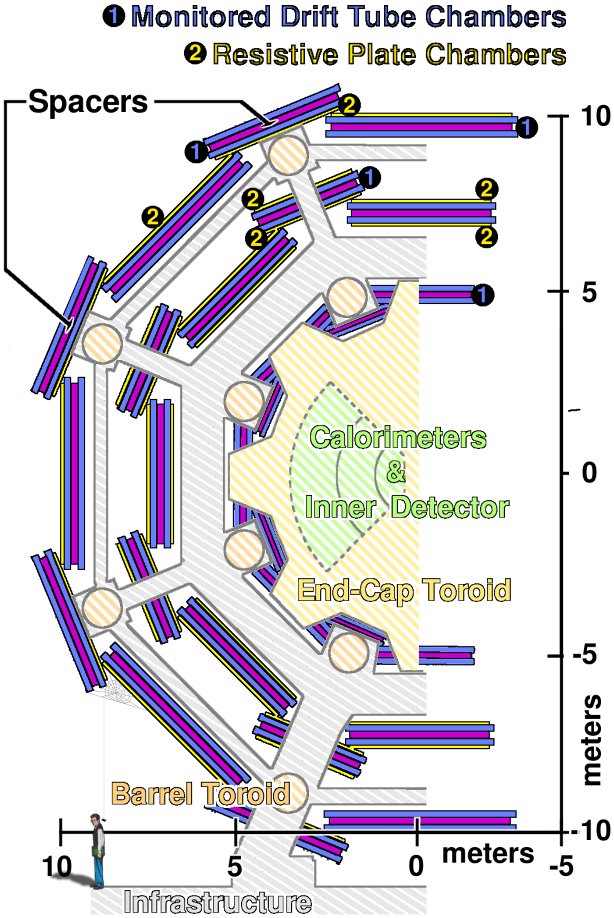

Figure 15: Cross section of ATLAS muon spectrometer in the barrel. [42]. The monitored drift tubes and resistive plate chambers are shown in blue and yellow.

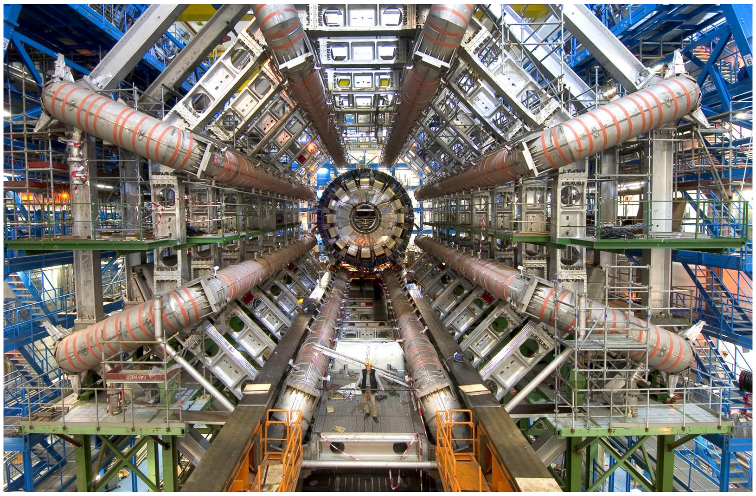

Figure 16: View of ATLAS toroid barrel magnet system with eight coils during construction [43].

2.2.4 Forward Detectors

Three smaller detectors are used to cover the forward region. The main relative luminosity detector is called LUminosity measurement using Cerenkov Integrating Detector (LUCID). The absolute luminosity detector using Roman pots is called Absolute Luminosity For ATLAS (ALFA). The Zero Degree Calorimeter (ZDC) is used primarily for heavy ion collisions.

LUCID LUCID is used for online monitoring of the instantaneous luminosity and for measuring the integrated luminosity. LUCID consists of tubes located 17 m away from the interaction point. The conical tubes are filled with C_4F_10 which provides a Cerenkov threshold of 2.8 GeVfor pions and 10 MeVfor electrons. A particle passing through one of the tubes will emit Cerenkov light which gets reflected before being measured by photomultiplier tubes (PMT's). The size of the PMT signal is proportional to the number of particles in the tube and the fast response time allows for measurements of individual bunch-crossings. Since LUCID is a relative luminosity detector, it must be calibrated using an absolute luminosity detector.

ALFA ATLAS uses an absolute luminosity detector that uses the Roman-pot technique with a scintillating fiber tracker. ALFA is located 240 m away from the interaction point. The absolute luminosity can be measured by using small angle elastic scattering and relating elastic scattering angle with the total cross-section by using the optical theorem. Since absolute luminosity measurements can only be carried out during special LHC fills, ALFA is usually offline during typical p-p collisions.

ZDC In addition, the Zero Degree Calorimeter (ZDC) is designed to measure forward neutrons during heavy ion collisions and is located 140 m from the interaction point.

2.2.5 Trigger System

ATLAS uses a three level trigger system to select interesting events for further analysis. The Level-1 (L1) trugger uses reduced granularity calorimeter information and muon detectors to find high E_T objects. The L1 calorimeter trigger uses calorimeter towers to find high E_T objects such as electrons, photons, hadronically decaying tau leptons, jets, high $E_{\mathrm{T}}^{\mathrm{miss}}$and high total transverse momentum. The towers are 0.1×0.1 in $\Delta\eta \times \Delta\phi$ but larger in the more forward regions in η. The L1 muon trigger uses the Resistive plate Chambers (RPC) in the barrel and Thin-gap Chambers (TGC) in the endcaps to find high p_{T}muons. The maximum acceptance rate for the L1 trigger is 75 kHz. The L1 trigger identifies Regions-Of-Interests (ROI) that are used to seed the Level-2 (L2) trigger. The L2 and the event filter (EF) triggers are referred to as the High-Level Trigger (HLT). Unlike the L1 trigger, the HLT uses full granularity information of the calorimeter and muon chambers. The L2 trigger selects a small fraction of data to be readout from the detector in the ROIs. The L2 trigger reduces the acceptance rate to 3.5 kHz. The event filter (EF) trigger uses offline procedures to fully reconstruct events and to further reduce the acceptance rate to the level at which events can be recorded for offline analysis. This is approximately 200 Hz.

2.3 ATLAS Reconstruction and Particle Identification

The reconstruction and identification of physics objects in the ATLAS detector is discussed in this section. Figure 17 illustrates how different physics objects interact with different parts of the detector. The inner detector measures the spatial trajectories (tracks) of charged particles which determine its momenta and charge. Track and vertex reconstruction are described in Sections 2.3.1 and 2.3.2, respectively. The calorimeters measure the energy of the particles and the shower shape reveals the electromagnetic or hadronic nature of the particle. The algorithms for electron and jet reconstruction are discussed in Section 2.3.3 and 2.3.4. The muon system provides additional information about the momenta and charge of muons that pass through it. Muon reconstruction is described in 2.3.5. Neutrinos escape undetected, but can be inferred from transverse momentum imbalance. Missing transverse momentum, $E_{\mathrm{T}}^{\mathrm{miss}}$, is described in Section 2.3.6.

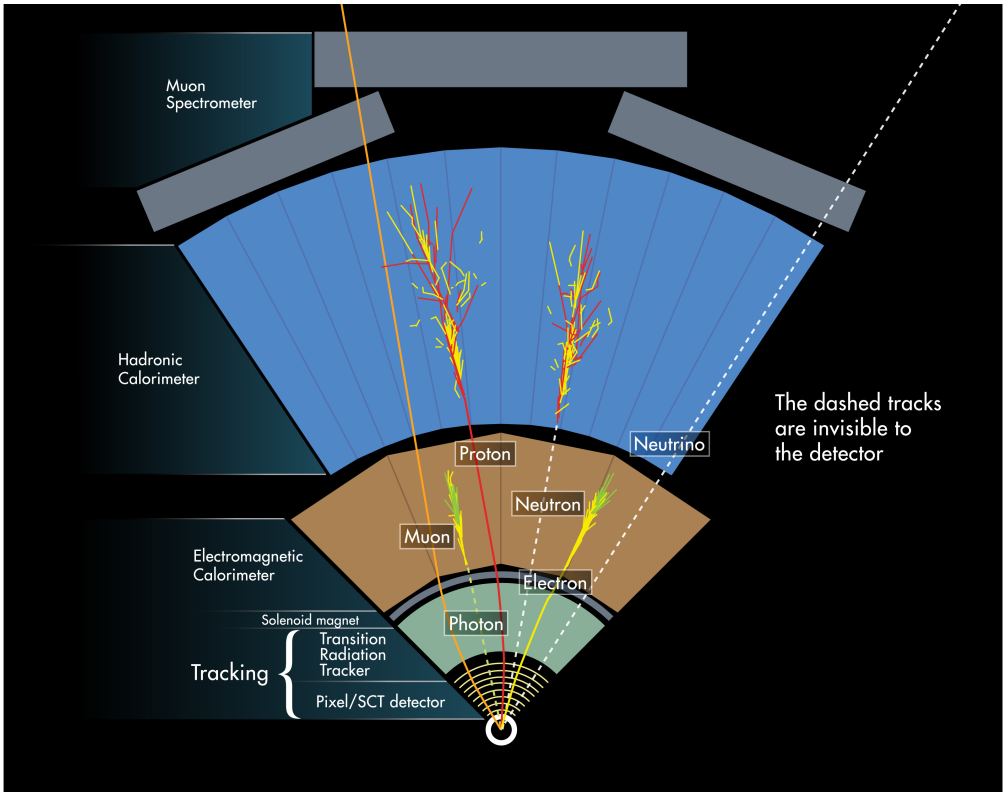

Figure 17: A slice of the ATLAS detector to illustrate how different physics objects interact with the detector subsystems.

2.3.1 Track Reconstruction

The path of a charged particle passing through the detector is called a track. Tracks can be reconstructed from spatial measurements from the pixel, silicon semiconductor tracker (SCT), and transition radiation tracker (TRT) subdetectors. Tracks can be reconstructed from the following algorithms. An inside-out algorithm starts with 3 point seeds in the innermost silicon detectors and then adds hits moving away from the interaction point using a Kalman Filter, eventually extending the track to the TRT. This algorithm is used for reconstructing tracks from primary charged particles. A primary particle is defined as particles with a mean lifetime greater than 3×10^{-11}s or from a decay of a particle with a mean lifetime less than 3×10^{-11}s. A back-tracking algorithm is used to reconstruct tracks from secondary vertices, such as those from b-quark hadrons. This algorithm starts with segments in the TRT and adds hits from the inner silicon detectors. If a TRT track cannot be extended by silicon hits, this is considered a TRT standalone track.

In high pileup conditions, hits from nearby particles can be incorrectly assigned to a track. This can result in fake tracks that cannot be matched to a primary or secondary vertex. The number of fake tracks from pileup can be reduced by requiring a certain number of hits or a lack of holes. A hit is a measurement point assigned to a track. A hole is the lack of a measured point when it is expected from the track trajectory. A hole is not counted when the point is at an inactive or dead module, where it is instead counted as a hit.

2.3.2 Vertex Reconstruction

Vertices are reconstructed from an iterative algorithm. The z-position at the beamline of the tracks are used as vertex seeds. Tracks found near the seeds are used in a χ^2 fit. A vertex is reconstructed if there are at least two tracks. Outlier tracks (those with $> 7\sigma$) are used to seed a new vertex and the procedure is repeated until there are no more vertex seeds. The primary vertex (or hard scatter vertex) is defined as the vertex with the largest summed p_{T}^2.

2.3.3 Electron Reconstruction and Identification

There are three main algorithms for reconstructing electrons:

Cluster reconstruction The standard electron algorithm is seeded by energy deposits (clusters) in the electromagnetic (EM) calorimeter. This mostly reconstructs high p_T electrons. The EM calorimeter is divided into towers of size 0.025×0.025 in $\Delta\eta \times \Delta\phi$, which corresponds to the granularity of the middle layer. The tower energy is taken as the energy from the front, middle, and back layer, including the presampler layer for $|\eta| < 1.8$. For cells in which the granularity is larger than the tower size, the energy is taken to be uniformly distributed. Clusters are seeded by towers with transverse energy greater than 2.5 GeVfound through a sliding window algorithm, with a window size of 3×5 tower units. The clustering algorithm is approximately 97% efficient for electrons with $E_{\mathrm{T}} = 7$ GeV and nearly 100% efficient for electrons with $E_{\mathrm{T}} > 20$ GeV.

Track association with the cluster A soft electron algorithm is seeded by tracks in the inner detector. This mostly reconstructs low p_T electrons. Tracks with $p_{\mathrm{T}} > 0.5$ GeV are extrapolated from their last measured point to the middle layer of the EM calorimeter. If a cluster is found with $\Delta\eta < 0.05$ of the extrapolated track, then the track and cluster are considered to be successfully matched. If at least one track can be matched to the cluster, the electron is reconstructed. Higher priority is given to tracks with hits in the pixel and SCT detectors, and the track with the smallest ΔR between the track and the seed cluster is used.

If there is no track matched to the cluster, the cluster is reconstructed as an unconverted photon. If there are closeby tracks that originate from a displaced vertex, this is used to distinguish between electrons and converted photons.

Forward electron reconstruction A third algorithm can be used to reconstruct electrons in the forward region ($2.5 < |\eta| < 4.9$). In this region, no tracking information is available, so electrons and photons cannot be differentiated from track and cluster matching. In comparison to the sliding window algorithm used in the barrel, a topological clustering algorithm is used in the forward region. Cells with energy significantly above noise thresholds are grouped together iteratively (See Section 2.3.4). The energy of the cluster is the total energy of the sum of the cells. The topological clustering algorithm is more than 99% efficient for electrons with $E_{\mathrm{T}} > 20$ GeV.

Electron Identification Electron identification criteria are used to differentiate between signal isolated electrons and background from misidentified hadrons, non-isolated electrons from heavy flavor decays, or electrons from photon conversions. To reject these backgrounds, discriminating variables are used. A set of criteria with increasing background rejection at the cost of reduced signal electron efficiency are the *loose*, *medium*, and *tight* criteria. In the cut-based identification, the tighter definitions use more stringent cutoff values and/or additional discriminating variables. A *tight* electron must also pass the *medium* criteria, and a *medium* electron must pass the *loose* criteria. The variables used in *loose* identification involve shower shape and energy in the first and second EM layers, as well as track and cluster matching quality. The *medium* definition adds to the *loose* criteria with a loose transverse impact parameter, the presence of transition radiation in the TRT, and a hit in the innermost layer of the pixel detector to reject photon conversions. The *tight* definition, in addition to more stringent requirements on the *medium* variables, also uses the ratio of the EM energy to the momentum, a veto on reconstructed photon vertices. A detailed description of the discriminating variables can be found in Ref. [44].

The likelihood-based identification uses the same variables corresponding to the cut-based identification in a multivariate likelihood discriminant. The *very tight* likelihood (LLH) identification corresponds to the cut-based *tight* identification with a similar signal efficiency but better background rejection.

2.3.4 Jet Reconstruction

Jet reconstruction algorithms are used for analyzing hadronic data. Quarks cannot propagate through the detector as isolated objects; they hadronize due to color confinement. The cone algorithms [45] used in earlier analyses are replaced by sequential recombination algorithms that are infrared and collinear safe. Infrared safety prevents irregularities or instability in the jet boundaries due to soft radiation. Collinear safety means that the jet clustering output is the same even if the energy of a particle is split into collinear particles. Figure 18 gives two examples of jet algorithms that are not collinear or infrared safe.

The clustering algorithms combine objects or particles in four momentum representation. Calorimeter jets use topological clusters or towers from the EM calorimeter as seeds. Calorimeter cells above a noise threshold are added iteratively to include other neighboring

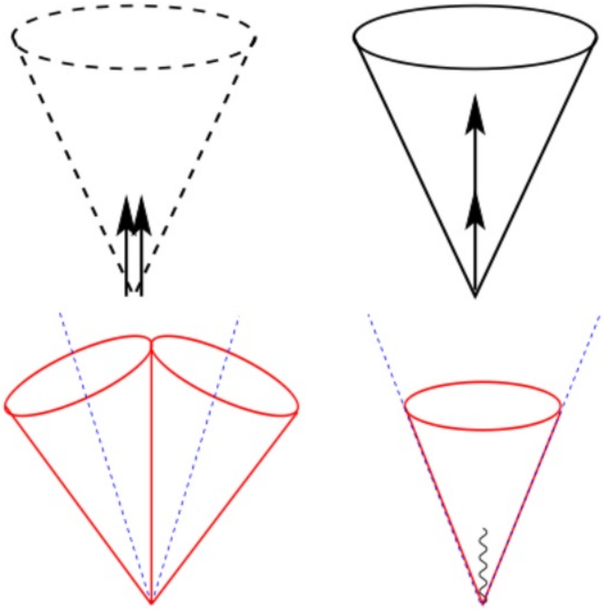

Figure 18: Collinear and Infrared Safety in jet algorithms. In the top figures, two collinear particles (top left) are merged into a single particle (top right) with the summed energy. In this example of a non-collinear safe algorithm, only the right scenario results in a jet. In the bottom left figure, two high p_{T}objects results in two jets. In the bottom right figure, a low p_{T}particle is added, resulting in a single merged jet, which is an example of a non-infrared safe algorithm. If the jet algorithm does not give the same results due to collinear splitting (top) or soft emissions (bottom), it is not collinear or infrared safe.

cells. Cells with $|E| > 4\sigma_{noise}$[4] are used as seeds, and neighboring cells with $|E| > 2\sigma_{noise}$ are added to the cluster iteratively. At the last step, all neighboring cells of those already accumulated are added to the cluster. An example of a topological clustering is given in Figure 19. These above threshold cells form a cluster such that the total energy of the cluster is the sum of the energy of the constituent cells. Track jets use tracks from the inner detector as seeds and truth jets use stable, long lived particles (except muons or neutrinos) from Monte Carlo simulations as seeds. In the recombination algorithms, a distance parameter is introduced for every pair of particles (d_{ij}) or between a particle and the beam (d_{iB}).

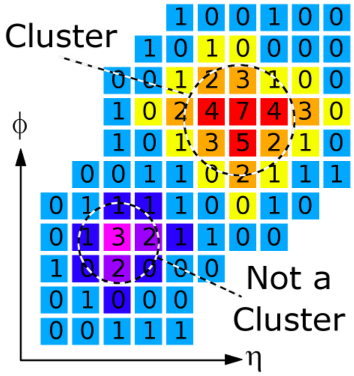

Figure 19: Example of a topological cluster [42]. The cells with $> 4\sigma$ above noise are used to seed the clusters, then neighboring cells with $> 2\sigma$ are included. Finally all neighbors are added to form the cluster (in yellow, orange, and red).

$$\begin{aligned} d_{ij} &= min(k_{Ti}^{2p}, k_{Tj}^{2p})\frac{\Delta_{ij}^2}{R^2} && (52) \\ d_{iB} &= k_{Ti}^{2p} && (53) \end{aligned}$$

where $\Delta_{ij}^2 = (y_i - y_j)^2 + (\phi_i - \phi_j)^2$ and k_{Ti}, y_i, and ϕ_i is the transverse momentum, rapidity, and azimuthal angle of the i-th particle, p gives the exponent on the transverse momentum, and R is the radius parameter. Starting with the smallest distance parameter, if the smallest is d_{ij}, particles i and j are combined and the distance parameters with the newly combined particles are recomputed. If the smallest is d_{iB}, then the i-th particle is called a jet and removed from the list. This process of recombination is repeated until there are no more particle seeds left.

For p=0, the Cambridge/Aachen algorithm [46, 47] is recovered, where the clustering has no dependence on the transverse momenta of the particles. For p=1, the k$_T$ algorithm primarily clusters close-by, low k_T objects first. For p=-1, this is referred to as the anti-k$_T$ algorithm, in which high k$_T$ close-by objects are clustered first. In ATLAS, jets are typically constructed using the anti-k$_T$ algorithm with R=0.4.

Pileup jet suppression using jet vertex fraction Jets can come from both hard scatter (signal) events as well as pileup interactions. The jet vertex fraction (JVF) [48] can be used

---

[4] σ_{noise} is the Gaussian width of the energy of the cell in randomly triggered events not during bunch crossings.

as a discriminant to distinguish hard scatter jets from pileup jets. The JVF is defined as the fraction of the sum $p_{\mathrm{T}}$of the tracks within the jet that originate from a particular vertex (in this case, the primary vertex) to the sum $p_{\mathrm{T}}$of all tracks associated with the jet (from any vertex). As defined, the JVF value can range from 0 to 1, with values close to 1 (0) corresponding to a high (low) probability for a jet to originate from a hard scatter. If, in the rare case, no tracks are matched to the jet, it is assigned a JVF value of -1. A schematic illustration of the jet vertex association is shown in Figure 20.

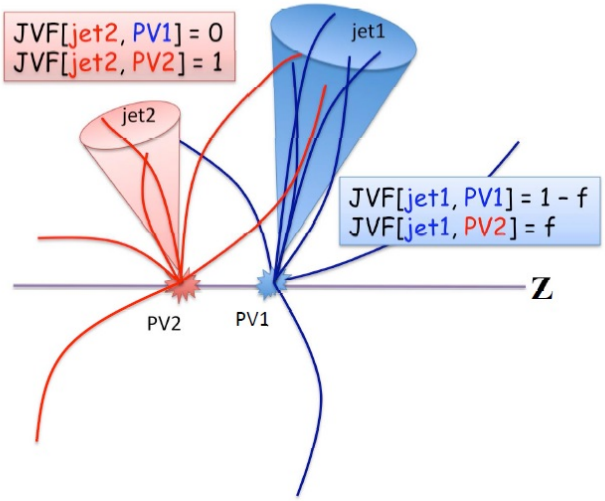

Figure 20: Schematic diagram of jet vertex association. Two jets with their jet vertex fractions (JVF) are shown with respect to the two vertices [49].

Track and vertex association is determined using the default primary vertex reconstruction as described in Section 2.3.2. The assignment of tracks to jets is done by ghost association[5]. Ghost association uses the active area concept of jets in Ref. [50]. The active area is defined as the calorimeter area that would or could contribute to a particular jet. This can be determined by considering a sea of uniformly distributed ghost particles with infinitesimally small energy. These ghost particles are then included in the jet combination algorithms. Since the algorithms are infrared safe, there should be no change in the final jets after adding the ghost particles. The active area of a particular jet is given by the positions of the ghost particles in that jet. Ghost track association uses the same idea. Tracks are taken with their usual η and ϕ positions, but with infinitesimally small energy. Then ghost tracks are assigned to jets by including them in the anti-k$_T$ (or k$_T$, Cambridge/Aachen, etc) algorithm as jet constituents.

Identifying jets from b-quarks Hadrons from b-quarks tend to live longer than those from lighter quarks. The long lived decay results in a reconstructed jet originating from a b-quark (b-jet) with a displaced secondary vertex away from jets originating from light quarks (light-jets). The impact parameter algorithm (IP3D) use the transverse and longitudinal

---

[5] In low pileup conditions, a simple ΔR matching could be used since anti-k$_T$ jets with R=0.4 or R=0.6 tended to be circular. However, in the high pileup conditions in 2011 and onwards, jets cannot be considered circular, especially when there are closeby jets.

impact parameter significance to differentiate signal b-jets from background light-jets using MC. A secondary vertex algorithm (SV1) reconstructs vertices away from the interaction point and uses the decay length significance to discriminate between b-jets and light-jets. A jet finding algorithm (JetFitter) uses a Kalman filter to find a line between the primary vertex and the b or c quark vertices. A multivariate algorithm (MV1) combines the IP3D, SV1, and JetFitter techniques in an artificial neural network, which gives a tag weight as output. The working points for the MV1 tagging algorithm correspond to fixed b-jet tagging efficiencies of 60%, 70%, 80% or 85%. Details on the b-tagging can be found in Refs. [51, 52].

2.3.5 Muon Reconstruction

Muons are reconstructed using information from the muon spectrometer (MS) and inner detector (ID) and, to a lesser extent, the calorimeter. Muons reconstructed from the various subdetectors are categorized accordingly.

Stand-Alone Muons The muons are reconstructed from tracks in the muon spectrometer only. The impact parameter at the interaction point is determined from extrapolation from the MS.

Segment-Tagged Muons Tracks in the inner detector are extrapolated to the MS, and if they match a straight line segment in the monitored drift tubes (MDT) or cathode strip chambers (CSC), a segment-tagged muon is reconstructed.

Calorimeter-tagged Muons An ID track is reconstructed as a muon if it points in the direction of an energy deposit in the calorimeter that is consistent with a muon (ie minimum ionizing particle). Calorimeter-tagged muons have low purity, but they can be used to recover inefficiencies from the uninstrumented region in the MS ($|\eta| < 0.1$).

Combined Muons The ID tracks and MS tracks are independently reconstructed. A combined track is reconstructed from the successful combination of the ID and MS tracks.

Combined muons give the highest purity, so this type of reconstructed muon should be used whenever possible. The efficiency of combined muons is greater than 95% except in the poorly instrumented regions. At $\eta \approx 0$, the region is used to provide services for the inner detector and calorimeters, leaving a small gap in MS coverage. In $1.1 < |\eta| < 1.3$, between the barrel and endcap, there are regions in which a muon in the MS can only transverse one layer of chambers. This makes momentum reconstruction impossible, resulting in inefficiencies for stand-alone muons and combined muons.

2.3.6 Missing Transverse Energy Reconstruction

The missing transverse energy ($E_{\mathrm{T}}^{\mathrm{miss}}$) calculation uses information from the calorimeters and the muon systems to find the momentum imbalance due to neutrinos. The two components are

$$\begin{aligned} E_x^{\text{miss}} &= E_x^{\text{miss,Calo}} + E_x^{\text{miss},\mu} \\ E_y^{\text{miss}} &= E_y^{\text{miss,Calo}} + E_y^{\text{miss},\mu} \end{aligned} \tag{54}$$

The transverse missing momentum is simply:

$$E_{\mathrm{T}}^{\text{miss}} = \sqrt{\left(E_x^{\text{miss}}\right)^2 + \left(E_y^{\text{miss}}\right)^2} \tag{55}$$

Calorimeter cells are associated with high p_{T}reconstructed objects in the following order: electrons, photons, hadronically decaying tau leptons, jets, and calorimeter muons.

$$E_{x(y)}^{\text{miss}} = E_{x(y)}^{\text{miss,e}} + E_{x(y)}^{\text{miss},\gamma} + E_{x(y)}^{\text{miss},\tau} + E_{x(y)}^{\text{miss,jet}} + E_{x(y)}^{\text{miss,calo}\mu} + E_{x(y)}^{\text{miss,CellOut}} \tag{56}$$

For each term,

$$E_x^{\text{miss,term}} = -\sum_{i=1}^{N_{cells}^{term}} E_i \sin\theta_i \cos\phi_i \tag{57}$$

$$E_y^{\text{miss,term}} = -\sum_{i=1}^{N_{cells}^{term}} E_i \sin\theta_i \sin\phi_i \tag{58}$$

where E_i, θ_i, and ϕ_i are the energy, polar angle, and azimuthal angle, respectively. The energy of associated cells is replaced by the well calibrated energy scale of the reconstructed objects. The last term, $E_{x,y}^{\text{miss,CellOut}}$, takes into account calorimeter cells not associated with any high p_{T}reconstructed object. These cells are built from topological clusters (See Section 2.3.4).

3 WW Cross-section measurement

3.1 Analysis strategy overview

The W^+W^- signal considered here is the $\ell^+\nu\ell^-\nu$ final state arising when both W's decay leptonically. The experimental signature is identified by two oppositely charged leptons, e or μ (which includes the leptonic decays of τ leptons), and missing transverse energy, $E_{\mathrm{T}}^{\mathrm{miss}}$. Several background processes can produce the same experimental signature:

- Z+jets, where the $Z \rightarrow \mu\mu$ or $Z \rightarrow ee$ and missing energy is due to mismeasurement, pileup events, or particles exiting down the beam pipe where its energy cannot be measured. For $Z \rightarrow \tau\tau$, in which the leptonic τ decay follows, the missing energy is due to neutrinos.
- $t\bar{t}$ or Wt, where $t \rightarrow Wb$ and the final state includes two W bosons with additional jets.
- $W\gamma$, where the γ is misidentified as an electron
- $WZ \rightarrow \ell\nu\ell\ell$ and $ZZ \rightarrow \ell\ell\ell\ell$, where only two leptons are identified and the others are lost.
- $ZZ \rightarrow \ell\ell\nu\nu$
- W+jets, where the W decays leptonically and a jet is misidentified as a lepton
- Multijet events, where both leptons are due to misidentified jets.

Background processes that include $Z \rightarrow \ell\ell$ can be reduced by removing events with an invariant mass that is consistent with that of a Z boson. The single top and $t\bar{t}$ contributions can be reduced with a jet veto, which requires no jets above a certain p_T threshold. Details on the event selection are given in Section 3.6.1

3.2 Theory and Modeling

3.2.1 Theoretical WW Production Cross Section

The full NNLO W^+W^- production cross section is $59.1^{+1.2}_{-1.0}$ pb (Ref. [53]), which corresponds to $63.2^{+2.1}_{-2.2}$ pb after adding the Higgs contribution. A partial NNLO cross section is used to normalize the Monte Carlo (MC) prediction, which includes NLO $qq\backslash qg\backslash gq \rightarrow WW$ (now referred to as qq), non-resonant $gg \rightarrow WW$ and resonant $gg \rightarrow H \rightarrow WW$ contributions. The qq and non-resonant gg contributions are determined using MCFM [34, 35]. The cross section for Higgs production is determined to be 4.1 ± 0.5 pb (Ref. [54]). Table 4 summarizes the theoretical cross section calculations for WW production.

Process	σ [pb]	Δ_σ^{Total} [pb]	Δ_σ^{Scale}	Δ_σ^{PDF}	$\Delta_\sigma^{Br.}$	Calculation
1) $q\bar{q} \to WW$	53.2	$^{+2.5}_{-2.2}$	$^{+2.3}_{-1.9}$	$^{+1.0}_{-1.1}$	-	NLO MCFM
2) $gg \to WW$	1.4	$^{+0.3}_{-0.2}$	$^{+0.3}_{-0.2}$	$^{+0.1}_{-0.1}$	-	LO MCFM
3) $q\bar{q} \to WW$	59.1	$^{+1.6}_{-1.7}$	$^{+1.2}_{-1.0}$	$^{+1.1}_{-1.2}$	-	NNLO [53]
4) $gg \to H \to WW$	4.1	±0.5	± 0.3	±0.3	±0.2	NNLO [54]
WWproduction (pNNLO)	58.7	$^{+3.0}_{-2.7}$		1)+2)+4)		
WWproduction (NNLO)	63.2	$^{+2.1}_{-2.2}$		3)+4)		

Table 4: The full and partial NNLO theoretical WW production cross section. The first row gives the predicted cross sections for the non resonant $q\bar{q} \to WW$production with the uncertainty from scale, PDF and α_s variations shown in pb. The second and fourth rows show the theoretical production cross section for the non-resonant $gg \to WW$ and the resonant $gg \to H \to WW$ process with their respective error decomposition. The NNLO cross section and its uncertainties for $q\bar{q} \to WW$production are given in the third row, the scale uncertainty comes from the NNLO paper while the PDF uncertainty is taken from the corresponding NLO calculation. The partial and full NNLO cross sections for WWproduction are shown in the fifth and sixth rows, the uncertainties of non-resonant and resonant (through Higgs decays) WWproductions are combined linearly.

3.2.2 Signal and Background Modeling

The signal and background processes are modeled with Monte Carlo (MC) generators. The details for each process are given in this section. A more general discussion on Monte Carlo techniques, generators, and parton showers are discussed in Section 1.4.

The $q\bar{q} \to W^+W^-$ signal process is modeled with the Powheg[55, 56] generator interfaced to Pythia[25] for parton showering. Powheg includes next-to-leading (NLO) QCD matrix elements, and the parton distribution function (PDF) CT10 is used for all Powheg samples. The non-resonant gluon fusion process ($gg \to W^+W^-$) is simulated with the `gg2WW` [57] generator interfaced to Jimmy/Herwig for parton showering with the CT10 PDF. In addition, WW production via Standard Model Higgs decay ($gg \to H \to W^+W^-$ with $m_H = 125$ GeV), is also simulated with Powheg and showered with Pythia. The MC signal normalization to the theoretical production cross section is described in Section 3.2.1.

The $t\bar{t}$ and single-top (except for t-channel production) processes are generated with MC@NLO [33] with the CT10 PDF set and interfaced with Jimmy/Herwig [58, 26] for parton shower and underlying event simulation. MC@NLO includes NLO QCD matrix elements. The single-top t-channel production is simulated with the leading order (LO) generator AcerMC [31] with the CTEQ6L1 PDF set and showered with Pythia.

$Z +$ jets and $W +$ jets are simulated with Alpgen [30] and interfaced with Pythia or Jimmy/Herwig, respectively. The leading order CTEQ6L1 PDF is used for generating events with Alpgen. For the $Z +$ jets process, PDF reweighting to CT10 was used to improve the modeling of lepton η distributions, with no other noticeable effect on other distributions. This is not needed for $W +$ jets, because it is determined fully from data control samples, and hence the analysis does not rely on the MC simulation for $W +$ jets production.

The diboson processes WZ and ZZ (including both $ZZ \rightarrow \ell\ell\ell\ell$ and $ZZ \rightarrow \ell\ell\nu\nu$) are simulated with Powheg and showered with Pythia. The Wγ process is simulated with Alpgen [30] and interfaced with Jimmy/Herwig. The Wγ^* process is simulated with Sherpa [24] with up to one additional parton in the matrix element.

All Monte Carlo (MC) samples include the full simulation of the ATLAS detector [59] based on the Geant4 program [60]. The reconstruction algorithms and analysis performed on data is identical in the treatment of Monte Carlo samples. In all samples, unless otherwise stated, only the leptonic decays (including leptonic τ decays) of W and Z/γ bosons are included.

A summary of the MC generators and parton shower/underyling event programs used in the simulation of the various signal and background processes is listed in Table 5.

Process	MC Generator	Parton Shower
$q\bar{q} \rightarrow W^+W^-$	Powheg	Pythia
$gg \rightarrow W^+W^-$	`gg2WW`	Jimmy/Herwig
$gg \rightarrow H \rightarrow W^+W^-$	Powheg	Pythia
$Z +$ jets, $W +$ jets	Alpgen	Pythia or Jimmy/Herwig
$t\bar{t}$, Wt,single-top (s-channel)	MC@NLO	Jimmy/Herwig
single-top (t-channel)	AcerMC	Pythia
WZ,ZZ	Powheg	Pythia
$W\gamma$	Alpgen	Jimmy/Herwig
$W\gamma^*$	Sherpa	–

Table 5: List of MC generators and parton shower/underlying event programs in the simulation of signal and background processes.

3.2.3 Monte Carlo Corrections

Several corrections are applied to Monte Carlo events to correct for known deficiencies in the simulation. These corrections are derived from comparisons between MC and data in control samples. Electron energy calibrations are applied to data and resolution smearing is applied to MC(Section 3.5.1). Muon momentum scale shifting and resolution smearing corrections are applied (Section 3.5.2) as well. Lepton reconstruction, identification, trigger, and isolation/impact parameter efficiency scale factors derived from tag-and-probe methods are used, as discussed in Section 3.5.3.

The z-position of the interaction vertex is corrected in MC by using event-by-event weights to match the z position of the MC generated interaction point to the beam spot position in data.

The average number of interactions per bunch crossing,$< \mu >$, is also corrected in MC. This is done by reweighting the MC generated distribution to the distribution in data as a function of the data-taking period. MC events are generated with a broad $< \mu >$ distribution to ensure that all pileup conditions can be represented.

3.3 Data Set

This analysis uses the full data set collected in 2012 at center of mass energy $\sqrt{s} = 8$ TeV. The total integrated luminosity after data quality selection is 20.3 fb^{-1} with an uncertainty of 2.8%. Several data quality checks are required:

- Good Run List (GRL) - Each run consists of lumiblocks, which are units of time for data-taking (approximately a minute or two). The GRL is an officially produced list of lumiblocks that can be used for physics analyses. The GRL uses data quality flags, usually from specific detectors, to determine the integrity of the detector information. The GRL also ensures that data is recorded when the LHC has stable beams and the magnets are on.

- Detector flags - Events that are affected by problems associated with a specific detector elements are flagged and removed. Events with noise bursts or data corruption in the LAr calorimeter are removed by requiring `larError≠2`. Events with tile corrupted events are removed by requiring `tileError≠2` and using the `TileTripReader` tool.

  In the case where a detector needs to be restarted for recovery, a Trigger, Timing, and Control (TTC) restart was developed in which data is continuously taken during the restart. This eliminates the loss from stopping and starting a new data-taking run. However, events during the TTC restart need to be removed due to incomplete detector information. Incomplete events from TTC restarts are removed by requiring `coreFlags&0x40000≠0`

- Energy Corrections and Masking - When a module or cell in a detector partition becomes problematic or dead for the duration of a run, it is flagged and the energy measurement of that problematic cell/module is no longer used. Instead, the energy is extrapolated using information from neighbors. This replacement of the problematic energy measurement is referred to as masking. Several data quality checks are related to problems with masked modules.

  Hot Tile Cleaning- In data taking Period B1 and B2, there were runs in which a tile calorimeter module was not masked during reconstruction. Events with jets pointing to this module should be removed.

  Problematic events- A particular tile channel was not always masked which results in fake energy readings. Corrupted events have to be removed by using the officially provided tool (`TileTripReader:checkEvent()`).

  BCH Cleaning- Studies have shown that high p_T jets that fall into a masked region have energies that are overcorrected while those that fall in modules that are adjacent to masked modules tend to have undercorrected energies. Events with good jets that fail `IsBadMediumBCH` are not used. This checks that no jets are in the core of the masked region and no jets with a combination of `emfrac`[6] and `BCH_CORR_CELL`[7] that is shown to cause overestimated jet response fall adjacent to a masked region.

---

[6] The fraction of the jet energy from the EM calorimeter divided by the total energy of the jet.

[7] The fraction of the jet energy coming from the cell corrections.

3.4 Trigger Selection

A combination of single-lepton and dilepton triggers are used in this analysis. The trigger names are listed in Table 6. The $e\mu$ dilepton trigger and the single lepton triggers are used for the $e\mu$ channel. The di-electron and di-muon triggers are used in the ee and $\mu\mu$ channels respectively.

Previously, only the single-lepton triggers were used but a switch to the dilepton triggers without the isolation requirements is preferred. It is better to not require isolation at trigger level in order to use a more broad *loose* lepton definition in the W+jets data-driven estimate (Section 3.8.5). Ideally, the *loose* lepton should be identified using as few requirements as possible, but practically this is limited by the trigger requirements.

The two electron (muon) single-lepton trigger efficiencies are comparable to the di-electron (di-muon) trigger efficiencies. However, the $e\mu$ trigger is only approximately 80% efficient with respect to the single lepton triggers. To recover the full efficiency, an "OR" of the single-lepton and $e\mu$ dilepton trigger is used for the $e\mu$ channel.

Trigger Type	Name	Channel
single-electron	EF_e24vhi_medium1, EF_e60_medium1	$e\mu$
single-muon	EF_mu24i_tight, EF_mu36_tight	$e\mu$
$e\mu$ di-lepton	EF_e12Tvh_medium1_mu8	$e\mu$
di-electron	EF_2e12Tvh_loose1(_L2StarB)	ee
di-muon	EF_mu18_tight_mu8_EFFS	$\mu\mu$

Table 6: Single lepton and dilepton trigger names. The logical "OR" of the single lepton triggers and the $e\mu$ dilepton trigger is used for the $e\mu$ channel. The di-electron and di-muon triggers are used in the ee and $\mu\mu$ channels respectively. The EF_2e12Tvh_loose1_L2StarB trigger is identical to EF_2e12Tvh_loose1 except it is has a more efficient tracking which was implemented in data-taking Period D.

3.5 Object Selection

3.5.1 Electron Selection

Electrons are required to be seeded by energy deposits in the calorimeter and/or from tracks in the inner detector for reconstruction. Electron reconstruction is discussed in Section 2.3.3. A multivariate likelihood (LH) based identification [44] is used to reject hadronic jets and electrons from photon conversions. The likelihood uses variables that describe the shower shape, track quality, impact parameter with respect to the primary vertex, track-to-cluster matching and photon conversion matching. The *very tight* LH identification is designed to have the same electron efficiency as the cut based *tight* identification [61], but with a better background rejection.

The electron energy scale is corrected in data and smearing is applied to MC. Electrons are required to have $p_{\mathrm{T}} > 7$ GeV and be within the geometrical acceptance of the EM calorimeter ($|\eta| < 2.47$) excluding the transition between the barrel and endcap ($1.37 < |\eta| < 1.52$). Electrons must have good object quality, which ensures that the clusters do not originate from problems with the calorimeter.

There are additional requirements on the impact parameters with respect to the primary vertex. The transverse impact parameter significance (ratio of transverse impact parameter, d_0, and its error, σ_{d_0}) is required to be less than 3. The longitudinal impact parameter, $z_0 \times \sin(\theta_{track})$[8], is required to be less than 4 mm.

Both calorimeter and track based isolation criteria are used to select well isolated electrons to reject hadronic jets. The calorimeter isolation requires that the energy within a cone of $\Delta R = 0.3$, excluding the energy of the electron itself, has to be less than a fraction of the energy of the electron. The fraction varies from 0.20 to 0.28 depending on the $p_{\mathrm{T}}$of the electron. Track isolation requires that the sum of the tracks within a cone of $\Delta R = 0.3$ or $\Delta R = 0.4$ (depending on the p_{T}), after subtracting the $p_{\mathrm{T}}$of the electron itself, must be less than 6-10% of the electron p_{T}.

A summary of the electron object selection criteria is listed in Table 7.

Electron Selection

Selection	Requirement
Reconstruction	Cluster seeded and/or track seeded, Good object quality
Identification	*Very tight* Likelihood
Kinematic acceptance	$p_{\mathrm{T}} > 7$ GeV
Geometrical acceptance	$\lvert\eta\rvert < 2.47$, excluding $1.37 < \lvert\eta\rvert < 1.52$
Transverse impact parameter	$\lvert d_0/\sigma_{d_0}\rvert < 3$
Longitudinal impact parameter	$\lvert z_0 \times \sin(\theta_{track})\rvert < 4mm$
Calorimeter isolation	$7 \text{ GeV} < p_{\mathrm{T}} < 15 \text{ GeV}: \left(\sum_{\Delta R<0.3} E_{\mathrm{T}}\right) - E_{\mathrm{T}}^{el} < 0.20 \times E_{\mathrm{T}}^{el}$ $15 \text{ GeV} < p_{\mathrm{T}} < 20 \text{ GeV}: \left(\sum_{\Delta R<0.3} E_{\mathrm{T}}\right) - E_{\mathrm{T}}^{el} < 0.24 \times E_{\mathrm{T}}^{el}$ $p_{\mathrm{T}} > 20 \text{ GeV}: \left(\sum_{\Delta R<0.3} E_{\mathrm{T}}\right) - E_{\mathrm{T}}^{el} < 0.28 \times E_{\mathrm{T}}^{el}$
Track isolation	$7 \text{ GeV} < p_{\mathrm{T}} < 15 \text{ GeV}: \left(\sum_{\Delta R<0.4} p_{\mathrm{T}}\right) - p_{\mathrm{T}}^{el} < 0.06 \times E_{\mathrm{T}}^{el}$ $15 \text{ GeV} < p_{\mathrm{T}} < 20 \text{ GeV}: \left(\sum_{\Delta R<0.3} p_{\mathrm{T}}\right) - p_{\mathrm{T}}^{el} < 0.08 \times E_{\mathrm{T}}^{el}$ $p_{\mathrm{T}} > 20 \text{ GeV}: \left(\sum_{\Delta R<0.3} p_{\mathrm{T}}\right) - p_{\mathrm{T}}^{el} < 0.10 \times E_{\mathrm{T}}^{el}$

Table 7: Summary of electron object selection requirements.

3.5.2 Muon Selection

Muons are identified by tracks in the inner detector (ID) and the muon spectrometer (MS). The momentum measurement of the muon uses the combined fits of tracks from both the ID and MS, while correcting for energy loss in the calorimeter. Momentum energy scale shift and resolution smearing corrections are applied to MC events. Requirements on the

---

[8] The $\sin(\theta_{track})$ is added to take into account the larger uncertainties on z_0 due to forward electrons, especially with $\lvert\eta\rvert > 2.0$, which have a longer projection on the z-axis.

number of hits in the ID are imposed to ensure good track quality. Muons are required to be within the geometrical acceptance of the inner detector ($|\eta| < 2.4$) and are required to have $p_{\mathrm{T}} > 7$ GeV.

The transverse impact parameter significance (ratio of transverse impact parameter, d_0, and its uncertainty, σ_{d_0}) is required to be less than 3. The longitudinal impact parameter, $z_0 \times \sin(\theta_{track})$, must be less than 1mm to reduce the contribution from cosmic ray muons.

Again, calorimeter and track based isolation requirements are used. The calorimeter isolation requires that the energy within a cone of $\Delta R = 0.3$, excluding the energy of the muon itself, has to be less than 6-30% of the energy of the muon. Track isolation requires that the sum of the tracks within a cone of $\Delta R = 0.3$ or $\Delta R = 0.4$ (depending on the p_{T}), after subtracting the $p_{\mathrm{T}}$of the muon itself, must be less than 6-12% of the muon p_{T}.

A summary of the muon object selection criteria is listed in Table 8.

Muon Selection

Selection	Requirement
Reconstruction	Combined (ID and MS)
Track Quality	hits here
Kinematic acceptance	$p_{\mathrm{T}} > 7$ GeV
Geometrical acceptance	$\|\eta\| < 2.4$
Transverse impact parameter	$\|d_0/\sigma_{d_0}\| < 3$
Longitudinal impact parameter	$\|z_0 \times \sin(\theta_{track})\| < 1mm$
Calorimeter isolation	$7 \text{ GeV} < p_{\mathrm{T}} < 15 \text{ GeV}: \left(\sum_{\Delta R<0.3} E_{\mathrm{T}}\right) - E_{\mathrm{T}}^{\mu} < 0.06 \times E_{\mathrm{T}}^{\mu}$ $15 \text{ GeV} < p_{\mathrm{T}} < 20 \text{ GeV}: \left(\sum_{\Delta R<0.3} E_{\mathrm{T}}\right) - E_{\mathrm{T}}^{\mu} < 0.12 \times E_{\mathrm{T}}^{\mu}$ $20 \text{ GeV} < p_{\mathrm{T}} < 25 \text{ GeV}: \left(\sum_{\Delta R<0.3} E_{\mathrm{T}}\right) - E_{\mathrm{T}}^{\mu} < 0.18 \times E_{\mathrm{T}}^{\mu}$ $p_{\mathrm{T}} > 25 \text{ GeV}: \left(\sum_{\Delta R<0.3} E_{\mathrm{T}}\right) - E_{\mathrm{T}}^{\mu} < 0.30 \times E_{\mathrm{T}}^{\mu}$
Track isolation	$7 \text{ GeV} < p_{\mathrm{T}} < 15 \text{ GeV}: \left(\sum_{\Delta R<0.4} p_{\mathrm{T}}\right) - p_{\mathrm{T}}^{\mu} < 0.06 \times E_{\mathrm{T}}^{\mu}$ $15 \text{ GeV} < p_{\mathrm{T}} < 20 \text{ GeV}: \left(\sum_{\Delta R<0.3} p_{\mathrm{T}}\right) - p_{\mathrm{T}}^{\mu} < 0.08 \times E_{\mathrm{T}}^{\mu}$ $p_{\mathrm{T}} > 20 \text{ GeV}: \left(\sum_{\Delta R<0.3} p_{\mathrm{T}}\right) - p_{\mathrm{T}}^{\mu} < 0.12 \times E_{\mathrm{T}}^{\mu}$

Table 8: Summary of muon object selection requirements.

3.5.3 Lepton efficiencies and scale factors

Electron efficiency measurements using a tag-and-probe method on $Z \to ee$ and $J/\psi \to ee$ decays are described in Refs. [44, 61]. The muon reconstruction efficiency measurement using tag-and-probe method on $Z \to \mu\mu$ events is described in Refs. [62, 63]. In the tag-and-probe method on electron pairs, a strict set of quality requirements is applied on one of the electrons (referred to as the "tag") and the efficiency is measured on the other electron (referred as the "probe"). The total efficiency for an electron can be separated into different components:

$$\epsilon_{total} = \epsilon_{reco} \times \epsilon_{id} \times \epsilon_{trig} \times \epsilon_{additional} \tag{59}$$

The reconstruction (reco), identification (id), trigger (trig), and additional efficiencies are determined with respect to one another. In other words, the identification efficiency is measured with respect to the reconstruction efficiency. The trigger efficiency is measured with respect to the identification efficiency. Additional criteria such as isolation requirements are more analysis dependent, so this is left for last, and measured with respect to the trigger efficiency. The efficiencies in MC can be corrected by multiplicative scale factors, defined as the ratio of the efficiency in data divided by the efficiency in MC. These scale factors are often within a few percent of unity, which indicates the reasonably good agreement between data and MC simulation. The electron reconstruction, identification, and trigger efficiency scale factors are provided by the eγ combined performance group. Scale factors are given in bins of $E_{\mathrm{T}}$and η. Correspondingly, muon reconstruction scale factors are provided by the muon combined performance group.

The electron isolation criteria was optimized by the $H \to WW$ working group and adopted for this analysis. The isolation and impact parameter scale factors[9] are derived using the tag-and-probe method on $Z \to ee$ events. The tag electron must pass basic selection criteria: $p_{\mathrm{T}} > 25$ GeV, $|\eta| < 2.47$ (excluding transition region), matched to single-electron trigger, and pass *very tight* likelihood identification. The tag and probe electrons must have opposite sign and have a mass consistent with the Z mass. The probe must pass all selection criteria except for the isolation and impact parameter requirements, and efficiencies for the probe to pass the isolation and impact parameter requirements are measured in data and MC. The electron isolation and impact parameter scale factors have been presented[10] to the eγ working group and approved for use in this analysis.

The muon isolation criteria and corresponding isolation and impact parameter scale factors were also inherited from the $H \to WW$ working group.

3.5.4 Jets

Jets are reconstructed using the anti-k_{T} algorithm with radius parameter R=0.4, seeded from topological calorimeter clusters. Jet reconstruction and calibration methods are described in Section 2.3.4. Jets are locally calibrated [64] with jet energy scale corrections applied. Jets are required to have $p_{\mathrm{T}} > 25$ GeV and be within $|\eta| < 4.5$. Jets are not selected if they fall into regions of the calorimeter where its energy cannot be well measured (by requiring `isUgly==0`), for example if it falls into a dead region of the calorimeter. Jets candidates are also removed if they originate from background or detector effects (by requiring `isBadLooseMinus==0`).

To reduce the number of jets resulting from pileup, a jet vertex fraction (JVF) requirement is applied for jets [48]. The JVF is defined as the fraction of the sum $p_{\mathrm{T}}$of the tracks within the jet that originate from a particular vertex (in this case, the primary vertex) to

---

[9] `https://svnweb.cern.ch/trac/atlasoff/browser/PhysicsAnalysis/HiggsPhys/HSG3/WWDileptonAnalysisCode/HWWIsolationScaleFactors/tags/HWWIsolationScaleFactors-00-00-01`

[10] `https://indico.cern.ch/event/281188/contribution/3/material/slides/0.pdf`

the sum $p_{\mathrm{T}}$of all tracks within the jet (from any vertex). For jets within the acceptance of the inner detector ($|\eta| < 2.4$) and with $p_{\mathrm{T}} < 50$ GeV, the JVF must be greater than 0.5. For jets with p_{T}above 50 GeV, the JVF requirement is not needed since the rejection of pileup jets is not significant at high p_{T}. The JVF requirement cannot be applied to jets that fall outside of the inner detector, where tracks cannot be reconstructed.

Jets are not considered if they overlap with an electron. Details on object overlap removal are discussed in Section 3.5.5.

A summary of the jet selection criteria is listed in Table 9.

Jet Selection

Selection	Requirement
Kinematic acceptance	$p_{\mathrm{T}} > 25$ GeV
Geometrical acceptance	$\|\eta\| < 4.5$
Jet vertex fraction	JVF > 0.5, only for jets with $p_{\mathrm{T}} < 50$ GeV and $\|\eta\| < 2.4$.

Table 9: Summary of jet selection requirements.

3.5.5 Object overlap removal

This section will discuss the object overlap removal between e/μ, e/jet, and jet/μ. The most important overlap is between electrons and jets. Since jets are reconstructed from topological clusters, energy clusters from high p_{T}electrons will also be reconstructed as a jet. In this case, two reconstructed objects represent the same physical object. If the electron candidate passes the strict electron selection requirements and overlaps with the jet with $\Delta R < 0.3$ (where $\Delta R = \sqrt{\Delta\phi^2 + \Delta\eta^2}$), then the jet candidate is removed and the electron is retained.

Unlike the case for electrons, muons are not usually reconstructed as jets since they do not usually deposit significant energy in the calorimeter. However, muons from heavy flavor jets can result in non-isolated reconstructed muons that are very close to a reconstructed jet. If a muon is within $\Delta R < 0.3$ of a jet, the muon is removed.

In the rare case where a muon emits a bremsstrahlung photon, the photon will deposit energy in the calorimeter which may be reconstructed as an electron. To remove this contribution, if an electron is within $\Delta R < 0.1$ of a muon, the electron is removed.

The objects remaining after overlap requirements depend on the order in which the steps are applied. To avoid ambiguities, the order in which object candidates are selected is first muons, then electrons, and finally jets.

3.5.6 Missing Transverse Energy

Missing transverse energy, $E_{\mathrm{T}}^{\mathrm{miss}}$, is determined using the energy measured by the electromagnetic and hadronic calorimeters as well as muon energy measured by the muon spectrometer and inner detector. $E_{\mathrm{T}}^{\mathrm{miss}}$is defined as a negative sum of the $p_{\mathrm{T}}$of electrons, photons, tau leptons, jets, muons and cells not associated with any of the previously mentioned reconstructed objects.

In this analysis, a projection of $E_{\mathrm{T}}^{\mathrm{miss}}$is used if there is a selected jet or lepton near the azimuthal direction of $E_{\mathrm{T}}^{\mathrm{miss}}$. This is done to reduce sensitivity of $E_{\mathrm{T}}^{\mathrm{miss}}$to mismeasurement in the leptons or jets. $E_{\mathrm{T,\ Rel}}^{\mathrm{miss}}$ is defined as

$$E_{\mathrm{T,\ Rel}}^{\mathrm{miss}} = \begin{cases} E_{\mathrm{T}}^{\mathrm{miss}} \times \sin\left(\Delta\phi_{\ell,j}\right) & \text{if } \Delta\phi_{\ell,j} < \pi/2 \\ E_{\mathrm{T}}^{\mathrm{miss}} & \text{if } \Delta\phi_{\ell,j} \geq \pi/2, \end{cases} \tag{60}$$

where $\Delta\phi_{\ell,j}$ is the difference in ϕ between the $E_{\mathrm{T}}^{\mathrm{miss}}$and nearest lepton ($\ell = e,\ \mu$) or jet.

Studies have shown that $E_{\mathrm{T}}^{\mathrm{miss}}$is sensitive to pileup effects and a pileup suppressed $E_{\mathrm{T}}^{\mathrm{miss}}$calculation is presented in Ref [65]. In this analysis, optimization studies have shown that the pileup suppressed $E_{\mathrm{T}}^{\mathrm{miss}}$is not as effective as using a track-based missing transverse momentum, as described in the next section.

3.5.7 Missing Transverse Momentum

A track-based missing transverse momentum provides complementary information to the usual calorimeter based $E_{\mathrm{T}}^{\mathrm{miss}}$. The track-based missing transverse momentum, $p_{\mathrm{T}}^{\mathrm{miss}}$, is defined as the negative vector sum of the $p_{\mathrm{T}}$of the tracks that satisfy:

- $p_{\mathrm{T}} > 500$ MeV
- $|\eta| < 2.5$
- $n_{SCT} \geq 6, n_{PIX} \geq 1$
- $|d_0| < 1.5$ mm
- $|z_0 \times \sin(\theta_{track})| < 1.5$ mm

where d_0 and z_0 are the transverse and longitudinal impact parameters (calculated with respect to the primary vertex), respectively, and n_{SCT} and n_{PIX} are the number of hits in the semiconductor tracker (SCT) and pixel (PIX) detector, which are discussed in Section 2.2.1. To improve on the $p_{\mathrm{T}}^{\mathrm{miss}}$ calculation, the tracks of the leptons are always included. The electron track is replaced with the p_{T}measurement using the calibrated calorimeter energy. The muon track $p_{\mathrm{T}}$is replaced with the combined measurement from the muon spectrometer and inner detector track p_{T}. $p_{\mathrm{T}}^{\mathrm{miss}}$ is more pileup robust, since it uses only tracks that originate from the primary vertex. However, is limited in the sense that only charged particles up to $|\eta| < 2.5$ are included in the $p_{\mathrm{T}}^{\mathrm{miss}}$ calculation, compared to the full coverage of $|\eta| < 4.9$ used in the $E_{\mathrm{T}}^{\mathrm{miss}}$calculation.

3.6 Event Selection

The production of opposite sign $WW \to \ell\nu\ell\nu$ yields a final state of two oppositely signed leptons ($\ell = e$ or μ) with $E_{\mathrm{T}}^{\mathrm{miss}}$. Three separate channels are considered: ee, $\mu\mu$, and $e\mu$. Each channel has slightly different final selection criteria, since the same-flavor channels (ee and $\mu\mu$) have different background contributions than the opposite-flavor channel (eμ).

3.6.1 WW Event Selection Criteria

The preliminary selection (sometimes referred to as the preselection) of WW events includes the following requirements:

1. Data quality - Events must pass the Good-Run-List (GRL), detector flags, and event cleaning checks described in Section 3.3
2. Trigger selection - For the same flavor channels, events must pass the corresponding dilepton trigger. For the opposite-flavor channel, the event must pass a logical OR of the single-lepton or dilepton triggers. Details on the trigger selection can be found in Section 3.4
3. Primary vertex selection - The primary vertex (PV) is defined as the vertex with the largest $\sum p_{\mathrm{T}}^2$. The primary vertex is required to have at least 3 tracks.
4. Object selection - Candidate muons, electrons, and jets are selected according to criteria described in Section 3.5. The overlap removal between these objects is described in Section 3.5.5
5. Dilepton Selection - Exactly two opposite sign leptons are required. The event is rejected if there is an additional third lepton with $p_{\mathrm{T}} > 7$ GeV to reject other diboson backgrounds. The leading (subleading) lepton must have $p_{\mathrm{T}} > 25(20)$ GeV.
6. Trigger Matching - The two leptons must be matched to corresponding trigger-level objects. For the same flavor channels, both leptons must be matched to the dilepton trigger objects. For the opposite flavor channels, either both leptons have to be matched to the dilepton trigger objects or at least one of the leptons with $p_{\mathrm{T}} > 25$ GeV has to match one of the single-lepton trigger objects.

After preselection, the vast majority of events ($> 99\%$) are from the $Z \to ee$ and $Z \to \mu\mu$ processes in the ee and $\mu\mu$ channels. The WW signal fraction is only 0.07% in the same-flavor channels. In comparison, the WW signal fraction is already 11% after preselection in the $e\mu$ channel. The relative background contributions in the $e\mu$ channel are 64% top, 22% $Z \to \tau\tau$, and 3% W+jets and diboson. The background composition in the same-flavor channels and the opposite-flavor channels is quite different, so different strategies have to be adopted to optimize the final selection criteria. The choice of discriminating variables and their selection values have been optimized by maximizing the significance, $\frac{S}{\sqrt{S+B}}$, while also considering the signal acceptance. The final WW selection requirements are:

1. M_{ll} - The dilepton invariant mass, M_{ll}, must be greater than 15 GeVin the same flavor channels to reduce the contribution from multijet events. $M_{ll} > 10$ GeV is required for the opposite flavor channel to remove the low mass spectrum that is not modeled in $Z+$jets MC. Figure 21 shows the dilepton invariant mass for the same flavor and different flavor channels after the preselection criteria.
2. Z Veto - To reduce the contribution from $Z \to ee$ and $Z \to \mu\mu$, the dilepton mass must be outside of the Z mass window: $|M_{ll} - M_Z| > 15$ GeV, with $M_Z = 91.2$ GeV. The Z veto is only applied for the same-flavor channels.

3. $E_{\mathrm{T,\ Rel}}^{\mathrm{miss}}$ - To further reduce the contribution from Z+jets, the relative missing transverse energy, $E_{\mathrm{T,\ Rel}}^{\mathrm{miss}}$, must be greater than 45(15) GeV in the same (different) flavor channel. $E_{\mathrm{T,\ Rel}}^{\mathrm{miss}}$ is defined in Equation 60.

4. $p_{\mathrm{T}}^{\mathrm{miss}}$ - In combination with the calorimeter-based $E_{\mathrm{T,\ Rel}}^{\mathrm{miss}}$, the track-based $p_{\mathrm{T}}^{\mathrm{miss}}$ further reduces the $Z+$jets background. $p_{\mathrm{T}}^{\mathrm{miss}}$ is required to be greater than 45 (20) GeVin the same (different) flavor channel.

5. $\Delta\phi(E_{\mathrm{T}}^{\mathrm{miss}}, p_{\mathrm{T}}^{\mathrm{miss}})$ - The difference in the azimuthal angle between $E_{\mathrm{T}}^{\mathrm{miss}}$and $p_{\mathrm{T}}^{\mathrm{miss}}$ is expected to be larger in events where the missing energy does not originate from neutrinos and hence $E_{\mathrm{T}}^{\mathrm{miss}}$and $p_{\mathrm{T}}^{\mathrm{miss}}$ are uncorrelated. This variable is useful in reducing $Z+$jets background. It is also shown that $\Delta\phi(E_{\mathrm{T}}^{\mathrm{miss}}, p_{\mathrm{T}}^{\mathrm{miss}})$ is uncorrelated with $E_{\mathrm{T}}^{\mathrm{miss}}$. $\Delta\phi(E_{\mathrm{T}}^{\mathrm{miss}}, p_{\mathrm{T}}^{\mathrm{miss}})$ is required to be less than 0.3 (0.6) for same (different) flavor channel.

6. Jet Veto - To reject top background, events are rejected if there is at least one selected jet with $p_{\mathrm{T}} > 25$ GeV passing the JVF requirement and quality criteria described in Section 3.5.4. Figure 22 shows the jet multiplicity before the jet veto requirement.

The observed number of events after each selection requirement is shown in Table 10. The observed number of events with MC predicted expected yields are shown in Table 11. Figures 23, 23, and 23 show kinematic distributions for events after all selection requirements in the $e\mu$, ee and $\mu\mu$ channels, respectively.

Data Cutflow				
Requirement	ee	$\mu\mu$	$e\mu$	Combined
$M_{ll} > 15(10)$ GeV	4918726	8357583	83042	13359351
$\lvert M_{ll} - M_Z\rvert > 15(0)$ GeV	412853	721978	—	1217873
$E_{\mathrm{T,\ Rel}}^{\mathrm{miss}} > 45(15)$ GeV	11594	19887	52142	83623
$p_{\mathrm{T}}^{\mathrm{miss}} > 45(20)$ GeV	5762	9152	43718	58632
$\Delta\phi(E_{\mathrm{T}}^{\mathrm{miss}}, p_{\mathrm{T}}^{\mathrm{miss}}) < 0.3(0.6)$	2613	4291	27591	34495
Jet Veto	594	975	5067	6636

Table 10: Event selection yields for data collected in 2012 at 8 TeV for $20.3\,\mathrm{fb}^{-1}$split in channels. For the M_{ll}, $E_{\mathrm{T,\ Rel}}^{\mathrm{miss}}$, $p_{\mathrm{T}}^{\mathrm{miss}}$ and $\Delta\phi(E_{\mathrm{T}}^{\mathrm{miss}}, p_{\mathrm{T}}^{\mathrm{miss}})$ requirements, two values are presented in first column, with the first one for same flavor channels and the second one for $e\mu$ channel.

Final State	ee Channel	$\mu\mu$ Channel	$e\mu$ Channel	Combined
Observed Events	594	975	5067	6636
Total MC prediction (S+B)	553.2± 13.0	903.9± 11.3	4427.9± 33.3	5884.9± 37.5
MC WW signal	349.6± 3.3	614.4± 4.5	3254.8± 10.3	4218.8± 11.7
Top	96.9± 4.8	131.4± 6.1	625.9± 12.5	854.2± 14.7
Z+jets	26.0± 13.9	41.8± 17.1	173.0± 16.7	0± 0
W+jets	21.6± 9.7	13.6± 4.3	225.3± 24.4	260.5± 26.6
Dibosons	29.8± 1.6	38.5± 1.3	157.3± 4.1	225.5± 4.5
Total Background	203.6± 12.6	289.5± 10.3	1173.1± 31.7	1666.1± 35.6

Table 11: Summary of observed data events and expected signal and background contributions as predicted by Monte Carlo simulations in the three channels and their combined results. Monte Carlo yields are normalized to an integrated luminosity of 20.3 fb^{-1}. Only statistical uncertainties are shown.

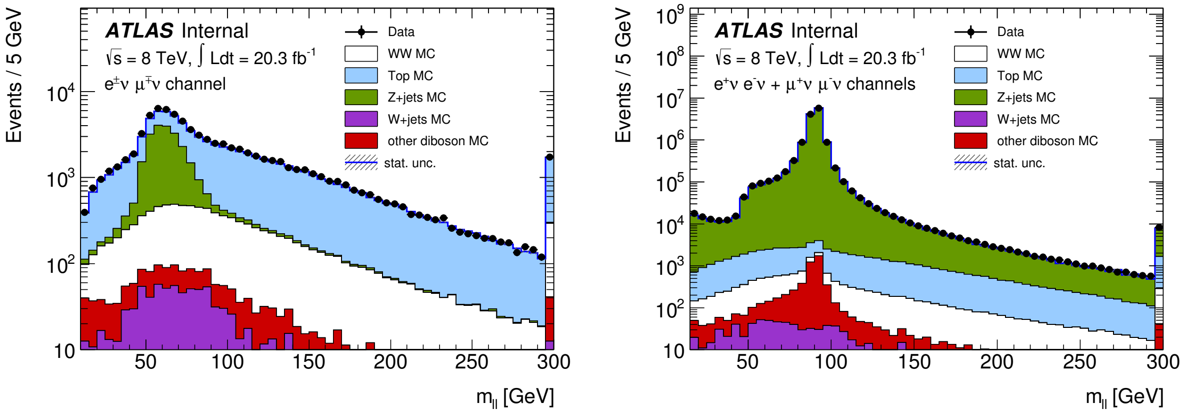

Figure 21: The dilepton invariant mass distributions for $e\mu$ (left) and $ee + \mu\mu$ (right) events after the dilepton selection and requiring $m_{ll} > 15/10\ GeV$ for the same-flavor or different-flavor channels respectively. Here, ee and $\mu\mu$ selected events have been summed in the same figure. The Drell-Yan process (labeled as Z+jets MC) with Z or γ^* decaying to same flavor leptons is the dominant contribution. For the $e\mu$ events, Drell-Yan production is only a minor background, mainly arising from Z decays into leptonically decaying τ-leptons. The points represent data and the stacked histograms are the MC predictions, which are normalized to 20.3 fb^{-1} using SM cross sections. The last bin is an overflow bin. Only statistical uncertainties are shown.

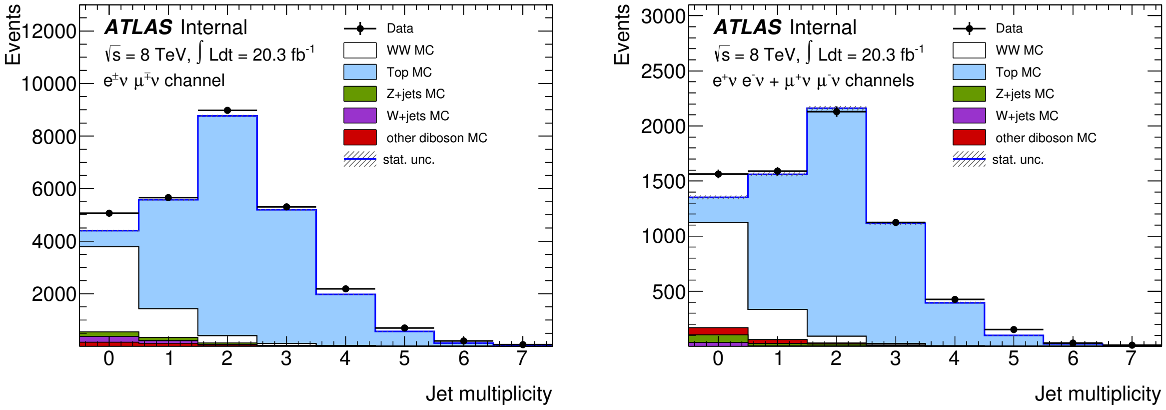

Figure 22: Jet multiplicity distributions for $e\mu$ (left) and $ee + \mu\mu$ (right) events before the jet-veto requirement is applied. The points represent data and the stacked histograms are the MC predictions, which are normalized to 20.3 fb^{-1} using SM cross sections. The $t\bar{t}$ contribution is normalized to the NNLO+NNLL theoretical calculation. Only statistical uncertainties are shown.

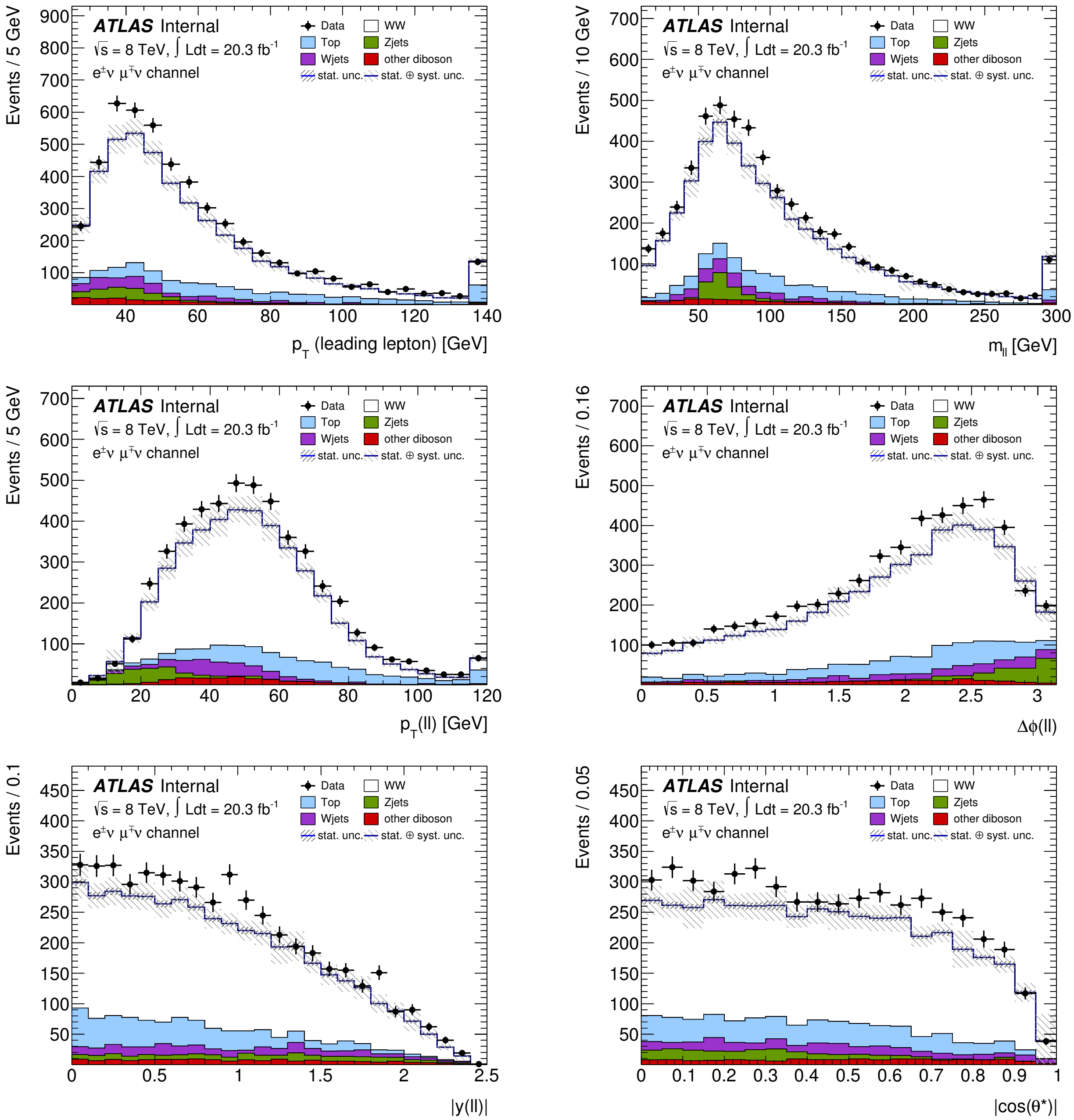

Figure 23: Kinematic distributions for selected data events after the full event selection for $e\mu$ final state. Data are shown together with MC predictions of signal and background production processes, scaled to 20.3 fb^{-1}using NLO SM cross-sections. Where applicable, the MC predictions have been replaced by the corresponding estimation using data-driven methods. Shown are (from left to right and top to bottom): the transverse momentum p_{T} of the leading lepton, $p_{\mathrm{T}}^{\mathrm{lead}}$, the transverse momentum of the dilepton system, $p_{\mathrm{T}}(\ell\ell)$, and its invariant mass $m_{\ell\ell}$ as well as the difference in azimuthal angle between the decay leptons, $\Delta\phi_{\ell\ell}$, their combined rapidity, $|y_{\ell\ell}|$ as well as the observable $|\cos(\theta^{*})|$, which is defined using the difference between the pseudorapidities of the leptons, $\Delta\eta_{\ell\ell}$. Statistical uncertainties are shown as gray bands in the main plot or as orange bands on the ratio plot.

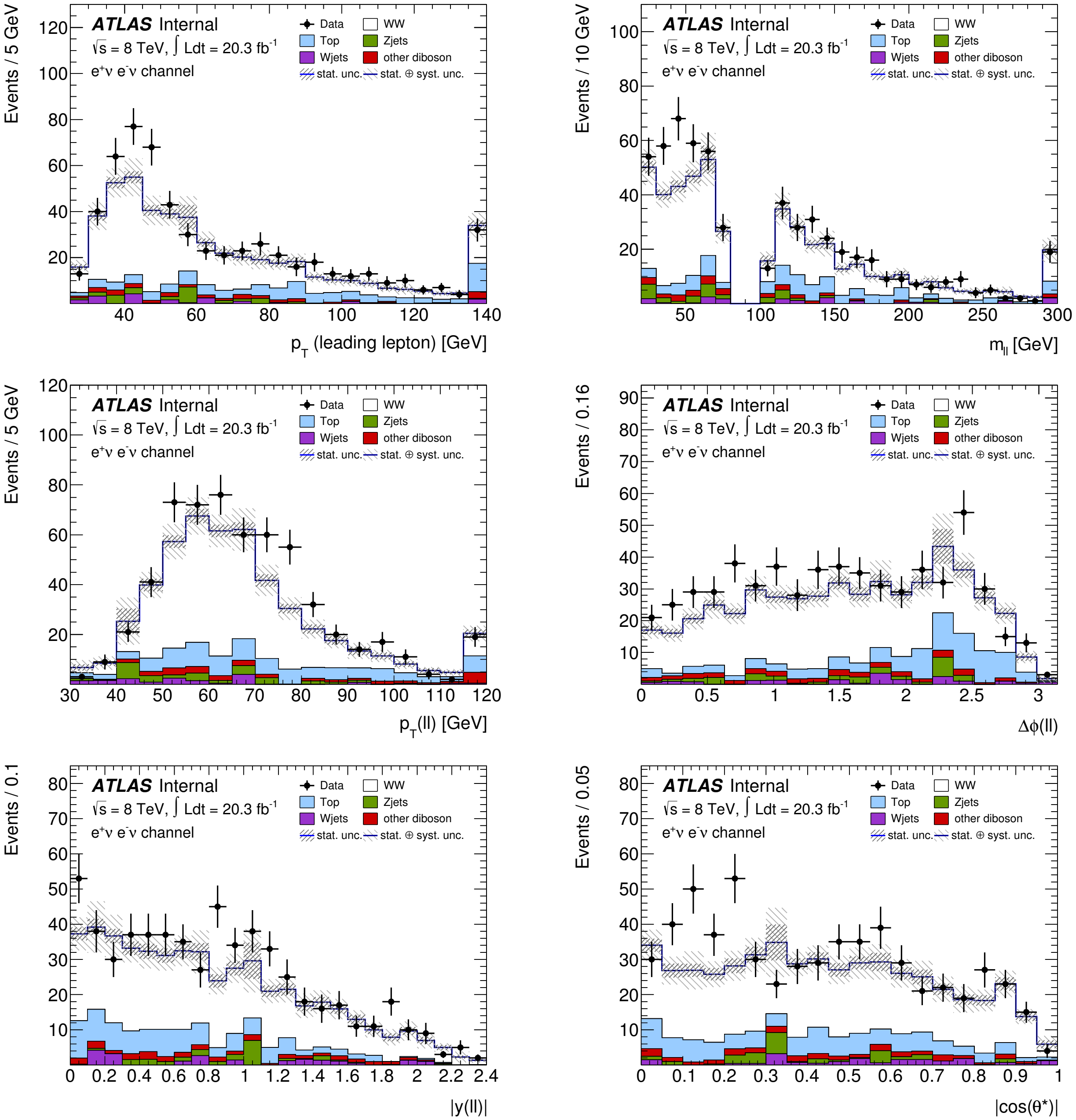

Figure 24: Kinematic distributions for selected data events after the full event selection for ee final state. Data are shown together with MC predictions of signal and background production processes, scaled to 20.3 fb^{-1}using NLO SM cross-sections. Where applicable, the MC predictions have been replaced by the corresponding estimation using data-driven methods. Shown are (from left to right and top to bottom): the transverse momentum p_{T} of the leading lepton, $p_{\mathrm{T}}^{\mathrm{lead}}$, the transverse momentum of the dilepton system, $p_{\mathrm{T}}(\ell\ell)$, and its invariant mass $m_{\ell\ell}$ as well as the difference in azimuthal angle between the decay leptons, $\Delta\phi_{\ell\ell}$, their combined rapidity, $|y_{\ell\ell}|$ as well as the observable $|\cos{(\theta^{*})}|$, which is defined using the difference between the pseudorapidities of the leptons, $\Delta\eta_{\ell\ell}$. Statistical uncertainties are shown as gray bands in the main plot or as orange bands on the ratio plot.

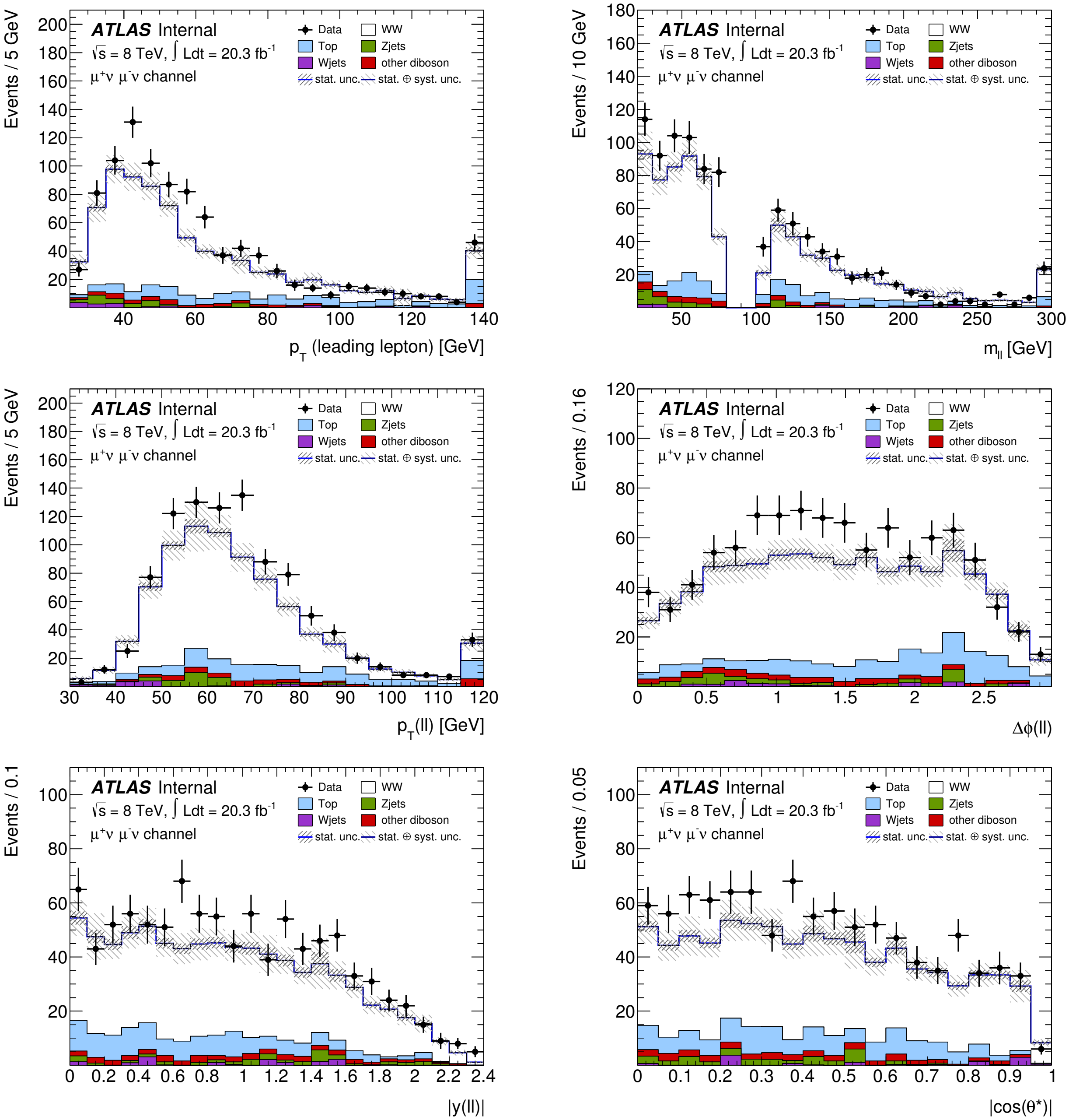

Figure 25: Kinematic distributions for selected data events after the full event selection for $\mu\mu$ final state. Data are shown together with MC predictions of signal and background production processes, scaled to 20.3 fb^{-1}using NLO SM cross-sections. Where applicable, the MC predictions have been replaced by the corresponding estimation using data-driven methods. Shown are (from left to right and top to bottom): the transverse momentum p_{T} of the leading lepton, $p_{\mathrm{T}}^{\mathrm{lead}}$, the transverse momentum of the dilepton system, $p_{\mathrm{T}}(\ell\ell)$, and its invariant mass $m_{\ell\ell}$ as well as the difference in azimuthal angle between the decay leptons, $\Delta\phi_{\ell\ell}$, their combined rapidity, $|y_{\ell\ell}|$ as well as the observable $|\cos{(\theta^{*})}|$, which is defined using the difference between the pseudorapidities of the leptons, $\Delta\eta_{\ell\ell}$. Statistical uncertainties are shown as gray bands in the main plot or as orange bands on the ratio plot.

3.7 Sources of Systematic Uncertainty

This section describes experimental and theoretical sources of systematic uncertainty that are propagated into all measurements, including data-driven background estimates and cross-section results described in the subsequent sections. The determination of experimental uncertainties on reconstructed leptons (Section 3.7.1), jets (Section 3.7.2), $E_{\mathrm{T}}^{\mathrm{miss}}$(Section 3.7.3), and $p_{\mathrm{T}}^{\mathrm{miss}}$ (Section 3.7.4) are described. Theoretical sources of systematic uncertainties are described generally in Section 3.7.5. The propagation of individual sources on background estimates and results are given in each of the corresponding sections. Uncertainties specific to a particular background estimate are described in the relevant background section and not described here.

3.7.1 Lepton Uncertainties

Lepton efficiencies and scale factors (SF) are described in Section 3.5.3. Systematic uncertainties for electrons and muons are considered separately. For electrons, reconstruction, identification (`tight`), trigger, and isolation efficiency scale factors are applied. For muons, identification (which combines both reconstruction and combined (CB) muon efficiencies), trigger, and isolation efficiency scale factors are applied. Each scale factor has a corresponding systematic uncertainty, also provided by the eγ and muon combined performance groups. Uncertainties on SF's are propagated throughout the analysis by using $SF \pm \sigma_{SF}$ in place of the central value.

Leptons also have energy scale and resolution systematic uncertainties. The systematic uncertainty on the energy scale is assessed by varying the lepton energy scale by $\pm 1\sigma$. Similarly, the uncertainty on the energy resolution is assessed by varying the lepton energy resolution by $\pm 1\sigma$. The systematic variation is applied to all electrons or muons at the same time. Since the calculation of $E_{\mathrm{T}}^{\mathrm{miss}}$uses calibrated energy of objects in place of the original cell energy, the systematically varied leptons are also propagated into this calculation. This properly takes into account the correlations between $E_{\mathrm{T}}^{\mathrm{miss}}$and the leptons.

3.7.2 Jet Uncertainties

The major sources of systematic uncertainties related to jets are due to jet energy scale and jet energy resolution. Jet energy measurement and its systematic uncertainties are documented in Reference [66]. The energy resolution uncertainty is assessed by scaling the energy by a random factor pulled from Gaussian distribution with a mean of 1 and standard deviation given by the systematic uncertainty. As for the case with leptons, the systematically varied jets are also propagated into the calculation of $E_{\mathrm{T}}^{\mathrm{miss}}$. The energy scale uncertainties are assessed in the same way as for leptons: by varying the energy by $\pm 1\sigma$. In this analysis, there are multiple components for the jet energy scale uncertainty. There is a total of 14 baseline nuisance parameters: 6 in-situ, 2 η intercalibration, non-closure, high p_{T}, and 4 pileup related nuisance parameters. In addition, there are 3 jet flavor nuisance parameters and a closeby jets uncertainty, which brings the total to 18 nuisance parameters. Descriptions of the 18 components of the jet energy scale uncertainties are listed below:

In-situ In-situ techniques are used to assess the ability of MC simulation in reproducing the data. Events with a jet and a well reconstructed and calibrated reference objects are used (such as photons or $Z \rightarrow ee$. The transverse momentum of the jet is balanced by the transverse momentum of the reconstructed reference object. This method can be used for jets with $15 < p_{\mathrm{T}} < 800$ GeV and $|\eta| < 2.8$.

η **intercalibration** The in-situ techniques described using a Z boson or photon will not work in the forward regions of the detector. Instead, forward, probe jets can be calibrated against a well calibrated (using Z-jet or photon-jet in-situ techniques) reference jet. This is called the central reference method. However, requiring both a central and a forward jet is statistically limiting. To recover more events, a matrix method can be used by replacing the probe and reference jet with left and right high transverse momentum jets, where the left and right jets are defined such that $\eta^{\mathrm{left}} < \eta^{\mathrm{right}}$. The matrix method can be applied in bins of η and p_{T}. The largest component of the intercalibration uncertainty is from modeling uncertainty, where the full difference between samples generated with Pythia and with Herwig (or the difference between data and whichever of the the two is larger) is taken as the uncertainty.

Non-closure - The jet calibration is based on MC12a samples with a particular detector geometry and pileup configuration. MC samples generated with different configurations will have a different jet response, hence this uncertainty is only applied for non-MC12a samples. In this analysis, all MC samples are MC12a (where this uncertainty has no effect) except for the Sherpa Wγ samples.

Flavor composition - The calorimeter response is different for light quark initiated jets than for gluon initiated jets [67]. The calibration is based on a particular composition of quark and gluon jets. This systematic uncertainty takes into account the amount of light quark jets and gluon jets which can differ for each analysis. This is not applied for b-quark initiated jets.

Flavor response - The flavor response is the uncertainty on the response for quark and gluon jets.

B-jet response - The jet response is also different for heavy flavor b-quark jets. This is only applied for jets that are matched to a B hadron in the MC.

The jet energy scale uncertainty components are summarized in Table 12.

The jet vertex fraction (JVF) requirement is applied for jets with $p_{\mathrm{T}} < 50$ GeV within the acceptance of the inner detector. A systematic uncertainty on the JVF calculation is assessed by varying the JVF for all applicable jets simultaneously by $\pm 1\sigma$.

3.7.3 $E_{\mathrm{T}}^{\mathrm{miss}}$Uncertainties

The calculation of the calorimeter based $E_{\mathrm{T}}^{\mathrm{miss}}$is described in Section 3.5.6. The $E_{\mathrm{T}}^{\mathrm{miss}}$calculation uses the reconstructed and calibrated objects (such as electrons, muons, jets) as well as calorimeter energy deposits not associated with any of those reconstructed objects (called

Sources	$e^+e^- E_{\mathrm{T}}^{\mathrm{miss}}$	$\mu^+\mu^- E_{\mathrm{T}}^{\mathrm{miss}}$	$e^\pm\mu^\mp E_{\mathrm{T}}^{\mathrm{miss}}$	Combined
JES Effective NP1	0.47%	0.57%	0.35%	0.39%
JES Effective NP2	0.68%	0.94%	0.57%	0.63%
JES Effective NP3	0.31%	0.40%	0.21%	0.24%
JES Effective NP4	0.08%	0.13%	0.06%	0.07%
JES Effective NP5	0.09%	0.14%	0.05%	0.07%
JES Effective NP6 rest term	0.07%	0.10%	0.05%	0.06%
JES Eta Intercalibration Modelling	0.22%	0.23%	0.14%	0.16%
JES Eta Intercalibration StatAndMethod	0.65%	0.80%	0.57%	0.61%
JES SingleParticle HighPt	0%	0%	0%	0%
JES Relative Non Closure	0%	0%	0%	0%
JES NPV Offset	0.23%	0.37%	0.22%	0.24%
JES Mu Offset	0.07%	0.09%	0.06%	0.07%
JES Pileup Pt	0.02%	0.01%	0.02%	0.02%
JES Pileup Rho	0.49%	0.69%	0.37%	0.42%
JES Closeby	0%	0%	0%	0%
JES Flavour Composition	0.55%	0.80%	0.46%	0.51%
JES Flavour Response	0.92%	1.25%	0.80%	0.87%
JES B Scale	0%	0.01%	0%	0%
JES Baseline	1.21%	1.52%	1.02%	1.10%
JES Total	1.65%	2.34%	1.56%	1.67%

Table 12: Jet energy scale uncertainty components for signal samples. JES Total refers to the overall estimate of the total uncertainty obtained from the tool (does not include pileup uncertainty for example). JES Baseline is a quadratic sum. of effective NP* components. Numbers are shown before the jet veto is applied.

the soft term). The systematic uncertainty on $E_{\mathrm{T}}^{\mathrm{miss}}$is comprised of the uncertainties propagated from the reconstructed objects as well as an uncertainties on the soft term. The uncertainty on soft term is measured using $Z \rightarrow \mu\mu$ events where there are no jets with $p_{\mathrm{T}} > 20\ \ \mathrm{GeV}$. Here, the $E_{\mathrm{T}}^{\mathrm{miss}}$calculation only involves the two leptons and a soft term. $E_{\mathrm{T}}^{\mathrm{miss}}$is projected along the direction of the Z boson and the difference between this projection in data and MC is taken as the uncertainty in the soft term scale. For the soft term resolution, the resolution of $E_{\mathrm{x}}^{\mathrm{miss}}$ or $E_{\mathrm{y}}^{\mathrm{miss}}$ is used instead.

3.7.4 $p_{\mathrm{T}}^{\mathrm{miss}}$ Uncertainties

The calculation of the track based $p_{\mathrm{T}}^{\mathrm{miss}}$ is described in Section 3.5.7. The systematic uncertainty on $p_{\mathrm{T}}^{\mathrm{miss}}$ is derived using a similar method used for the calorimeter based $E_{\mathrm{T}}^{\mathrm{miss}}$using $Z \rightarrow \mu\mu$ data events. The scale and resolution ratios between data and MC is used to determine systematic uncertainties.

3.7.5 Theoretical Uncertainties

In addition to experimental uncertainties, there are also theoretical uncertainties from choices in renormalization and factorization scales, parton distribution function (PDF) sets, generator and parton shower programs.

Renormalization and Factorization Scales After renormalization, the coupling "constant" has a scale dependency that varies according to the renomalization group (RG) equations. This scale is referred to as the renormalization scale, μ_R. The factorization scale, μ_F, is the cutoff scale that separates perturbative and non-perturbative QCD. Below the factorization scale, soft infrared (IR) divergences take over and the effects can be summarized in PDFs. Above the factorization scale, Feynman diagrams calculations can be used to calculate the hard scatter process. The factorization scale is not arbitrary and is usually set to the hard scale (eg: m_{WW} for WW production) for a particular process. The renormalization scale is typically taken to be the same as the factorization scale to avoid large logarithms. QCD observables (when taken to all orders) cannot depend on scale choices, but in practice a fixed order calculation will. To determine the scale uncertainties, the nominal scale is typically varied by a factor of 1/2 and 2 and the uncertainty is taken to be the largest of the variations. To be conservative, the factorization and renormalization scales can be varied independently (ie: in opposite directions) in determining scale uncertainties.

PDF The uncertainty on the PDF set is determined by taking a nominal choice (such as CT10) and comparing the results with a different PDF set (such as MSTW2008NLO). Of course, (NLO) LO PDF sets should only be compared with other (NLO) LO PDF sets with the same order. The uncertainty on the parton distribution itself is determined by using the 1σ uncertainties[11] for the nominal PDF set and taking the largest variation with respect to the central values.

---

[11] The uncertainties for a particular PDF set can be determined from the member PDFs in LHAPDF, although the exact definitions of the member PDFs may vary from set to set.

Generator/Parton Shower MC programs may have differences in the way that they implement matrix element calculations or how they model hadronization or radiation. These differences are considered as a theoretical modeling uncertainty on the choice of MC generator or parton shower program. This uncertainty can be determined by comparing events generated using the same generator with a different parton shower program or vice versa. Since the generator and parton shower uncertainty overlaps with the jet veto uncertainty (which is discussed next), the generator and parton shower uncertainties are assessed with all selection requirements except for the jet veto.

Jet Veto It has been shown in Ref. [68] that accidental cancellations of large logarithms can lead to underestimated uncertainties in a jet binned analysis. The Stewart-Tackmann proposal is to assume that the inclusive jet binned cross sections are uncorrelated. The jet veto acceptance, ϵ, can then be estimated using the following method:

$$\frac{\delta\epsilon}{\epsilon} = \left(\frac{1-\epsilon}{\epsilon}\right)\sqrt{\left(\frac{\delta\sigma_{\geq 0 \text{ jet}}}{\sigma_{\geq 0 \text{ jet}}}\right)^2 + \left(\frac{\delta\sigma_{\geq 1 \text{ jet}}}{\sigma_{\geq 1 \text{ jet}}}\right)^2} \tag{61}$$

where $\sigma_{\geq i \text{ jet}}$ is the inclusive fiducial cross section in jet bins and the uncertainties are taken from scale variations. The Stewart-Tackmann method is applied at NNLO using results from private communications with the authors of Ref. [53]. The jet veto acceptance uncertainty for $qq \to WW$ is 2.9% using the Stewart-Tackmann method at NNLO. The jet veto acceptance uncertainty for $gg \to WW$ is 11% from Ref. [69]. This uncertainty is determined from the envelope of the Stewart-Tackmann method and a conservative estimate using three jet veto efficiencies. The total jet veto uncertainty for the WW signal is 3.4% after assuming full correlations between qq and gg induced processes.

3.8 Background Estimation

3.8.1 Overview

The following sections describe the data-driven or MC predicted background determinations. The top background estimate is determined using the jet veto survival probability method (Section 3.8.2). It uses two control regions to calculate the probability for top events to survive a jet veto. The other diboson background contributions ($WZ/ZZ/W\gamma^{(*)}$) are determined from MC predictions (Section 3.8.3). The $W+$jets and QCD background estimates are determined using a data driven matrix method (Section 3.8.5). This method relates the lepton identification requirements (*loose* or *tight*) to the nature of the lepton (*real* or *fake*) using lepton efficiencies and fake rates measured in data control samples. The $Z+$jets background estimate is determined using a simultaneous fit that extracts the normalizations for signal and Drell-Yan simultaneously in signal and control regions using differential distributions (Section 3.8.6).

3.8.2 Top - Jet Veto Survival Probability Method

The top quark background contribution is estimated using the data-driven jet veto survival probability (JVSP) method, which follows closely the method used in the $H \to WW$ analysis [70]. This method uses two control regions, which are described below, to calculate the probability for top events to survive the jet veto. This method uses the observed number of events without a jet veto requirement and applies the expected jet veto survival probability for data.

Probability in full jet events The first control region has all the nominal analysis selection requirements except for the jet veto requirement. To reduce the signal contamination, there is also a $H_T > 130$ GeV requirement, where H_T is the scalar sum of the lepton p_{T}'s and jet p_{T}'s. The efficiency for this H_T requirement is 95% for top events and 29% for WW signal events, determined from MC events. The full jet veto survival probability is measured in MC events, where $P_{\mathrm{full}}^{\mathrm{MC}}$ is defined as

$$P_{\mathrm{full}}^{\mathrm{MC}} = \frac{N_{\mathrm{Top}}^{\mathrm{MC}}(0-\mathrm{jets})}{N_{\mathrm{Top}}^{\mathrm{MC}}(\mathrm{all})} \tag{62}$$

where the numerator is the total MC prediction normalized to 20.3 fb^{-1} in the first control region with exactly no jets. The denominator is similarly defined but without any requirements on the number of jets. The jet selection requirements are identical to those in the nominal analysis selection (mainly $p_{\mathrm{T}} > 25$ GeV).

Probability in events with b-tagged jets The second control region is a subset of the first control region. In this control region, events are only used if there is at least one jet that is b-tagged at the 85% efficiency operating point. B-tagging is discussed in Section 2.3.4. The jet with the highest probability of originating from a b-quark is referred to as a the tagged jet. All other jets (if any) are referred to as probe jets. With these definitions, each event will contain exactly one tagged jet and 0 or more probe jets. The survival probability for probe jets is defined as

$$P_{\mathrm{btag}} = \frac{N_{\mathrm{btag}}(0-\mathrm{probe\ jets})}{N_{\mathrm{btag}}(\mathrm{all})} \tag{63}$$

$P_{\mathrm{btag}}^{\mathrm{MC}}$ is determined from MC predicted events in the second control region and $P_{\mathrm{btag}}^{\mathrm{data}}$ is determined from observed events in the second control region.

Probability in data The full jet veto survival probability for top events is the square of the jet survival probability in events with a b-tagged jet.

$$P_{\mathrm{full}}^{\mathrm{Data}} = \left(P_{\mathrm{btag}}^{\mathrm{Data}}\right)^2 \times \frac{P_{\mathrm{full}}^{\mathrm{MC}}}{\left(P_{\mathrm{btag}}^{\mathrm{MC}}\right)^2} \tag{64}$$

where the full probability is taken in the first control region and the probability in b-tagged events is taken in the second control region.

The number of top events in the 0-jet signal region is

$$\begin{aligned} N_{\mathrm{Top}}^{\mathrm{Data}}(0-\mathrm{jet}) =& \frac{N_{\mathrm{Top}}^{\mathrm{Data}}(\mathrm{all})}{\epsilon_{H_T}} \times P_{\mathrm{full}}^{\mathrm{Data}} \\ =& \frac{(N^{\mathrm{Data}}(\mathrm{all}) - N_{\mathrm{Non-Top}}^{\mathrm{MC}}(\mathrm{all}))}{\epsilon_{H_T}} \times (P_{\mathrm{btag}}^{\mathrm{Data}})^2 \frac{P_{\mathrm{full}}^{\mathrm{MC}}}{(P_{\mathrm{btag}}^{\mathrm{MC}})^2} \end{aligned} \tag{65}$$

N^{Data}(all) and $N^{\mathrm{MC}}_{\mathrm{Non-Top}}$(all) are determined in the first control region. ϵ_{H_T} is the efficiency for top events to pass the H_T requirement, which is determined from MC. The non-top contribution (as predicted from MC) is subtracted from the total data yield to give $N^{\mathrm{Data}}_{\mathrm{Top}}$. Table 13 gives the data yields and MC yields used for the non-top subtraction after the H_T requirement.

Final State	ee Channel	$\mu\mu$ Channel	$e\mu$ Channel	combined
Observed Events	1966	3444	22134	27544
Top	1897.7 ± 18.1	3016.8 ± 23.4	20073.5 ± 59.6	24987.4 ± 66.5
WW	187.7 ± 3.2	341.8 ± 4.2	1847.2 ± 9.7	2376.1 ± 11.1
W+jets	2.67 ± 2.67	4.72 ± 4.72	118.0 ± 23.3	125.4 ± 23.9
Z+jets	10.1 ± 1.5	31.5 ± 8.4	73.8 ± 18.5	115.4 ± 20.4
Other diboson	18.6 ± 1.2	19.4 ± 0.9	99.7 ± 3.1	137.8 ± 3.4
Total non-top background	219.1 ± 4.6	397.6 ± 10.6	2138.76 ± 31.5	2755.5 ± 33.6

Table 13: Summary of observed data events and MC expected top and non-top background contributions in the first control region (full selection except for jet veto requirement and with $H_T > 130$ GeV) in the three channels and their combined results. The uncertainties of the non-top processes include statistical uncertainties only.

Systematic errors Theoretical and experimental uncertainties on the MC can enter through the ratio $\frac{P^{\mathrm{MC}}_{\mathrm{full}}}{(P^{\mathrm{MC}}_{\mathrm{btag}})^2}$ or through the MC subtraction term, $N^{\mathrm{MC}}_{\mathrm{Non-Top}}$. Sources for systematic uncertainties are described below

- Jet Uncertainties - The relative uncertainty on the ratio due to jet energy scale and resolution uncertainties are 4.0% and 1.8% respectively. These uncertainties are low due to the partial cancellation in the ratio. The uncertainty on the ratio due to b-tagging related systematic sources is 3.5%.

- Efficiency of H_T requirement - Experimental uncertainties are propagated to the efficiency for events to pass the H_T requirement. This is a 0.87% effect. Also, an additional 1% is assigned to account for the differences in efficiency between data and MC.

- MC Subtraction - A systematic uncertainty is assigned for the subtraction of the non-top contribution. Uncertainties of 50% on Z+jets and W+jets, 15% on other dibosons, and 15% for WW are assigned. These are conservative estimates. These uncertainties correspond to a relative uncertainty of 2.1% on the subtraction term.

- Single-top cross section - The single-top cross section is varied by 30%, which corresponds to a 1% uncertainty on the ratio.

- MC Generator, Parton shower - To account for differences due to the choice of generator or parton shower, comparisons were made where the one is fixed to be the same and the other is varied. Generator comparisons between the nominal MC@NLO MC samples interfaced with Jimmy and alternative Powheg MC samples also interfaced

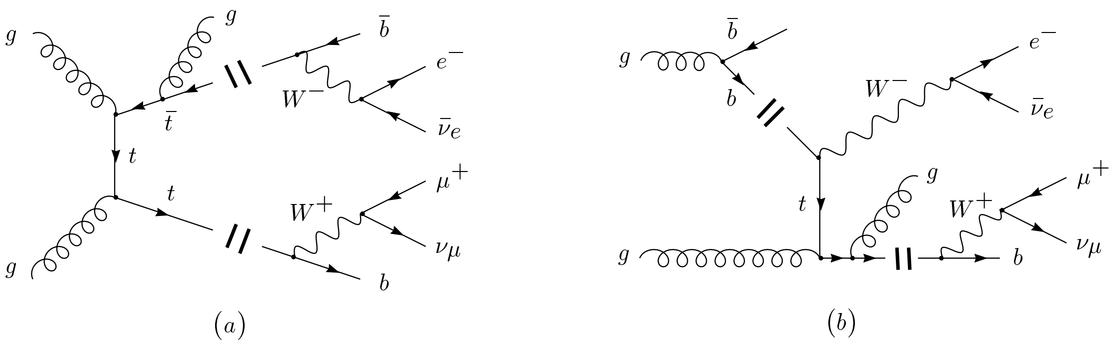

Figure 26: Feynman diagrams for $t\bar{t}$ and Wt production with the same final states, leading to interference effects [71]

with Jimmy give a systematic uncertainty of 5.1%. A comparison of parton shower and hadronization differences between Powheg+Jimmy and Powheg+Pythia gives a systematic uncertainty of 3.7% on the ratio.

- Factorization and renormalization scale - The factorization and renormalization scales are varied by a factor of 1/2 and 2. The largest variation of 1.9% is taken to be the systematic uncertainty for this source.
- Single-top and $t\bar{t}$ interference - The NLO Wt process and LO $t\bar{t}$ process share the same final states, which leads to interference between these two processes [71]. The relevant Feynman diagrams are shown in Figure 26. A systematic certainty is assigned by comparing two different overlap removal schemes: diagram removal (the diagrams in the NLO Wt amplitudes that are doubly resonant are removed) and diagram subtraction (the NLO Wt cross section is modified by implementing a subtraction term designed to cancel locally the $t\bar{t}$ cross section.). This systematic uncertainty is 1.1%.
- PDF - The systematic uncertainty due to the CT10 PDF is 1.7%.

Results The jet veto probabilities are given in Table 14 and the data-driven top estimate using the JVSP method is given in Table 15.

Channel	$P_{\rm btag}^{\rm MC}$	$P_{\rm btag}^{\rm Data}$	$P_{\rm full}^{\rm MC}$	$P_{\rm full}^{\rm MC}/(P_{\rm btag}^{\rm MC})^2$
ee	0.229 ± 0.004	0.231 ± 0.010	0.040 ± 0.002	0.762 ± 0.025
$\mu\mu$	0.186 ± 0.004	0.185 ± 0.009	0.036 ± 0.002	0.937 ± 0.021
$e\mu$	0.221 ± 0.001	0.217 ± 0.003	0.029 ± 0.001	0.593 ± 0.012

Table 14: Jet veto survival probabilities in the control regions in MC and data. $P_{\rm full}$ is measured in the first control region, which includes all selection requirements except for the jet veto and with $H_T > 130$ GeV. $P_{\rm btag}$ is measured in a subset of the first control region, but also requiring events with at least one b-tagged jet. The last column is the MC ratio used in the estimate, with potential cancellation of uncertainties. Only statistical uncertainties are shown.

Channel	Top JVSP Estimate	Top MC Prediction
ee	$91.8 \pm 7.3 \pm 7.9$	96.9 ± 4.8
$\mu\mu$	$127.2 \pm 9.4 \pm 10.9$	131.4 ± 6.1
$e\mu$	$608.6 \pm 17.5 \pm 52.3$	625.9 ± 12.5

Table 15: Summary of results for the top estimation using the jet veto survival probability (JVSP) method and as predicted by MC. The first error is statistical and the second systematic for the data-driven method. Only statistical errors are shown for the MC predictions.

3.8.3 Other Dibosons - MC

A non-negligible background to WW production comes from other diboson production, which includes WZ, ZZ, and $W\gamma^{(*)}$. The diboson contribution is estimated from MC.

The $ZZ \to \ell\ell\ell\ell$ and $WZ \to \ell\nu\ell\ell$ background processes can pass the selection when only two of the leptons are reconstructed. If one of the Z bosons in ZZ events decays into neutrinos ($ZZ \to \ell\ell\nu\nu$) there are exactly two leptons, but this contribution is suppressed by the Z mass veto. The ZZ decay states with four charged leptons and two charged leptons are both included in this analysis. The WZ and ZZ processes are modeled by Powheg interfaced with Pythia. The theoretical uncertainty for WZ (ZZ) production is 8% (13%) which includes a 5% (4%) uncertainty on the NLO cross-section prediction from MCFM [35], a 5% (12%) uncertainty due to higher order corrections [72, 73], and a jet veto uncertainty of 3% (assumed to be the same as for the WW signal).

The $W\gamma$ process can enter into the signal selection when the photon is misidentified as an electron. This process is modeled by Alpgen+Jimmy. A theoretical uncertainty of 11% is assigned on the normalization of $W\gamma^*$ using MCFM to calculate a NLO k-factor in the zero jet bin [74]. The 7 TeVmeasurement of the $W\gamma$ cross-section yields a 30% excess [75]. To be conservative, this is included as a systematic uncertainty, resulting in a total systematic uncertainty of 32%.

By convention, the distinction between WZ and $W\gamma^*$ is the Z/γ mass. In general, it is difficult for generators to produce events with a very low $m_{Z/\gamma}$[12]. A dedicated Sherpa sample was produced with $m_{Z/\gamma}$ down to 1 MeV. The $W\gamma^*$ samples have a high mass cut of $m_{Z/\gamma} < 7$ GeV and the WZ samples have a low mass cut of $m_{Z/\gamma} > 7$ GeV to prevent overlap between the two samples. The $W\gamma^*$ process is modeled by Sherpa with up to one additional parton in the matrix element calculation, which is important in boosting the $W\gamma^*$ system to produce leptons with high p_{T}. A k-factor with scale uncertainties of 0.979 ± 0.076 is calculated with MCFM. Jet-binned corrections (Table 16) are derived using Sherpa with up to two additional partons with leading/sub-leading lepton p_{T}cuts of 25/20 GeV. The combined theoretical uncertainty on the $W\gamma^*$ normalization is 18%.

The diboson background contributions in each channel are listed in Table 17. The systematic uncertainties are listed in Table 18.

A same-sign region documented in Section 3.8.5 is used to validate the diboson and $W + \text{jets}$ estimates.

N_{jets}	C_i	k-factor $\times C_i$
0	1.01 ± 0.16	0.989 ± 0.18
≥ 1	0.99 ± 0.14	0.969 ± 0.16

Table 16: Jet-binned corrections, C_i, for $W\gamma^*$ process. The k-factor is 0.979 ± 0.76. The uncertainties included here are scale uncertainties.

---

[12] At some point, MadGraph was the only generator capable of doing this, but it was later discovered that very low mass events were generated with TeVscale p_{T}! These events were clearly un-physical and had to be removed. Low mass events had to be given extra weight in order to make up for the loss and to keep a similar total cross section.

Channel	ee	$\mu\mu$	$e\mu$	Combined
WZ	7.72 ± 0.68	19.35 ± 1.00	62.86 ± 1.75	89.92 ± 2.12
ZZ	10.61 ± 0.43	16.06 ± 0.54	2.76 ± 0.14	29.43 ± 0.70
Wγ	3.67 ± 0.81	0.00 ± 0.00	41.08 ± 2.72	44.75 ± 2.84
Wγ^*	5.35 ± 0.83	2.96 ± 0.60	42.98 ± 2.31	51.28 ± 2.5 3
Total Background	27.34 ± 1.41	38.36 ± 1.28	149.68 ± 3.98	215.39 ± 4.41

Table 17: Other diboson background yields and their statistical uncertainties as determined from MC for 20.3 fb^{-1}.

Sources	ee	$\mu\mu$	$e\mu$	Combined
Luminosity	2.8%	2.8%	2.8%	2.8%
Pileup	1.57%	0.28%	0.92%	0.88%
Trigger Efficiency SF (muons)	0%	2.84%	0.44%	0.79%
Trigger Efficiency SF (electrons)	2.75%	0%	0.44%	0.67%
Muon MS Resolution	0.55%	3.12%	2.14%	2.09%
Muon ID Resolution	0.93%	2.29%	0.38%	0.53%
Muon Scale	0%	0.65%	0.06%	0.16%
Muon Efficiency SF	0%	0.80%	0.38%	0.40%
Muon Isolation SF	0%	1.12%	0.59%	0.60%
Electron Resolution	0.88%	0%	0.11%	0.07%
Electron Scale	0.55%	0%	1.10%	0.82%
Electron Efficiency SF	2.30%	0%	1.33%	1.24%
Electron Isolation SF	0.46%	0%	0.27%	0.25%
Jet Vertex Fraction	0.40%	0.41%	0.23%	0.29%
Jet Energy Resolution	0.58%	2.32%	0.31%	0.26%
Jet Energy Scale	5.59%	5.25%	6.74%	6.33%
Missing $E_{\mathrm{T,\ Rel}}^{\mathrm{miss}}$ Reso Soft Terms	1.10%	0.42%	0.48%	0.39%
Missing $E_{\mathrm{T,\ Rel}}^{\mathrm{miss}}$ Scale Soft Terms	1.98%	2.19%	1.00%	1.33%
Missing p_{T}Reso Soft Terms	0.51%	0.79%	0.45%	0.41%
Missing p_{T}Scale Soft Terms	0.34%	1.10%	0.08%	0.18%
Theory	16%	11%	18%	16%
Total	17.86%	13.94%	19.71%	17.76%

Table 18: Systematic uncertainties for the combined "other diboson" background processes (WZ, ZZ, $W\gamma$ and $W\gamma^*$). The total systematic uncertainty includes theoretical uncertainties for various diboson processes.

3.8.4 W+jets and QCD: Matrix Method

3.8.5 Wjets Estimation using Matrix Method

The background contributions from the $W+\text{jets}$ and QCD processes involving the misidentifcation of jets as isolated leptons is estimated using data control samples.

The matrix method relates the identification quality of the lepton (*loose* or *tight*) to the physical nature of the lepton (*real* or *fake*) using efficiencies and fake rates measured in data control samples. For the $W+\text{jets}$ process, the lepton originating from the W is considered a *real* lepton, while a misidentified jet that is reconstructed as a lepton is considered a *fake* lepton. For the QCD process, there are two *fake* leptons.

The *tight* definition is identical to the stringent lepton selection requirements used in the analysis. The *loose* definition is ideally the largest possible superset of the *tight* definition. The set of events with exactly two leptons, each passing at least the *loose* criteria is

$$N_{total} = N_{LL} + N_{TT} + N_{LT} + N_{LL} \tag{66}$$

where the first index gives the identification quality of the leading lepton and the second index is for the sub-leading lepton. Here, the index "L" means that the lepton passes the *loose* requirements but not the *tight* requirements and "T" means that the lepton passes the *tight* requirements. A system of linear equations relates the identification quality of the leptons to the quality of the leptons using the efficiencies and fake rates.

$$\begin{pmatrix} N_{TT} \\ N_{TL} \\ N_{LT} \\ N_{LL} \end{pmatrix} = \begin{pmatrix} r_1 r_2 & r_1 f_2 & f_1 r_2 & f_1 f_2 \\ r_1(1-r_2) & r_1(1-f_2) & f_1(1-r_2) & f_1(1-f_2) \\ (1-r_1)r_2 & (1-r_1)f_2 & (1-f_1)r_2 & (1-f_1)f_2 \\ (1-r_1)(1-r_2) & (1-r_1)(1-f_2) & (1-f_1)(1-r_2) & (1-f_1)(1-f_2) \end{pmatrix} \begin{pmatrix} N_{RR} \\ N_{RF} \\ N_{FR} \\ N_{FF} \end{pmatrix} \tag{67}$$

where r_1 and r_2 are the efficiencies for a real leading lepton or sub-leading lepton to pass the *tight* identification and f_1 and f_2 are the probabilities for a fake leading lepton or sub-leading lepton to pass the *tight* identification criteria.

The matrix can be inverted to calculate the number of events with *real* or *fake* leptons. The estimated $W+\text{jets}$ and QCD contribution is

$$N_{W+jets} = N_{RF} \cdot r_1 f_2 + N_{FR} \cdot f_1 r_2 \tag{68}$$

$$N_{QCD} = N_{FF} \cdot f_1 f_2 \tag{69}$$

Loose Lepton Definition The *loose* lepton definition is the same as the full analysis selection but without explicit isolation or impact parameter requirements. For electrons, instead of requiring *very tight* likelihood identification, only the *medium* likelihood identification is needed.

Trigger Bias Although the isolation requirement has been removed in the *loose* lepton definition, it may be required as part of the trigger. The single lepton triggers with the lower thresholds have an isolation requirement (as indicated by the "i" in the trigger name). Also, the electron identification used for the trigger does not match exactly the likelihood identification used here. To account for these two effects, the fake rates and efficiencies are measured for each of the triggers used. In the ee and $\mu\mu$ channel, where there is only one dilepton trigger used, there is no ambiguity and only one set of fake rates and efficiencies are calculated. In the $e\mu$ channel, the majority ($> 80\%$) of the events are triggered by the dilepton trigger, so the efficiencies with this trigger is used by default. For $e\mu$ events that are not triggered by the dilepton trigger, the single-lepton triggers are used. In the very rare case where one of the leptons is not triggered by any of the single-lepton triggers, the following prescaled supporting triggers are used. For an untriggered electron, the logical `OR` of `EF_g20_etcut` and `EF_g24_etcut` triggers are used. For an untriggered muon, the `EF_mu15` trigger is used.

Determination of Efficiencies Real lepton efficiencies are measured using the full set of MC samples used in the analysis. Scale factor corrections are applied to match the efficiencies in data. These efficiency corrections are described in Section 3.5.3. The uncertainties on the efficiency scale factors are propagated to the systematic uncertainties on the real lepton efficiencies. The efficiency measurement is a weighted average of the efficiencies in signal and background. They are weighted according to the relative contributions in the nominal analysis. The efficiencies are measured in bins of $p_{\mathrm{T}}$and η for each of the triggers.

Determination of Fake Rates Fake rates are measured using di-jet data, in which one of the jets is reconstructed as a lepton passing with at least the *loose* selection and a jet is found opposite of the fake lepton candidate. There are no longer two jets in the event due to the overlap removal of the jet that is faking a lepton. The event selection criteria for the measurement of the fake rates are:

- Exactly one lepton passing at least the *loose* selection
- Exactly one jet in the event
- $|\Delta\phi(\mathrm{jet}, \mathrm{fake\ lepton})| > 2$
- Z boson veto: Reject if there is more than one *loose* lepton
- W boson veto: Reject if either $E_{\mathrm{T}}^{\mathrm{miss}} > 25$ GeV or $M_T > 40$ GeV

The last two requirements are added to remove contributions from real leptons from $W \to \ell\nu$ and $Z \to \ell\ell$ decays. A systematic uncertainty is assigned to account for the M_T and $E_{\mathrm{T}}^{\mathrm{miss}}$cuts that are not applied in the nominal analysis. This uncertainty is determined by calculating the difference between the fake rates with and without these cuts. Events that pass this selection still have a large contribution from real leptons from W or Z decays. These are removed using MC predictions. Finally, fake rates are measured in bins of pt and two bins in η (barrel and end-cap) for each trigger.

Additional Systematic Uncertainties To account for the different pileup conditions between the di-jet data with pre-scaled triggers and that for the nominal analysis, a systematic variation is determined by only considering events with $\mu > 20$ or $\mu < 20$.

The largest systematic uncertainty comes from the different composition of jets in di-jet data and in $W + \text{jets}$. This is quantified by comparing the fake rates measured using di-jet data and in $W + \text{jets}$ MC events with one *loose* lepton and no jets after overlap removal. A flat uncertainty of 40-55% is assigned for electron fake-rates and 18-26% for muon fake-rates, which varies by trigger.

W+γ Removal The matrix method is used to estimate the contributions from events with one real lepton and one fake lepton, where the fake lepton is a misidentified jet. $W + \gamma$ events can also produce a real lepton with a fake lepton, but here a photon is misidentified as an electron. Since the MC is expected to model this type of misidentification very well, the contribution from $W + \gamma$ in the matrix method must be removed. The matrix method is applied to $W + \gamma$ MC and its contribution is subtracted.

Closure Test A cross-check on the matrix method is done to check the results with the MC prediction of $W + \text{jets}$. The matrix method is applied to $W + \text{jets}$ MC, where the fake rates and efficiencies are taken from MC without scale factors applied. The estimate from the closure test can be compared to the MC predictions in Table 19.

Channel	Closure	$W + \text{jets}$ MC
ee	13.59 ± 2.46	21.75 ± 9.69
$e\mu$	111.07 ± 7.13	127.61 ± 17.39
$\mu\mu$	13.04 ± 3.17	13.67 ± 4.32
μe	106.34 ± 7.96	94.24 ± 16.73

Table 19: Closure test on matrix method. The matrix method is applied on $W + \text{jets}$ MC by measuring fake rates and efficiencies in $W + \text{jets}$ MC and comparing results (in the second column) with the MC prediction (in the third column). Only statistical errors are shown.

Results Table 20 gives the data-driven estimates for the $W + \text{jets}$ and QCD background using the matrix method in each channel.

Channel	$W + \text{jets}$ and QCD Estimate using Matrix Method							MC Prediction
	± (stat	$+\sigma_r$	$-\sigma_r$	$+\sigma_f$	$-\sigma_f$	$+\sigma_{f_{samp}}$	$-\sigma_{f_{samp}}$)	± (stat)
ee	13.9 ± 4.9	3.2	-3.3	3.4	-2.9	17.7	-7.1	21.6 ± 9.7
$e\mu$	150.1 ± 11.8	17.9	-18.5	2.9	-27.9	73.7	-69.7	127.6 ± 17.4
$\mu\mu$	6.1 ± 5.0	9.9	-10.3	-6.5	1.4	-3.4	-1.8	13.6 ± 4.3
μe	98.7 ± 9.7	19.4	-20.1	6.2	-12.5	68.9	-52.1	97.7 ± 17.0

Table 20: Results for the $W + \text{jets}$ and QCD data-driven estimate using the matrix method. The central estimates are given in the first column with the statistical errors. The middle columns given the systematic uncertainties due to the efficiencies (r), fake rates (f), and sample dependence on the fake rates (f_{samp}). The last column gives the MC predictions for $W + \text{jets}$ with statistical uncertainties.

Same sign region The $W+$jets and diboson estimates are cross checked using a same-sign region for validation. The same-sign region has all the standard analysis requirements except requiring that the two leptons have the same sign instead of opposite sign. In the ee channel, Drell-Yan has a large contribution due to charge flips in electrons, but the MC modeling overestimates the charge flip rate. To reduce this contribution from large charge mis-identification, electrons are required to have $\eta < 2.01$ in the same-sign region. The $E_{\mathrm{T}}^{\mathrm{miss}}$and m_{ll} distributions in the $e\mu$ channel in the same sign region are shown in Figure 27. The total number of observed events in the same sign region is 208 ± 14 compared to the prediction of 229 ± 17.

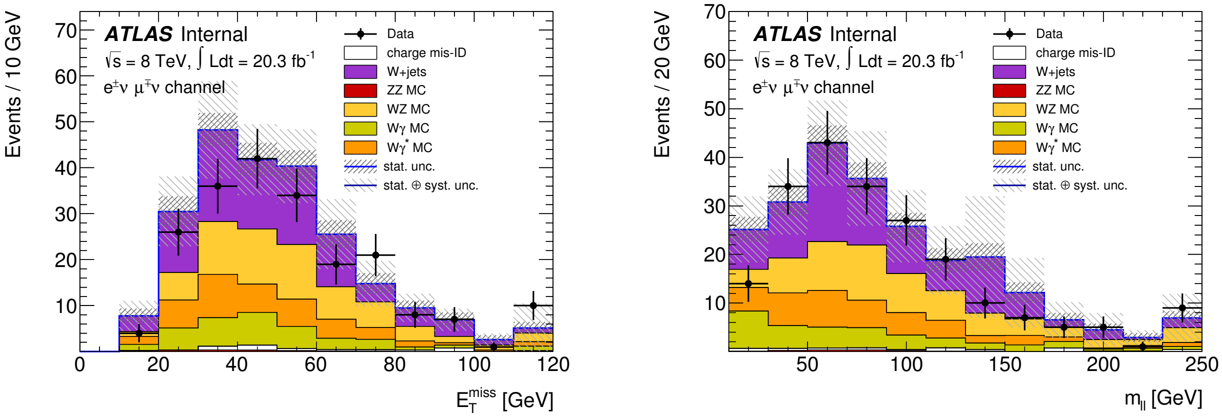

Figure 27: $E_{\mathrm{T}}^{\mathrm{miss}}$and m_{ll} distribution for the same-sign validation sample in the $e\mu$ channel. The last bin is an overflow bin. The selected leptons are required to have the same charge. All other analysis selection criteria are applied. The uncertainties shown include statistical and systematic uncertainties on the $W+$jets estimate as well as statistical uncertainties on all MC predictions. For the diboson samples, the theoretical uncertainty on the cross section predictions are also included. The experimental systematic uncertainties for the diboson are not included.

Same-sign events in $e\mu$ channel	
WZ	64.8 ± 1.8
$W\gamma$	39.2 ± 2.1
$W\gamma^*$	25.6 ± 2.2
ZZ	1.7 ± 0.1
$W+$jets (data-driven)	$89.9 \pm 7.8 \pm 14.3$
WW, top, $Z+$jets	7.7 ± 3.1
Total predicted	229 ± 17
Observed	208 ± 14

Table 21: Event yields in the $e\mu$ channel same-sign region. All analysis cuts are applied except that the two leptons are required to have the same charge instead of opposite charge, and electrons are required to have $|\eta| < 2.01$ due to large charge mis-identification in the endcaps. The $W+$jets estimate is from the Matrix method updated with same sign $W+$jets fake rates used in the sample dependence. Only statistical uncertainties are shown for the MC predictions, whereas the $W+$jets estimate includes both statistical and systematic uncertainties, respectively.

3.8.6 Z+jets - Simultaneous fit

The $Z+\text{jets}$ background is estimated using the simultaneous fit method. The simultaneous fit method, which can extract normalizations for signal, top, and $Z+$jets simultaneously, will be explained. Due to the lower systematic uncertainties from the jet veto survival probability (JVSP) method for the top quark background estimation, the simultaneous fit will only be used to extract normalizations for signal and $Z+\text{jets}$.

Likelihood function The simultaneous fit method uses a likelihood function, similar to the one that is used in the cross-section combination in Equation 76. The likelihood is a product of the Poisson probability density functions for the signal and background in each bin in both the signal region and control regions. The likelihood function is fitted to data, with normalizations as free parameters and systematic uncertainties included as nuisance parameters. For the $Z+\text{jets}$ estimate, the free parameters are the signal and $Z+\text{jets}$ normalizations.

Signal and control regions The signal region is defined by applying all the standard analysis requirements and is dominated by WW signal. The signal and control regions are defined to be orthogonal to one another, so that events are not counted more than once in the fit. The top control region applies the same analysis selection requirements except requiring exactly two jets, instead of the jet veto. The $Z+\text{jets}$ control region has the same analysis selection requirements up to the $p_{\mathrm{T}}^{\mathrm{miss}}$ requirement, which is inverted ($5\ \text{GeV} < p_{\mathrm{T}}^{\mathrm{miss}} < 45/20\ \text{GeV}$ for the same-flavor and different-flavor channels), and the $\Delta\phi(E_{\mathrm{T}}^{\mathrm{miss}}, p_{\mathrm{T}}^{\mathrm{miss}})$ requirement is not applied. The signal, top, and $Z+$jets regions in the ee, $\mu\mu$, and $e\mu$ channel are shown in Figure 28. All three regions can be used to determine the normalizations for the signal, top quark background and $Z+\text{jets}$ background.

Inputs to Simultaneous Fit The signal and background shapes can be taken from MC estimates or fixed to data-driven estimates where applicable. The $W+\text{jets}$ shape is taken from the data-driven matrix method, since the $W+$jets MC does not have sufficient statistics for the simultaneous fit. The diboson, $Z+\text{jets}$, and signal shapes and normalizations are taken from MC predictions. In the determination of the $Z+\text{jets}$ background estimate using the simultaneous fit method, the top background shape and normalization is fixed to the jet veto survival probability background estimate (Section 3.8.2).

Systematic uncertainties Both flat (uniform) and shape (binned) systematic uncertainties are considered as nuisance parameters in the fit. The nuisance parameters have nominal values of zero but are allowed to vary within Gaussian constraints. Experimental systematic uncertainties, as described in Section 3.7, are included as shape variations on the signal and $Z+$jets MC input. In the case that a systematic source has an up and a down variation (such as jet energy scale), the shape is taken from the direction that gives the largest integrated difference with respect to the nominal.

The binned systematic uncertainties on the efficiencies and fake rates in the $W+\text{jets}$ matrix method are included. A flat systematic on the normalization for the top background

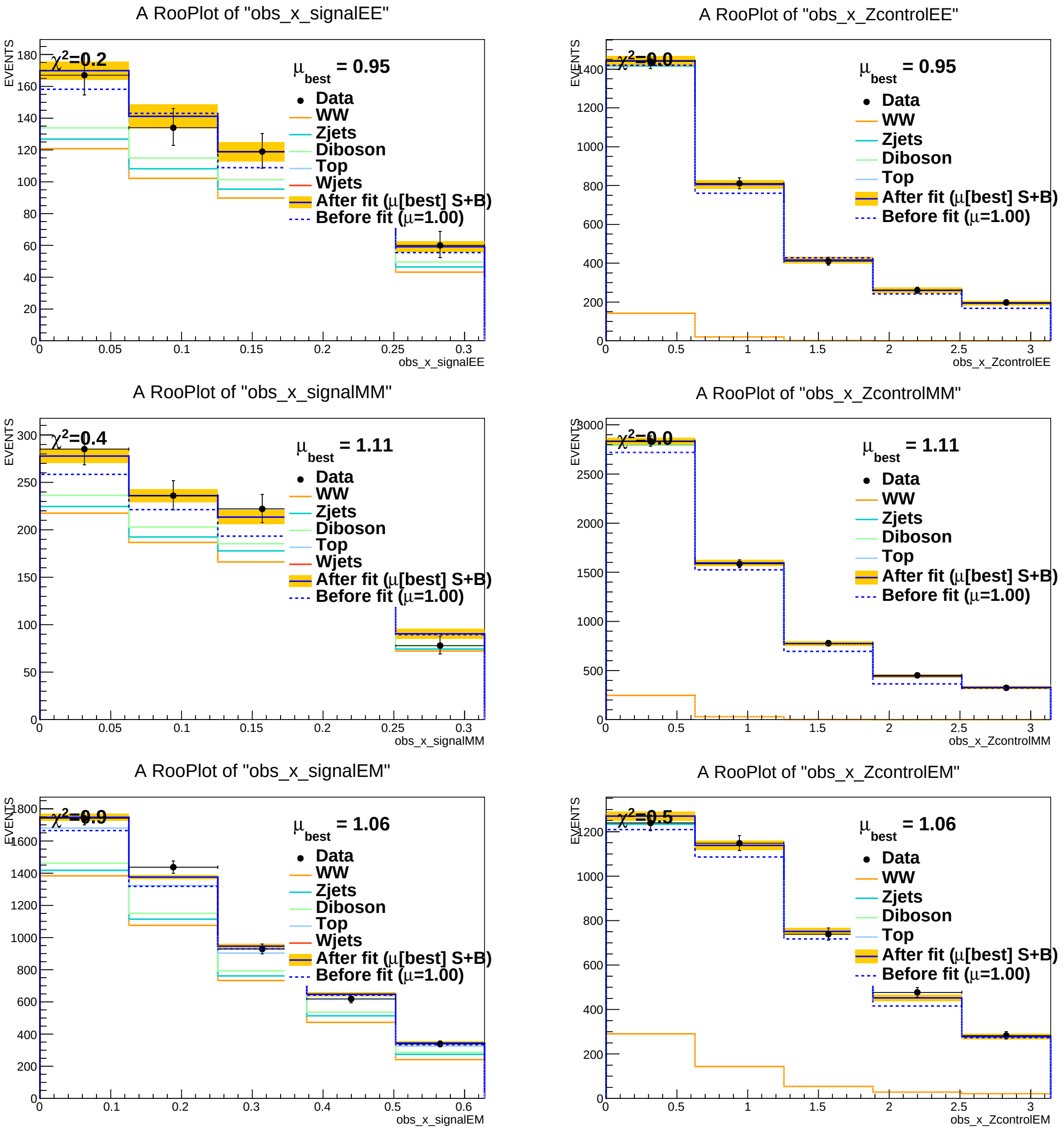

Figure 28: $\Delta\phi(E_{\mathrm{T}}^{\mathrm{miss}}, p_{\mathrm{T}}^{\mathrm{miss}})$ distributions in the signal region (left) and Drell-Yan control region (right) for the ee, the $\mu\mu$ and the $e\mu$ channels from top to bottomwith inputs in the simultaneous fit. The Drell-Yan estimate before and after the fit are also shown.

using the JVSP method is also included as a nuisance parameter. Additional theoretical uncertainties are also included.

- Parton shower - A systematic uncertainty on the parton shower modeling is done by comparing fit results using Alpgen+Jimmy samples and Alpgen+Pythia samples. This results in a difference of 8.5%.
- PDF - The PDF uncertainty of 1% is assigned by taking the difference between results with the CT10 PDF and CTEQ6 PDF.
- Scale - Samples were generated with factorization and renormalization scales that scaled by a factor of 1/2 or 2. The largest difference in the DY estimation using these scale varied samples is 3.5%.

Results The MC and data-driven estimate of Drell-Yan events is given in Table 22 using the simultaneous fit method. Normalization factors returned from the fit are also given.

	ee	$\mu\mu$	$e\mu$
DD estimation	28.0 ± 13.0	32.9 ± 17.4	174.5 ± 18.1
MC prediction	26.0 ± 13.9	41.8 ± 17.1	173.0 ± 16.7
Normalization factor	$0.95^{+0.18}_{-0.14}$	$1.11^{+0.23}_{-0.17}$	$1.06^{+0.09}_{-0.08}$

Table 22: The MC prediction for the DY estimation with its statistical uncertainty and the result of the fit with its combined statistical and systematic uncertainty is shown along with the normalization factor returned by the fit. The estimation does not scale exactly according to the normalization factor because there are nuisance parameters fixed to non-zero values.

3.9 Cross Section Results

The total WW production cross-section can be calculated according to the following equation:

$$\sigma_{WW}^{total} = \frac{N_{obs} - N_{bkg}}{\epsilon \mathcal{A} \mathcal{L} \ Br} \tag{70}$$

where $\epsilon\mathcal{A}$ is the efficiency times acceptance (treated as a single number), $\mathcal{L}$ is the integrated luminosity, and Br is the branching ratio for $WW \to \ell\nu\ell\nu$ (where $\ell = e, \mu$) decays.

The number of events is measured within the geometrical (detector coverage) and kinematic (p_{T}thresholds of leptons, triggers, etc) constraints imposed by the selection. In order to calculate the total cross section, the acceptance and efficiency factors are extrapolated from the limited phase space where the measurement was carried to the full phase space. This extrapolation includes theoretical uncertainties, which are minimized by measuring the fiducial cross section. The total cross section is related to the fiducial cross section, as shown below.

$$\sigma_{WW}^{total} = \frac{\sigma_{WW}^{fiducial}}{A_{WW} \ Br} \tag{71}$$

where A_{WW} is the fiducial acceptance factor. Here, the fiducial cross section is only extrapolated to the phase space within geometrical and kinematic requirements used in the measurement. The fiducial cross section is obtained by

$$\sigma_{WW}^{fiducial} = \frac{N_{obs} - N_{bkg}}{C_{WW} \, \mathcal{L}} \tag{72}$$

where C_{WW} is a correction factor that takes into account detector resolution effects, geometrical acceptance, and efficiencies in the fiducial region. C_{WW} is the ratio of the reconstruction-level event yield in the fiducial region divided by the generator-level event yield in the fiducial region.

3.9.1 Definition of Fiducial Region

The correction factor, C_{WW}, uses the MC predicted event yields in a fiducial phase region. The fiducial region is described in this section.

The leptons are truth electrons or muons that come from a W boson parent in the hard scatter. The leptons are dressed, meaning that all photons within $\Delta R < 0.1$ are added to the lepton's four momentum. The fiducial cuts are as close to the analysis-level cuts as possible. The leading and sub-leading p_{T}requirement for leptons is unchanged, requiring $p_{\mathrm{T}} > 25/20$ GeV. Also, the η requirements for electrons ($|\eta| < 2.47$ excluding transition region) and muons ($|\eta| < 2.4$) are also unchanged.

The $M_{ll} > 15/10$ GeV and Z mass veto cuts ($|M_{ll} - M_Z| < 15$ GeV for ee and $e\mu$ channels) are also applied in the fiducial cuts. $E_{\mathrm{T}}^{\mathrm{miss}}$and $p_{\mathrm{T}}^{\mathrm{miss}}$ are analogously defined as the sum of the four momenta of the two neutrinos from the W boson decays, $p^{\mu}(\nu + \bar{\nu})$. The projection $E_{\mathrm{T,\ Rel}}^{\mathrm{miss}}$, or $p_{\mathrm{T,Rel}}^{\nu\bar{\nu}}$, is calculated in the same way as in the analysis using nearby leptons. $p_{\mathrm{T}}^{\nu\bar{\nu}}$ is required to be greater than 45/20 GeV. $p_{\mathrm{T,Rel}}^{\nu\bar{\nu}}$ is required to be greater than 45/15 GeV. Since $E_{\mathrm{T}}^{\mathrm{miss}}$and $p_{\mathrm{T}}^{\mathrm{miss}}$ are identical in the fiducial definition, the $\Delta\phi(E_{\mathrm{T}}^{\mathrm{miss}}, p_{\mathrm{T}}^{\mathrm{miss}})$cut is not applied.

Truth jets are built using the same anti-k_T algorithm with R=0.4 with truth particle four momenta as inputs. These truth jets are built from all stable particles, which include electrons and muons, so truth jets are removed from consideration if they are within $\Delta R < 0.3$ of a truth lepton. For the jet veto, the event is rejected if there are any truth jets with $p_{\mathrm{T}} > 25$ GeV and $|\eta| < 4.5$.

Since the selection cuts are identical in the ee and $e\mu$ channels except for the η cuts for electrons and muons, the fiducial cross sections for these two channels are expected to be somewhat similar. The cuts in the $e\mu$ channel are looser than those used in the same-flavor channels, which will be reflected in a larger fiducial cross-section for this channel.

3.9.2 Contributions from τ decays

The WW decays involving τ leptons are treated as a background in the fiducial measurement. The A_{WW} and C_{WW} definitions are different with respect to the 7 TeV version of this analysis, where the τ lepton contributions were included.

$$C_{WW\rightarrow\ \ell\nu\ell'\nu} = \frac{N^{reco\ infiducial\ region}_{WW\rightarrow l\nu l'\nu}}{N^{gen\ infiducial\ region}_{WW\rightarrow\ \ell\nu\ell'\nu}} \text{ and } A_{WW\rightarrow\ \ell\nu\ell'\nu} = \frac{N^{gen\ infiducial\ region}_{WW\rightarrow\ell\nu\ell'\nu}}{N^{all\ gen}_{WW\rightarrow\ell\nu\ell'\nu}} \tag{73}$$

where l, l' indicate all leptons (e, μ and τ) and ℓ, ℓ' only prompt e and μ. This notation is used throughout the rest of this section. The A_{WW} and C_{WW} factors with their uncertainties are listed in Table 23, where $\epsilon\mathcal{A} = A_{WW} \times C_{WW}$, is also given. Details on the systematic sources and their uncertainties on C_{WW} and A_{WW} are given in Table 24.

Channel	A_{WW}	C_{WW}	$A_{WW} \times C_{WW} = \epsilon\mathcal{A}$
$e\nu e\nu$	$0.0855 \pm 0.0003 \pm 0.0038$	$0.2913 \pm 0.0023 \pm 0.0174$	$0.0249 \pm 0.0002 \pm 0.0019$
$\mu\nu\mu\nu$	$0.0930 \pm 0.0004 \pm 0.0041$	$0.4740 \pm 0.0025 \pm 0.0297$	$0.0441 \pm 0.0003 \pm 0.0034$
$e\nu\mu\nu$	$0.2274 \pm 0.0004 \pm 0.0098$	$0.5124 \pm 0.0011 \pm 0.0240$	$0.1165 \pm 0.0003 \pm 0.0075$
Combined	$0.1583 \pm 0.0002 \pm 0.0069$	$0.4769 \pm 0.0010 \pm 0.0231$	$0.0755 \pm 0.0002 \pm 0.0049$

Table 23: The WW overall acceptance $A_{WW} \times C_{WW}$, fiducial phase space acceptance A_{WW} and correction factor C_{WW} and their uncertainties. The first errors are statistical and the second errors represent systematic uncertainties.

The total and fiducial cross sections for WW to prompt electrons and muons are given by

$$\sigma^{tot}_{WW\rightarrow\ell\nu\ell'\nu} = \frac{N^{obs}_{l\nu l'\nu} - N^{bkg}_{l\nu l'\nu}}{\mathcal{L} \times Br\{WW \rightarrow \ell\nu\ell'\nu\} \times A_{WW\rightarrow\ell\nu\ell'\nu} \times C_{WW\rightarrow\ell\nu\ell'\nu}} \times \left(1 - \frac{N^{MC}_{\tau}}{N^{MC}_{WW\rightarrow l\nu l'\nu}}\right) \tag{74}$$

$$\sigma^{fid}_{WW\rightarrow\ell\nu\ell'\nu} = \frac{N^{obs}_{l\nu l'\nu} - N^{bkg}_{l\nu l'\nu}}{\mathcal{L} \times C_{WW\rightarrow\ell\nu\ell'\nu}} \times \left(1 - \frac{N^{MC}_{\tau}}{N^{MC}_{WW\rightarrow l\nu l'\nu}}\right) \tag{75}$$

where, $N^{obs}_{l\nu l'\nu}$ and $N^{bkg}_{l\nu l'\nu}$ denote the number of observed and expected background events respectively, possibly including non-prompt e and μ from τ leptonic decays. Since it is impossible to remove the τ contribution in data, an extra factor is used. N^{MC}_{τ} is the number

Sources	$e^{\pm}\mu^{\mp}$	$e^{+}e^{-}$	$\mu^{+}\mu^{-}$
A_{WW} **uncertainties**			
PDF	0.8%	0.9%	0.9%
Scale	0.2%	0.2%	0.2%
PS+GEN	2.5%	2.6%	2.7%
EWCorr	0.5%	0.4%	0.4%
Jet-Veto	3.4%	3.4%	3.4%
Total A_{WW} **uncertainties**	4.3%	4.4%	4.5%
C_{WW} **uncertainties**			
Pileup	1.3%	1.9%	2.0%
e trigger efficiency	0.3%	2.5%	–
μ trigger efficiency	0.3%	–	2.8%
Muon MS resolution	0.0%	–	0.1%
Muon ID resolution	0.5%	–	1.5%
Muon scale	0.1%	–	0.4%
Muon efficiency	0.4%	–	0.8%
Muon isolation/IP	0.6%	–	1.1%
Electron resolution	0.0%	0.2%	–
Electron energy scale	0.4%	1.4%	–
Electron efficiency	0.9%	2.0%	–
Electron isolation/IP	0.2%	0.4%	–
Jet vertex fraction	0.2%	0.2%	0.2%
Jet energy scale	2.6%	2.6%	2.6%
Jet energy resolution	2.3%	2.2%	2.9%
$E_{\mathrm{T}}^{\mathrm{miss}}$soft term resolution	0.3%	0.3%	0.5%
$E_{\mathrm{T}}^{\mathrm{miss}}$soft term scale	2.3%	4.2%	3.8%
$p_{\mathrm{T}}^{\mathrm{miss}}$ soft term resolution	0.1%	0.2%	0.1%
$p_{\mathrm{T}}^{\mathrm{miss}}$ soft term scale	0.2%	0.4%	0.3%
Residual Theory	0.7%	1.2%	1.0%
Total C_{WW} **uncertainties**	4.7%	6.0%	6.3%
$A_{WW} \times C_{WW}$ **uncertainties**			
PDF	0.9%	1.3%	1.0%
Scale	0.7%	0.7%	0.7%
PS+GEN	2.5%	3.0%	2.9%
EWCorr	0.5%	0.3%	0.4%
Jet-Veto	3.4%	3.4%	3.4%
Total $A_{WW} \times C_{WW}$ **uncertainties**	6.4%	7.6%	7.7%
Luminosity	2.8%	2.8%	2.8%
Full WW signal estimation uncertainty	8.8%	9.6%	9.8%

Table 24: Uncertainty sources and associated relative uncertainties for WWsignal acceptance estimations for $e\mu$, ee and $\mu\mu$.

of events simulated where at least one of the bosons decays in a τ and $N^{MC}_{WW\to l\nu l'\nu}$ is the number of MC signal events with fully leptonic final state (potentially including τ leptonic decays). This ratio effectively corrects for the contribution from τ decays. The MC signal predictions relevant to N^{MC}_{τ} and $N^{MC}_{WW\to l\nu l'\nu}$ are listed in Table 25. The branching ratio for both W bosons to decay into prompt e or μ is simply the square of $\mathrm{Br}(W \to l\nu) = 0.108$, with an extra combinatoric factor of 2 for the $e\mu$ channel.

Selections	$e\mu$ Channel		ee Channel		$\mu\mu$ Channel	
	$e\nu\mu\nu$	$\tau\nu\ell'\nu$	$e\nu e\nu$	$\tau\nu\ell'\nu$	$\mu\nu\mu\nu$	$\tau\nu\ell'\nu$
Total	27821	10655	13911	5327	13911	5327
Trigger, Lepton ID and lepton p_{T}	7977	872	3052	353	5020	507
$m_{ll} > 10/15$ GeV	7971	872	3030	351	4978	503
$\lvert m_{ll} - m_Z\rvert < 15$ GeV	7971	872	2345	261	3840	376
$E^{\mathrm{miss}}_{\mathrm{T,\ Rel}} > 15/45$ GeV	6180	639	892	77	1531	118
$p^{\mathrm{miss}}_{\mathrm{T}} > 20/45$ GeV	5522	574	698	54	1196	81
$\Delta\phi(E^{\mathrm{miss}}_{\mathrm{T}}, p^{\mathrm{miss}}_{\mathrm{T}}) < 0.6/0.3$	4313	440	453	35	786	53
Jet-veto requirement	2941	284	325	21	574	36
Efficiency	10.6%	2.7%	2.3%	0.4%	4.1%	0.7%

Table 25: MC signal predictions for prompt leptons and non-prompt leptons. The number of events are the signal predictions based on the MC simulation and the predicted SM cross sections (as listed in Section 3.2.1), integrated luminosity and relevant branching fractions after each selection requirement. For each channel measurement the separate contributions from direct W decay leptons and from indirect τ decay leptons ($\tau\nu\ell'\nu$, where ℓ' refers to e, μ or τ) are shown. Where two cut values are listed for a selection requirement, the first refers to the different flavor channel, whilst the second is the value for th e same flavor channels. The statistical uncertainties range from 0.3% to 1% depending on the channel for the prompt decays into muons or electrons. For the samples with WWdecaying to τ leptons, the statistical uncertainty ranges from 1 to 3%.

3.9.3 Cross-section combination

The single-channel and three-channel combined measurement of the total or fiducial cross section is calculated by minimizing a log-likelihood function. The log-likelihood function is

$$-\ln L(\sigma, \{x_k\}) = \sum_{i=1}^{3} -\ln\left(\frac{e^{-(N^i_s(\sigma,\{x_k\})+N^i_b(\{x_k\}))} \times (N^i_s(\sigma, \{x_k\}) + \ N^i_b(\{x_k\}))^{N^i_{obs}}}{(N^i_{obs})!}\right) + \sum_{k=1}^{n} \frac{x_k^2}{2}. \tag{76}$$

where the sum is taken over the channels ($i = 1, 2, 3$ for ee, $\mu\mu$, $e\mu$). N^i_s is the expected signal contribution, N^i_b is the expected background contribution, and N^i_{obs} is the observed number of events in the corresponding *i-th* channel. The expected number of signal events can be rewritten from Equation 74

$$N^i_s(\sigma^{tot}_{WW}, \{x_k\}) = \sigma^{tot}_{WW} \times Br \times L \times A_{WW} \times C_{WW} \times (1 + \sum_{k=1}^{n} x_k S^i_k) \tag{77}$$

A similar equation for the fiducial cross section can be obtained by removing the C_{WW} and Br factors in the above equation and replacing σ_{WW}^{tot} with σ_{WW}^{fid}.

The expected number of background events is

$$N_b^i(\{x_k\}) = N_b^i(1 + \sum_{k=1}^{n} x_k B_k^i). \tag{78}$$

The impact of systematic uncertainties on the signal and background contributions are included in the set of nuisance parameters, $\{x_k\}$.

A single-channel cross-section calculation only uses one particular i value corresponding to the appropriate channel. The three-channel combination sums over all three. The minimization and error calculation is done using the MINUIT package.

3.9.4 Summary of observations and predictions

The number of expected signal and background yields (using the data-driven methods where applicable) are given in Table 26.

Channel	$e\mu$	ee	$\mu\mu$
Observed Events	5067	594	975
Total expected events	$4418 \pm 26 \pm 522$	$507 \pm 10 \pm 73$	$817 \pm 12 \pm 105$
MC WW signal	$3238 \pm 10 \pm 284$	$346 \pm 3 \pm 33$	$613 \pm 5 \pm 60$
Top(data-driven)	$609 \pm 18 \pm 52$	$92 \pm 7 \pm 8$	$127 \pm 9 \pm 11$
W+jets(data-driven)	$249 \pm 15 \pm 139$	$14 \pm 5 \pm 14$	$6 \pm 5 \pm 12$
Z+jets (data-driven)	$175 \pm 3 \pm 18$	$28 \pm 1 \pm 13$	$33 \pm 1 \pm 17$
Other dibosons (MC)	$150 \pm 4 \pm 30$	$27 \pm 1 \pm 5$	$39 \pm 1 \pm 5$
Total background	$1182 \pm 24 \pm 238$	$161 \pm 9 \pm 40$	$205 \pm 11 \pm 45$

Table 26: Summary of observed events and expected signal and background contributions in three dilepton channels. The first error is statistical, the second systematic. For each source of systematic uncertainty, the total systematic uncertainties for total background and total expectation are calculated assuming full correlation between the same systematic sources for all signal or background processes.

3.9.5 Cross-Section results

The results for the WW production fiducial and total cross sections determined using the likelihood fit are summarized in Table 27 and Table 28. The fiducial cross section predictions in Table 27 are calculated in by taking the total NNLO cross section prediction and multiplying by the the fiducial acceptance factor from Powheg and the square of the leptonic branching fraction.

The measured total WW cross section using the combination of the three measurements is

$$\sigma_{\mathrm{WW}}^{\mathrm{total}} = 71.0^{+1.1}_{-1.1}(\mathrm{stat})^{+3.2}_{-3.1}(\mathrm{theory})^{+4.8}_{-3.9}(\mathrm{exp})^{+2.1}_{-2.0}(\mathrm{lumi})\ \mathrm{pb} \tag{79}$$

The total WW cross section prediction taken from the NNLO calculation [53] is

$$\sigma_{\mathrm{WW}}^{\mathrm{theory}} = 63.2^{+1.6}_{-1.4}(\mathrm{scale}) \pm 1.2(\mathrm{PDF})\ \mathrm{pb} \tag{80}$$

Channel	Measured $\sigma_{WW}^{\mathrm{fiducial}}$ [fb]	Theory
$e\mu$	$373.8^{+6.9}_{-6.8}$ (stat) $^{+2.6}_{-2.6}$ (theory) $^{+24.9}_{-22.4}$ (exp) $^{+11.2}_{-10.5}$ (lumi)	335.3 ± 17.7
ee	$73.3^{+4.2}_{-4.1}$ (stat) $^{+0.8}_{-0.8}$ (theory) $^{+6.4}_{-5.5}$ (syst) $^{+2.2}_{-2.1}$ (lumi)	63.0 ± 3.4
$\mu\mu$	$80.1^{+3.3}_{-3.2}$ (stat) $^{+0.8}_{-0.8}$ (theory) $^{+6.4}_{-5.5}$ (syst) $^{+2.4}_{-2.3}$ (lumi)	68.6 ± 3.7

Table 27: Measured fiducial WWproduction cross sections in the three channels and Standard Model predictions. The fiducial cross section predictions are calculated in by taking the total NNLO cross section prediction and multiplying by the the fiducial acceptance factor from Powheg and the square of the leptonic branching fraction.

Channel	$\sigma_{WW}^{\mathrm{total}}$ [pb]
$e\mu$	$70.5^{+1.3}_{-1.3}$ (stat) $^{+3.2}_{-3.0}$ (theory)$^{+4.9}_{-4.1}$ (exp) $^{+2.1}_{-2.0}$ (lumi)
ee	$73.5^{+4.2}_{-4.1}$ (stat) $^{+3.6}_{-3.4}$ (theory)$^{+6.6}_{-5.4}$ (exp) $^{+2.3}_{-2.1}$ (lumi)
$\mu\mu$	$73.9^{+3.0}_{-3.0}$ (stat) $^{+3.5}_{-3.3}$ (theory)$^{+6.1}_{-4.9}$ (exp) $^{+2.2}_{-2.1}$ (lumi)
Combined	$71.0^{+1.1}_{-1.1}$ (stat) $^{+3.2}_{-3.1}$ (theory)$^{+4.8}_{-3.9}$ (exp) $^{+2.1}_{-2.0}$ (lumi)
Theory	$63.2^{+1.6}_{-1.4}$(scale) $\pm$ 1.2(PDF) pb

Table 28: Measured total WWproduction cross sections in each channel and their combination and Standard Model prediction at NNLO.

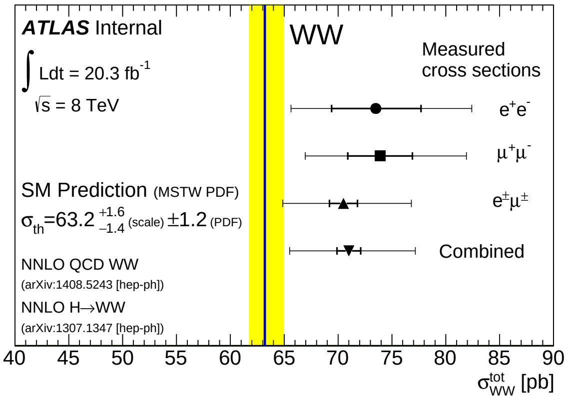

Figure 29: Comparison between predicted WW production cross section at NNLO and the measured cross section in $e\mu$, ee, $\mu\mu$ and combined channels. The yellow band represents the total theoretical uncertainty. The filled symbols show the measured total cross section with the statistical and total uncertainty.

3.10 Differential Distributions and Unfolding

3.10.1 Introduction

In an experiment, an observed distribution can differ from the corresponding true distribution. The measured distribution can be distorted from the true distribution due to detector acceptance, efficiencies, and resolution effects. In order to compare experimental distributions with theoretical calculations, these differences must be considered. One possible approach is to assume that a mathematical function that parameterizes the detector effects. This is referred to as parametric inference (or "fitting"), where the main task is in estimating parameters using a least squares or maximum likelihood method. An alternative approach can be used without assuming any analytic functions. In unfolding (or deconvolution), the aim is to transform the measured binned distribution such that the bin contents fluctuate to get the corresponding true distribution. The relationship between the observed experimental distribution $f_{obs}(y)$, and the true theoretical distribution $f_{true}(x)$, is given by a convolution

$$f_{obs}(y) = \int R(y|x) f_{true}(x) dx \tag{81}$$

where the response function $R(y|x)$ gives the probability of observing y given a true x and this function incorporates physics and detector effects. If the x and y distributions are discretized into M and N bins respectively, then

$$y_i = \sum_{j=1}^{M} R_{ij} x_j \tag{82}$$

where R_{ij} is the response matrix (or detector smearing matrix) with indices $i = 1 \dots N, j = 1 \dots M$ corresponding to the probability of observing y_i given true x_j in bins i and j. Two approaches can be used to make comparisons between observed and theory distributions.

Folding Theorists can include detector effects by applying the detector response to the theory distribution and the smeared result $y = Rx$ is compared to data.

Unfolding Experimentalists can undo detector effects and the unsmeared result $x = R^{-1}y$ is compared to theory.

The process of folding is more computationally intensive since it requires full detector simulation and reconstruction with the same algorithms as those used by the experiments. Also, folding must be repeated for each experimental measurement, since different detectors will have different acceptances, efficiencies, and resolutions. In practice, the information needed to properly simulate the detector effects is not easily available, which leads theorists to use approximations that result in larger systematic uncertainties in folding compared to unfolding. The process of unfolding is preferred since exact simulation and reconstruction algorithms are known within experiments. Also, unfolding only needs to be done once so that any theory can make a direct comparison.

3.10.2 Methodology

Several unfolding methods are described briefly in this section to illustrate the advantages and disadvantages of each method. The method of bin-by-bin corrections is the simplest and quickest approach but it fails to include bin-by-bin correlations in events. The matrix inversion method takes event correlations into account but is sensitive to large statistical fluctuations (especially in low occupancy bins). Regularized unfolding methods attempt to lower variance by trading in the maximal likelihood solution for a smoother solution with a lower likelihood. Finally, the iterative Bayesian unfolding method uses Bayesian probability to relate the observed and true distributions and the method is repeated and improved until a stable solution is found. The iterative Bayesian unfolding method is chosen for this analysis and will be discussed in greater detail.

Bin-by-Bin Corrections A simple approach for unfolding is to use the method of bin-by-bin corrections. It is assumed that the number of observed and true bins is the same and R is assumed to be diagonal (no large bin-to-bin migrations). In this method, bin-by-bin corrections, C_i are applied to the observed number of events N_i^{data} for each bin i.

$$\begin{aligned} N^{unfolded} =& C_i N_i^{data} \\ C_i =& y_i^{MC}/x_i^{MC} \end{aligned} \tag{83}$$

where y_i and x_i are the expected number of reconstructed and true events. Although this method is straightforward and quick, it can only be used when there are very small bin variances. This method is also generally criticized for considering bin-to-bin correlations, since each bin is treated independently in this method.

Matrix Inversion Another straightforward method for unfolding uses matrix inversion, which incorporates bin-to-bin correlations. The response matrix in Equation 82 is determined using Monte Carlo simulation to calculate the efficiency rate for reconstructed events to fall in a particular bin in the corresponding true distribution. The matrix is inverted and applied on the observed distribution in order to obtain the true distribution. Matrix inversion problems be avoided by constructing bins such that R is not singular, but this method is sensitive to large statistical fluctuations. Since the method is applied to one instance of the observed distribution and not the expectation value of a large ensemble, statistical fluctuations are treated as real distortions from detector effects and these errors are propagated into the final result.

Regularized Unfolding It can be shown that matrix inversion and maximum likelihood approaches are essentially equivalent. As discussed previously, the maximum likelihood solution may have large fluctuations, but one can trade goodness of fit to reduce variance. In regularized unfolding methods, one chooses a “smoother” but “worse” solution (with a lower likelihood). A regularization function determines how far away from the maximal likelihood solution is acceptable.

$$\ln L(x) \geq \ln L_{max} - \Delta \ln L(x) \tag{84}$$

This is equivalent to maximizing

$$\Phi(x) = \alpha \ln L_{max} + S(x) \tag{85}$$

where α depends on $\Delta \ln L(x)$ and $S(x)$ is the smoothness function. For $\alpha = \infty$, the maximum likelihood solution is recovered. For $\alpha = 0$, the fit quality is disregarded and the maximally smooth function is chosen. The choice of α is not universal and will depend on whether reducing bias or variance is more important for a particular analysis. The choice of a smoothing function is also not unique. In Tikhonov regularization [76], the smoothness function is based on the derivative of the unfolded distribution, $f_{true}(x)$.

$$S[f_{true}(x)] = -\int dx \left(\frac{d^k f_{true}(x)}{dx^k} \right)^2 \tag{86}$$

where $k = 2$ but can generally be any power.

Bayesian Iterative Unfolding The unfolding method used in this analysis is based on Bayes theorem, which states

$$P(x|y) = \frac{P(y|x)P(x)}{P(y)} = \frac{P(y|x)P(x)}{\int P(y|x)P(x)dx} \tag{87}$$

where $P(x|y)$ is the conditional probability of having a true x given that y has been observed and vice versa, $P(x)$ is the probability of having a true x, $P(y)$ is the probability of observing y. $P(y)$ is referred to as the prior probability. Equation 87 can be inverted to solve for the probability density of the unfolded distribution $P(x)$.

$$P(x) = \frac{P(x|y)P(y)}{P(y|x)} \tag{88}$$

The probabilities densities $P(x)$ and $P(y)$ differ only from the distributions by normalization factors. For discrete distributions, $P(y_i|x_j)$ can be replaced by the response matrix R_{ij}. The prior probability $P(x)$ is assumed to be a flat spectrum for the first iteration but will be improved upon in subsequent iterations.

$$x_j^{(0)} = N_{data} p_j^{(0)} = N_{data} \frac{1}{M} \tag{89}$$

where the prior probability p_j is the probability density in the j-th bin for the true distribution, and the superscript denote the number of iterations. where M is the number of bins in the true distribution. The unfolded distribution x_j can be determined by

$$x_j = \frac{1}{\epsilon_j} \sum_{i=1}^{N} \frac{R_{ji} p_i}{R_{ik} p_k} \tag{90}$$

where the efficiency is given by $\epsilon_j = \sum_i R_{ij}$. For the next iteration, the prior probability is taken using p_j from the previous iteration. Not having enough iterations will lead to results that depend heavily on the choice of the initial prior, which may be quite different from the true distribution in reality. In the limit of infinite iterations, one obtains the results from matrix inversion which had problems large statistical fluctuations. Typically two or three iterations are sufficient in obtaining stable results with Bayesian unfolding.

3.10.3 Implementation

This section describes how the truth and reconstruction level distributions are defined and used to construct the response matrix, R, using Monte Carlo signal events. The response matrix only uses events that pass both the reconstruction level kinematic requirements and also the fiducial selection defined by truth level requirements. The unfolded truth (x_j) and reconstruction (y_i) level distributions are defined by

$$\begin{aligned} y_i &= (n_i - b_i) \cdot f_i \\ x_j &= (R_{ij}^{-1} y_i) \cdot c_j \end{aligned} \tag{91}$$

where n_i is the data distribution, b_i is the sum of the background distributions, f_i and c_j are fiducial and correction factors.

$$\begin{aligned} c_j &= \frac{N_j^{reco}}{N_j^{truth}}\Big|_{fid} \\ f_i &= \frac{N_i^{fid}}{N_i^{total}}\Big|_{reco} \end{aligned} \tag{92}$$

c_j is defined for bin j in the truth distribution for events that pass the fiducial acceptance. It is the number of reconstructed events divided by the number of truth events. This corrects for acceptance and efficiencies losses at reconstruction level. f_i is defined for bin i in the reconstruction level distribution. It is the fraction of events that pass the fiducial requirements divided by the the total number of events that pass the reconstruction level requirements.

Statistical and Systematic Uncertainties The statistical uncertainty on the unfolded distribution is determined from 200 MC tests where the data distribution is fluctuated according to Poisson probabilities and the unfolding procedure is repeated. The RMS of the set of unfolded results is taken as the statistical uncertainty. The systematic uncertainties are determined from propagating each systematic source (Section 3.7) into the unfolding method (which includes recomputing the response matrix and correction factors) and obtaining results from each source separately. For the cases where the systematic source is not symmetric, the larger of the $+1\sigma$ or -1σ variations is used to define the symmeterized uncertainty. All symmeterized signal and background systematic sources are assumed to be uncorrelated. In addition to the usual experimental and theoretical systematic sources, an additional systematic uncertainty on the unfolding method is assigned. The nominal method of unfolding is the iterative Bayesian method with three iterations and the unfolding procedure was repeated with two and four iterations. Also, a regularized unfolding method of singular value decomposition (SVD) was tested. The differences in the unfolded leading lepton p_{T}distribution after changing the number of iterations or unfolding method are less than 3%. A modeling uncertainty is assigned from a data-driven closure test described in Section 3.10.4.

3.10.4 Closure tests

Two tests were used to validate and check the results from unfolding.

Technical Closure Test The first test is a technical closure test. This is used as a sanity check to ensure that there are no problems in the implementation of the unfolding procedure and to catch potential bugs in the source code. In this test, the signal MC events are used in place of the observed yields in data, such that MC pseudo-data is used for unfolding. The same signal MC events are used to construct the response matrix as usual. The expected outcome of this test should result in an unfolded distribution that matches the MC truth distribution, since the MC pseudo-data matches exactly the expected MC distribution. The results from this technical closure test are given in Figure 30 and shows perfect agreement.

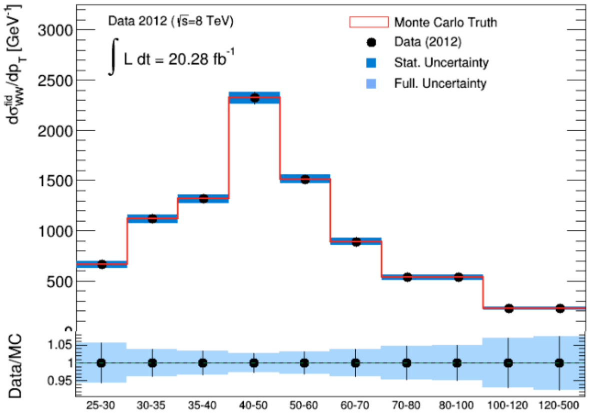

Figure 30: Results of technical closure test on leading lepton p_{T}.

Data-driven test In this data-driven closure test, the differences between data and MC at reconstruction level are compared. It is assumed that the differences at reconstruction level arises from improper modeling in MC. In this test, the truth distribution is reweighted using a smooth function such that the corresponding reconstructed distribution matches data very well after reweighting. The reweighted truth level distribution is folded to obtain the corresponding new reconstruction level distribution. It is important to note that the response matrix with the reweighted distributions distributions will differ from the usual response matrix. A comparison can be made between the unfolded results of this new reconstructed distribution and the reweighted truth distribution.

$$\begin{aligned} &\text{New Reco x New Response Matrix} \Leftrightarrow \text{Reweighted truth distribution} \\ &\text{New Reco x Old Response Matrix} \Leftrightarrow \text{Unfolded distribution} \end{aligned} \tag{93}$$

The difference can be attributed to the difference between the usual response matrix and the new response matrix from the reweighting. This difference is taken as a modeling uncertainty and is included in the unfolded results in the next section.

3.10.5 Unfolded distributions and results

Several differential distributions were considered for unfolding. The binning choice for each distribution has been optimized such that the statistical and systematic uncertainties are not too large for each bin and the bin purity is high. Figure 31 gives the response matrix and unfolded results for leading lepton p_{T}, dilepton p_{T}, and dilepton mass. Figure 32 gives the response matrix and unfolded results for the absolute difference in the rapidity ($|y_{ll}|$), azimuthal angle ($|\Delta\phi_{ll}|$), and $\cos(\theta^*_{ll})$ of the two lepton system, where $\cos(\theta^*_{ll})$ is defined as

$$\cos(\theta^*_{ll}) = \tanh(\Delta\eta_{ll}), \qquad \Delta\eta_{ll} = \eta_{l_1} - \eta_{l_2} \tag{94}$$

Other distributions (such as the $p_{\mathrm{T}}$of the dilepton and $E_{\mathrm{T}}^{\mathrm{miss}}$) system were considered but the bin purity was very low, even with very few bins.

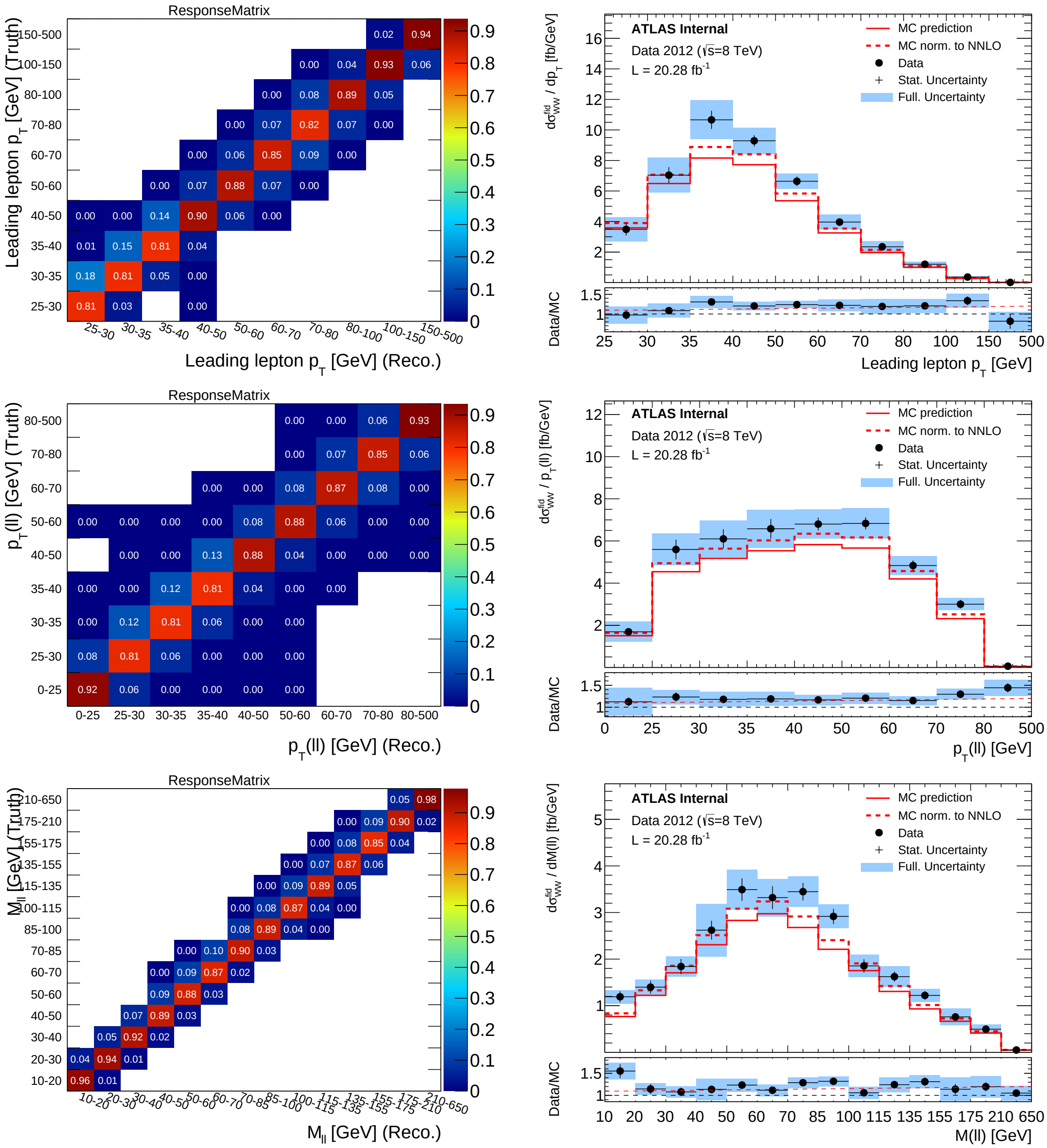

Figure 31: Response matrix and unfolded distributions. The response matrix (left) and results for unfolded distributions (right) for leading lepton p_{T}(top), dilepton p_{T}(middle), and dilepton mass (bottom).

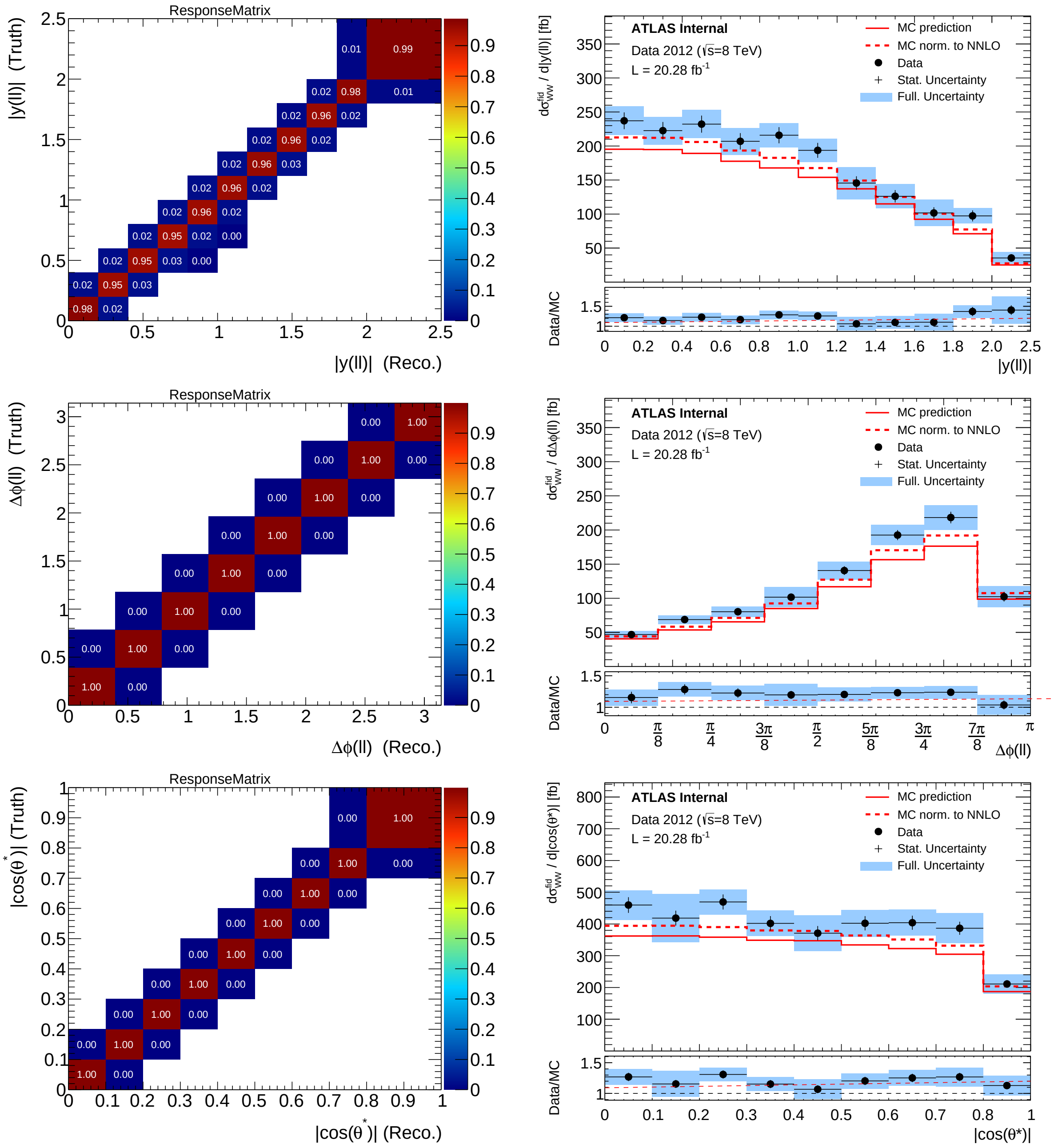

Figure 32: Response matrix and unfolded distributions. The response matrix (left) and results for unfolded distributions (right) for the absolute difference in rapidity, $|y_{ll}|$, azimuthal angle $|\Delta\phi_{ll}|$, and $\cos(\theta^*_{ll})$ of the two lepton system as defined in Equation 94.

4 Sensitivity to Anomalous Couplings

4.1 MC Samples and Generator Comparisons

Powheg, MC@NLO, and BHO [77, 78, 79] are all next-to-leading order generators capable of producing diboson events with anomalous couplings. Table 29 lists the MC samples generated with Powheg+Pythia and MC@NLO+Jimmy/Herwig with full detector simulation and object reconstruction.

Generator	Couplings	Dataset ID
Powheg+Pythia	SM	126928-126936
MC@NLO+Jimmy/Herwig	SM	129933-129941
MC@NLO+Jimmy/Herwig	$\Delta g_1^Z = 0.6, \Delta\kappa^Z = 0.2, \lambda^Z = 0.2$	129942-129950
MC@NLO+Jimmy/Herwig	$\Delta g_1^Z = 0.6$	129951-129959

Table 29: MC samples for $WW \to \ell\nu\ell\nu$ production (where ℓ can be e, μ, or τ lepton) with SM or anomalous triple gauge boson couplings. For the case of non-SM, the non-zero coupling parameters are listed.

To avoid the large computational requirements involved in generating many events at different anomalous coupling parameters, a reweighting procedure is desired. The reweighting procedure is used to scale the events produced with a particular set of fixed values for anomalous coupling parameters to a different set of values. The disadvantage of using BHO or Powheg is that these generators do not give anomalous coupling weights directly. Previously, the BHO generator was used in the 7 TeV version of this analysis[16]. That analysis developed a 3D reweighting procedure as a binned function of the p_T of the leptons and $E_{T,Rel}^{miss}$.

MC@NLO provides event-by-event weights to allow easy calculation of alternate anomalous coupling parameter values, which is described in Section 4.2. Since these weights are given for each event, the generator already accounts for kinematic dependencies. MC@NLO and its built-in reweighting procedure is used for the WW signal predictions with anomalous couplings.

Powheg is used to simulate the WW signal in the 8 TeV cross section measurement, therefore, it is important to make comparisons between Powheg and MC@NLO after full reconstruction. Standard model kinematic distributions using the Powheg and MC@NLO generators after the full analysis selection (in the eμ channel) are shown in Figure 33 and Figure 34. The agreement is acceptable, considering the large statistical uncertainties in the high energy tails of these distributions.

To make very high precision comparisons, generator level comparisons were made between BHO and MC@NLO. WW events with SM couplings and aTGC's were privately generated with MC@NLO and BHO without detector simulation or reconstruction but with very high statistics. Jimmy and Herwig were interfaced with MC@NLO for underlying event and parton shower simulation. No parton shower was used for BHO.

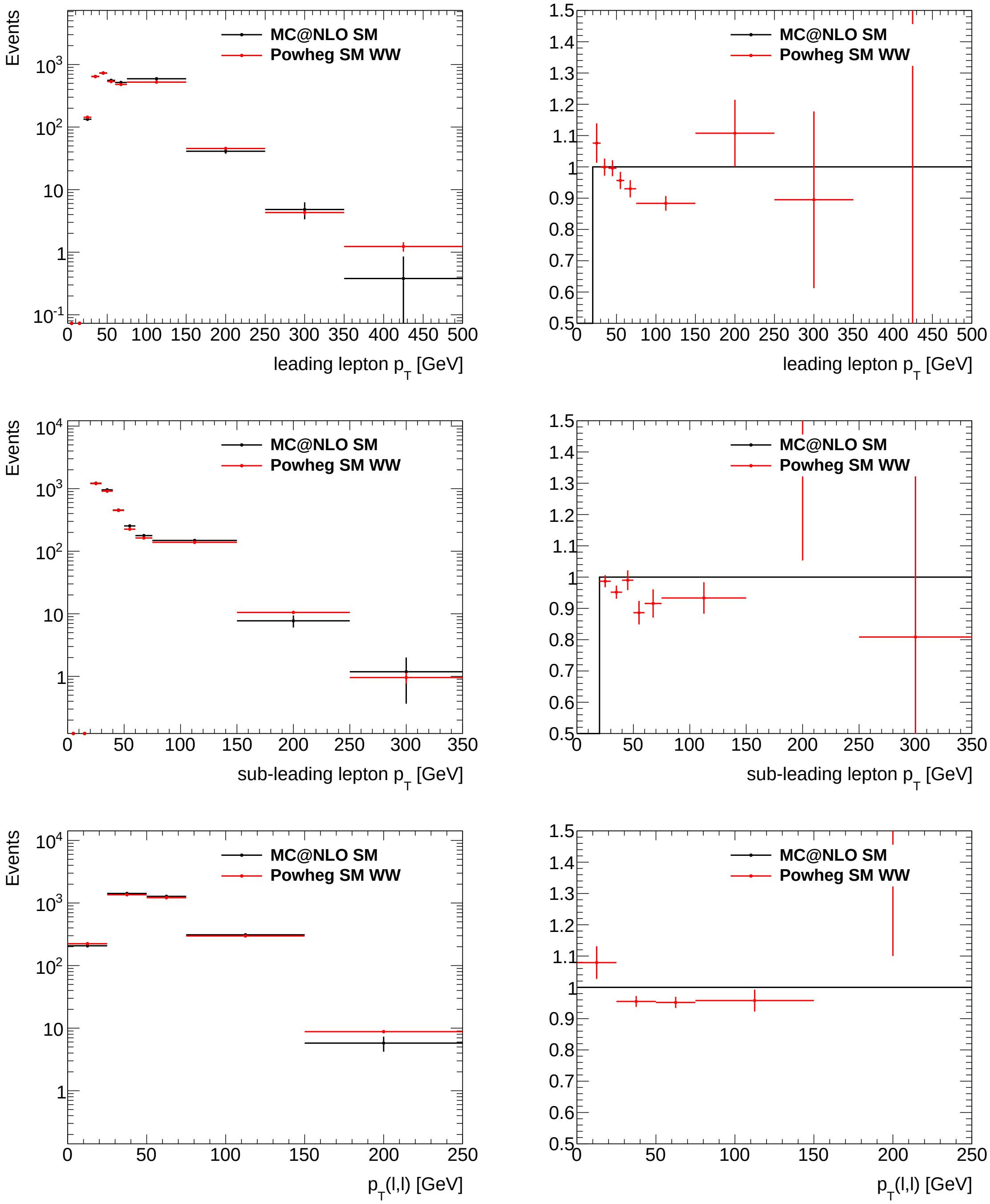

Figure 33: Comparison of reconstruction level Standard Model WW kinematic distributions after all final selection cuts (in the eμ channel) from using Powheg+Pythia (red) and MC@NLO+Jimmy/Herwig (black). Events are normalized to 20.3 fb^{-1}.

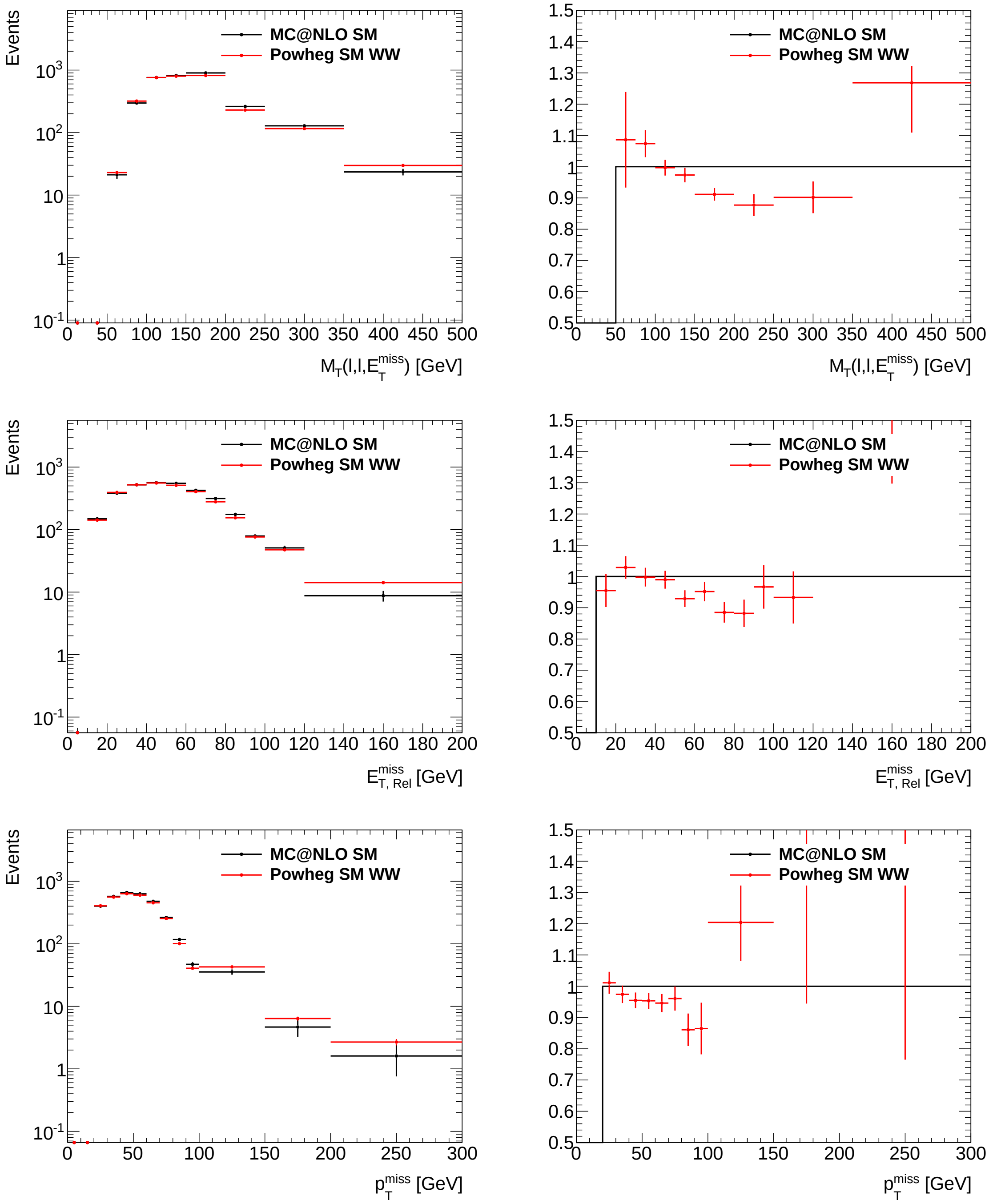

Figure 34: Comparison of reconstruction level Standard Model WW kinematic distributions after all final selection cuts (in the $e\mu$ channel) from using Powheg+Pythia (red) and MC@NLO+Jimmy/Herwig (black). Events are normalized to 20.3 fb^{-1}.

4.2 Reweighting Method with MC@NLO

The reweighting method for MC@NLO is described in this section. Reweighting is used to scale events generated with particular anomalous coupling parameters to another set of parameters. The number of signal events scales with the cross section and the amplitude squared.

$$N_{sig} \propto \sigma \propto \mathcal{A}^2 \tag{95}$$

The amplitude can be written:

$$\mathcal{A} = \mathcal{A}_{SM} + \mu_1 \mathcal{A}_{\mu_1} + \cdots + \mu_n \mathcal{A}_{\mu_n} \tag{96}$$

where μ_i are the n anomalous coupling parameters, . Note that the first term is for Standard Model only, so here $\mu_0 = 1$. `MC@NLO` allows for up to six anomalous coupling parameters, $\boldsymbol{\mu} = \{1, \Delta g_1^Z, \Delta\kappa^Z, \lambda^Z, \Delta g_1^\gamma, \Delta\kappa^\gamma, \lambda^\gamma\}$. Additional constraints will lower the number of free parameters. Event weights are calculated by the generator:

$$\begin{aligned} w_{TOT} = w_0 &+ (\Delta g_1^Z)^2 w_1 + (\Delta\kappa^Z)^2 w_2 + (\lambda^Z)^2 w_3 \\ &+ (\Delta g_1^\gamma)^2 w_4 + (\Delta\kappa^\gamma)^2 w_5 + (\lambda^\gamma)^2 w_6 \\ &+ 2\Delta g_1^Z w_7 + \cdots + 2\lambda^\gamma w_{12} \\ &+ 2\Delta g_1^Z \Delta\kappa^Z w_{13} + \cdots + 2\Delta\kappa^\gamma \lambda^\gamma w_{27} \end{aligned} \tag{97}$$

The anomalous coupling event weights, $a_i \equiv w_i / w_{TOT}$ are stored in the branch `mcevt_weight` as a vector:

$$\texttt{mcevt\_weight} = \{\texttt{mc\_weight}, a_0, \ldots, a_{27}\} \tag{98}$$

where `mc_weight` is the generator weight which is 1 or -1 for MC@NLO. These weights can be used to calculate the event-by-event weight to a new set of aTGC parameters.

$$weight(\Delta g_{1,new}^Z, \ldots, \lambda_{new}^\gamma) = a_0 + a_1 (\Delta g_{1,new}^Z)^2 + \cdots + 2a_{27} \Delta\kappa_{new}^\gamma \lambda_{new}^\gamma \tag{99}$$

This parameterisation gives the most general reweighting function with up to 6 independent parameters with no constraints between them. The parameterisation after applying additional constraints in the LEP, HISZ, Equal couplings, and EFT scenarios reduce the number of free parameters, so basis transformations have been applied to the reweighting function for each of these scenarios.

The reweighting method must be validated by comparing a generated sample with a reweighted sample generated at a different aTGC point. This is to ensure that the reweighting procedure gives a compatible result with directly generating the sample. Figure 35 and Figure 36 show the ratio of reweighted events as a function of leading lepton p_T to the directly generated distribution at reconstruction level and generator level, respectively. Officially produced samples were used to obtain the reconstruction level distributions while privately generated samples were used to create high statistics distributions at generator level. Due to higher statistics in the MC@NLO sample generated with $\Delta g_1^Z = 0.6, \Delta\kappa^Z = 0.2, \lambda^Z = 0.2$, this sample is used to parameterize the aTGC modeling. Using the other MC@NLO samples will result in larger statistical errors in the regions where the aTGC sensitivities lie. From now on, the coupling parameters refer to after reweighting the MC@NLO sample generated at $\Delta g_1^Z = 0.6, \Delta\kappa^Z = 0.2, \lambda^Z = 0.2$.

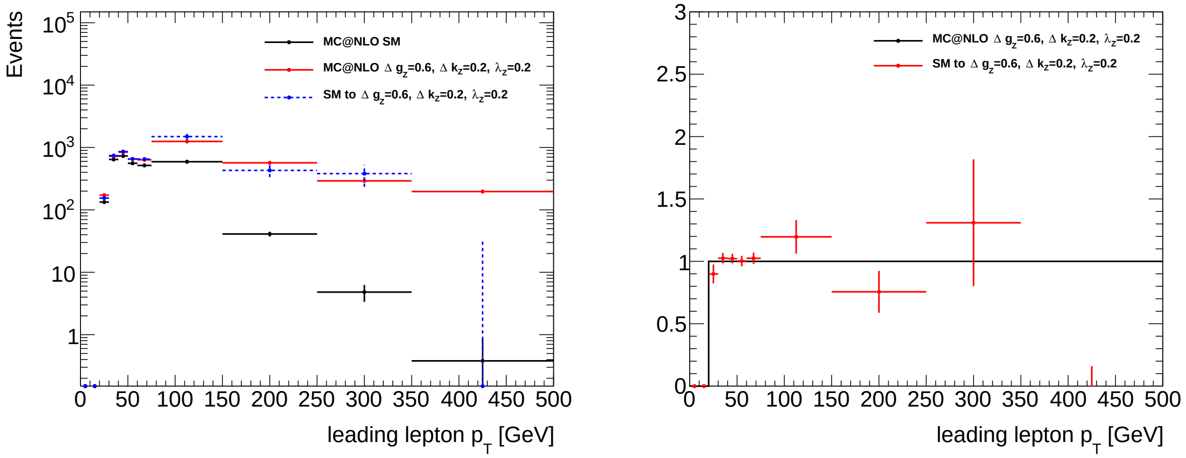

(a) Reweighting to aTGC point

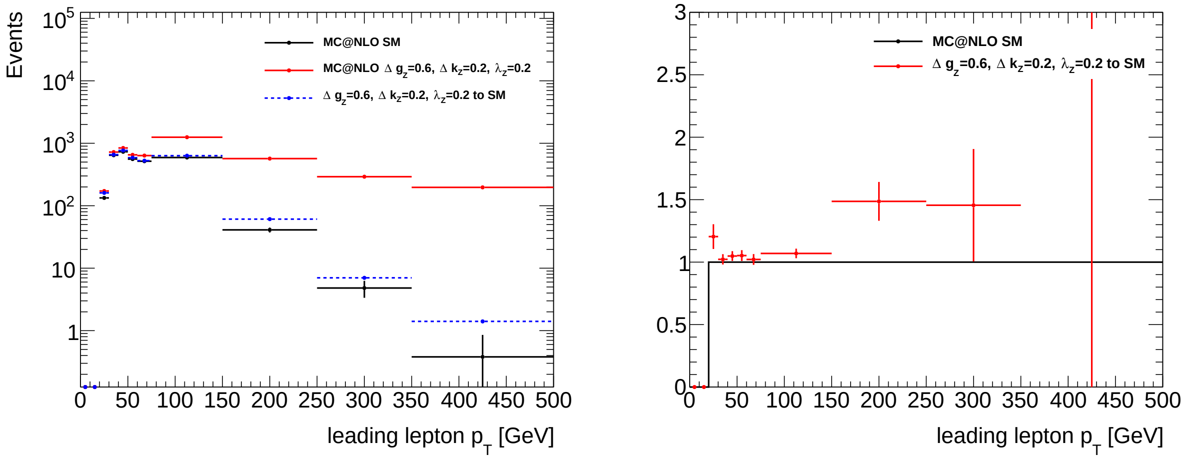

(b) Reweighting to SM

Figure 35: Comparison of reconstruction level leading lepton p_{T}distributions between directly generating events with SM (black) or with anomalous couplings $\Delta g_1^Z = 0.6, \Delta\kappa^Z = 0.2, \lambda^Z = 0.2$ (red) to the reweighted distributions (blue). (a) On the top plots, the dashed blue line corresponds to SM events after reweighting to the aTGC point. (b) On the bottom plots, the dashed blue line corresponds to aTGC events after reweighting to SM. The plots on the right show the ratio of the reweighted sample to the sample after direct generation.

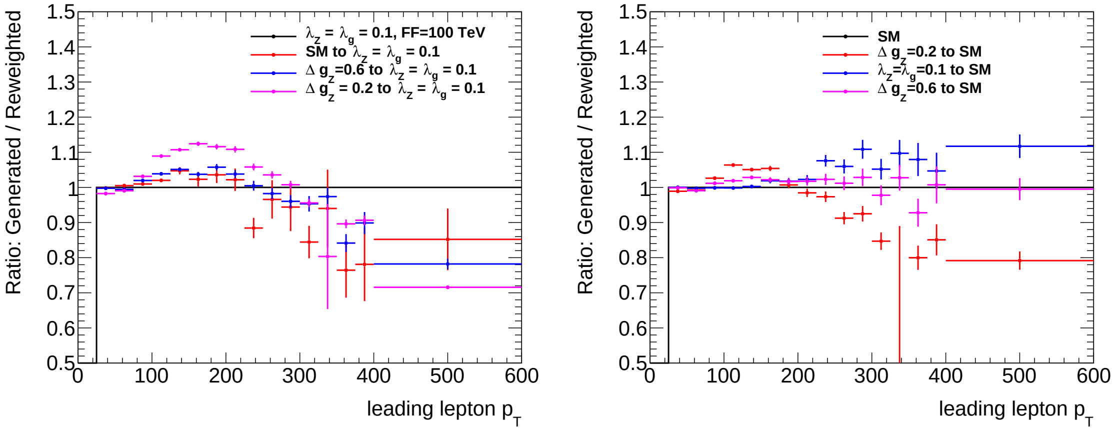

(a) Reweighting to aTGC point

(b) Reweighting to SM

Figure 36: (a) Comparison of generator (truth) level leading lepton distributions between directly generating events with $\lambda^Z = \lambda^\gamma = 0.1$ (black) to SM or different aTGC generated events (colors) reweighted to $\lambda^Z = \lambda^\gamma = 0.1$. (b) Comparison of generator (truth) level leading lepton distributions between directly generated SM events (black) to aTGC generated events (colors) reweighted to SM.

4.3 Determination of 95% Confidence Interval Limits

Section 4.3.1 will give an overview of how the number of events is parameterised in the likelihood function. Two methods are used for the determination of 95% confidence level intervals. The Delta Log Likelihood method and Feldman Cousins frequentist approach are detailed in Section 4.3.2. The Asimov dataset used for expected limits are also described in that section.

4.3.1 Likelihood Function and Nuisance Parameters

The number of SM+aTGC signal events, N_{sig}, depends on n anomalous coupling parameters, $\boldsymbol{\mu} = \{1, \mu_1, \ldots, \mu_n\}$. The Poisson probability of observing N_{data} events is

$$p(N_{data}, N_{sig}(\boldsymbol{\mu}) + N_{bkg}) = \frac{(N_{sig}(\boldsymbol{\mu}) + N_{bkg})^{N_{data}} e^{-(N_{sig}(\boldsymbol{\mu}) + N_{bkg})}}{N_{data}!} \tag{100}$$

where

N_{sig} is the expected number of signal events which depends on μ

N_{bkg} is the expected number of background events

N_{data} is the number of observed data events

In the context of aTGCs, signal only refers only to $qq \to WW$, as there is no triple gauge vertex in $gg \to WW$ or $gg \to H \to WW$. The gluon fusion processes are parameterized as background. The number of events in each leading lepton p_T bin is given in Table 30.

Number of events	25-75	75-150	150-250	250-350	350-1000
Observed	4053	936	75	2	1
Signal	2538.35	580.62	51.45	5.60	1.15
W+jets	219.05	26.16	3.23	0.13	0.27
Z+jets	166.22	9.60	1.30	0	0
Diboson	129.93	19.26	1.07	0.41	0.03
Top	334.78	238.21	31.05	3.06	$-0.01 \to 0$
$gg \to WW$	174.04	24.28	3.25	0.34	0.30

Statistical uncertainty	25-75	75-150	150-250	250-350	350-1000
Signal	1.51%	2.59%	5.05%	6.43%	7.06%
W+jets	6.22%	25.05%	64.24%	265.62%	119.16%
Diboson	2.80%	7.61%	21.90%	48.35%	89.13%
Top	3.98%	4.44%	11.91%	44.63%	505.05%
gg	0.96%	2.79%	7.66%	22.11%	25.76%

Table 30: Number of events (top) and statistical uncertainties in signal and backgrounds (using data driven estimates for W+jets, Z+jets, and top) in each leading lepton p_T bin. Signal events are given under SM expectations with electroweak corrections applied to the SM-only term. The top background yield is negative in the last bin because MC@NLO allows for negative generator weights. The yield is set to zero for limit setting, as it is unphysical. The combined statistical and systematic uncertainty on the Z+jets background is given in Table 34.

The number of signal events scales with terms up to quadratic dependence of the n anomalous coupling parameters. Let the coefficients F^{ij} be defined such that

$$N_{sig}(\boldsymbol{\mu}) = \sum_{i,j} F^{ij}\mu_i\mu_j, \qquad i,j = \{1,\ldots,n\} \tag{101}$$

It is straightforward to match the coefficients F^{ij} with the MC@NLO anomalous coupling weights as listed in Equation 97. Table 31 gives the signal parameterisation (after applying electroweak corrections as described in Section 4.3.3) as given by the MC@NLO generator weights.

Define a bin index i={0, ... ,m} where m is the total number of bins. There may be binned statistical or systematic uncertainties associated with N_{sig} and N_{bkg}, so nuisance parameters, $\boldsymbol{\theta} = \{\theta_1, ..., \theta_{2m}\}$, are introduced. Note that $\boldsymbol{\mu}$ are the parameters of interest (aTGCs) and $\boldsymbol{\theta}$ are nuisance parameters with limited accuracy and are allowed to be fixed at values different from their nominal values of zero.

$$N^i_{tot}(\boldsymbol{\mu},\boldsymbol{\theta}) = N^i_{sig}(\boldsymbol{\mu})(1+\theta_i) + N^i_{bkg}(1+\theta_{i+m}) \tag{102}$$

The covariance matrix, C, is given by

$$C_{ij} = \sum_k \rho\sigma_{ik}\sigma_{jk} \tag{103}$$

where σ_{ik} and $\sigma_{(i+m)k}$ are the the fractional systematic uncertainties on N^i_{sig} and N^i_{bkg} due to the k-th source. $\rho = 1$ or $\rho = 0$ if assuming full correlation or no correlation. The likelihood

Leading lepton p_{T}(GeV)	25-75	75-150	150-250	250-350	350-1000
w0	2538.3511	580.6191	51.445	5.6007	1.1535
w1	403.8496	446.2231	169.6013	52.5405	28.4782
w2	1090.4524	2810.4971	2844.4399	1879.9718	2435.0181
w3	1867.9723	5260.8721	5535.0732	3709.8433	4842.2754
w4	55.0165	70.5879	31.0981	11.1002	6.423
w5	159.5249	481.7927	536.6505	403.4465	551.4489
w6	275.0844	906.0109	1045.1257	796.311	1096.6353
w7	-21.5405	-79.6714	-12.7283	-1.8791	-0.5073
w8	-61.6708	-187.1691	-66.8313	-20.5484	-11.817
w9	12.1891	-59.2387	-5.4303	-0.2373	0.3681
w10	-18.0217	-32.6403	-5.695	-0.9255	-0.2612
w11	-35.2449	-80.0386	-31.278	-10.5907	-6.3282
w12	-9.2589	-28.9713	-3.8634	-0.465	0.0179
w13	441.3488	578.8314	255.0313	84.5859	48.5844
w14	569.7651	797.5406	356.2559	119.0714	69.4078
w15	59.1645	70.7196	28.6899	9.3102	5.1566
w16	65.117	92.0646	43.1749	14.9939	8.7882
w17	83.7941	126.7233	60.3253	21.1098	12.5492
w18	312.9323	360.1221	153.8068	50.1005	27.7609
w19	65.117	92.0646	43.1749	14.9939	8.7882
w20	166.0535	460.094	486.35	334.8567	441.7253
w21	46.4399	57.406	26.0246	8.878	5.0271
w22	83.7941	126.7233	60.3253	21.1098	12.5492
w23	46.4399	57.406	26.0246	8.878	5.0271
w24	285.6671	862.782	946.6754	660.8354	878.4234
w25	60.8929	92.2435	46.9195	17.9032	10.9199
w26	77.8205	126.9126	65.6638	25.2243	15.5773
w27	43.9654	57.5744	28.1752	10.5821	6.2625

Table 31: Signal anomalous coupling parameterization assuming no constraints using 28 MC@NLO generator weights (described in Equation 97). The parameterization is given in bins of leading lepton p_{T}in GeV. Electroweak corrections are applied.

with nuisance parameters is given by

$$\mathcal{L}(N_{data}, \boldsymbol{\mu}, \boldsymbol{\theta}) = \prod_{i=1}^{m} p(N^i_{data}, N^i_{tot}(\boldsymbol{\mu}, \boldsymbol{\theta})) \frac{1}{(2\pi)^m} e^{-\frac{1}{2}(\boldsymbol{\theta} \cdot C^{-1} \cdot \boldsymbol{\theta})} \tag{104}$$

Systematic uncertainties on both background and signal are included as nuisance parameters. There are generally two types of systematic uncertainties:

1. Flat: All bins are varied coherently up or down for each source. In other words, the overall normalisation of the distribution is varied but not the shape. Examples include cross section uncertainties or luminosity.
2. Shape: Bin-by-bin correlations are included for systematic sources that take into account bin migrations. In other words, the shape information for a systematic variation is used. Examples include lepton energy scale and resolution.

Statistical uncertainties for all processes are included as listed in Table 30. The shape systematics applied on both $qq \to WW$ and $gg \to WW$ events are listed in Table 32 in each leading lepton p_T bin. Similarly, the shape systematics applied on background diboson events is listed on Table 33. Flat systematic uncertainties on the data driven Z+jets and top background of 15.8% and 8.6% are applied, respectively. A flat cross-section uncertainty of 18% for dibosons is included. The binned shape systematic uncertainties (fake rate, efficiency, and sample dependence) on the data driven W+jets estimate and data-driven top background are also included (Table 34) The binned shape systematic from theoretical uncertainties on the data-driven top background is also included. A flat luminosity uncertainty of 2.8% is applied on all MC predictions including $qq \to WW$, $gg \to WW$, and background diboson events. In addition, PDF and scale uncertainties of 3%-10% (10%) and 5% (20%) respectively are applied to $qq \to WW$ ($gg \to WW$) events. The parton shower and generator uncertainties for $qq \to WW$ and $gg \to WW$ were found to be shape dependent. The theoretical uncertainties on are summarized in Table 35.

4.3.2 Delta Log Likelihood Limits and Frequentist Limits

95% confidence level intervals can be determined using a dLogL method or a Feldman Cousins frequentist method. In addition, Asimov datasets are used in the calculation of expected limits. They are all described below.

dLogL The Delta Log Likelihood method is equivalent to a chi-squared method for calculating confidence intervals. The likelihood as defined in Equation 104 is Gaussian and and the log of the likelihood is parabolic.

$$-\ln \mathcal{L}(N_{data}, \boldsymbol{\mu}, \boldsymbol{\theta}) = -\ln \mathcal{L}_{max} + s^2/2 \tag{105}$$

where $\ln \mathcal{L}_{max}$ is the maximum likelihood (ML) and s is the standard deviation. The 1-dimensional (1D) 95% confidence level limit for an anomalous coupling parameter, where all others are set to zero, is the set of values for that parameter in which the negative Log-Likelihood increases by no more than 1.92 with respect to the minimum. The 2-dimensional

Source	25-75	75-150	150-250	250-350	350-1000
Pileup	1.77%	1.40%	1.64%	-0.93%	2.59%
TrigMatchMu	-0.25%	-0.09%	-0.06%	-0.06%	-0.03%
TrigMatchEl	-0.26%	-0.20%	-0.26%	-0.27%	-0.28%
MuMSSmear	-0.02%	0.12%	0.16%	1.86%	0.22%
MuIDSmear	-0.51%	-0.92%	-1.20%	-0.92%	-2.51%
MuScale	0.05%	0.04%	0.35%	0.00%	0.00%
MuIso	-0.57%	-0.52%	-0.51%	-0.51%	-0.51%
MuEff	-0.43%	-0.46%	-0.50%	-0.56%	-0.60%
ElRes	-0.02%	-0.10%	0.14%	-2.37%	0.00%
ElScaleZeeAll	-0.24%	-0.89%	-1.10%	0.04%	0.00%
ElScaleR12Stat	-0.25%	0.55%	1.21%	1.20%	0.39%
ElScalePSStat	-0.07%	0.11%	0.22%	0.00%	0.00%
ElScaleLowPt	-0.01%	0.00%	0.00%	0.00%	0.00%
ElEffID	-0.85%	-0.97%	-1.05%	-1.04%	-0.97%
ElEffTrk	-0.26%	-0.40%	-0.46%	-0.44%	-0.42%
ElIso	-0.22%	-0.19%	-0.18%	-0.18%	-0.17%
METSoftReso	-0.28%	-0.25%	-0.18%	1.18%	-4.32%
METSoftScale	-2.41%	-2.07%	-0.94%	0.41%	2.13%
MPTSoftReso	-0.03%	-0.13%	0.18%	-0.97%	0.00%
MPTSoftScale	-0.33%	-0.36%	-0.04%	0.00%	0.00%
JVF	0.22%	0.23%	0.25%	0.16%	0.00%
JER	-1.37%	-1.14%	-0.40%	-1.48%	0.59%
JESEffectiveNP 1	-0.77%	-0.96%	-0.84%	-2.77%	-1.22%
JESEffectiveNP 2	1.37%	1.50%	2.04%	1.91%	3.05%
JESEffectiveNP 3	-0.59%	-0.70%	-0.58%	-1.08%	0.00%
JESEffectiveNP 4	-0.23%	-0.26%	-0.15%	-0.49%	0.00%
JESEffectiveNP 5	-0.27%	-0.34%	-0.25%	-0.49%	0.00%
JESEffectiveNP 6restTerm	-0.11%	-0.14%	-0.12%	-0.49%	0.00%
JESEtaIntercalibration Modelling	1.56%	1.71%	2.15%	1.49%	3.59%
JESEtaIntercalibration StatAndMethod	-0.39%	-0.49%	-0.36%	-0.64%	0.00%
JESSingleParticle HighPt	0.00%	0.00%	0.00%	0.00%	0.00%
JESRelativeNonClosure	0.00%	0.00%	0.00%	0.00%	0.00%
JESNPVOffset	-0.51%	-0.83%	-0.65%	-2.27%	0.00%
JESMuOffset	-0.24%	-0.38%	-0.39%	-0.94%	0.00%
JESPileupPt	-0.01%	-0.01%	0.00%	0.00%	0.00%
JESPileupRho	-1.05%	-1.24%	-1.18%	-2.77%	-1.22%
JESCloseby	0.00%	0.00%	0.00%	0.00%	0.00%
JESFlavourComp	1.81%	2.07%	2.53%	1.91%	3.05%
JESFlavourResp	1.07%	1.14%	1.38%	1.07%	3.05%
JESBScale	-0.01%	-0.01%	0.00%	0.00%	0.00%

Table 32: Systematic experimental uncertainties on WW signal ($qq \to WW$) and WW background ($gg \to WW$) events in leading lepton p_T (GeV) bins.

Source	25-75	75-150	150-250	250-350	350-1000
Pileup	0.20%	2.38%	-4.12%	1.03%	-1.79%
TrigMatchMu	0.45%	0.12%	0.05%	0.02%	0.03%
TrigMatchEl	0.36%	0.27%	0.32%	0.14%	0.10%
MuMSSmear	-1.07%	0.75%	0.96%	0.00%	0.00%
MuIDSmear	-0.41%	0.40%	-2.15%	42.77%	0.00%
MuScale	0.21%	0.05%	0.00%	0.00%	0.00%
MuIso	0.60%	0.53%	0.51%	0.50%	0.50%
MuEff	0.42%	0.45%	0.51%	0.52%	0.41%
ElRes	-0.17%	0.04%	-1.87%	56.13%	0.00%
ElScaleZeeAll	0.47%	-0.22%	2.69%	0.00%	0.00%
ElScaleR12Stat	0.65%	-2.69%	1.15%	0.00%	-88.37%
ElScalePSStat	0.03%	-0.38%	0.00%	0.00%	0.00%
ElScaleLowPt	0.08%	0.00%	0.00%	0.00%	0.00%
ElEffID	1.27%	1.33%	1.27%	0.94%	1.00%
ElEffTrk	0.34%	0.55%	0.53%	0.38%	0.46%
ElIso	0.27%	0.23%	0.22%	0.14%	0.14%
METSoftReso	0.09%	1.73%	8.03%	-0.73%	0.00%
METSoftScale	3.08%	0.88%	16.13%	0.00%	0.00%
MPTSoftReso	0.64%	-0.24%	1.86%	49.14%	0.00%
MPTSoftScale	0.04%	0.16%	0.00%	0.00%	0.00%
JVF	0.15%	1.02%	0.00%	0.00%	0.00%
JER	0.52%	2.31%	32.08%	-14.21%	0.00%
JESEffectiveNP 1	1.10%	1.35%	5.22%	0.23%	0.00%
JESEffectiveNP 2	1.84%	2.01%	17.31%	0.23%	0.00%
JESEffectiveNP 3	0.74%	1.20%	5.55%	0.23%	0.00%
JESEffectiveNP 4	0.43%	0.34%	5.55%	0.00%	0.00%
JESEffectiveNP 5	0.43%	1.10%	5.55%	0.00%	0.00%
JESEffectiveNP 6restTerm	0.36%	0.02%	5.55%	0.00%	0.00%
JESEtaIntercalibration Modelling	2.54%	2.70%	15.14%	0.23%	0.00%
JESEtaIntercalibration StatAndMethod	0.68%	0.36%	5.55%	0.23%	0.00%
JESSingleParticle HighPt	0.00%	0.00%	0.00%	0.00%	0.00%
JESRelativeNonClosure	0.00%	0.00%	0.00%	0.00%	0.00%
JESNPVOffset	0.88%	2.01%	11.76%	0.23%	0.00%
JESMuOffset	0.30%	0.87%	0.00%	0.23%	0.00%
JESPileupPt	0.00%	0.00%	0.00%	0.00%	0.00%
JESPileupRho	1.42%	1.80%	17.31%	0.23%	0.00%
JESCloseby	0.00%	0.00%	0.00%	0.00%	0.00%
JESFlavourComp	2.34%	2.81%	31.38%	0.23%	0.00%
JESFlavourResp	1.45%	1.54%	17.31%	0.23%	0.00%
JESBScale	0.00%	0.00%	0.00%	0.00%	0.00%

Table 33: Systematic uncertainties on diboson background events in leading lepton p_T (GeV) bins.

Shape systematic uncertainties	25-75	75-150	150-250	250-350	350-1000
W+jets Efficiency	12.67%	33.55%	21.71%	26.69%	2.52%
W+jets Fake rate	8.31%	-45.74%	82.28%	61.04%	65.50%
W+jets Sample dependence	47.22%	133.03%	122.52%	99.81%	134.92%
Top Shape	10.36%	11.37%	8.76%	0.00%	0.00%
Top Normalization	8.6%	8.6%	8.6%	8.6%	8.6%
Z+jets Stat+Syst	14.16%	76.90%	28.40%	0.00%	0.00%

Table 34: Systematic uncertainties on data-driven backgrounds in leading lepton p_T (GeV) bins.

Source	25-75	75-150	150-250	250-350	350-1000
EWCorrErr(qq only)	-0.01%	-0.41%	-1.67%	-3.95%	-7.08%
PDF (qq only)	3%	3%	3%	5%	10%
PDF (gg only)	10%	10%	10%	10%	10%
Scale (qq only)	5%	5%	5%	5%	5%
Scale (gg only)	20%	20%	20%	20%	20%
Parton Shower (qq only)	5%	5%	0%	0%	0%
Generator (qq only)	5%	15%	20%	20%	20%
Parton Shower+Generator (gg only)	40%	50%	50%	80%	80%

Table 35: Systematic theoretical uncertainties on WW signal ($qq \rightarrow WW$) and WW background ($gg \rightarrow WW$) events in leading lepton p_T (GeV) bins.

limit for two of the anomalous coupling parameters is the set of values for the two parameters in which the negative Log-Likelihood increases by no more than 2.99 with respect to the minimum. This method is used in the optimization studies in Section 4.4 since it is not computationally intensive compared to the frequentist approach used in the final results.

Frequentist Limits The standard frequentist approach [80, 81] is used in the final results. A large number of pseudo experiments is generated for different test values for the anomalous coupling parameters, α.

$$q(\alpha) = -ln \frac{L(n|\alpha, \hat{\hat{\beta}})}{L(n|\hat{\alpha}, \hat{\beta})} \tag{106}$$

where n is the number of events, β are the nuisance parameters, $\hat{\hat{\beta}}$ is the ML estimator of β that maximizes the numerator for the fixed test value of α, and $\hat{\alpha}$ and $\hat{\beta}$ are the values of α and β which maximize the denominator. For the denominator this means that the minimization is done with α and β free $L(n|\hat{\alpha}, \hat{\beta})$, and for the numerator different values of α are tried and β is minimized, $L(n|\alpha, \hat{\hat{\beta}})$.

Pseudo experiments are generated where n is taken from a Poisson distribution where the mean is the expected number of events for a fixed value of α and the nuisance parameters, β are allowed to fluctate within Gaussian constraints. The p-value for each fixed value of α is calculated as the fraction of pseudo experiments whose test statistic $q_{\text{pe}}(\alpha)$ is smaller than the observed value $q_{\mathrm{obs}}(\alpha)$:

$$p = \frac{N_{pe}(q_{\mathrm{pe}}(\alpha) < q_{\mathrm{obs}}(\alpha))}{N_{pe}} \tag{107}$$

The observed value of the test statistic, $q_{\mathrm{obs}}(\alpha)$, is found by using the observed data $n = n_{\mathrm{obs}}$.

The number of pseudo experiments, is chosen to be 10,000 to ensure that a p-value of 5% can be determined to a reasonable statistical precision of ±0.2%.

Asimov Dataset The Asimov dataset is used to extract expectation values without the computationally intensive frequentist approach. The expected limits are performed by replacing N_{data} with pseudo-data from an Asimov dataset. Effectively this is done by using N_{data} values and maximizing the likelihood while holding $\boldsymbol{\mu} = 0$ (SM values) to find the set of nuisance parameters that best describe the data in the SM hypothesis. The Asimov variance is calculated by

$$\sigma_A^2 = \frac{\boldsymbol{\mu}^2}{-2\ln q(\boldsymbol{\mu})} \tag{108}$$

4.3.3 Electroweak Corrections

The next-to-leading order electroweak (EW) contribution of $\mathcal{O}(\alpha_{EW}^3)$ on diboson production is described in Refs [82, 15, 13, 14]. The corrections have been implemented in the `EWCorrector` tool, which gives an event-by-event EW k-factor (k_{EW}) that is finely binned in the Mandelstam variables s and t, calculated from the MC generator level kinematics of the initial state quarks. The calculation uses the narrow width approximation, so it should only be used when the bosons are on-shell. A systematic uncertainty is applied when at least one of the bosons are off-shell (defined when its mass is outside of a 25 GeVmass window from m_W). Events that are beyond the kinematically allowed regions ($\sqrt{s} > 2m_W$) of the calculation will be assigned $k_{EW} = 1$ (no correction applied). No systematic uncertainty is assigned for events where no correction is applied. The calculation assumes a factorizing ansatz such that the electroweak corrections are valid if the corrections from QCD are small. The aplanarity parameter, ρ, is found to be correlated with large QCD effects (See Figure 8 in Ref. [83]).

$$\rho = \frac{|\sum_i \vec{\ell}_{i,T} + \vec{p}_{T,miss}|}{\sum_i |\ell_{i,T}| + |p_{T,miss}|} \tag{109}$$

where $\vec{\ell}_{i,T}$ is the transverse momentum of the i-th lepton and $i = 1, 2$ for WW production and $\vec{p}_{T,miss}$ is the transverse momentum of the neutrinos from WW production. A systematic uncertainty the size of the correction is also assigned for events with a large QCD effect, when $\rho > 0.3$. This only affects 1-2% of the events after final selection. The size of the EW correction and its uncertainty as a function of leading lepton $p_{\mathrm{T}}$is given in Table 36.

Currently only the Standard Model EW corrections are available, so that the interplay between EW corrections and anomalous couplings is not known. In the effective field theory interpretation of anomalous couplings, the anomalous parameters arise from higher order operators that are suppressed by factors of $1/\Lambda^2$. Electroweak corrections are NLO corrections, so they are loop suppressed. The mixed electroweak corrections with anomalous couplings will be doubly suppressed. To a first approximation, these mixed terms can be

Leading lepton p_{T}[GeV]	25-75	75-150	150-250	250-350	350-1000
k_{EW}	$< 1\%$	-4%	-10%	-16%	-24%
δk_{EW}	0.1%	0.4%	1.7%	4.0%	7.1%

Table 36: Size of electroweak correction, k_{EW} and its systematic uncertainty (δk_{EW}) as a function of leading lepton p_{T}bins in GeV.

ignored, so that the dominant contributions will be the pure SM contribution, corrections to the SM part from EW corrections, and deviations from anomalous couplings. In the study of anomalous couplings, the EW corrections are applied to the SM only term (w_0 in Equation 97) and ignored in all other terms. The electroweak k-factors have been applied to our nominal Powheg+Pythia $qq \rightarrow WW$ samples. The relative corrections are then applied to the MC@NLO $qq \rightarrow WW$ with anomalous coupling weights. No corrections are applied to gluon initiated WW production.

4.4 Optimization

4.4.1 Binning optimisation

The effect of anomalous couplings can be seen at high leading lepton p_T (Figure 35). Most of the events fall in the low p_T region, but it is the high p_T region that gives the most discriminating power between Standard Model and anomalous couplings. More stringent limits on anomalous couplings can be placed by effectively binning the leading lepton p_T distribution such that it exploits the changes in the high p_T tails in the presence of non-zero anomalous couplings. Figure 37 shows the large deviations from the SM prediction from anomalous couplings in the high p_{T}region. Expected limits are calculated with various bin boundaries to find the optimal binning.

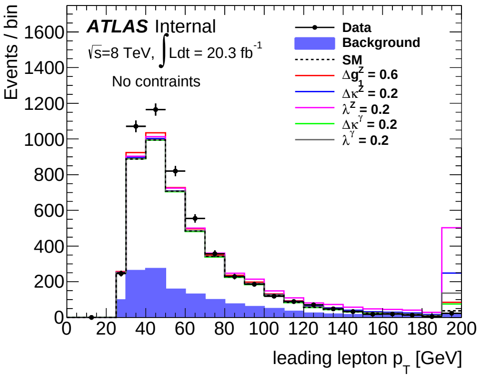

Figure 37: Leading lepton p_{T}distribution with various aTGC parameters. The largest deviations from the SM prediction is in the high p_{T}tails of the distribution. The last bin is an overflow bin.

The bin optimisation procedure is as follows. First, a single bin in leading lepton p_T is considered (25 GeV - 1000 TeV) and the expected limits are calculated for each constraint scenario and each coupling parameter. Then an additional bin boundary is added which splits the single inclusive bin into two bins. The bin boundary that gives the most stringent limits on the coupling parameters, while considering all scenarios, is taken and the single bin is split at the optimised bin boundary. The process is repeated iteratively such that each bin is considered for splitting until the limits differ by less than 1%. The optimum binning in leading lepton p_T is [25, 75, 150, 250, 350, 1000] GeV.

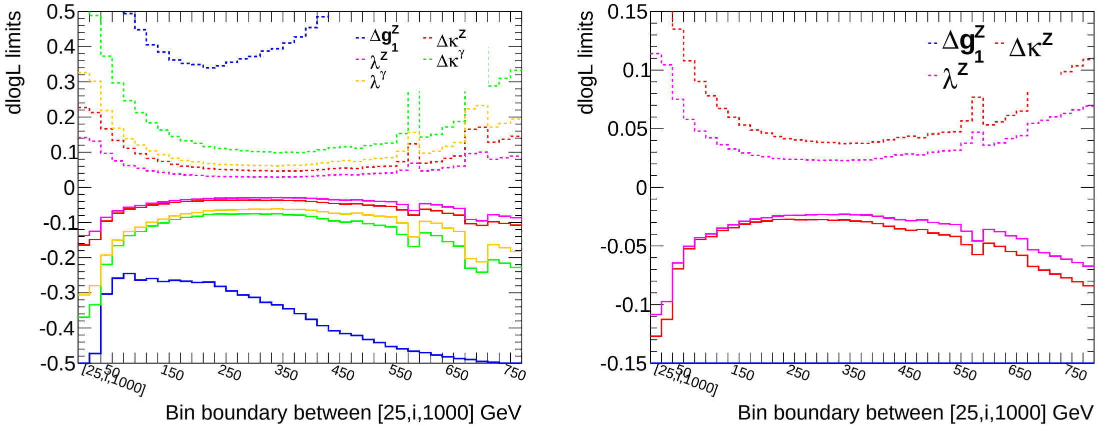

(a) No correlation (b) Equal Couplings

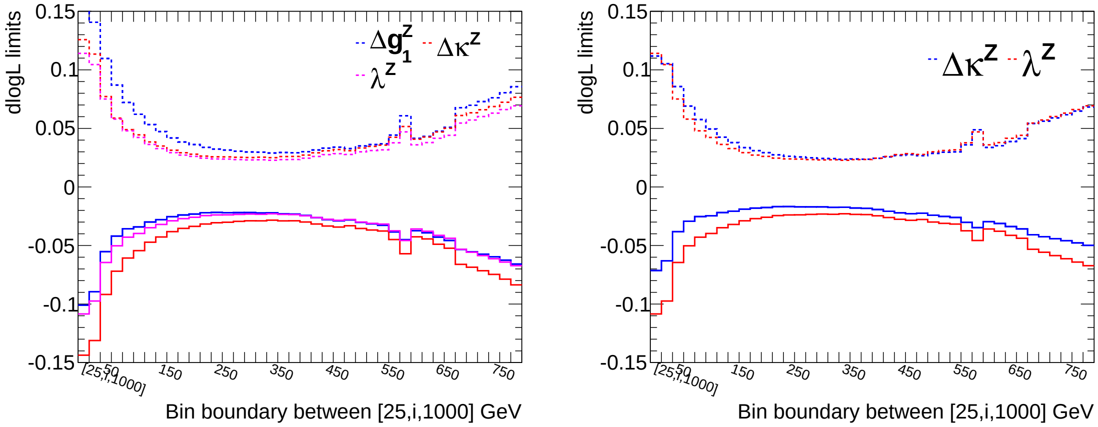

(c) LEP (d) HISZ

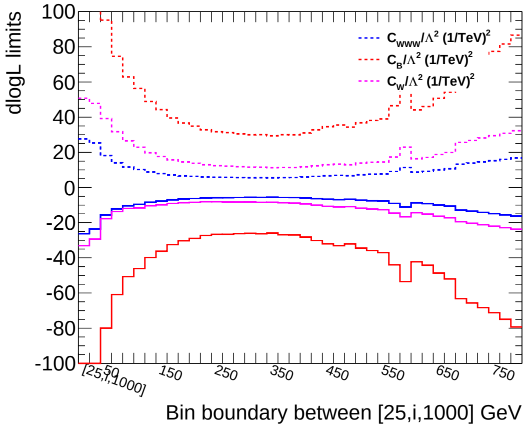

(e) EFT

Figure 38: 95% confidence intervals as a function of bin boundary assuming various constraint scenarios on (a-d) anomalous coupling parameters with no form factor and (e) effective field theory coupling parameters. The first bin gives the one bin (25 GeV - 1 TeV) confidence interval (ie: no additional bin boundary). The rest of the bin adds an additional bin boundary between 25 GeV and 1 TeV in leading lepton p_T as given by the x-axis label.

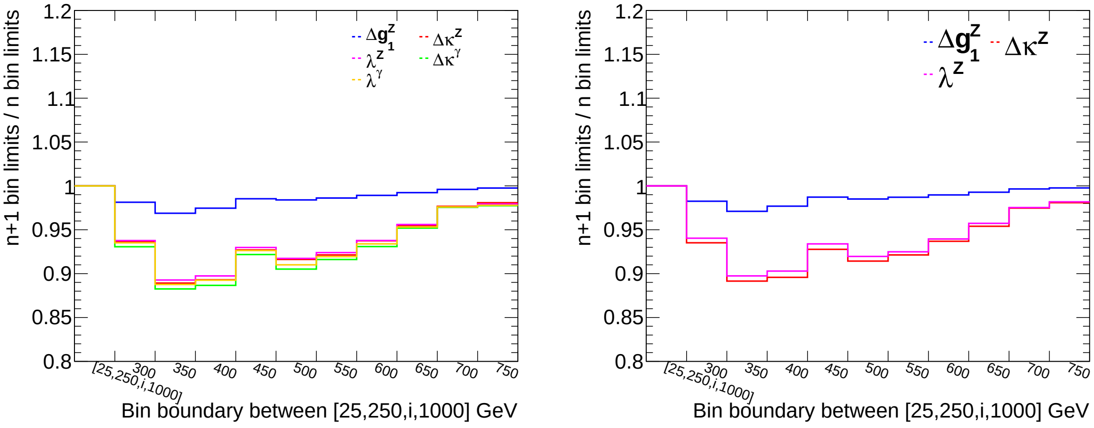

(a) No correlation (b) Equal Couplings

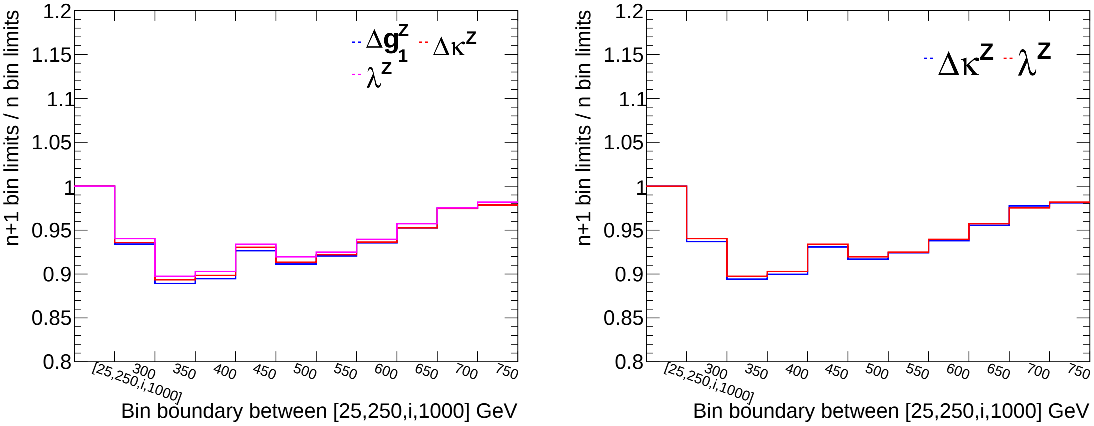

(c) LEP (d) HISZ

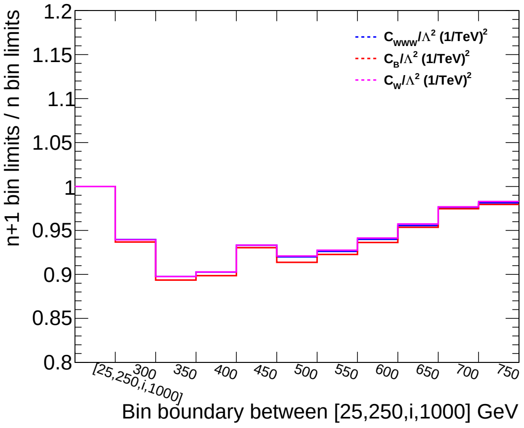

(e) EFT

Figure 39: 95% confidence intervals as a function of bin boundary assuming various constraint scenarios on (a-d) anomalous coupling parameters with no form factor and (e) effective field theory coupling parameters. The first bin gives the two bin (25, 250, 1000 GeV) confidence interval (ie: no additional bin boundary). The rest of the bin adds an additional bin boundary between 250 GeV and 1 TeV in leading lepton p_T as given by the x-axis label.

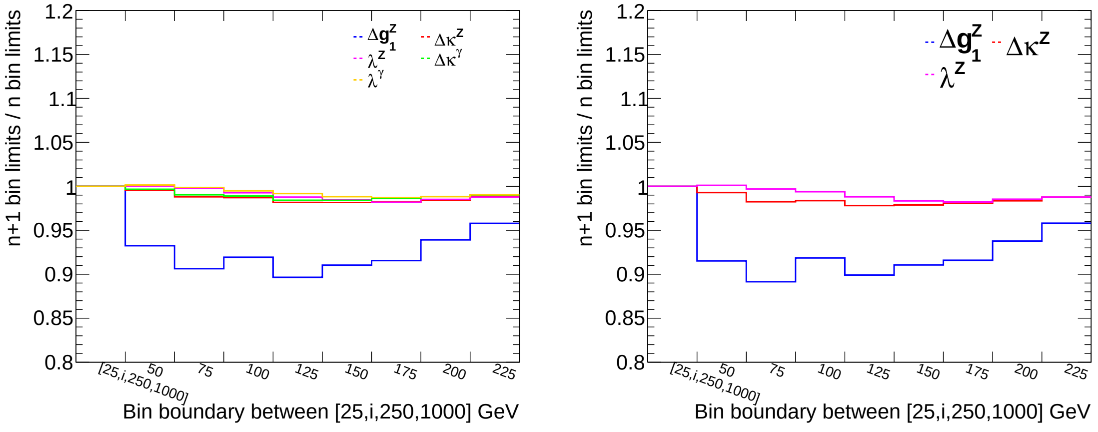

(a) No correlation (b) Equal Couplings

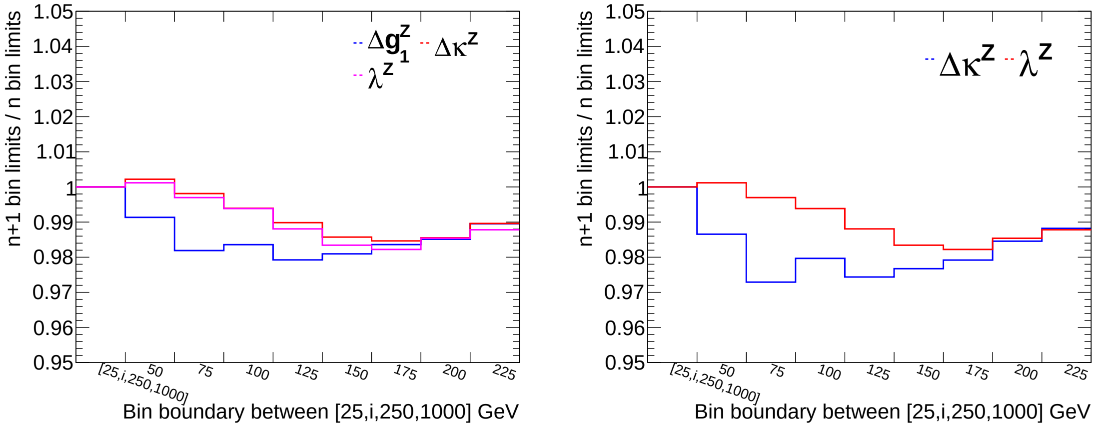

(c) LEP (d) HISZ

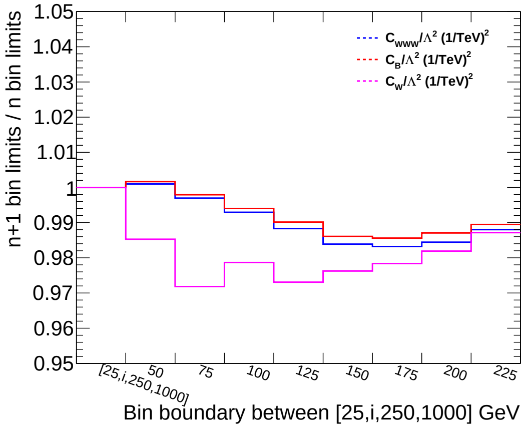

(e) EFT

Figure 40: 95% confidence intervals as a function of bin boundary assuming various constraint scenarios on (a-d) anomalous coupling parameters with no form factor and (e) effective field theory coupling parameters. The first bin gives the two bin (25, 250, 1000 GeV) confidence interval (ie: no additional bin boundary). The rest of the bin adds an additional bin boundary between 25 GeV and 250 GeV in leading lepton p_T as given by the x-axis label.

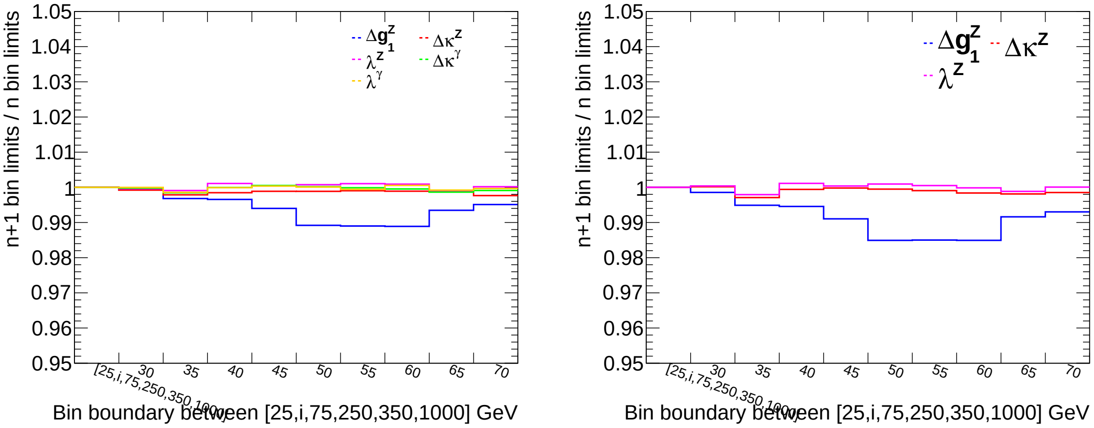

(a) No correlation (b) Equal Couplings

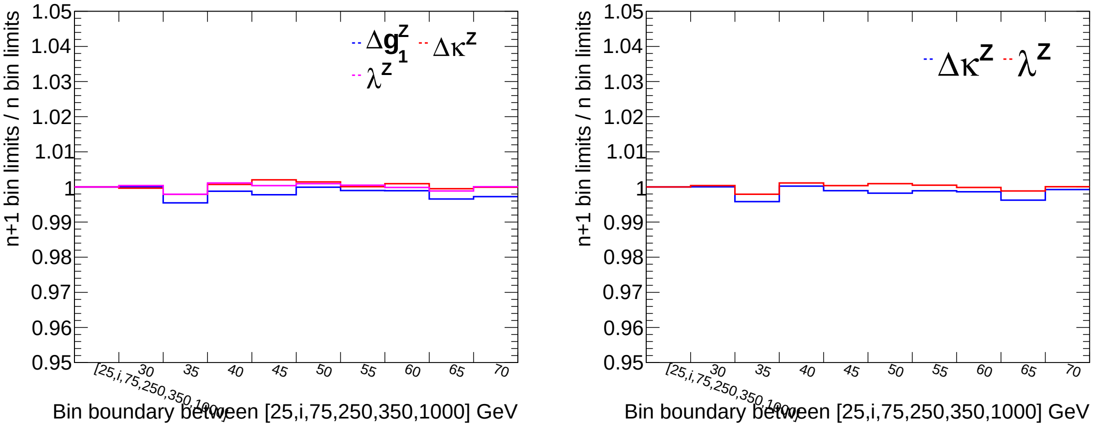

(c) LEP (d) HISZ

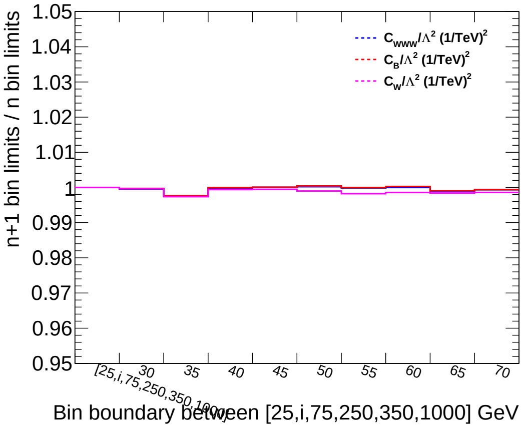

(e) EFT

Figure 41: 95% confidence intervals as a function of bin boundary assuming various constraint scenarios on (a-d) anomalous coupling parameters with no form factor and (e) effective field theory coupling parameters. The first bin gives the four bin (25, 75, 250, 350, 1000 GeV) confidence interval (ie: no additional bin boundary). The rest of the bin adds an additional bin boundary between 25 and 75 GeV in leading lepton p_T as given by the x-axis label.

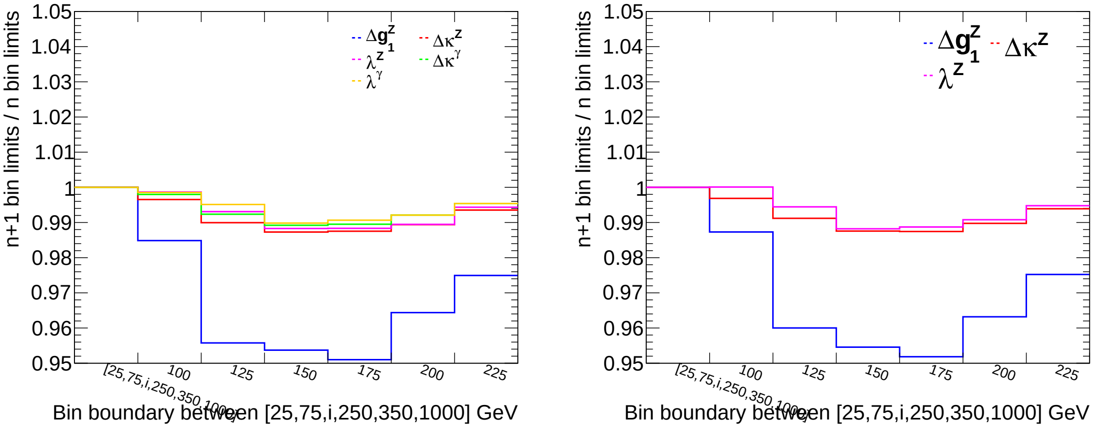

(a) No correlation

(b) Equal Couplings

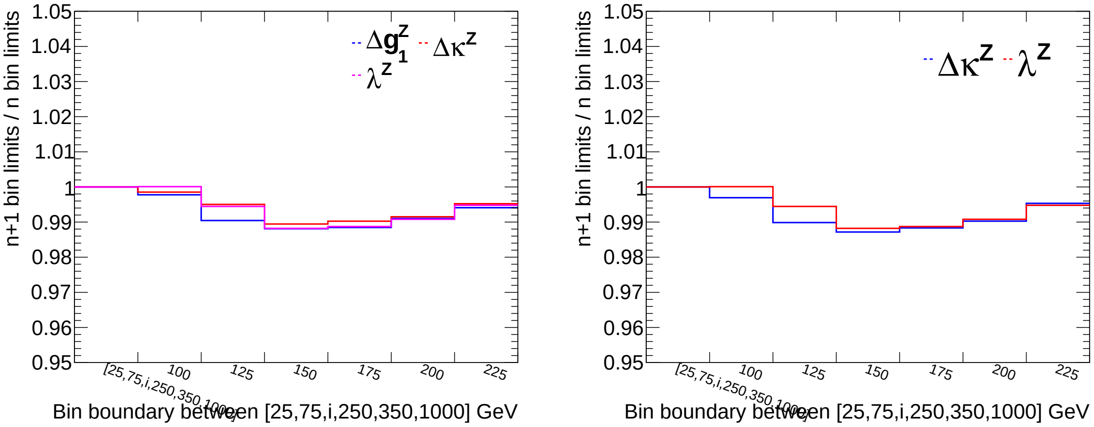

(c) LEP

(d) HISZ

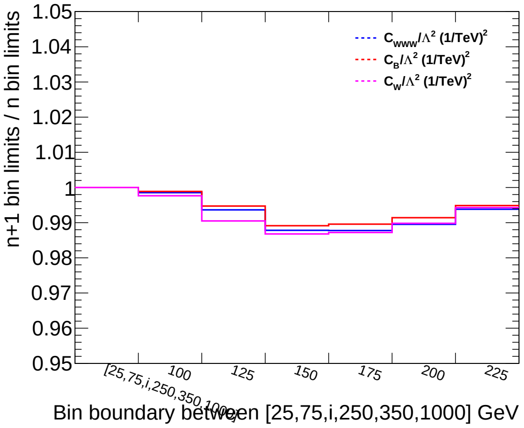

(e) EFT

Figure 42: 95% confidence intervals as a function of bin boundary assuming various constraint scenarios on (a-d) anomalous coupling parameters with no form factor and (e) effective field theory coupling parameters. The first bin gives the four bin (25, 75, 250, 350, 1000 GeV) confidence interval (ie: no additional bin boundary). The rest of the bin adds an additional bin boundary between 75 and 250 GeV in leading lepton p_T as given by the x-axis label.

4.4.2 Variable choice optimization

In the choice of variable optimization, the following variables have been considered: dilepton $p_{\mathrm{T}}(\mathrm{p}_{\mathrm{T,ll}})$, transverse mass ($\mathrm{M}_{\mathrm{T}}$), dilepton mass ($\mathrm{M}_{\mathrm{ll}}$) and leading lepton p_{T}. The binning optimization is done independently for each variable. The binning procedure is the same as before, but in generally coarser step sizes. The bin optimization steps are terminated when the gain from adding an additional bin boundary is smaller than the difference between the limits between the variables. The optimized binning for this study was found to be:

Leading lepton [0, 50, 150, 250, 350, 1000] GeV

Mll [0, 175, 300, 550, 700, 1000] GeV

MT [0, 250, 325, 525, 800, 1000] GeV

Ptll [0, 125, 225, 300, 1000] GeV

The 95% confidence level upper and lower limits for the four variables are given in Table 37. The most stringent limits are found with leading lepton p_{T}. Transverse mass and dilepton p_{T}give 20% worse limits with respect to leading lepton p_{T}, while dilepton mass gave 40-80% worse limits.

Lower limits	$\mathrm{p}_{\mathrm{T,ll}}$	M_{T}	M_{ll}	lep1 p_{T}
Δg_1^Z	-0.282	-0.233	-0.345	-0.226
$\Delta\kappa^Z$	-0.038	-0.036	-0.055	-0.031
λ^Z	-0.032	-0.031	-0.044	-0.026
$\Delta\kappa^\gamma$	-0.081	-0.076	-0.117	-0.064
λ^γ	-0.067	-0.067	-0.095	-0.056

Upper limits	$\mathrm{p}_{\mathrm{T,ll}}$	M_{T}	M_{ll}	lep1 p_{T}
Δg_1^Z	0.37	0.329	0.435	0.309
$\Delta\kappa^Z$	0.053	0.053	0.070	0.043
λ^Z	0.032	0.031	0.044	0.026
$\Delta\kappa^\gamma$	0.114	0.117	0.150	0.093
λ^γ	0.068	0.068	0.094	0.056

Table 37: ATGC results with different variables. Upper and lower bounds on the 95% confidence level limits with 5 bins optimized for each variable: $\mathrm{p}_{\mathrm{T,ll}}$, M_{T}, M_{ll}, leading lepton $p_{\mathrm{T}}$are shown. Leading lepton p_{T}gives the most stringent limits on the anomalous couplings for the variables tested. The results obtained for optimization studies do not include the latest systematic uncertainties (in particular the large theoretical uncertainties on the signal) so the y will not match the tables in the final results.

4.4.3 eμ channel vs inclusive channel

As shown in the results for the cross section combination, the combined results is heavily dominated by the results in the $e\mu$ channel. For the extraction of limits on anomalous triple gauge couplings and unfolded results, obtaining binned systematic uncertainties on the data-driven backgrounds in the same flavor channels is quite challenging. Also the same flavor channels have far fewer events and a much higher statistical uncertainty than the $e\mu$ channel. For these reasons, only the $e\mu$ channel is used. To estimate the loss from using the full inclusive results, the expected and observed limits were computed with just the $e\mu$ channel and also with all three channels. The systematic uncertainties for the Drell-Yan and top backgrounds are assumed to be flat for this study. The results from Table 38 show that the expected limits would be better by at most 8-15% if all channels are included.

Scenario	Parameter	Inclusive	em
No scenario	Δg_1^Z	[-0.189 , 0.274]	[-0.209 , 0.302]
	$\Delta\kappa^Z$	[-0.026 , 0.038]	[-0.029 , 0.042]
	λ^Z	[-0.022 , 0.022]	[-0.025 , 0.025]
	$\Delta\kappa^\gamma$	[-0.054 , 0.081]	[-0.061 , 0.090]
	λ^γ	[-0.047 , 0.048]	[-0.054 , 0.054]
LEP	Δg_1^Z	[-0.016 , 0.024]	[-0.018 , 0.026]
	$\Delta\kappa^Z$	[-0.023 , 0.019]	[-0.026 , 0.021]
	λ^Z	[-0.018 , 0.018]	[-0.020 , 0.020]
HISZ	$\Delta\kappa^Z$	[-0.012 , 0.019]	[-0.014 , 0.021]
	λ^Z	[-0.018 , 0.018]	[-0.020 , 0.020]
Equal Couplings	$\Delta\kappa^Z$	[-0.020 , 0.031]	[-0.022 , 0.034]
	λ^Z	[-0.018 , 0.018]	[-0.020 , 0.020]
EFT	C_{WWW}/Λ^2	[-4.35 , 4.34]	[-4.88 , 4.88]
	C_B/Λ^2	[-19.9 , 23.9]	[-22.3 , 26.5]
	C_W/Λ^2	[-5.83 , 9.26]	[-6.64 , 10.21]

Table 38: 95% confidence level expected limits on anomalous coupling parameters assuming no scenario, LEP, HISZ, or Equal couplings scenarios, and Effective Field Theory (EFT) with leading lepton p_{T}bins of [25,75,150,250,350,1000] GeVfor the em channel only (right) and inclusively (ee+mm+em, left).

4.4.4 Removal of low p_{T}bins

The 95% confidence level limits for the anomalous coupling parameters using the fully optimized leading lepton p_{T}binning of [25,75,150,250,350,1000] GeVresult in p-values at the level of 0.1% for fitting. This is due to a poor fit in the low leading lepton p_{T}region where there is an excess in data in the bulk of the distribution. One possible approach is to remove the first two low p_{T}bins in the fits for anomalous coupling limits. This is not expected to decrease the sensitivity significantly because the effect of anomalous coupling lies mostly in the high p_{T}tails of the distribution. A comparison of the expected limits between a 5-bin results and 3-bin results show that there is a difference of 7-12% after removing the first two bins, with only one exception. In the case of Δg_1^Z in the no constraint scenario, the 3-bin confidence interval limit is larger by 22.5%. The p-value for the 3-bin fits is at the level of 2-3%.

Several alternatives have been considered but not applied. Another solution is to scale the WW signal by a scale factor such that it matches the data yield. Although this will fix the apparent discrepancy between data and MC predictions, this biases the measurement in anomalous coupling limits. The interpretation of the results can be misleading if in reality the excess is explained by non-SM coupling parameters which is removed by the scaling factor. In other words, the use of a scale factor can potentially hide new physics. Also, a scale factor of 1.21 is not theoretically justified.

Another approach is to incorporate recent higher order corrections to WW production. Full NNLO results [53] for inclusive WW production predict a 10% increase with respect to NLO predictions. The effect on this analysis will be smaller than that since partial NNLO results are already included for $gg \to WW$. The current inclusive results may not be appropriate to use for this analysis. Ideally, a 0-jet cross section with binned k-factors in leading lepton $p_{\mathrm{T}}$is most appropriate, but currently these results are not available.

4.5 Results

The final results are obtained using events in the $e\mu$ channel only with three bins in leading lepton p_{T}using the Feldman Cousins frequentist confidence intervals. Table 39 gives the 1-dimensional expected and observed 95% confidence level limits on anomalous coupling parameters (with no form factors applied) with the no scenario, LEP, HISZ, or Equal couplings scenario and also under the effective field theory scenario. Limits on anomalous coupling parameters with a form factor of 7 TeVare given in Table 40. The 7 TeVform factor is about the upper bound for most aTGCs parameters if the unitary is required, therefore the limits set with 7 TeVform factor give a baisc idea what are the best limits while still preserving the unitary. Expected and observed limits with additional form factors are given in Tables 41 and 42 and Figure 43.

The 2-dimensional limits are calculated by fitting two anomalous coupling parameters and setting all others to zero. The 2D 95% confidence level contours under the LEP constraints and effective field theory framework are shown in Figure 44 and Figure 46 respectively.

Scenario	Parameter	Expected	Observed
No scenario	Δg_1^Z	[-0.498,0.524]	[-0.215,0.267]
	$\Delta\kappa^Z$	[-0.053,0.059]	[-0.027,0.042]
	λ^Z	[-0.039,0.038]	[-0.024,0.024]
	$\Delta\kappa^\gamma$	[-0.109,0.124]	[-0.054,0.092]
	λ^γ	[-0.081,0.082]	[-0.051,0.052]
LEP	Δg_1^Z	[-0.033,0.037]	[-0.016,0.027]
	$\Delta\kappa^Z$	[-0.037,0.035]	[-0.025,0.020]
	λ^Z	[-0.031,0.031]	[-0.019,0.019]
HISZ	$\Delta\kappa^Z$	[-0.026,0.030]	[-0.012,0.022]
	λ^Z	[-0.031,0.031]	[-0.019,0.019]
Equal Couplings	$\Delta\kappa^Z$	[-0.041,0.048]	[-0.020,0.035]
	λ^Z	[-0.030,0.030]	[-0.019,0.019]
EFT	C_{WWW}/Λ^2	[-7.62,7.38]	[-4.61,4.60]
	C_B/Λ^2	[-35.8,38.4]	[-20.9,26.3]
	C_W/Λ^2	[-12.58,14.32]	[-5.87,10.54]

Table 39: 95% confidence level expected and observed limits on anomalous coupling parameters assuming no scenario, LEP, HISZ, or Equal couplings scenarios, and Effective Field Theory (EFT) with leading lepton p_{T}bins of [150,250,350,1000] GeVin the $e\mu$ channel. The results are shown with $\Lambda = \infty$ for scenarios under the anomalous couplings framework. Electroweak corrections have been applied to the SM only term.

Scenario	Parameter	Expected	Observed
No scenario	Δg_1^Z	[-0.519,0.563]	[-0.226,0.279]
	$\Delta\kappa^Z$	[-0.057,0.064]	[-0.028,0.045]
	λ^Z	[-0.043,0.042]	[-0.026,0.025]
	$\Delta\kappa^\gamma$	[-0.118,0.136]	[-0.057,0.099]
	λ^γ	[-0.088,0.089]	[-0.055,0.055]
LEP	Δg_1^Z	[-0.035,0.041]	[-0.017,0.029]
	$\Delta\kappa^Z$	[-0.041,0.038]	[-0.027,0.021]
	λ^Z	[-0.033,0.033]	[-0.020,0.020]
HISZ	$\Delta\kappa^Z$	[-0.028,0.033]	[-0.013,0.024]
	λ^Z	[-0.033,0.034]	[-0.020,0.020]
Equal Couplings	$\Delta\kappa^Z$	[-0.045,0.052]	[-0.021,0.037]
	λ^Z	[-0.034,0.033]	[-0.020,0.020]

Table 40: 95% confidence level expected and observed limits on anomalous coupling parameters assuming no scenario, LEP, HISZ, or Equal couplings scenarios with leading lepton p_{T}bins of [150,250,350,1000] GeVin the $e\mu$ channel. The results are shown with $\Lambda = 7$ TeV for scenarios under the anomalous couplings framework. Electroweak corrections have been applied to the SM only term.

FF (TeV)	Δg_1^Z		$\Delta\kappa^Z$		λ^Z		$\Delta\kappa^\gamma$		λ^γ	
2	-0.728	0.836	-0.100	0.115	-0.076	0.076	-0.213	0.247	-0.158	0.159
3	-0.615	0.686	-0.074	0.085	-0.057	0.055	-0.156	0.182	-0.117	0.115
4	-0.561	0.617	-0.066	0.074	-0.049	0.048	-0.136	0.157	-0.101	0.102
5	-0.540	0.580	-0.061	0.069	-0.046	0.045	-0.126	0.147	-0.096	0.093
6	-0.535	0.575	-0.059	0.066	-0.044	0.043	-0.122	0.140	-0.091	0.089
7	-0.519	0.563	-0.057	0.064	-0.043	0.042	-0.118	0.136	-0.088	0.089
8	-0.515	0.541	-0.056	0.063	-0.042	0.041	-0.118	0.132	-0.084	0.084
10	-0.503	0.535	-0.055	0.061	-0.041	0.041	-0.113	0.131	-0.084	0.084
100	-0.498	0.524	-0.053	0.059	-0.039	0.038	-0.109	0.124	-0.081	0.082

Table 41: 95% confidence level expected limits on anomalous coupling parameters with no constraints with leading lepton p_{T}bins of [150,250,350,1000] GeVin the $e\mu$ channel with for different form factors (FF). The form factors are given in the first column in units of TeV. Here, $\Lambda = 100$ TeV is sufficiently high that it can be considered as $\Lambda = \infty$ or not applying a form factor. Electroweak corrections have been applied to the SM only term.

FF (TeV)	Δg_1^Z		$\Delta\kappa^Z$		λ^Z		$\Delta\kappa^\gamma$		λ^γ	
2	-0.298	0.390	-0.042	0.070	-0.038	0.039	-0.083	0.157	-0.083	0.085
3	-0.247	0.328	-0.034	0.056	-0.031	0.031	-0.068	0.121	-0.066	0.065
4	-0.237	0.295	-0.031	0.050	-0.028	0.028	-0.063	0.110	-0.060	0.061
5	-0.232	0.285	-0.029	0.048	-0.027	0.027	-0.059	0.105	-0.057	0.058
6	-0.228	0.283	-0.028	0.046	-0.026	0.026	-0.058	0.101	-0.055	0.056
7	-0.226	0.279	-0.028	0.045	-0.026	0.025	-0.057	0.099	-0.055	0.055
8	-0.219	0.276	-0.027	0.044	-0.025	0.025	-0.056	0.098	-0.054	0.054
10	-0.215	0.274	-0.027	0.044	-0.025	0.025	-0.056	0.094	-0.052	0.054
100	-0.215	0.267	-0.027	0.042	-0.024	0.024	-0.054	0.092	-0.051	0.052

Table 42: 95% confidence level observed limits on anomalous coupling parameters with no constraints with leading lepton p_{T}bins of [150,250,350,1000] GeVin the $e\mu$ channel with for different form factors (FF). The form factors are given in the first column in units of TeV. Here, $\Lambda = 100$ TeV is sufficiently high that it can be considered as $\Lambda = \infty$ or not applying a form factor. Electroweak corrections have been applied to the SM only term.

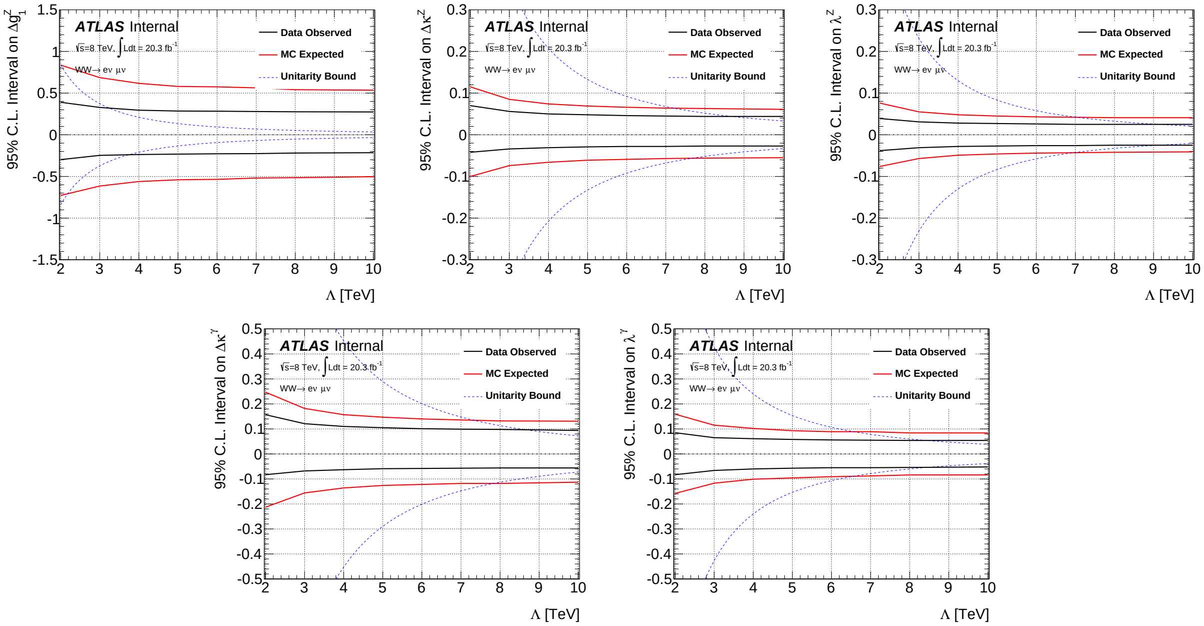

Figure 43: 95% confidence level limits with form factors with $\Lambda = 2$ to $\Lambda = 10$ TeV. The unitarity bounds (Equation 40) are given by the dashed blue lines.

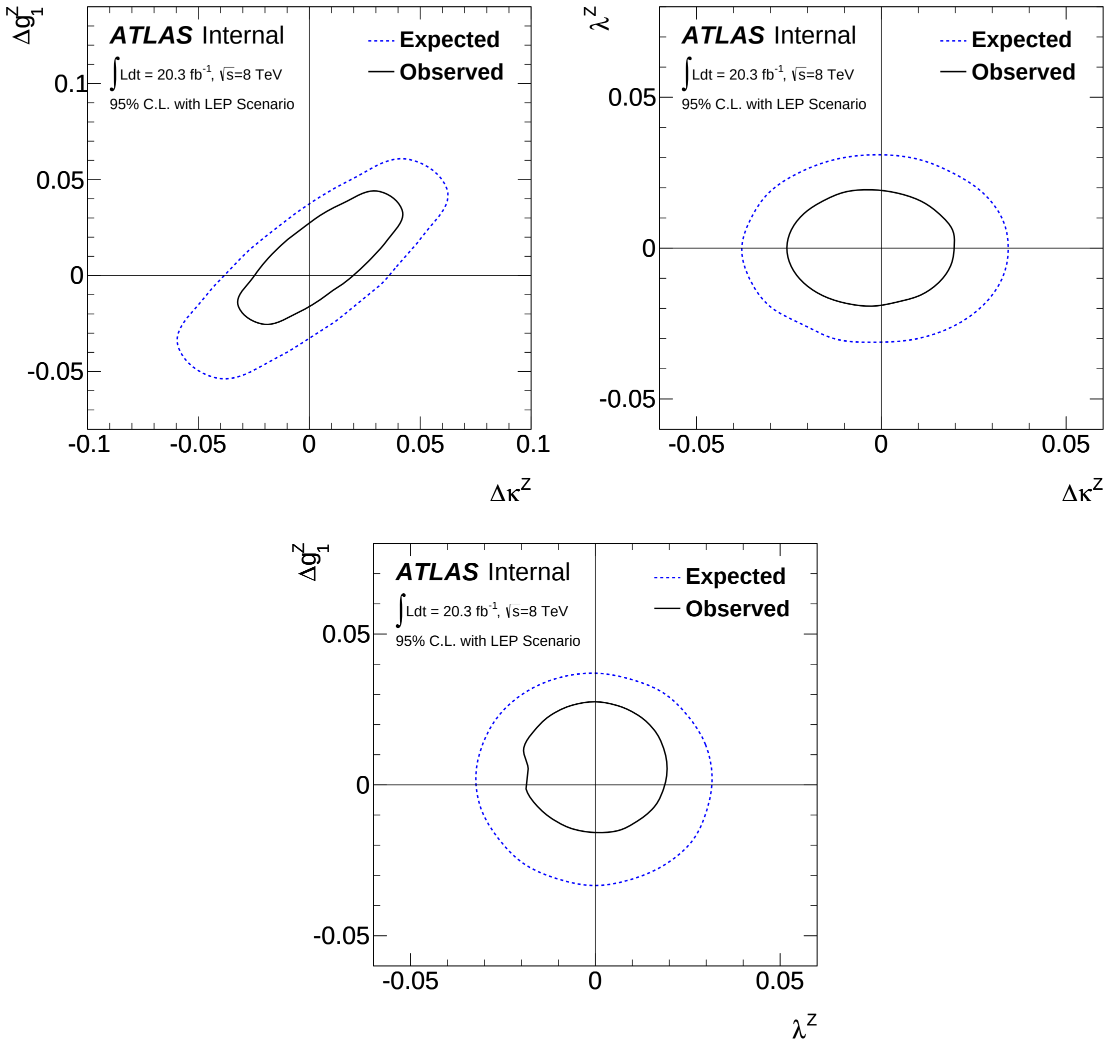

Figure 44: 2-dimensional 95% confidence level contours assuming the LEP constraint scenario. Except for the two anomalous coupling parameters under study, all others are set to zero.

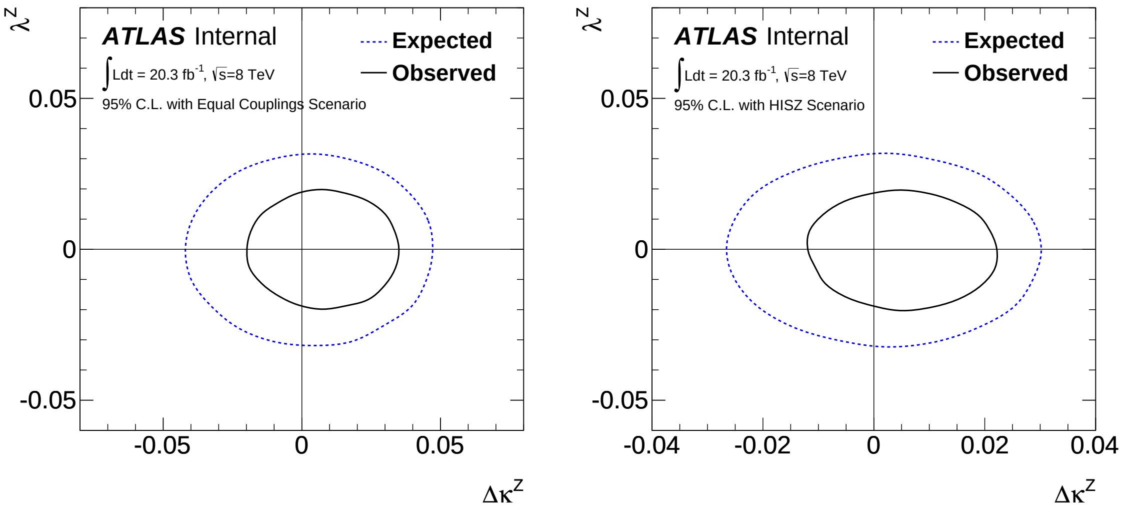

Figure 45: 2-dimensional 95% confidence level contours assuming the Equal couplings scenario (left) and the HISZ scenario (right).

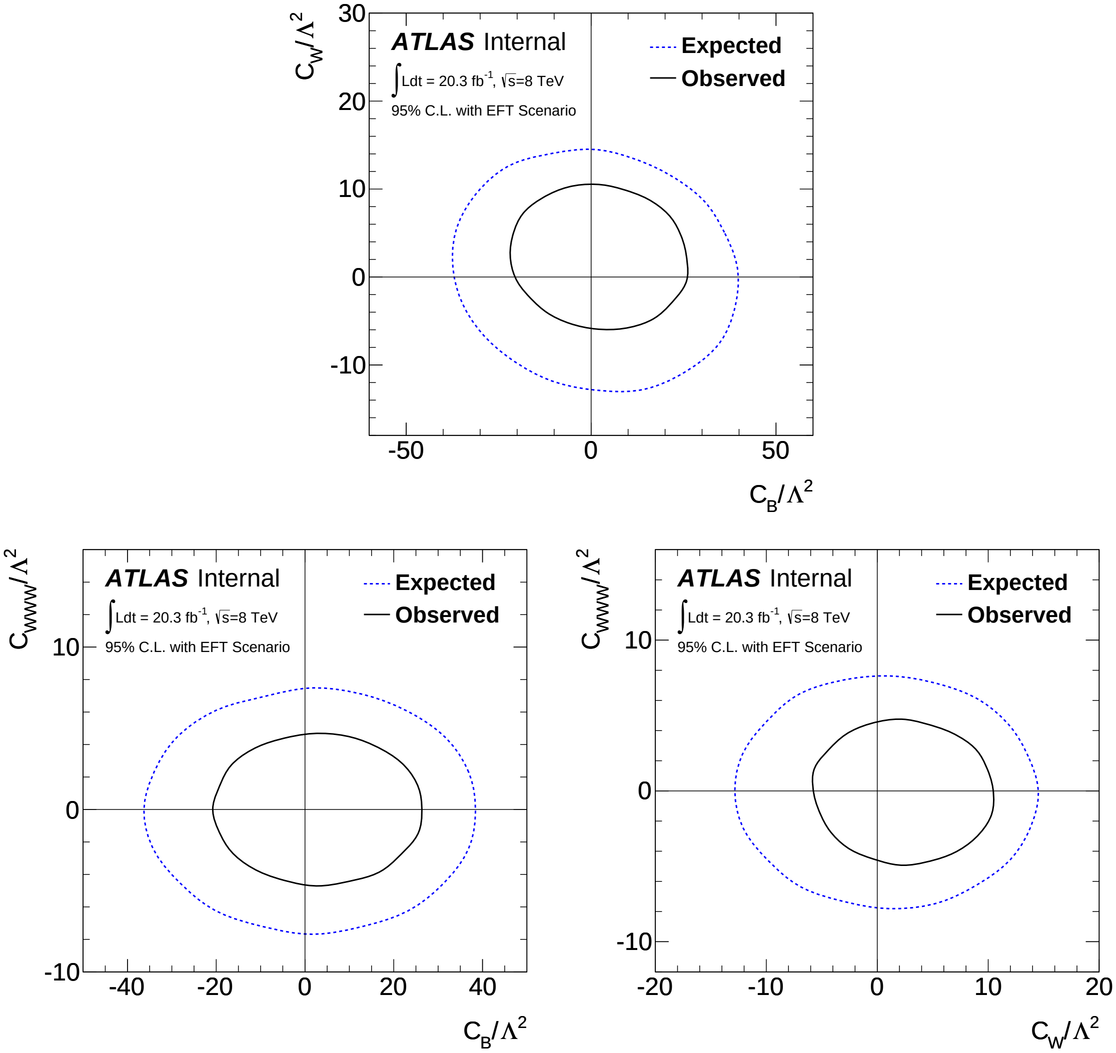

Figure 46: 2-dimensional 95% confidence level contours for the coupling parameters under the effective field theory framework. Except for the two effective field theory couplings under study, the third is set to zero.

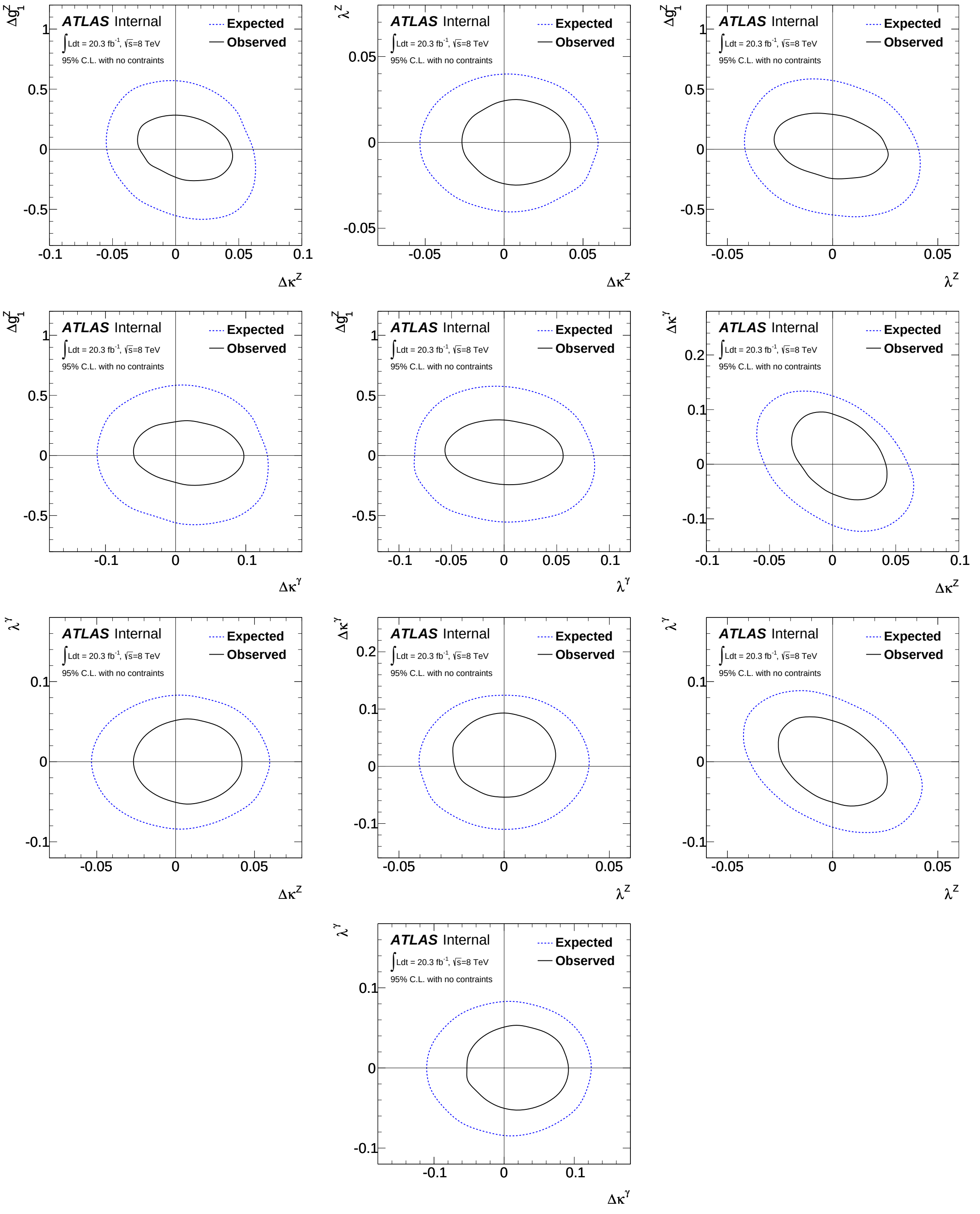

Figure 47: 2-dimensional 95% confidence level contours no constraints between anomalous coupling parameters. Except for the two anomalous coupling parameters under study, all others are set to zero.

5 Conclusions

The WW production cross section is measured with p-p collisions at $\sqrt{s} = 8$ TeV with 20.3 fb^{-1} of data collected by the ATLAS detector at the LHC. The measurement is conducted in three leptonic final states: ee, $\mu\mu$, and $e\mu$, all accompanied by $E_{\mathrm{T}}^{\mathrm{miss}}$. The measured W^+W^- production total cross section is

$$\sigma_{\mathrm{WW}}^{\mathrm{total}} = 71.0^{+1.1}_{-1.1}(\mathrm{stat})^{+3.2}_{-3.1}(\mathrm{theory})^{+4.8}_{-3.9}(\mathrm{exp})^{+2.1}_{-2.0}(\mathrm{lumi})\ \mathrm{pb} \tag{110}$$

For comparison, the theoretical cross section prediction at NNLO is

$$\sigma_{\mathrm{WW}}^{\mathrm{theory}} = 63.2^{+1.6}_{-1.4}(\mathrm{scale}) \pm 1.2(\mathrm{PDF})\ \mathrm{pb} \tag{111}$$

The measured cross section and the Standard Model prediction at NNLO show good agreement. Fiducial cross sections for each channel have also been reported and are also in good agreement with the Standard Model prediction. Several kinematic distributions have been unfolded to correct for detector acceptance and smearing effects. These distributions can be used to constrain parameters in new physics models.

Limits on anomalous WWZ and WWγ triple gauge couplings and coupling parameters in the effective field theory model have been determined using the high leading lepton p_{T}distribution in the $e\mu$ channel. All parameters are found to be consistent with the Standard Model values, and the constraints the anomalous coupling parameters have been improved with respect to the previous 7 TeVWW analysis.

References

[1] M. K. Gaillard, P. D. Grannis, and F. J. Sciulli, *The Standard model of particle physics*, Rev.Mod.Phys. **71** (1999) S96–S111, `arXiv:hep-ph/9812285 [hep-ph]`.

[2] D. Curtin, P. Jaiswal, and P. Meade, *Charginos Hiding In Plain Sight*, Phys.Rev. **D87** (2013) no. 3, 031701, `arXiv:1206.6888 [hep-ph]`.

[3] B. Feigl, H. Rzehak, and D. Zeppenfeld, *New Physics Backgrounds to the $H \to WW$ Search at the LHC?*, Phys.Lett. **B717** (2012) 390–395, `arXiv:1205.3468 [hep-ph]`.

[4] K. Rolbiecki and K. Sakurai, *Light stops emerging in WW cross section measurements?*, JHEP **1309** (2013) 004, `arXiv:1303.5696 [hep-ph]`.

[5] H. Aihara, T. Barklow, U. Baur, J. Busenitz, S. Errede, et al., *Anomalous gauge boson interactions*, `arXiv:hep-ph/9503425 [hep-ph]`.

[6] C. Degrande, N. Greiner, W. Kilian, O. Mattelaer, H. Mebane, T. Stelzer, S. Willenbrock, and C. Zhang, *Effective Field Theory: A Modern Approach to Anomalous Couplings*, Annals Phys. **335:21** (2012) , `arXiv:1205.4231 [hep-ph]`.

[7] G. Gounaris, J. Kneur, D. Zeppenfeld, Z. Ajaltouni, A. Arhrib, et al., *Triple gauge boson couplings*, `arXiv:hep-ph/9601233 [hep-ph]`.

[8] K. Hagiwara, S. Ishihara, R. Szalapski, and D. Zeppenfeld, *Low energy effects of new interactions in the electroweak boson sector*, Phys. Rev. D **48** (Sep, 1993) 2182–2203. `http://link.aps.org/doi/10.1103/PhysRevD.48.2182`.

[9] ATLAS Collaboration, *Observation of a new particle in the search for the Standard Model Higgs boson with the ATLAS detector at the LHC*, Phys.Lett. **B716** (2012) 1–29, `arXiv:1207.7214 [hep-ex]`.

[10] CMS Collaboration, *Observation of a new boson at a mass of 125 GeV with the CMS experiment at the LHC*, Phys.Lett. **B716** (2012) 30–61, `arXiv:1207.7235 [hep-ex]`.

[11] B. Jager, C. Oleari, and D. Zeppenfeld, *Next-to-leading order QCD corrections to W+W- production via vector-boson fusion*, JHEP **0607** (2006) 015, `arXiv:hep-ph/0603177 [hep-ph]`.

[12] A. Alboteanu, W. Kilian, and J. Reuter, *Resonances and Unitarity in Weak Boson Scattering at the LHC*, JHEP **0811** (2008) 010, `arXiv:0806.4145 [hep-ph]`.

[13] J. Baglio, L. D. Ninh, and M. M. Weber, *Massive gauge boson pair production at the LHC: a next-to-leading order story*, Phys.Rev. **D88** (2013) 113005, `arXiv:1307.4331`.

[14] A. Bierweiler, T. Kasprzik, and J. H. Kuhn, *Vector-boson pair production at the LHC to $\mathcal{O}(\alpha^3)$ accuracy*, JHEP **1312** (2013) 071, `arXiv:1305.5402 [hep-ph]`.

[15] M. Billoni, S. Dittmaier, B. Jger, and C. Speckner, *Next-to-leading order electroweak corrections to $pp \to WW \to 4$ leptons at the LHC in double-pole approximation*, JHEP **1312** (2013) 043, `arXiv:1310.1564 [hep-ph]`.

[16] ATLAS Collaboration, *Measurement of W^+W^- production in pp collisions at $\sqrt{s} = 7$ TeV on anomalous WWZ and WWγ couplings*, Phys.Rev. **D87** (2013) no. 11, 112001, `arXiv:1210.2979 [hep-ex]`.

[17] CMS Collaboration, *Measurement of the W^+W^- Cross section in pp Collisions at $\sqrt{s} = 7$ TeV and Limits on Anomalous $WW\gamma$ and WWZ couplings*, Eur.Phys.J. **C73** (2013) no. 10, 2610, `arXiv:1306.1126 [hep-ex]`.

[18] P. Jaiswal and T. Okui, *An Explanation of the WW Excess at the LHC by Jet-Veto Resummation*, `arXiv:1407.4537 [hep-ph]`.

[19] P. Meade, H. Ramani, and M. Zeng, *Transverse momentum resummation effects in W^+W^- measurements*, `arXiv:1407.4481 [hep-ph]`.

[20] P. M. Nadolsky, H.-L. Lai, Q.-H. Cao, J. Huston, J. Pumplin, et al., *Implications of CTEQ global analysis for collider observables*, Phys.Rev. **D78** (2008) 013004, `arXiv:0802.0007 [hep-ph]`.

[21] A. Martin, W. Stirling, R. Thorne, and G. Watt, *Parton distributions for the LHC*, Eur.Phys.J. **C63** (2009) 189–285, `arXiv:0901.0002 [hep-ph]`.

[22] NNPDF Collaboration, R. D. Ball et al., *A Determination of parton distributions with faithful uncertainty estimation*, Nucl.Phys. **B809** (2009) 1–63, `arXiv:0808.1231 [hep-ph]`.

[23] R. D. Ball, L. Del Debbio, S. Forte, A. Guffanti, J. I. Latorre, et al., *A first unbiased global NLO determination of parton distributions and their uncertainties*, Nucl.Phys. **B838** (2010) 136–206, `arXiv:1002.4407 [hep-ph]`.

[24] T. Gleisberg, S. Hoeche, F. Krauss, M. Schonherr, S. Schumann, et al., *Event generation with SHERPA 1.1*, JHEP **0902** (2009) 007, `arXiv:0811.4622 [hep-ph]`.

[25] T. Sjostrand, S. Mrenna, and P. Z. Skands, *PYTHIA 6.4 Physics and Manual*, JHEP **0605** (2006) 026, `arXiv:hep-ph/0603175`.

[26] G. Corcella et al., *HERWIG 6.5: an event generator for Hadron Emission Reactions With Interfering Gluons (including supersymmetric processes)*, JHEP **0101** (2001) 010, `arXiv:hep-ph/0011363`.

[27] Z. Nagy, *High Precision QCD Tools for the LHC*, Presented at the SMU Seminar, 2008. `{http://www.physics.smu.edu/osg/seminars/seminar_archive/Spring2008/ZNagy.pdf}`.

[28] S. Jadach, J. H. Khn, and Z. Was, {*TAUOLA*} *- a library of Monte Carlo programs to simulate decays of polarized tau leptons*, Computer Physics Communications **64** (1991) no. 2, 275 – 299.

[29] E. Barberio, B. van Eijk, and Z. Was, *Photos a universal Monte Carlo for* {*QED*} *radiative corrections in decays*, Computer Physics Communications **66** (1991) no. 1, 115 – 128.

[30] M. L. Mangano, M. Moretti, F. Piccinini et al., *ALPGEN, a generator for hard multiparton processes in hadronic collisions*, JHEP **0307** (2003) 001.

[31] B. P. Kersevan and E. Richter-Was, *The Monte Carlo event generator AcerMC version 2.0 with interfaces to PYTHIA 6.2 and HERWIG 6.5*, `arXiv:hep-ph/0405247`.

[32] J. Alwall et al., *MadGraph/MadEvent v4: The New Web Generation*, JHEP **09** (2007) 028, `arXiv:0706.2334 [hep-ph]`.

[33] S. Frixione and B. R. Webber, *Matching NLO QCD computations and parton shower simulations*, JHEP **06** (2002) 029, `arXiv:hep-ph/0204244`.

[34] J. M. Campbell and R. K. Ellis, *An Update on vector boson pair production at hadron colliders*, Phys.Rev. **D60** (1999) 113006, `arXiv:hep-ph/9905386 [hep-ph]`.

[35] J. M. Campbell, R. K. Ellis, and C. Williams, *Vector boson pair production at the LHC*, JHEP **1107** (2011) 018, `arXiv:1105.0020 [hep-ph]`.

[36] L. Evans and P. Bryant, *LHC Machine*, Journal of Instrumentation **3** (2008) no. 08, S08001. `{http://stacks.iop.org/1748-0221/3/i=08/a=S08001}`.

[37] ATLAS Collaboration, *The ATLAS Experiment at the CERN Large Hadron Collider*, JINST **3** (2008) S08003.

[38] J. Pequenao, *Computer generated images of the Pixel, part of the ATLAS inner detector.*, Mar, 2008.

[39] J. Pequenao, *Computer generated image of the ATLAS inner detector*, Mar, 2008.

[40] J. Pequenao, *Computer Generated image of the ATLAS calorimeter*, Mar, 2008.

[41] J. Pequenao, *Computer generated image of the ATLAS Muons subsystem*, Mar, 2008.

[42] J. Goodson, *Search for Supersymmetry in States with Large Missing Transverse Momentum and Three Leptons including a Z-Boson.* PhD thesis, Stony Brook University, May, 2012. Presented 17 Apr 2012.

[43] M. Brice, *Installing the ATLAS calorimeter. Vue centrale du dtecteur ATLAS avec ses huit toroides entourant le calorimtre avant son dplacement au centre du dtecteur*, Nov, 2005.

[44] J. Alison, C. Anastopoulos, G. Artoni, E. Benhar Noccioli, A. Bocci, B. Brellier, K. Brendlinger, F. Bhrer, T. Cornelissen, M. Delmastro, O. Ducu, F. Dudziak, M. Elsing, O. Fedin, R. Fletcher, D. Froidevaux, I. Gavrilenko, T. Guillemin, S. Heim, F. Hubaut, L. Iconomidou-Fayard, M. Karnevskiy, T. Koffas, J. Kretzschmar, J. Kroll, C. Lester, K. Lohwasser, J. Maurer, A. Morley, G. Psztor, E. Richter-Was, A. Schaffer, T. Serre, P. Sommer, K. Tackmann, E. Tiouchichine, G. Unal, K. Whalen, and H. Williams, *Supporting document on electron efficiency measurements using the 2012 LHC proton-proton collision data*, Tech. Rep. ATL-COM-PHYS-2013-1295, CERN, Geneva, Sep, 2013.

[45] G. C. Blazey, J. R. Dittmann, S. D. Ellis, V. D. Elvira, K. Frame, et al., *Run II jet physics*, `arXiv:hep-ex/0005012 [hep-ex]`.

[46] Y. L. Dokshitzer, G. Leder, S. Moretti, and B. Webber, *Better jet clustering algorithms*, JHEP **9708** (1997) 001, `arXiv:hep-ph/9707323 [hep-ph]`.

[47] M. Wobisch and T. Wengler, *Hadronization corrections to jet cross-sections in deep inelastic scattering*, `arXiv:hep-ph/9907280 [hep-ph]`.

[48] ATLAS Collaboration, *Tagging and suppression of pileup jets with the ATLAS detector*, Tech. Rep. ATLAS-CONF-2014-018, CERN, Geneva, May, 2014. `https://cds.cern.ch/record/1700870`.

[49] D. W. Miller, A. Schwartzman, and D. Su, *Pile-up jet energy scale corrections using the jet-vertex fraction method*, Tech. Rep. ATL-COM-PHYS-2009-180, CERN, Geneva, Apr, 2009.

[50] M. Cacciari, G. P. Salam, and G. Soyez, *The Catchment Area of Jets*, JHEP **0804** (2008) 005, `arXiv:0802.1188 [hep-ph]`.

[51] ATLAS Collaboration, *Commissioning of the ATLAS high-performance b-tagging algorithms in the 7 TeV collision data*, Tech. Rep. ATLAS-CONF-2011-102, CERN, Geneva, Jul, 2011.

[52] *Calibration of the performance of b-tagging for c and light-flavour jets in the 2012 ATLAS data*, Tech. Rep. ATLAS-CONF-2014-046, CERN, Geneva, Jul, 2014.

[53] T. Gehrmann, M. Grazzini, S. Kallweit, P. Maierhfer, A. von Manteuffel, et al., *W^+W^- production at hadron colliders in NNLO QCD*, `arXiv:1408.5243 [hep-ph]`.

[54] LHC Higgs Cross Section Working Group Collaboration, S. Heinemeyer et al., *Handbook of LHC Higgs Cross Sections: 3. Higgs Properties*, `arXiv:1307.1347 [hep-ph]`.

[55] P. Nason, *A New method for combining NLO QCD with shower Monte Carlo algorithms*, JHEP **0411** (2004) 040, `arXiv:hep-ph/0409146 [hep-ph]`.

[56] S. Frixione, P. Nason, and C. Oleari, *Matching NLO QCD computations with Parton Shower simulations: the POWHEG method*, JHEP **0711** (2007) 070, `arXiv:0709.2092 [hep-ph]`.

[57] T. Binoth, M. Ciccolini, N. Kauer, and M. Kramer, *Gluon-induced W-boson pair production at the LHC*, JHEP **12** (2006) 046, `arXiv:hep-ph/0611170`.

[58] J. M. Butterworth et al., *Multiparton interactions in photoproduction at HERA*, Z. Phys. **C72** (1996) 637–646.

[59] ATLAS Collaboration, *The ATLAS Simulation Infrastructure*, Eur. Phys. J. **C70** (2010) 823–874, `arXiv:1005.4568 [physics.ins-det]`.

[60] GEANT4 Collaboration, S. Agostinelli et al., *GEANT4: A simulation toolkit*, Nucl. Instrum. Meth. **A506** (2003) 250–303.

[61] ATLAS Collaboration, *Electron performance measurements with the ATLAS detector using the 2010 LHC proton-proton collision data*, The European Physical Journal C **72** (2012) no. 3, 1–46. `http://dx.doi.org/10.1140/epjc/s10052-012-1909-1`.

[62] ATLAS Collaboration, *Muon reconstruction efficiency in reprocessed 2010 LHC proton-proton collision data recorded with the ATLAS detector*, ATLAS-CONF-2011-063. `https://cdsweb.cern.ch/record/1345743`.

[63] ATLAS Collaboration, *Preliminary results on the muon reconstruction efficiency, momentum resolution, and momentum scale in ATLAS 2012 pp collision data*, ATLAS-CONF-2013-088. `http://cdsweb.cern.ch/record/1580207`.

[64] ATLAS Collaboration, *Jet energy measurement with the ATLAS detector in proton-proton collisions at $\sqrt{s} = 7\ TeV$*, Eur.Phys.J. **C73** (2013) 2304, `arXiv:1112.6426 [hep-ex]`.

[65] ATLAS Collaboration, *Pile-up Suppression in Missing Transverse Momentum Reconstruction in the ATLAS Experiment in Proton-Proton Collisions at sqrts = 8 TeV*, Tech. Rep. ATLAS-CONF-2014-019, CERN, Geneva, May, 2014. `https://cds.cern.ch/record/1702055`.

[66] ATLAS Collaboration, *Jet energy measurement and its systematic uncertainty in proton-proton collisions at $\sqrt{s} = 7$ TeV with the ATLAS detector*, `arXiv:1406.0076 [hep-ex]`.

[67] ATLAS Collaboration, *Light-quark and Gluon Jets in ATLAS*, Tech. Rep. ATLAS-CONF-2011-053, CERN, Geneva, Apr, 2011.

[68] Carola F. Berger, Claudio Marcantonini, Iain W. Stewart, Frank J.Tackmann, Wouter J. Waalewijn, *Higgs Production with a Central Jet Veto at NNLL+NNLO*, (2011) , `arXiv:1012.4480 [hep-ph]`.

[69] ATLAS Collaboration, *Observation and measurement of Higgs boson decays to WW^* with the ATLAS detector*, `arXiv:1412.2641 [hep-ex]`.

[70] B. Mellado, X. Ruan, and Z. Zhang, *Extraction of Top Backgrounds in the Higgs Boson Search with the $H \to WW^\star \to \ell\ell + E_{\mathrm{T}}^{\mathrm{miss}}$ Decay with a Full-Jet Veto at the LHC*, Phys. Rev. **D84** (2011) 096005, `arXiv:1101.1383 [hep-ph]`.

[71] N. Kauer and D. Zeppenfeld, *Finite width effects in top quark production at hadron colliders*, Phys.Rev. **D65** (2002) 014021, `arXiv:hep-ph/0107181 [hep-ph]`.

[72] F. Campanario and S. Sapeta, *WZ production beyond NLO for high-pT observables*, Phys.Lett. **B718** (2012) 100–104, `arXiv:1209.4595 [hep-ph]`.

[73] F. Cascioli et al., *ZZ production at hadron colliders in NNLO QCD*, (2014) , `arXiv:1405.2219 [hep-ph]`.

[74] M. Chelstowska, S. Chen, B. Chow, B. Di Micco, S. Diglio, L. Feremenga, J. Griffiths, D. Hall, C. Hays, N. Ilic, J. Jovicevic, R. Kehoe, K. Koeneke, Y. Li, J. Long, W. Okamura, P. Onyisi, J. Qian, D. Schaefer, E. Schmidt, D. Schouten, A. Walz, H. Wang, J. Yu, L. Yuan, Z. Zhang, and L. Zhou, *Theoretical studies for the H to WW measurement with the ATLAS detector*, Tech. Rep. ATL-COM-PHYS-2013-1541, CERN, Geneva, Nov, 2013.

[75] ATLAS Collaboration, *Measurements of $W\gamma$ and $Z\gamma$ production in pp collisions at $\sqrt{s}$=7TeV with the ATLAS detector at the LHC*, Phys.Rev. **D87** (2013) no. 11, 112003, `arXiv:1302.1283 [hep-ex]`.

[76] A. Tikhonov, *On the solution of improperly posed problems and the method of regularization*, Sov. Math. **5** (1963) 1035.

[77] U. Baur, S. Errede, and G. Landsberg, *Rapidity correlations in $W\gamma$ production at hadron colliders*, Phys. Rev. **D50** (1994) no. 3, 1917.

[78] U. Baur, T. Han, and J. Ohnemus, *WZ*, Phys. Rev. D **51** (Apr, 1995) 3381–3407. `http://link.aps.org/doi/10.1103/PhysRevD.51.3381`.

[79] U. Baur, T. Han, and J. Ohnemus, *QCD corrections and nonstandard three vector boson couplings in W^+W^- production at hadron colliders*, Phys.Rev. **D53** (1996) 1098–1123, `arXiv:hep-ph/9507336 [hep-ph]`.

[80] G. Cowan, K. Cranmer, E. Gross, and O. Vitells, *Asymptotic Formulae for Likelihood-Based Tests of New Physics*, Eur. Phys. J. C **71** (2011) 1554, `arXiv:hep-ph/1007.1727v2`.

[81] G. J. Feldman and R. D. Cousins, *A Unified approach to the classical statistical analysis of small signals*, Phys.Rev. **D57** (1998) 3873–3889, `arXiv:physics/9711021 [physics.data-an]`.

[82] A. Bierweiler, T. Kasprzik, J. H. Kühn, and S. Uccirati, *Electroweak corrections to W-boson pair production at the LHC*, JHEP **1211** (2012) 093, `arXiv:1208.3147 [hep-ph]`.

[83] S. Gieseke, T. Kasprzik, and J. H. Kühn, *Vector-boson pair production and electroweak corrections in HERWIG++*, `arXiv:1401.3964 [hep-ph]`.

[84] ATLAS Collaboration, *Electron performance measurements with the ATLAS detector using the 2010 LHC proton-proton collision data*, Eur.Phys.J. **C72** (2012) 1909, `arXiv:1110.3174 [hep-ex]`.

Appendices

A Impact of WW p_{T}resummation

The effect of WW p_{T}resummation [19] is expected to be 3-7% on the total WW cross section, depending on the choice of generator, parton shower, and tunes. To investigate the impact of p_{T}resummation, the reweighting procedure is be repeated with the exact MC samples used in this analysis. Figure 48 compares the resummed WW p_{T}calculation versus the simulated WW $p_{\mathrm{T}}$from the same Powheg+Pythia $qq \to WW$ samples used to model our signal. These distributions are normalized to unity such that the reweighting procedure does not alter the total cross-section, only the shape of WW p_{T}. The p_{T}resummed event weight is the ratio of the resummed/truth(Powheg+Pythia) events taken bin by bin. For events with $p_T^{WW} > 160$ GeV the event weight is 1, as recommended by the authors. This affects 3% of total events but since events with high p_T^{WW} are unlikely to pass the jet veto, this is a negligible effect. Table 43 gives the signal yields after reconstruction level selection criteria after applying reweighting. The effect of p_{T}resummation reweighting was an increase of 4% in the final selection yields for $qq \to WW$. Figure49 shows the $p_T(ll + E_{\mathrm{T}}^{\mathrm{miss}})$ and leading lepton p_{T}distribution before and after reweighting.

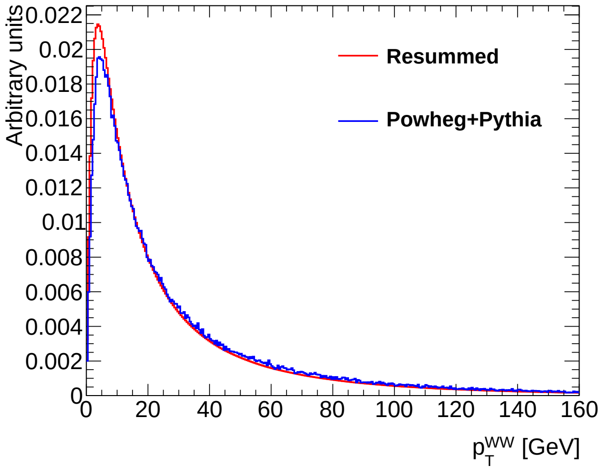

Figure 48: Comparison of resummed p_T^{WW} (red) and generator+parton shower level distribution using Powheg+Pythia (blue).

Selection Requirement	ee	mm	em
$M_{l,l}$	-0.2%	0.0%	-0.1%
Z Veto	-0.3%	0.0%	-0.1%
$E_{\mathrm{T}}^{\mathrm{miss}}$	-0.3%	0.0%	0.0%
$p_{\mathrm{T}}^{\mathrm{miss}}$	-0.3%	0.0%	-0.1%
$\Delta\phi(E_{\mathrm{T}}^{\mathrm{miss}}, p_{\mathrm{T}}^{\mathrm{miss}})$	1.1%	1.3%	1.0%
Jet Veto	4.0%	3.9%	4.2%

Table 43: Change in signal yields in the ee, $\mu\mu$, and $e\mu$ channels after reconstruction level selection criteria and applying WW p_{T}resummation reweighting.

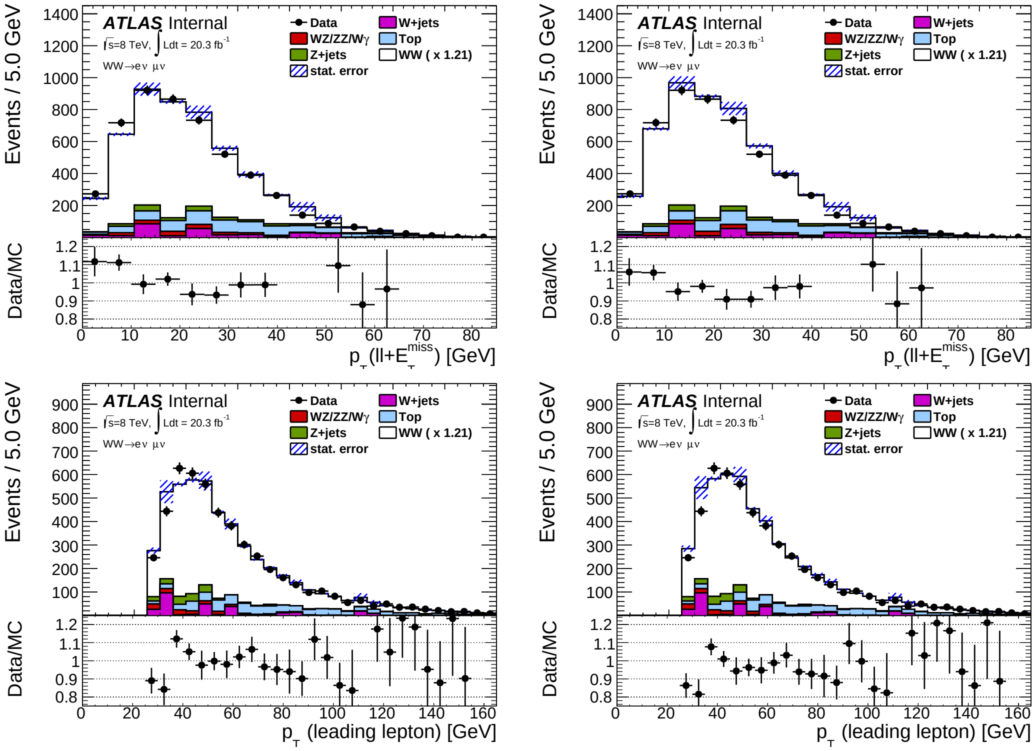

Figure 49: Comparison before (left) and after (right) WW p_{T}reweighting for $p_T(ll + E_{\mathrm{T}}^{\mathrm{miss}})$ (top) and leading lepton p_{T}(bottom). The reweighting is only applied to $qq \to WW$. The total WW signal is scaled by 1.21 and MC predicted background yields are used.

B List of Monte Carlo Samples

Process	ATLAS dataset name
$qq \to WW$	mc12_8TeV.126928.PowhegPythia8_AU2CT10_WpWm_ee.merge.NTUP_SMWZ.e1280_s1469_s1470_r3752_r3549_p1328/
	mc12_8TeV.126929.PowhegPythia8_AU2CT10_WpWm_me.merge.NTUP_SMWZ.e1280_s1469_s1470_r3542_r3549_p1328/
	mc12_8TeV.126930.PowhegPythia8_AU2CT10_WpWm_te.merge.NTUP_SMWZ.e2348_s1581_s1586_r4485_r4540_p1328/
	mc12_8TeV.126931.PowhegPythia8_AU2CT10_WpWm_em.merge.NTUP_SMWZ.e1280_s1469_s1470_r3542_r3549_p1328/
	mc12_8TeV.126932.PowhegPythia8_AU2CT10_WpWm_mm.merge.NTUP_SMWZ.e1280_s1469_s1470_r3542_r3549_p1328/
	mc12_8TeV.126933.PowhegPythia8_AU2CT10_WpWm_tm.merge.NTUP_SMWZ.e2348_s1581_s1586_r4485_r4540_p1328/
	mc12_8TeV.126934.PowhegPythia8_AU2CT10_WpWm_et.merge.NTUP_SMWZ.e1280_s1469_s1470_r3542_r3549_p1328/
	mc12_8TeV.126935.PowhegPythia8_AU2CT10_WpWm_mt.merge.NTUP_SMWZ.e2348_s1581_s1586_r4485_r4540_p1328/
	mc12_8TeV.126936.PowhegPythia8_AU2CT10_WpWm_tt.merge.NTUP_SMWZ.e2348_s1581_s1586_r4485_r4540_p1328/
$g \to H \to WW$	mc12_8TeV.161005.PowhegPythia8_AU2CT10_ggH125_WW2lep_EF_15_5.merge.NTUP_SMWZ.e1285_s1469_s1470_r3542_r3549_p1328/
$g \to WW$	mc12_8TeV.169471.gg2wwJimmy_AUET2CT10_WpWmenuenu.merge.NTUP_SMWZ.e1723_s1581_s1586_r3658_r3549_p1328/
	mc12_8TeV.169472.gg2wwJimmy_AUET2CT10_WpWmenumunu.merge.NTUP_SMWZ.e1723_s1581_s1586_r3658_r3549_p1328/
	mc12_8TeV.169473.gg2wwJimmy_AUET2CT10_WpWmenutaunu.merge.NTUP_SMWZ.e1723_s1581_s1586_r3658_r3549_p1328/
	mc12_8TeV.169474.gg2wwJimmy_AUET2CT10_WpWmmunumunu.merge.NTUP_SMWZ.e1723_s1581_s1586_r3658_r3549_p1328/
	mc12_8TeV.169475.gg2wwJimmy_AUET2CT10_WpWmmunuenu.merge.NTUP_SMWZ.e1723_s1581_s1586_r3658_r3549_p1328/
	mc12_8TeV.169476.gg2wwJimmy_AUET2CT10_WpWmmunutaunu.merge.NTUP_SMWZ.e1723_s1581_s1586_r3658_r3549_p1328/
	mc12_8TeV.169477.gg2wwJimmy_AUET2CT10_WpWmtaunutaunu.merge.NTUP_SMWZ.e1723_s1581_s1586_r3658_r3549_p1328/
	mc12_8TeV.169478.gg2wwJimmy_AUET2CT10_WpWmtaunuenu.merge.NTUP_SMWZ.e1723_s1581_s1586_r3658_r3549_p1328/
	mc12_8TeV.169479.gg2wwJimmy_AUET2CT10_WpWmtaunumunu.merge.NTUP_SMWZ.e1723_s1581_s1586_r3658_r3549_p1328/
WZ	mc12_8TeV.129477.PowhegPythia8_AU2CT10_WZ_Wm11Z11_mll0p250d0_2LeptonFilter5.merge.NTUP_SMWZ.e1300_s1469_s1470_r3542_r3549_p1328/
	mc12_8TeV.129478.PowhegPythia8_AU2CT10_WZ_Wm11Z13_mll0p4614d0_2LeptonFilter5.merge.NTUP_SMWZ.e1300_s1469_s1470_r3542_r3549_p1328/
	mc12_8TeV.129479.PowhegPythia8_AU2CT10_WZ_Wm11Z15_mll3p804d0_2LeptonFilter5.merge.NTUP_SMWZ.e2372_s1469_s1470_r3542_r3549_p1328/
	mc12_8TeV.129480.PowhegPythia8_AU2CT10_WZ_Wm13Z11_mll0p250d0_2LeptonFilter5.merge.NTUP_SMWZ.e1300_s1469_s1470_r3542_r3549_p1328/
	mc12_8TeV.129481.PowhegPythia8_AU2CT10_WZ_Wm13Z13_mll0p4614d0_2LeptonFilter5.merge.NTUP_SMWZ.e1300_s1469_s1470_r3542_r3549_p1328/
	mc12_8TeV.129482.PowhegPythia8_AU2CT10_WZ_Wm13Z15_mll3p804d0_2LeptonFilter5.merge.NTUP_SMWZ.e2372_s1469_s1470_r3542_r3549_p1328/
	mc12_8TeV.129483.PowhegPythia8_AU2CT10_WZ_Wm15Z11_mll0p250d0_2LeptonFilter5.merge.NTUP_SMWZ.e2372_s1469_s1470_r3542_r3549_p1328/
	mc12_8TeV.129484.PowhegPythia8_AU2CT10_WZ_Wm15Z13_mll0p4614d0_2LeptonFilter5.merge.NTUP_SMWZ.e2372_s1469_s1470_r3542_r3549_p1328/
	mc12_8TeV.129485.PowhegPythia8_AU2CT10_WZ_Wm15Z15_mll3p804d0_2LeptonFilter5.merge.NTUP_SMWZ.e2372_s1469_s1470_r3542_r3549_p1328/
	mc12_8TeV.129486.PowhegPythia8_AU2CT10_WZ_W11Z11_mll0p250d0_2LeptonFilter5.merge.NTUP_SMWZ.e1300_s1469_s1470_r3542_r3549_p1328/
	mc12_8TeV.129487.PowhegPythia8_AU2CT10_WZ_W11Z13_mll0p4614d0_2LeptonFilter5.merge.NTUP_SMWZ.e1300_s1469_s1470_r3542_r3549_p1328/
	mc12_8TeV.129488.PowhegPythia8_AU2CT10_WZ_W11Z15_mll3p804d0_2LeptonFilter5.merge.NTUP_SMWZ.e2372_s1469_s1470_r3542_r3549_p1328/
	mc12_8TeV.129489.PowhegPythia8_AU2CT10_WZ_W13Z11_mll0p250d0_2LeptonFilter5.merge.NTUP_SMWZ.e1300_s1469_s1470_r3542_r3549_p1328/
	mc12_8TeV.129490.PowhegPythia8_AU2CT10_WZ_W13Z13_mll0p4614d0_2LeptonFilter5.merge.NTUP_SMWZ.e1300_s1469_s1470_r3542_r3549_p1328/
	mc12_8TeV.129491.PowhegPythia8_AU2CT10_WZ_W13Z15_mll3p804d0_2LeptonFilter5.merge.NTUP_SMWZ.e2372_s1469_s1470_r3542_r3549_p1328/
	mc12_8TeV.129492.PowhegPythia8_AU2CT10_WZ_W15Z11_mll0p250d0_2LeptonFilter5.merge.NTUP_SMWZ.e2372_s1469_s1470_r3542_r3549_p1328/
	mc12_8TeV.129493.PowhegPythia8_AU2CT10_WZ_W15Z13_mll0p4614d0_2LeptonFilter5.merge.NTUP_SMWZ.e2372_s1469_s1470_r3542_r3549_p1328/
	mc12_8TeV.129494.PowhegPythia8_AU2CT10_WZ_W15Z15_mll3p804d0_2LeptonFilter5.merge.NTUP_SMWZ.e2372_s1469_s1470_r3542_r3549_p1328/
Wγ	mc12_8TeV.146436.AlpgenJimmy_AUET2CTEQ6L1_WgammaNp0_LeptonPhotonFilter.merge.NTUP_SMWZ.e1601_s1499_s1504_r3658_r3549_p1328/
	mc12_8TeV.146437.AlpgenJimmy_AUET2CTEQ6L1_WgammaNp1_LeptonPhotonFilter.merge.NTUP_SMWZ.e1601_s1499_s1504_r3658_r3549_p1328/
	mc12_8TeV.146438.AlpgenJimmy_AUET2CTEQ6L1_WgammaNp2_LeptonPhotonFilter.merge.NTUP_SMWZ.e1601_s1499_s1504_r3658_r3549_p1328/
	mc12_8TeV.146439.AlpgenJimmy_AUET2CTEQ6L1_WgammaNp3_LeptonPhotonFilter.merge.NTUP_SMWZ.e1601_s1499_s1504_r3658_r3549_p1328/
	mc12_8TeV.146434.AlpgenJimmy_AUET2CTEQ6L1_WgammaNp4.merge.NTUP_SMWZ.e1601_s1499_s1504_r3658_r3549_p1328/
	mc12_8TeV.146435.AlpgenJimmy_AUET2CTEQ6L1_WgammaNp5.merge.NTUP_SMWZ.e1601_s1499_s1504_r3658_r3549_p1328/

ZZ	mc12_8TeV.126937.PowhegPythia8_AU2CT10_ZZ_4e_mll4_2pt5.merge.NTUP_SMWZ.e1280_s1469_s1470_r3542_r3549_p1328/
	mc12_8TeV.126938.PowhegPythia8_AU2CT10_ZZ_2e2mu_mll4_2pt5.merge.NTUP_SMWZ.e1280_s1469_s1470_r3752_r3549_p1328/
	mc12_8TeV.126939.PowhegPythia8_AU2CT10_ZZ_2e2tau_mll4_2pt5.merge.NTUP_SMWZ.e2372_s1469_s1470_r3542_r3549_p1328/
	mc12_8TeV.126940.PowhegPythia8_AU2CT10_ZZ_4mu_mll4_2pt5.merge.NTUP_SMWZ.e1280_s1469_s1470_r3752_r3549_p1328/
	mc12_8TeV.126941.PowhegPythia8_AU2CT10_ZZ_2mu2tau_mll4_2pt5.merge.NTUP_SMWZ.e2372_s1469_s1470_r3542_r3549_p1328/
	mc12_8TeV.126942.PowhegPythia8_AU2CT10_ZZ_4tau_mll4_2pt5.merge.NTUP_SMWZ.e2372_s1469_s1470_r3542_r3549_p1328/
	mc12_8TeV.126949.PowhegPythia8_AU2CT10_ZZllnunu_ee_mll4.merge.NTUP_SMWZ.e1280_s1469_s1470_r3752_r3549_p1328/
	mc12_8TeV.126950.PowhegPythia8_AU2CT10_ZZllnunu_mm_mll4.merge.NTUP_SMWZ.e1280_s1469_s1470_r3542_r3549_p1328/
	mc12_8TeV.126951.PowhegPythia8_AU2CT10_ZZllnunu_tt_mll4.merge.NTUP_SMWZ.e2372_s1469_s1470_r3542_r3549_p1328/
Top	mc12_8TeV.110001.McAtNloJimmy_CT10_ttbar_dilepton.merge.NTUP_SMWZ.e1576_s1499_s1504_r3658_r3549_p1328/
	mc12_8TeV.117360.AcerMCPythia_AUET2BCTEQ6L1_singletop_tchan_e.merge.NTUP_SMWZ.e1346_s1499_s1504_r3658_r3549_p1328/
	mc12_8TeV.117361.AcerMCPythia_AUET2BCTEQ6L1_singletop_tchan_mu.merge.NTUP_SMWZ.e1346_s1499_s1504_r3658_r3549_p1328/
	mc12_8TeV.117362.AcerMCPythia_AUET2BCTEQ6L1_singletop_tchan_tau.merge.NTUP_SMWZ.e1346_s1499_s1504_r3658_r3549_p1328/
	mc12_8TeV.108343.McAtNloJimmy_AUET2CT10_SingleTopSChanWenu.merge.NTUP_SMWZ.e1525_s1499_s1504_r3658_r3549_p1328/
	mc12_8TeV.108344.McAtNloJimmy_AUET2CT10_SingleTopSChanWmunu.merge.NTUP_SMWZ.e1525_s1499_s1504_r3658_r3549_p1328/
	mc12_8TeV.108345.McAtNloJimmy_AUET2CT10_SingleTopSChanWtaunu.merge.NTUP_SMWZ.e1525_s1499_s1504_r3658_r3549_p1328/
	mc12_8TeV.108346.McAtNloJimmy_AUET2CT10_SingleTopWtChanIncl.merge.NTUP_SMWZ.e1525_s1499_s1504_r3658_r3549_p1328/
$W +$ jets	mc12_8TeV.147025.AlpgenPythia_Auto_P2011C_WenuNp0.merge.NTUP_SMWZ.e1879_s1581_s1586_r3658_r3549_p1328/
	mc12_8TeV.147026.AlpgenPythia_Auto_P2011C_WenuNp1.merge.NTUP_SMWZ.e1879_s1581_s1586_r3658_r3549_p1328/
	mc12_8TeV.147027.AlpgenPythia_Auto_P2011C_WenuNp2.merge.NTUP_SMWZ.e1879_s1581_s1586_r3658_r3549_p1328/
	mc12_8TeV.147028.AlpgenPythia_Auto_P2011C_WenuNp3.merge.NTUP_SMWZ.e1879_s1581_s1586_r3658_r3549_p1328/
	mc12_8TeV.147029.AlpgenPythia_Auto_P2011C_WenuNp4.merge.NTUP_SMWZ.e1879_s1581_s1586_r3658_r3549_p1328/
	mc12_8TeV.147030.AlpgenPythia_Auto_P2011C_WenuNp5incl.merge.NTUP_SMWZ.e1879_s1581_s1586_r3658_r3549_p1328/
	mc12_8TeV.147033.AlpgenPythia_Auto_P2011C_WmunuNp0.merge.NTUP_SMWZ.e1880_s1581_s1586_r3658_r3549_p1328/
	mc12_8TeV.147034.AlpgenPythia_Auto_P2011C_WmunuNp1.merge.NTUP_SMWZ.e1880_s1581_s1586_r3658_r3549_p1328/
	mc12_8TeV.147035.AlpgenPythia_Auto_P2011C_WmunuNp2.merge.NTUP_SMWZ.e1880_s1581_s1586_r3658_r3549_p1328/
	mc12_8TeV.147036.AlpgenPythia_Auto_P2011C_WmunuNp3.merge.NTUP_SMWZ.e1880_s1581_s1586_r3658_r3549_p1328/
	mc12_8TeV.147037.AlpgenPythia_Auto_P2011C_WmunuNp4.merge.NTUP_SMWZ.e1880_s1581_s1586_r3658_r3549_p1328/
	mc12_8TeV.147038.AlpgenPythia_Auto_P2011C_WmunuNp5incl.merge.NTUP_SMWZ.e1880_s1581_s1586_r3658_r3549_p1328/
	mc12_8TeV.147041.AlpgenPythia_Auto_P2011C_WtaunuNp0.merge.NTUP_SMWZ.e1881_s1581_s1586_r3658_r3549_p1328/
	mc12_8TeV.147042.AlpgenPythia_Auto_P2011C_WtaunuNp1.merge.NTUP_SMWZ.e1881_s1581_s1586_r3658_r3549_p1328/
	mc12_8TeV.147043.AlpgenPythia_Auto_P2011C_WtaunuNp2.merge.NTUP_SMWZ.e1881_s1581_s1586_r3658_r3549_p1328/
	mc12_8TeV.147044.AlpgenPythia_Auto_P2011C_WtaunuNp3.merge.NTUP_SMWZ.e1881_s1581_s1586_r3658_r3549_p1328/
	mc12_8TeV.147045.AlpgenPythia_Auto_P2011C_WtaunuNp4.merge.NTUP_SMWZ.e1881_s1581_s1586_r3658_r3549_p1328/
	mc12_8TeV.147046.AlpgenPythia_Auto_P2011C_WtaunuNp5incl.merge.NTUP_SMWZ.e1881_s1581_s1586_r3658_r3549_p1328/
	mc12_8TeV.200256.AlpgenPythia_Auto_P2011C_WbbNp0.merge.NTUP_SMWZ.e1930_s1581_s1586_r3658_r3549_p1328/
	mc12_8TeV.200257.AlpgenPythia_Auto_P2011C_WbbNp1.merge.NTUP_SMWZ.e1930_s1581_s1586_r3658_r3549_p1328/
	mc12_8TeV.200258.AlpgenPythia_Auto_P2011C_WbbNp2.merge.NTUP_SMWZ.e1930_s1581_s1586_r3658_r3549_p1328/
	mc12_8TeV.200259.AlpgenPythia_Auto_P2011C_WbbNp3incl.merge.NTUP_SMWZ.e1930_s1581_s1586_r3658_r3549_p1328/
	mc12_8TeV.200056.AlpgenPythia_Auto_P2011C_WcNp0.merge.NTUP_SMWZ.e1930_s1581_s1586_r3658_r3549_p1328/
	mc12_8TeV.200057.AlpgenPythia_Auto_P2011C_WcNp1.merge.NTUP_SMWZ.e1930_s1581_s1586_r3658_r3549_p1328/
	mc12_8TeV.200058.AlpgenPythia_Auto_P2011C_WcNp2.merge.NTUP_SMWZ.e1930_s1581_s1586_r3658_r3549_p1328/
	mc12_8TeV.200059.AlpgenPythia_Auto_P2011C_WcNp3.merge.NTUP_SMWZ.e1930_s1581_s1586_r3658_r3549_p1328/
	mc12_8TeV.200060.AlpgenPythia_Auto_P2011C_WcNp4incl.merge.NTUP_SMWZ.e1930_s1581_s1586_r3658_r3549_p1328/
	mc12_8TeV.200156.AlpgenPythia_Auto_P2011C_WccNp0.merge.NTUP_SMWZ.e1930_s1581_s1586_r3658_r3549_p1328/
	mc12_8TeV.200157.AlpgenPythia_Auto_P2011C_WccNp1.merge.NTUP_SMWZ.e1930_s1581_s1586_r3658_r3549_p1328/
	mc12_8TeV.200158.AlpgenPythia_Auto_P2011C_WccNp2.merge.NTUP_SMWZ.e1930_s1581_s1586_r3658_r3549_p1328/
	mc12_8TeV.200159.AlpgenPythia_Auto_P2011C_WccNp3incl.merge.NTUP_SMWZ.e1930_s1581_s1586_r3658_r3549_p1328/

$Z+$ jets	mc12_8TeV.147105.AlpgenPythia_Auto_P2011C_ZeeNp0.merge.NTUP_SMWZ.e1879_s1581_s1586_r3658_r3549_p1328/
	mc12_8TeV.147106.AlpgenPythia_Auto_P2011C_ZeeNp1.merge.NTUP_SMWZ.e1879_s1581_s1586_r3658_r3549_p1328/
	mc12_8TeV.147107.AlpgenPythia_Auto_P2011C_ZeeNp2.merge.NTUP_SMWZ.e1879_s1581_s1586_r3658_r3549_p1328/
	mc12_8TeV.147108.AlpgenPythia_Auto_P2011C_ZeeNp3.merge.NTUP_SMWZ.e1879_s1581_s1586_r3658_r3549_p1328/
	mc12_8TeV.147109.AlpgenPythia_Auto_P2011C_ZeeNp4.merge.NTUP_SMWZ.e1879_s1581_s1586_r3658_r3549_p1328/
	mc12_8TeV.147110.AlpgenPythia_Auto_P2011C_ZeeNp5incl.merge.NTUP_SMWZ.e1879_s1581_s1586_r3658_r3549_p1328/
	mc12_8TeV.147113.AlpgenPythia_Auto_P2011C_ZmumuNp0.merge.NTUP_SMWZ.e1880_s1581_s1586_r3658_r3549_p1328/
	mc12_8TeV.147114.AlpgenPythia_Auto_P2011C_ZmumuNp1.merge.NTUP_SMWZ.e1880_s1581_s1586_r3658_r3549_p1328/
	mc12_8TeV.147115.AlpgenPythia_Auto_P2011C_ZmumuNp2.merge.NTUP_SMWZ.e1880_s1581_s1586_r3658_r3549_p1328/
	mc12_8TeV.147116.AlpgenPythia_Auto_P2011C_ZmumuNp3.merge.NTUP_SMWZ.e1880_s1581_s1586_r3658_r3549_p1328/
	mc12_8TeV.147117.AlpgenPythia_Auto_P2011C_ZmumuNp4.merge.NTUP_SMWZ.e1880_s1581_s1586_r3658_r3549_p1328/
	mc12_8TeV.147118.AlpgenPythia_Auto_P2011C_ZmumuNp5incl.merge.NTUP_SMWZ.e1880_s1581_s1586_r3658_r3549_p1328/
	mc12_8TeV.147121.AlpgenPythia_Auto_P2011C_ZtautauNp0.merge.NTUP_SMWZ.e1881_s1581_s1586_r3658_r3549_p1328/
	mc12_8TeV.147122.AlpgenPythia_Auto_P2011C_ZtautauNp1.merge.NTUP_SMWZ.e1881_s1581_s1586_r3658_r3549_p1328/
	mc12_8TeV.147123.AlpgenPythia_Auto_P2011C_ZtautauNp2.merge.NTUP_SMWZ.e1881_s1581_s1586_r3658_r3549_p1328/
	mc12_8TeV.147124.AlpgenPythia_Auto_P2011C_ZtautauNp3.merge.NTUP_SMWZ.e1881_s1581_s1586_r3658_r3549_p1328/
	mc12_8TeV.147125.AlpgenPythia_Auto_P2011C_ZtautauNp4.merge.NTUP_SMWZ.e1881_s1581_s1586_r3658_r3549_p1328/
	mc12_8TeV.147126.AlpgenPythia_Auto_P2011C_ZtautauNp5incl.merge.NTUP_SMWZ.e1881_s1581_s1586_r3658_r3549_p1328/
	mc12_8TeV.146860.AlpgenJimmy_Auto_AUET2CTEQ6L1_Filtered_ZeeNp0Excl_Mll10to60.merge.NTUP_SMWZ.e1600_s1499_s1504_r3658_r3549_p1328/
	mc12_8TeV.146861.AlpgenJimmy_Auto_AUET2CTEQ6L1_Filtered_ZeeNp1Excl_Mll10to60.merge.NTUP_SMWZ.e1600_s1499_s1504_r3658_r3549_p1328/
	mc12_8TeV.146862.AlpgenJimmy_Auto_AUET2CTEQ6L1_Filtered_ZeeNp2Excl_Mll10to60.merge.NTUP_SMWZ.e1600_s1499_s1504_r3658_r3549_p1328/
	mc12_8TeV.146863.AlpgenJimmy_Auto_AUET2CTEQ6L1_Filtered_ZeeNp3Excl_Mll10to60.merge.NTUP_SMWZ.e1600_s1499_s1504_r3658_r3549_p1328/
	mc12_8TeV.146864.AlpgenJimmy_Auto_AUET2CTEQ6L1_Filtered_ZeeNp4Excl_Mll10to60.merge.NTUP_SMWZ.e1600_s1499_s1504_r3658_r3549_p1328/
	mc12_8TeV.146870.AlpgenJimmy_Auto_AUET2CTEQ6L1_Filtered_ZmumuNp0Excl_Mll10to60.merge.NTUP_SMWZ.e1600_s1499_s1504_r3658_r3549_p1328/
	mc12_8TeV.146871.AlpgenJimmy_Auto_AUET2CTEQ6L1_Filtered_ZmumuNp1Excl_Mll10to60.merge.NTUP_SMWZ.e1600_s1499_s1504_r3658_r3549_p1328/
	mc12_8TeV.146872.AlpgenJimmy_Auto_AUET2CTEQ6L1_Filtered_ZmumuNp2Excl_Mll10to60.merge.NTUP_SMWZ.e1600_s1499_s1504_r3658_r3549_p1328/
	mc12_8TeV.146873.AlpgenJimmy_Auto_AUET2CTEQ6L1_Filtered_ZmumuNp3Excl_Mll10to60.merge.NTUP_SMWZ.e1600_s1499_s1504_r3658_r3549_p1328/
	mc12_8TeV.146874.AlpgenJimmy_Auto_AUET2CTEQ6L1_Filtered_ZmumuNp4Excl_Mll10to60.merge.NTUP_SMWZ.e1600_s1499_s1504_r3658_r3549_p1328/
	mc12_8TeV.146880.AlpgenJimmy_Auto_AUET2CTEQ6L1_Filtered_ZtautauNp0Excl_Mll10to60.merge.NTUP_SMWZ.e1551_s1499_s1504_r3658_r3549_p1328/
	mc12_8TeV.146881.AlpgenJimmy_Auto_AUET2CTEQ6L1_Filtered_ZtautauNp1Excl_Mll10to60.merge.NTUP_SMWZ.e1551_s1499_s1504_r3658_r3549_p1328/
	mc12_8TeV.146882.AlpgenJimmy_Auto_AUET2CTEQ6L1_Filtered_ZtautauNp2Excl_Mll10to60.merge.NTUP_SMWZ.e1551_s1499_s1504_r3658_r3549_p1328/
	mc12_8TeV.146883.AlpgenJimmy_Auto_AUET2CTEQ6L1_Filtered_ZtautauNp3Excl_Mll10to60.merge.NTUP_SMWZ.e1551_s1499_s1504_r3658_r3549_p1328/
	mc12_8TeV.146835.AlpgenJimmy_Auto_AUET2CTEQ6L1_ZeeNp5Incl_Mll10to60.merge.NTUP_SMWZ.e1600_s1499_s1504_r3658_r3549_p1328/
	mc12_8TeV.146845.AlpgenJimmy_Auto_AUET2CTEQ6L1_ZmumuNp5Incl_Mll10to60.merge.NTUP_SMWZ.e1600_s1499_s1504_r3658_r3549_p1328/
	mc12_8TeV.146854.AlpgenJimmy_Auto_AUET2CTEQ6L1_ZtautauNp4Excl_Mll10to60.merge.NTUP_SMWZ.e1348_s1469_s1470_r3542_r3549_p1328/
	mc12_8TeV.146855.AlpgenJimmy_Auto_AUET2CTEQ6L1_ZtautauNp5Incl_Mll10to60.merge.NTUP_SMWZ.e1600_s1499_s1504_r3658_r3549_p1328/
Wγ^*	mc12_8TeV.181452.Sherpa_CT10_Wgstaree_1p_lt7.merge.NTUP_SMWZ.e2225_s1581_s1586_r4485_r4540_p1328/
	mc12_8TeV.181453.Sherpa_CT10_Wgstarmumu_1p_lt7.merge.NTUP_SMWZ.e2225_s1581_s1586_r4485_r4540_p1328/
	mc12_8TeV.181454.Sherpa_CT10_Wgstartautau_1p_lt7.merge.NTUP_SMWZ.e2225_s1581_s1586_r4485_r4540_p1328/

Table 44: Full ATLAS dataset names for Monte Carlo samples

C Isolation and Impact Parameter Scale Factors

	15-20 GeV	20-25 GeV	25-30 GeV	30-35 GeV	35-40 GeV	40-45 GeV	45-50 GeV	> 50 GeV
$[-2.47, -2.37]$	1.004 ± 0.014	0.992 ± 0.008	1.007 ± 0.006	1.004 ± 0.004	1.003 ± 0.004	$1.005 \pm 0.00\ 3$	1.001 ± 0.004	1.004 ± 0.005
$[-2.37, -2.01]$	1.006 ± 0.006	1.000 ± 0.003	1.003 ± 0.003	0.997 ± 0.002	0.996 ± 0.002	$0.995 \pm 0.00\ 1$	0.994 ± 0.002	0.993 ± 0.002
$[-2.01, -1.81]$	1.024 ± 0.010	1.002 ± 0.005	0.999 ± 0.003	0.996 ± 0.002	1.000 ± 0.002	$0.994 \pm 0.00\ 2$	0.997 ± 0.002	0.996 ± 0.002
$[-1.81, -1.52]$	0.995 ± 0.007	1.003 ± 0.004	0.997 ± 0.003	1.001 ± 0.002	0.998 ± 0.002	$0.998 \pm 0.00\ 2$	0.998 ± 0.002	0.995 ± 0.002
$[-1.37, -1.15]$	1.015 ± 0.010	1.008 ± 0.006	0.998 ± 0.004	0.999 ± 0.002	0.997 ± 0.002	$0.996 \pm 0.00\ 1$	0.998 ± 0.002	0.997 ± 0.002
$[-1.15, -0.8]$	0.994 ± 0.009	0.995 ± 0.004	1.002 ± 0.003	0.997 ± 0.002	0.997 ± 0.001	$0.998 \pm 0.00\ 1$	0.996 ± 0.001	1.001 ± 0.001
$[-0.8, -0.6]$	0.995 ± 0.009	1.012 ± 0.006	0.998 ± 0.003	0.997 ± 0.002	0.997 ± 0.002	$0.996 \pm 0.00\ 1$	0.996 ± 0.002	0.997 ± 0.002
$[-0.6, -0.1]$	0.990 ± 0.007	0.996 ± 0.004	0.991 ± 0.002	0.995 ± 0.001	0.996 ± 0.001	$0.994 \pm 0.00\ 1$	0.994 ± 0.001	0.994 ± 0.001
$[-0.1, 0]$	0.978 ± 0.013	0.997 ± 0.007	0.999 ± 0.004	0.994 ± 0.003	0.995 ± 0.003	$0.994 \pm 0.00\ 2$	0.989 ± 0.002	0.993 ± 0.002
$[0, 0.1]$	1.052 ± 0.056	0.996 ± 0.007	0.983 ± 0.004	0.998 ± 0.003	0.996 ± 0.002	$0.992 \pm 0.00\ 2$	0.997 ± 0.003	0.992 ± 0.003
$[0.1, 0.6]$	0.986 ± 0.006	0.994 ± 0.004	0.994 ± 0.002	0.993 ± 0.001	0.993 ± 0.001	$0.994 \pm 0.00\ 1$	0.995 ± 0.001	0.994 ± 0.001
$[0.6, 0.8]$	0.992 ± 0.009	0.997 ± 0.006	0.991 ± 0.003	0.997 ± 0.002	0.995 ± 0.002	$0.996 \pm 0.00\ 2$	0.995 ± 0.002	0.997 ± 0.002
$[0.8, 1.15]$	1.003 ± 0.010	1.014 ± 0.005	0.999 ± 0.002	0.997 ± 0.002	0.996 ± 0.001	$0.998 \pm 0.00\ 1$	0.997 ± 0.001	0.994 ± 0.001
$[1.15, 1.37]$	0.998 ± 0.010	1.003 ± 0.005	1.000 ± 0.004	1.002 ± 0.003	0.999 ± 0.002	$0.998 \pm 0.00\ 1$	0.999 ± 0.002	0.998 ± 0.002
$[1.52, 1.81]$	1.006 ± 0.007	0.997 ± 0.004	1.002 ± 0.003	1.002 ± 0.002	0.996 ± 0.002	$0.994 \pm 0.00\ 1$	0.995 ± 0.002	0.995 ± 0.003
$[1.81, 2.01]$	1.014 ± 0.009	0.996 ± 0.005	1.005 ± 0.003	0.998 ± 0.003	0.998 ± 0.002	$0.997 \pm 0.00\ 2$	0.998 ± 0.002	0.996 ± 0.003
$[2.01, 2.37]$	1.008 ± 0.006	0.998 ± 0.003	1.002 ± 0.004	0.995 ± 0.002	0.997 ± 0.001	$0.996 \pm 0.00\ 2$	0.996 ± 0.002	0.994 ± 0.002
$[2.37, 2.47]$	1.004 ± 0.013	0.999 ± 0.008	1.002 ± 0.005	1.000 ± 0.004	1.000 ± 0.004	$0.999 \pm 0.00\ 3$	1.009 ± 0.004	1.010 ± 0.005

Table 45: Isolation scale-factors for isolation and impact requirements for electrons. Shown are the central values with their systematic uncertainties.

D Impact of sporadically noisy cells in liquid argon calorimeter

Karen Chen[a], John Hobbs[a], Hideki Okawa[b]
[a] *Stony Brook University*
[b] *Brookhaven National Laboratory*

We studied the impact of noisy cells in the liquid argon (LAr) calorimeter on reconstructed electrons using data corresponding to 14fb^{-1}of integrated luminosity collected by the ATLAS detector in 2012. Electrons were selected according to criteria similar to analyses involving $W \to e\nu$ or $Z \to ee$ decay channels. Comparisons were made for a subset of the data between electrons with and without masked cells to check for biases that may be introduced by the treatment of problematic cells.

D.1 Introduction

The liquid argon (LAr) sampling electromagnetic (EM) calorimeter is an important part of the ATLAS detector. It allows for the identification and energy measurement of electrons, photons, and jets. The LAr calorimeter has 182468 readout channels which are monitored daily in calibration runs and offline LAr data quality shifts. The calorimeter as a whole is stable but there is a small fraction of pathological channels that can affect the tails of physics distributions. One pathology results in permanently noisier cells, which are flagged as “highNoise” and masked for the duration of the run. Another results in sporadically noisy cells in which affected channels fluctuate with time. If unaccounted for, the noise is propagated from the cells to reconstructed objects such as electrons. The treatment of noisy cells and the impact on electrons that may be used in analyses is studied.

D.2 Energy replacement for problematic cells

If a cell is identified as problematic, the energy of that cell may not be used. Instead, the energy of the problematic cell is replaced by the simple average of the good neighbors. This is referred to as masking a cell. There are several types of cells in which the energy replacement algorithm is used: dead cells, high noise cells, and sporadically noisy cells with a large quality factor, Q. The energy replacement is always done for dead cells or high noise cells. In the case for sporadically noisy cells, the energy replacement is only done if Q $>$ 4000 for that event. Otherwise, the energy is treated as normal. The quality factor is a measure of how well the measured pulse shape fits the predicted pulse shape used in reconstructing the cell energy.

If an electron is reconstructed with a cell that has had its energy replaced, this is stored in the electron object quality, el_OQ, bitmask. There are separate bits for when masking occurs in the cluster core (bit 10) or cluster edge. Bits 11-14 correspond to masking in the cluster edge in the presampler (PS), front (S1), middle (S2), and back (S3) layer respectively. The cluster core is defined as the 3 by 3 array of cells in the second sampling layer (S2) of the sliding window cluster. The cluster edge is defined all other cells in the cluster that are not in the core. Since most of the electron energy comes from the cells in the core, if there is a masked cell in the core, it is not recommended to use this electron in physics analyses.

D.3 Data samples

The data sample, corresponding to an integrated luminosity of 14 pb^{-1}, consists of events taken in 2012 running from period A-H and is selected from the e/γ stream with production tag p1196. The official good run list (GRL)

- data12_8TeV.periodAllYear_DetStatus-v54-pro13-04_DQDefects-00-00-33_PHYS_ \CombinedPerf_Egamma_Eg_standard.xml

is applied to data.

D.4 Event and Object Selection

Events are required to pass the EF_e24vhi_medium1 trigger and must have at least one good primary vertex. A good vertex must contain at least three tracks and have $|z| < 2$cm. Events are rejected if $larError > 1$, which indicates a problem with the LAr calorimeter usually associated with data corruption or significant noise bursts.

Good electrons are selected according to e/γ recommendations[84] and must satisfy kinematic requirements and object quality requirements. To make the study relevant to physics analyses, further requirements are applied. These are chosen to mimic those typical of analyses involving $W \to e\nu$ or $Z \to ee$ decay channels. They include calorimeter and track based isolation as well as impact parameter requirements. The number of events and electrons that pass requirements are listed in Table 46. The electron selection criteria are summarized below:

- $author = 1$ or $author = 3$: The electron was reconstructed using a calorimeter seeded algorithm or a combination of calorimeter and track based algorithms.
- $|z_0| < 2mm$: The longitudinal impact parameter, z_0 must be less than 2 mm.
- d_0 significance < 6: The ratio of the transverse impact paramter, d_0, to its uncertainty (d_0 significance) must be less than 6
- $|\eta| < 2.47$ and not in crack between barrel and endcap, $1.37 < |\eta| < 1.52$
- Track based isolation: The scalar sum of the p_{T} of the tracks within $\Delta R^{13} = 0.3$ around the electron must be less than 13% of the electron E_{T}
- Calorimeter based isolation: The total calorimeter E_{T} in a cone of $\Delta R = 0.3$ around the electron, excluding the E_{T} of the electron itself, must be less than 14% of the electron E_{T}.
- $p_{\mathrm{T}} > 25$ GeV
- $larError \leq 1$
- Tight++ identification
- Object quality: Reject bad quality clusters using object quality flag (el_OQ&1446) == 0

To quantify the effect of masking on reconstructed W/Z boson masses, candidate electrons from W/Z decays must meet the previous event and electron requirements and the following additional requirements. For $W \rightarrow e\nu$ candidates, the event must have missing transverse energy $E_{\mathrm{T}}^{\mathrm{miss}} > 25$ GeV and have exactly one reconstructed electron candidate. For $Z \rightarrow ee$ candidates, the event must have exactly two reconstructed electron candidates.

D.5 Results

D.5.1 Electrons with masked cells

Figure 50 gives the fraction of electrons (after event and object selection) with masking in each layer for each run. Figure 51 shows the $\eta - \phi$ distributions of electrons with masked cells in each layer. To check for hot spots, a corresponding set (Fig. 52) shows the fraction of electrons with masked cells out of all electrons in the same $\eta - \phi$ bin. This was done by taking panes (b) - (e) in Figure 51 and dividing by the $\eta - \phi$ distribution of all electrons.

The total energy and transverse energy for electrons with and without masked cells are shown in Fig. 53(a) and Fig. 53(b) respectively. Missing transverse energy is shown in Fig. 53(c) and its ϕ distribution is shown in Fig. 53(d).

---

[13] The angular distance, ΔR, is defined as $\Delta R = \sqrt{\Delta\phi^2 + \Delta\eta^2}$

Cut	Events	Efficiency
All	467867844	
GRL	447343109	95.6%
Vertex	446711557	95.5%
Trigger	188326543	40.3%
Cut	Electrons	Efficiency
All	1284937751	
Author	473047742	36.8%
Object Quality	471342694	36.7%
z_0	335251675	26.1%
d_0 significance	314964663	24.5%
$\|\eta\| < 2.47$, not in crack	298474014	23.2%
Track isolation	138899860	10.8%
Calorimeter isolation	115309032	9.0%
$p_{\mathrm{T}} > 25$ GeV	107168594	8.3%
$larError \leq 1$	106660082	8.3%
Tight++	78158878	6.1%
Candidate W electrons	Electrons	Efficiency
$n_{electrons} = 1, E_{\mathrm{T}}^{\mathrm{miss}} > 25$ GeV	53045782	67.9%
Candidate Z electrons	Electrons	Efficiency
$n_{electrons} = 2$	6252462	8.0%

Table 46: Number of events (electrons) that pass selection criteria.

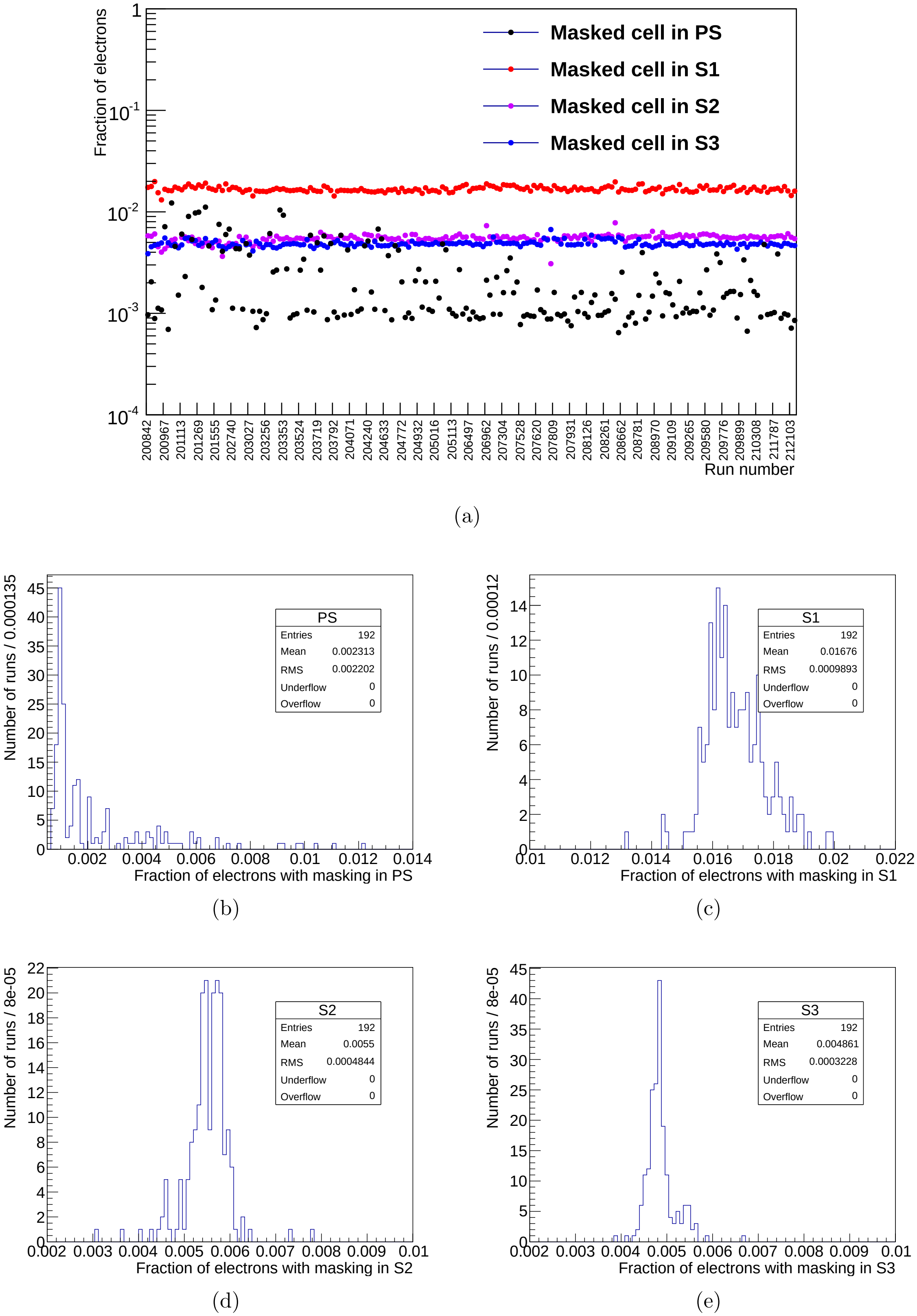

(a)

(b)

(c)

(d)

(e)

Figure 50: (a) Fraction of electrons with masked cells for each run. (b)-(e) give the distribution of the fraction of electrons with masked cells in each layer.

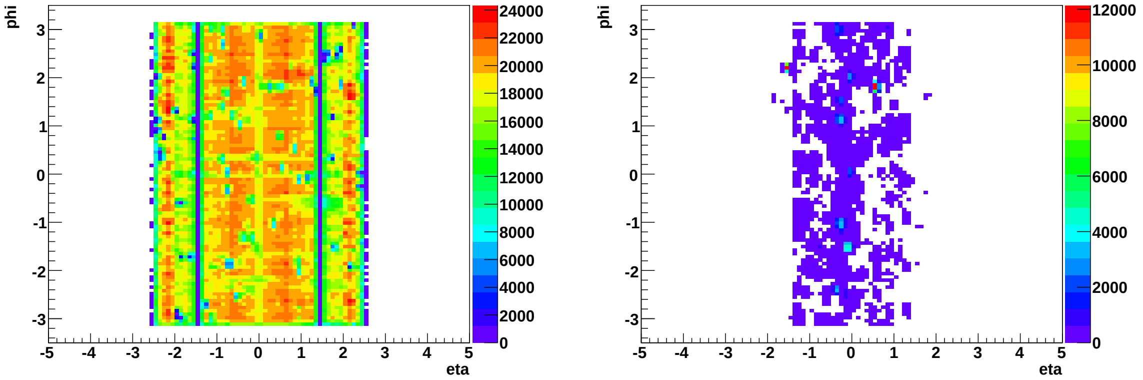

(a) Electrons without any masked cells (b) Electrons with masked cell in presampler

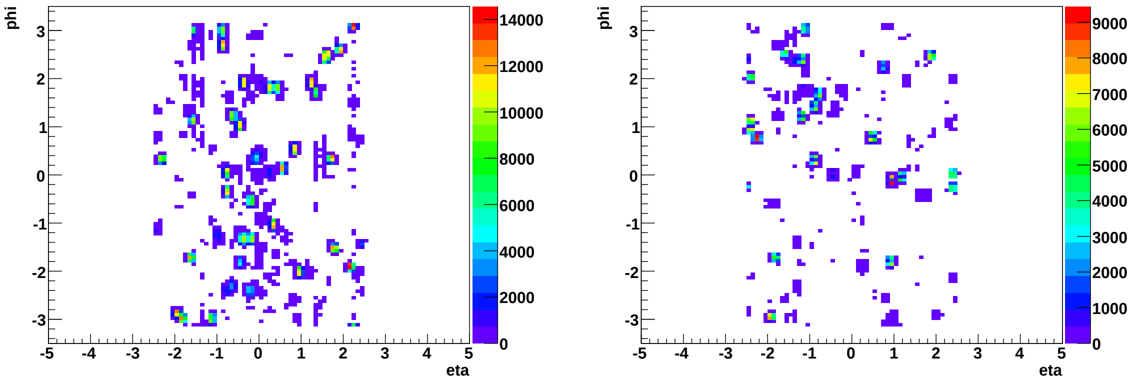

(c) Electrons with masked cell in S1 (d) Electrons with masked cell in S2

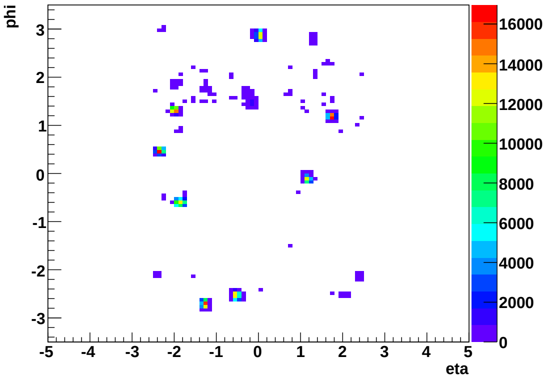

(e) Electrons with masked cell in S3

Figure 51: $\eta - \phi$ distributions for electrons without any masked cells (51(a)), with masked cells in presampler(51(b)), front layer (51(c)), middle layer (51(d)), and back layer (51(e))for all runs.

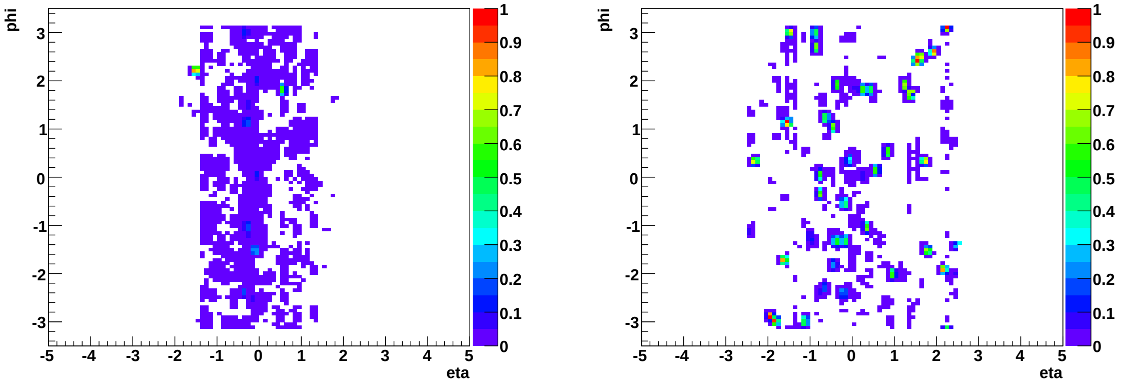

(a) Fraction of electrons with masked cell in presampler

(b) Fraction of electrons with masked cell in S1

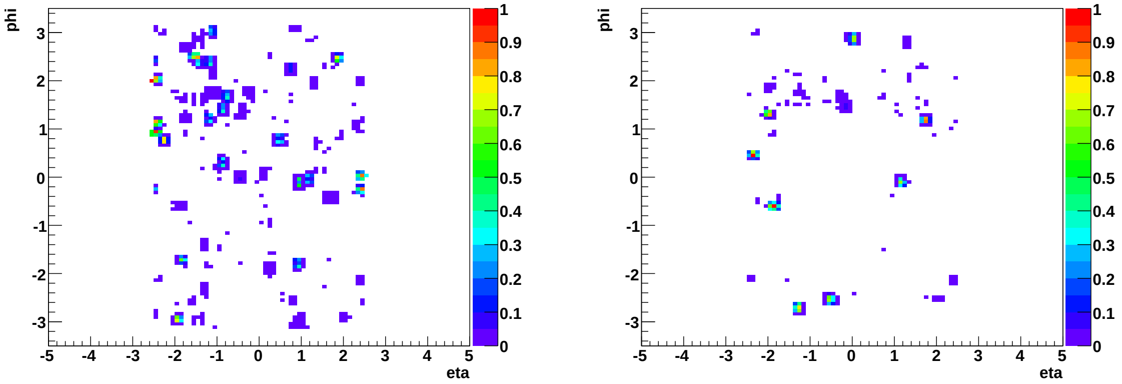

(c) Fraction of electrons with masked cell in S2

(d) Fraction of electrons with masked cell in S3

Figure 52: Fraction of electrons with masked cells in presampler(52(a)), front layer (52(b)), middle layer (52(c)), and back layer (52(d)) out of all electrons in the same $\eta - \phi$ bin.

The impact of masking can also affect reconstructed masses. The transverse mass, m_T, in W candidate events is calculated from the electron transverse momentum and $E_{\mathrm{T}}^{\mathrm{miss}}$. The m_T distributions for electrons with and without masked cells is shown in Fig. 53(e). There is a large low mass tail and attempts were made to estimate QCD contribution (in which jets from QCD fake an electron) but they were not successful. The calculated mean and RMS are in Table 47 for 40 GeV $< m_T <$ 120 GeV. The di-electron mass, m_{ee}, in Z candidate events is calculated using the p_{T} of the two electron candidates. The m_{ee} distributions (Fig. 53(f)) are fitted using a convolution of a Breit-Wigner and Crystal Ball function in the range 75 GeV $< m_{ee} <$ 105 GeV and the fit results can be found in Fig. 54 and Table 48. The functional form for a Breit-Wigner is given by:

$$\frac{1}{(x-\mu)^2 + \frac{1}{4}\Gamma^2} \tag{112}$$

The Crystal Ball function is given by:

$$e^{-\frac{1}{2}\left(\frac{x-m}{s}\right)^2}\Bigg|_{\frac{x-m}{s}>-|a|}, \quad \frac{\left(\frac{n}{|a|}\right)^n e^{-\frac{1}{2}a^2}}{\left(\frac{n}{|a|} - |a| - \frac{x-m}{s}\right)^n}\Bigg|_{\frac{x-m}{s}<-|a|} \tag{113}$$

Since the means of the two functions are not independent, the mean of the Cystal Ball function, m, is set to zero and the mean of the Breit-Wigner, μ, is allowed to float.

Fit to 40 GeV $< m_T <$ 120 GeV	Mean [GeV]	RMS [GeV]
No Masked Cells	74.005±0.002	14.407±0.002
Masked PreSamplerB Cell	74.143±0.044	14.363±0.031
Masked EMB1 Cell	74.295±0.018	14.469±0.013
Masked EMB2 Cell	74.332±0.033	14.629±0.023
Masked EMB3 Cell	74.039±0.035	14.438±0.025

Table 47: Mean and RMS of transverse mass distribution for $W \to e\nu$ candidate events with exactly one electron and $E_{\mathrm{T}}^{\mathrm{miss}} > 25$ GeV in the region 40 GeV $< m_T <$ 120 GeV.

D.5.2 Reprocessed run with sporadic noise masking turned off

As mentioned in the previous subsection, problematic cells are masked for the following problems: sporadically noisy cells with a high Q factor, high noise cells, and dead cells. Since high noise cells and dead cells are few and unchanging with time, of particular interest is the case of sporadically noisy cells. However, after electron reconstruction, the information needed to separate the three cases is no longer available. In order to study sporadically noisy cells only, a subset of events in Run 209381 was reprocessed with masking due to sporadically noisy cells turned off. The treatment of other types of masking (high noise, dead cells) was unchanged. This was done by adding the following during reprocessing:

- preExec='jobproperties.CaloCellFlags.doLArSporadicMasking.set_Value_and_Lock(False)'

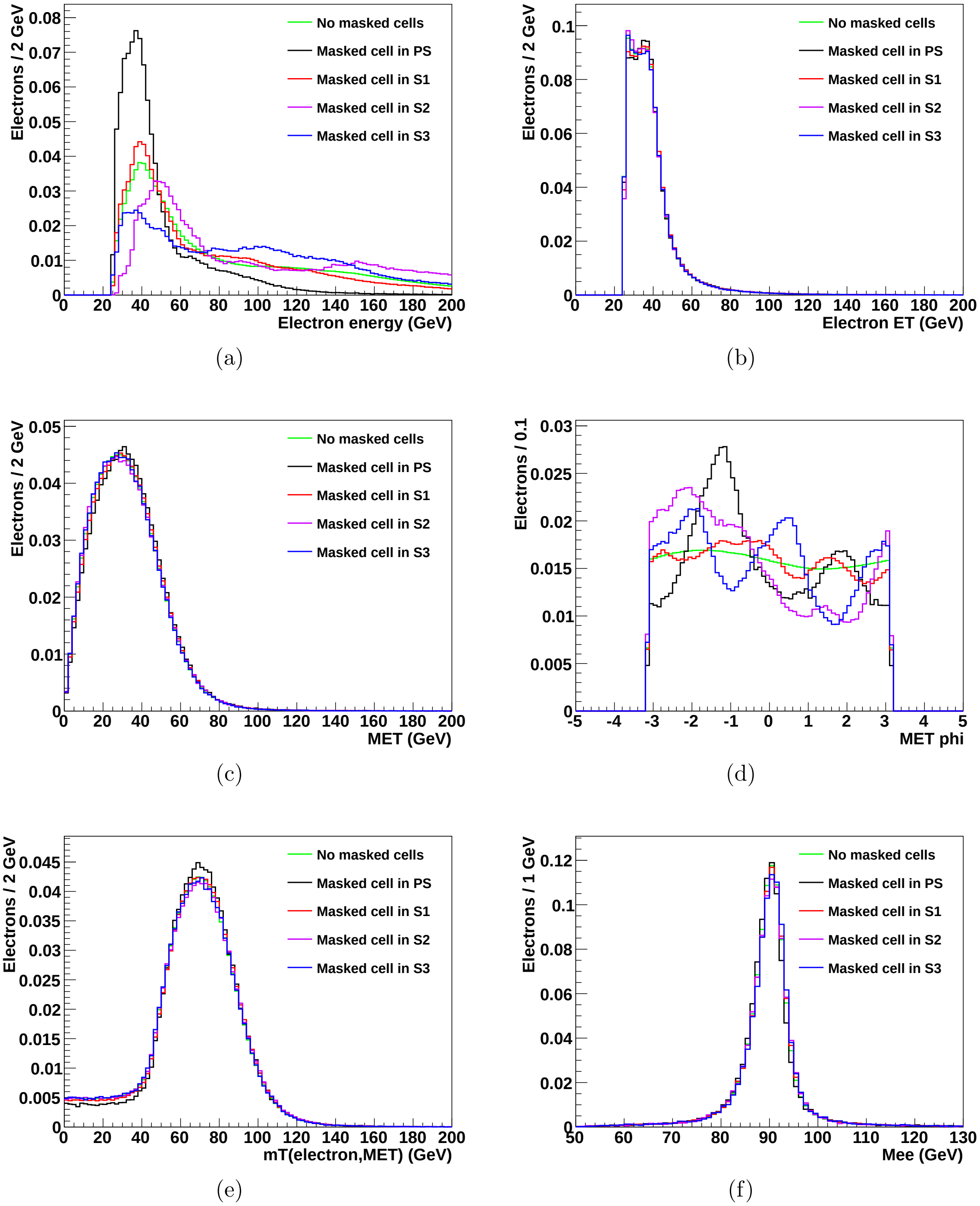

(a)

(b)

(c)

(d)

(e)

(f)

Transverse mass, m_T (53(e)), for events with $E_{\mathrm{T}}^{\mathrm{miss}} > 25$ GeV and exactly one electron. Di-electron mass, m_{ee}(53(f)), for events with exactly two electrons.

Figure 53: Kinematic distributions for electrons reconstructed with/without masked cells. Electron energy (53(a)) and transverse energy (53(b)). Missing transverse energy, (53(c)) and its phi direction(53(d)).

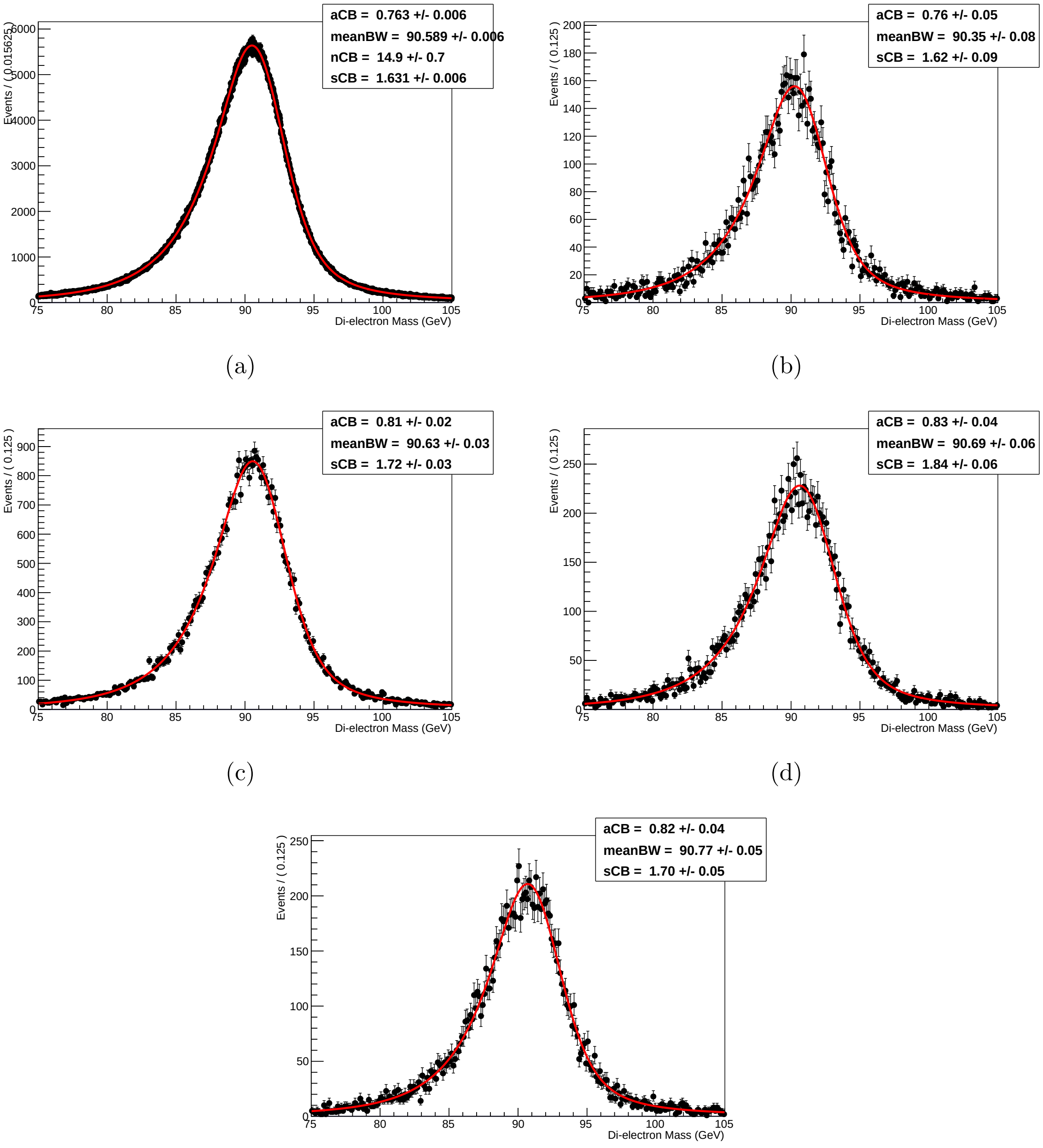

(a)

(b)

(c)

(d)

(e)

Figure 54: Fit results to di-electron mass (in the region 75 GeV $< m_{ee} <$ 105 GeV) using a convolution of a Breit-Wigner and Crystal Ball function for $Z \rightarrow ee$ candidate events with exactly two electrons. The fits are done separately for each case: (a) Electrons without any masked cells, and electrons with at least one masked cell in the (b) PS, (c) S1, (d) S2, and (e) S3. For the electrons with masked cell cases, the power, n, in the tail is fixed to 15. For all cases, the width of the Breit-Wigner is fixed to 2.77.

Sample	μ(BW) [GeV]	s(CB) [GeV]	a(CB)	n(CB)
No Masked Cells	90.589±0.006	1.631±0.006	0.763±0.006	15±1
Masked PS Cell	90.35±0.08	1.62±0.09	0.76±0.05	$n = 15$
Masked S1 Cell	90.63±0.03	1.72±0.03	0.81±0.02	$n = 15$
Masked S2 Cell	90.69±0.06	1.84±0.06	0.83±0.04	$n = 15$
Masked S3 Cell	90.77±0.05	1.70±0.05	0.82±0.04	$n = 15$

Sample	$\chi^2/ndof$
No Masked Cells	1.183
Masked PS Cell	1.019
Masked S1 Cell	1.040
Masked S2 Cell	0.958
Masked S3 Cell	0.774

Table 48: (Top) Fit values to di-electron mass (in the region 75 GeV $< m_{ee} <$ 105 GeV) using a convolution of a Breit-Wigner (BW) and Crystal Ball (CB) function for $Z \to ee$ candidate events with exactly two electrons. For the electrons with masked cell cases, the power, n, in the tail is fixed to 15. The fits are separately done for electrons with/without masked cells. (Bottom) χ^2 per degree of freedom for the fits.

The electrons from the reprocessed run (without masking due to sporadic noise) were matched to electrons with the nominal processing (with masking due to sporadic noise) by requiring that the event number is identical and difference in η and ϕ is less than 0.01 separately. Only electrons in the barrel, with $|\eta| < 1.3$ were studied.

The majority of electrons (97%) have no masked cells originally, thus reprocessing had no effect on the energy of the electron in each layer. For electrons that have a masked cell originally and also after reprocessing (2.3%), the reason for masking must be due to high noise or dead cells because only masking due to sporadic noise was turned off. The electron energy in each layer is identical after reprocessing for this case as well. The most interesting case is when electrons become unmasked after reprocessing (0.7%). The change in energy due to unmasking sporadically noisy cells in each of the layers is shown in Fig. 55. There were no cases in which an electron was originally unmasked but had a masked cell after reprocessing, which should be impossible.

D.6 Discussion

The fraction of electrons with masked cells in the front, middle, and back layers is very stable with respect to time or run number. The mean (RMS) fraction of electrons with masked cells for all runs are 0.23% (0.22%), 1.6% (0.09%), 0.55% (0.048%), and 0.49% (0.032%) for the presampler, front, middle, and back layer respectively.

The locations of masked cells does not change much within these layers except for the presampler. The list of sporadically noisy cells in the presampler changes frequently for each run, which corresponds to a large variation in the fraction of electrons with a masked cell in that layer.

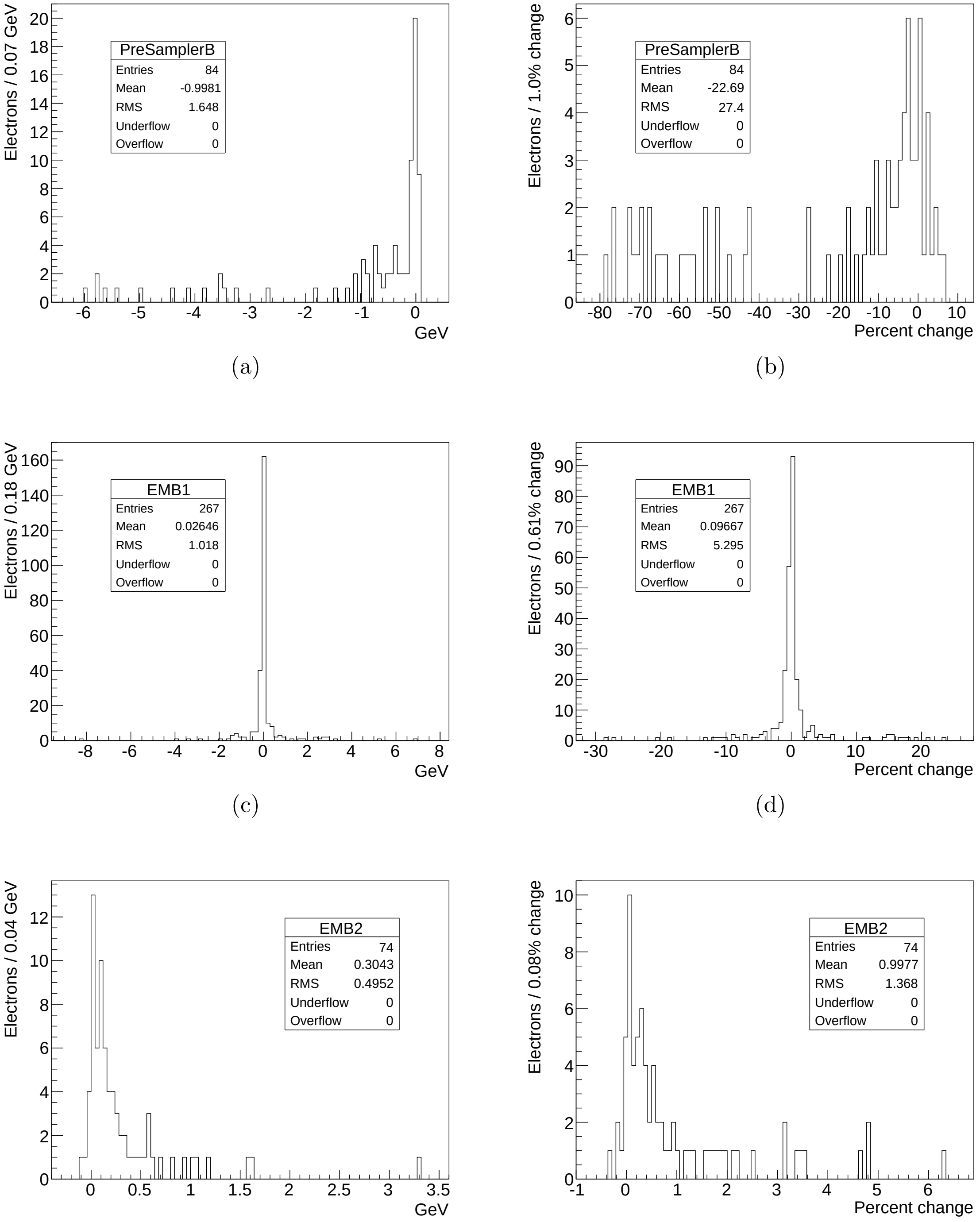

(a) (b)

(c) (d)

(e) (f)

Figure 55: The absolute change in electron energy in the presampler (55(a)), strip layer (55(c)), and middle layer (55(e)) between electrons reconstructed with and without masking due to sporadic noise. The sign of the difference was chosen such that a positive sign indicates that the electron energy was increased after masking. The percentage change is defined as the difference divided by the energy in the layer (before masking) is shown on the right plots. Here, only electrons located in the barrel, $|\eta| < 1.3$ are shown. The histogram is only filled if there is masking due to sporadic noise in that layer. There is no corresponding figure for the back layer as there were no electrons with a masked cell in EMB3 in the reprocessed run.

Differences in kinematic distributions for electrons with/without masked cells can reveal biases caused by masking in each layer. Although the total electron energy is quite different, especially when comparing electrons with masked cells in the presampler to those without masked cells, this can be explained by the correlation between η and energy. Since electrons with a masked cell in the presampler are located primarily in the low η region, these electrons have lower energy than those in the higher η regions. A better variable for comparison is the transverse electron energy, which shows much smaller differences. $E_{\mathrm{T}}^{\mathrm{miss}}$ distributions for electrons with/without masking are also very similiar. Note that the ϕ direction of $E_{\mathrm{T}}^{\mathrm{miss}}$ is quite different because the electrons without masking is highly non-uniform in η and ϕ.

Small differences in kinematic variables are propagated to calculated quantities such as invariant mass. For $Z \to ee$ events, the di-electron invariant mass is calculated for events with exactly two electrons and the distribution was fitted using a convolution of a Breit-Wigner and Crystal Ball function in the region 75 GeV $< m_{ee} <$ 105 GeV. The largest shift in the mean was 239 ± 80 MeV for the case of electrons with a masked cell in the presampler. The largest difference in the width was 209 ± 60 MeV for the case of an electrons with a masked S2 cell. For $W \to e\nu$ events, the transverse mass is calculated for events with exactly one electron and with $E_{\mathrm{T}}^{\mathrm{miss}} > 25$ GeV. In the region 40 GeV $< m_T <$ 120 GeV, the largest difference in the mean was 327 ± 44 MeV and the largest difference in the width (RMS) was 222 ± 23 MeV when comparing electrons with no masked cells to electrons with a masked cell in layer 2.

The reprocessed run with sporadically noisy cell masking turned off can revealed information not normally available. Previously masking due to high noise, dead cells, or sporadicically noisy cells could not be distinguished. It was found that 0.7% of electrons have masked cells due to sporadic noise compared to the 2.3% of electrons that have masked cells from other reasons.

The change in electron energy due to masking is dependent on the layer where the masking occurred. If in presampler, masking usually reduces the energy up to 80% of the original, unmasked energy in that layer. This is to be expected because the masking procedure is intended to reduce otherwise unusually high energy spikes in problematic cells. If masking occured in the front layer, the change in energy due to masking is quite small and usually less than 10%. For the middle layer, masking usually increases the energy up to 6%. The apparent change in sign may be explained by our exclusion of electrons that have masking in the cluster core, where the majority of the electron energy is deposited in the middle layer. In that case, the masking procedure may be systematically lowering the energy in that layer since it is replacing the energy in the cluster edge with the energy of neighbors that are in the cluster core.

D.7 Summary and conclusion

The impact of masked cells on reconstructed electrons was studied using 14pb^{-1}of data collected with the ATLAS detector in 2012. Approximately 0.7% of good quality electrons have at least one masked cell due to sporadic noise and 2.3% of electrons have high noise or dead cells. The fraction of electrons with masked cells in the front, middle, and back sampling layers is stable with time, but in the presampler, this fraction fluctuates much more than in the other layers. The energy replacement of sporadically noisy cells had a small effect ($< 10\%$) on the electron energy in the affected layer except in the presampler. When comparing electrons with masked cells to those without, no significant biases in physics distributions were found.

D.8 Acknowledgements

We thank Isabelle Wingerter, Stephanie Majewski, Benjamin Trocme, Walter Lampl, and Marco Delmastro for the helpful discussions and guidance.